VNIVERSITAT DE VALÈNCIA

Properties of exotic mesons in vacuum and embedded in a medium

Víctor Montesinos Llácer

Director/es: **Miguel Albaladejo Serrano**
Juan Miguel Nieves Pamplona
Laura Tolós Rigueiro

Programa de Doctorat en Física – 3126

Institut de Física Corpuscular

Octubre, 2025

Agradecimientos

Cuatro años han pasado desde que comencé el doctorado. Aunque otros períodos de formación suelen extenderse a lo largo de un tiempo comparable, al mirar atrás tengo la sensación de que estos años han transcurrido con sorprendente rapidez (excepto, quizá, los últimos meses dedicados a la escritura). Tal vez sea cierto, como dicta la sabiduría popular, que esta sensación es reflejo de que *he disfrutado*. Tanto por ese disfrute personal como por la consecución del trabajo que hoy culmina en este documento, considero esencial dedicar unas palabras a las personas sin las cuales nada de esto habría sido posible.

En primer lugar, agradecer enormemente a mis tutores: Juan, Miguel, Laura. Miguel, Laura, Juan. Laura, Juan, Miguel. Y las permutaciones impares también. No quiero poner a nadie delante de nadie, porque vosotros habéis hecho exactamente eso: acompañarme siempre de forma conjunta. Me habéis dedicado todo el tiempo que he necesitado (que no ha sido poco) y me habéis ayudado a superar todas las dificultades que presenta la vida doctoral. Si solo me hubierais orientado en la tesis, resolviendo con rapidez mis dudas conceptuales, analíticas y numéricas, ya habría sido más que suficiente. Pero además me habéis apoyado también en mis tropiezos burocráticos y en las decisiones laborales que tanto miedo me daba tomar en ciertos momentos. Agradezco en especial a Laura porque, a pesar de la distancia entre Valencia y Barcelona, siempre he sentido que estabas cerca. Por todo esto, y mucho más, mi más sincero agradecimiento a los tres. Me siento muy afortunado de haber tenido una terna tan excepcional, y mi mayor aspiración como físico y futuro tutor es llegar algún día a parecerme, aunque sea un poco, a cualquiera de vosotros. ¡Gracias de corazón!

I am also greatly thankful to Meng-Lin Du. I first met him in Valencia in the early years of my PhD, and he was very kind to me during that time. Later, I was fortunate to spend two research stays under his supervision at UESTC in Chengdu, China. The time I spent with him only deepened my admiration for him, both as a physicist and as a person. On a personal level, he was extremely caring, something I greatly appreciated, especially during the first weeks of adapting to life in a different country. Thanks to him, I overcame

much of my fear of living abroad. For this and much more, I wish to express my heartfelt gratitude. 杜孟林老师，衷心感谢。

I would also like to thank En Wang and Feng-Kun Guo for kindly hosting me in Zhengzhou and Beijing during my second stay in China. They were extremely kind and welcoming to me, and made both of these stays a very pleasant and enriching experience.

También me gustaría agradecer a todas las personas con quienes he tenido el placer de colaborar. A Eulogio Oset, a quien le debo una parte del trabajo aquí presentado, y cuya gran intuición física es fuente de inspiración. Agradezco también a Glòria Montaña, por toda su inestimable ayuda con los cálculos a temperatura finita, sin la cual esta tesis no habría sido posible. *I would also like to express my gratitude to Natsumi Ikeno, Wei-Hong Liang and Jing Song. It has been both an honor and a pleasure to meet you and collaborate with you.*

Agradezco también a los profesores con quienes tuve la suerte de iniciarme en la docencia en la Universitat de València, y de quienes aprendí muchísimo. Esta experiencia ha sido muy enriquecedora y no habría sido posible sin su apoyo. Muchas gracias a Santiago Noguera, Émilie Passemar, Francisco Campanario y Francisco José Botella. Quiero agradecer asimismo a los estudiantes de las asignaturas de Oscilaciones y Ondas, Mecánica I y Mecánica Cuántica II por su paciencia conmigo en clase y por enseñarme muchísimo. Gracias a todos.

Desde un punto de vista más personal, no puedo omitir un agradecimiento sentido también para mis compañeros y amigos doctorandos (algunos ya doctores) con quienes he compartido tantos buenos momentos a lo largo de estos años. Muchas gracias, Gustavo Guerrero, *maestro*, por tus siempre interesantes reflexiones y por tu sentido del humor. Disfruté mucho del mes que coincidimos en Chengdú. Muchas gracias a mi *hermana mayor de tesis*, Neus, con quien compartí muchos ratos divertidos en el despacho y muchos viajes Valencia-Crevillent durante los primeros años, y cuyo espíritu feminista me hizo caer en cuenta de la importancia de esta lucha. Agradecerte, además, por ayudarme a corregir el resumen en valenciano de esta tesis de manera *exprés*, justo antes del depósito. Muchísimas gracias de corazón por todo. Gracias a los Fernandos por su excelente *performance* cómica día tras día. En particular, a Fer Alv le agradezco sus propuestas de planes locos y el estupendo mes que compartimos la primera vez que fuimos a China (*unos baos?*). A Fer Gil darle las gracias por ser una de las personas más divertidas que conozco. Muchas gracias, *bonico*, por todo tu apoyo y *descante*, por todos los buenos ratos y por acogerme tantas tardes en tu casa. Agradezco también a Amador los descansitos juntos y su disposición para ayudarme siempre con mis dudas físicas. Muchas gracias, Julián, por todas esas noches de videojuegos, series y películas, y por tu loco sentido del humor. Lo he pasado en grande contigo. *Thank you, ZeJian, for your kindness. Our time in ZhengZhou was also very enjoyable.* Muchas

gracias también a Pablo Muñoz, con quien tantas divertidas charlas y tardes de juegos he compartido. Me alegra enormemente haberte conocido. No puedo dejar de mencionar a Gustavo Alcalá, por sus grandes dotes culinarias (¡gracias por esas *arepas*, maestro!) y su pasmante habilidad para terminar con toda la comida. De entre las incorporaciones más recientes, agradecer a David por su apoyo y sus memes de "*¿cómo va la tesis?*"; a Pietro agradecerle sus planes culturales y el sacarme de casa; a Pablo Encarnación, por popularizar los *Martes de Kebab* y por los ratos de desconexión que ahí hemos pasado. A mis nuevos compis de despacho, Mikel y Marta, agradecer los divertidos momentos que hemos pasado en las comidas, sus ánimos con la escritura de este documento en estos últimos meses, y su ayuda con el formato de algunas de las figuras que aquí se recogen. A Jesús le agradezco por los desayunos, las conversaciones frikis (principalmente sobre *Half-Life*) y por la ayuda con la traducción al valenciano del resumen de esta tesis, *and I am grateful to YiYao for our shared coffee breaks in the afternoon and his chinese lessons.*

También me gustaría agradecer al grupo de teoría hadrónica y nuclear por su apoyo y su cálida acogida desde el primer momento. Muchas gracias, Manolo, Luis, Raquel, Albert, PanPan, Alessandro, Juanma, Valerio, JiaXin y ZiYing. También agradezco a todas las integrantes de la CID, y a aquellas personas del IFIC con las que he mantenido conversaciones en los pasillos. Agradezco también a José Antonio Oller por su tutela durante mis primeros pasos en la investigación, y por dirigirme con muy buen criterio hacia Valencia. Asimismo, agradezco a todos mis profesores del grado de física en Murcia, de los que aprendí muchísimo.

Por supuesto, no puedo finalizar estos agradecimientos sin mencionar a algunas de las personas que han estado conmigo desde mucho antes de que empezara mi aventura doctoral. Gracias a Jaime, por estar ahí desde que tengo uso de razón. Gracias a Deivo, Diego, Fer, Erin, Joaquín, Kai y Laura por haberme acompañado ya más de doce años, y gracias a Alfredo, Ana, *Antoñico*, Leandro, Javi, Elisa, Pablo, Pedro, Eloísa (y a muchos más), por los muchos buenos momentos durante la carrera y después. Un sentido agradecimiento también para toda mi familia, empezando por la *familia Ricoteña*, que tanto me apoya y me ha apoyado. Gracias María Jesús, Alberto, Laura y Olaya. Gracias a la *familia Murciana*, Concha y Agustín, por ser mis tíos adoptivos desde que tengo memoria, y por supuesto gracias a la *familia Valenciana*, por todo su apoyo y afecto durante toda mi vida. Aunque no os mencione a todos, sabed que os llevo siempre conmigo. A quien sí he de mencionar es a mi *yayi*, Pepe, quien ha seguido y sigue de cerca mis aventuras al estilo *Marco Polo*, apoyándome en todo momento. Gracias también a las que no han podido estar aquí en esta última etapa, mis *yayas*, Ángeles y Guillermina, y mi abuelo Juan. Y sobre todo, muchísimas gracias a mis padres Pilar y Felipe por haberme

apoyado en esta etapa más que nunca, y por haberlo hecho en todas y cada una de las etapas de mi vida. A ellos también les debo mi gusto por la ciencia, ya que siempre fomentaron mi curiosidad y respondieron alegremente a mis preguntas sobre el mundo. Por esto y por todo lo demás, no hay palabras para expresar la gratitud que siento hacia vosotros.

A todos los que menciono aquí y a los que no he podido,
¡muchísimas gracias de corazón!

Valencia, 4 de octubre de 2025.
Víctor Montesinos Llácer.

Acknowledgment of Financial Support

The doctoral studies of V.M. were supported by the Generalitat Valenciana (GVA) through Grant No. ACIF/2021/290. The research stay in China was funded by the GVA under the mobility Grant No. CIBEFP/2023/051.

The works contained in this thesis have also benefited from financial support provided by the Spanish *Ministerio de Ciencia e Innovación* (MCIN/AEI/10.13039/501100011033) under contracts No. PID2019-110165GB-I00, No. PID2020-112777GB-I00, and No. PID2022-139427NB-I00, with FEDER co-funding from the European Union. Additional support was received from the Generalitat Valenciana under contract PROMETEO/2020/023, from the excellence programs CEX2020-001058-M (Unidad de Excelencia "María de Maeztu") and CEX2023-001292-S (Centro de Excelencia "Severo Ochoa"), and from the Horizon 2020 STRONG-2020 project (Grant Agreement No. 824093, H2020-INFRAIA-2018-1). Further support came from the CRC-TR 211 "Strong-interaction matter under extreme conditions" (project No. 315477589 – TRR 211) and from the Generalitat de Catalunya under contract 2021 SGR 171.

Nomenclature

AMPT A Multi-Phase Transport Model

BNL Brookhaven National Laboratory

BSE Bethe–Salpeter Equation

CBM Compressed Baryonic Matter Experiment

ChPT Chiral Perturbation Theory

EFT Effective Field Theory

FAIR Facility for Antiproton and Ion Research

FCA Fixed Center Approximation

HHChPT Heavy-Hadron ChPT

HIC Heavy-Ion Collision

HMChPT Heavy-Meson ChPT

HQET Heavy–Quark Effective Theory

HQFS Heavy–Quark Flavor Symmetry

HQSS Heavy–Quark Spin Symmetry

ITF Imaginary Time Formalism

LEC Low-Energy Constant

LHC Large Hadron Collider

LQCD Lattice QCD

LSE Lippmann–Schwinger Equation

NICA Nuclotron-based Ion Collider fAcility

PANDA antiProton ANnihilation at DArmstadt

QCD Quantum Chromodynamics

QFT Quantum Field Theory

QGP Quark–Gluon Plasma

RHIC Relativistic Heavy Ion Collider

SPS Super Proton Synchrotron

WT Weinberg-Tomozawa

Abstract

Quantum Chromodynamics (QCD), the theory of the strong interaction among quarks and gluons—the fundamental constituents of hadrons—stands as one of the pillars of the Standard Model of particle physics. A landmark refinement in the development of hadron spectroscopy was the relativized quark model of Godfrey and Isgur, whose predictions successfully reproduced much of the observed hadron spectrum and established a framework that remains influential today. Yet, the conventional quark model has intrinsic limitations. Long-standing puzzles, such as the $\Lambda(1405)$ resonance, defied a simple quark-model interpretation and pointed to the need for alternative explanations. Over the past two decades, hadron spectroscopy has undergone remarkable progress—sometimes referred to as the "second revolution of hadron physics"—driven by the discovery of numerous states that cannot, or can only unnaturally, be accommodated within the conventional quark model. These are collectively known as *exotic states*. A second major frontier in hadron physics concerns the behavior of strongly interacting matter under extreme conditions of baryon density and/or temperature. Mapping the QCD phase diagram remains one of the central open challenges in the field, with implications that span from the early Universe to the structure of neutron stars, as well as to our theoretical understanding of confinement and chiral symmetry breaking. This thesis brings together these two lines of research by exploring the properties of exotic hadronic states both in vacuum and in hot or dense strongly interacting matter.

We begin in Chapter 2 by examining how two prominent exotic states—the $T_{cc}(3875)$ and the $D_{s0}^*(2317)$, hereafter referred to as T_{cc} and D_{s0}^*—together with their heavy–quark spin symmetry (HQSS) partners, are modified in a dense nuclear medium. These states are modeled as $D^{(*)}D^*$ and $D^{(*)}K$ hadronic molecules, respectively. After reviewing the theoretical framework of nuclear matter, we introduce the concepts of self–energy and spectral functions and describe how they can be computed using effective field theories constrained by heavy–quark and chiral symmetries. We then analyze in-medium meson–meson scattering, employing interactions tuned to reproduce different molecular probabilities in the wave function. Our results demonstrate that increasing

nuclear density and molecular probability leads to a broadening of the scattering amplitudes and spectral functions. In addition, we find a marked charge–conjugation asymmetry—especially pronounced for the D^*_{s0}—which further enhances the density and molecular–probability dependence of the results. If such modifications could be measured, they would provide a novel probe of meson–meson interactions, meson– and antimeson–nucleon interactions, and the internal structure of these exotic states.

Turning to the question of how to access density–dependent hadron properties experimentally, Chapter 3 examines the feasibility of measuring such effects for the D meson, a key constituent of the exotic states previously discussed. The study relies on the *transparency ratio* technique, successfully applied to the η' meson, in which the particle of interest is photoproduced off various nuclei A via $\gamma A \to D^+ D^- A'$. The corresponding cross section depends both on the D–meson photoproduction on a bound nucleon and on its absorption probability while propagating through the nucleus. By normalizing to the ^{12}C cross section, one cancels the production mechanism and isolates the absorption probability, which scales approximately with the nuclear radius. This absorptive component is directly related to the imaginary part of the D–meson self–energy in nuclear matter. Using a simple nuclear model together with theoretical predictions for the D self–energy, we obtain transparency ratios of about 0.6 for heavy nuclei. Such values suggest that these measurements could be realistically achieved at future facilities such as the EIC, EicC, or a possible upgrade of GlueX.

Chapter 4 shifts the focus from density to temperature, presenting a study of the exotic T_{cc} and its HQSS partner in a hot pionic bath. We begin by introducing the main ideas of *thermal field theory* in the *imaginary–time* (Matsubara) formalism. The analysis builds on the $D^{(*)}D^*$ interaction model developed in Chap. 2, which dynamically generates the T_{cc} pole in the amplitude and allows the molecular probability to be tuned. For this purpose, the D and D^* self–energies and spectral functions in a hot pion medium are required; these are taken from the literature, after briefly discussing their computation. In close analogy with the high–density case, we obtain a T_{cc} spectral function that is strongly dependent on the molecular probability. For large probabilities, the resonance melts at temperatures of the order of 100 MeV, whereas for small probabilities the results are highly sensitive to the details of the $D^{(*)}D^*$ interaction. These findings suggest that experimental information on $D^{(*)}D^*$ scattering at finite T—as accessible at RHIC or the LHC—could provide valuable insight into the molecular nature of the T_{cc} and its HQSS partner. Furthermore, combining such studies with potential measurements of their spectral properties at finite density (e.g. at FAIR) would offer strong complementary constraints on their structure and composition.

Lastly, in Chapter 5 we return to the free space (vacuum) to explore

another exotic–like configuration: three–body bound states. Motivated by the discovery of the T_{cc} and the implied attractive interaction between D and D^* mesons, we investigate the possibility of a DND^* bound system. The DN and D^*N interactions, previously employed in Chapter 2 to study charmed–meson spectral functions in nuclear matter, are revisited here. The analysis is carried out using the fixed–center approximation to the Faddeev equations, which provides an appropriate framework for the three–body dynamics. Assuming the D^*N subsystem to be bound into either the $\Lambda_c(2940)$ or $\Lambda_c(2910)$, depending on the total spin of the three-body system, we find resonant–like structures in the $J^P = 1/2^+$ and $3/2^+$ channels. Qualitatively similar results emerge when instead considering the DN pair bound into the $\Lambda_c(2765)$. Within the uncertainties of the approach, these findings support the possible existence of such states. Their experimental confirmation would provide valuable information on the DN and D^*N interactions, thereby clarifying the role of molecular dynamics in the Λ_c^* spectrum.

The work presented in this thesis has led to the publication of several articles [1–5] (four published and one under review), as well as presentations at international conferences [6–8].

Resumen

La Cromodinámica Cuántica (QCD), la teoría que describe la interacción fuerte entre quarks y gluones (los constituyentes fundamentales de los hadrones), constituye uno de los pilares del Modelo Estándar de la física de partículas. Un avance clave en el desarrollo de la espectroscopía hadrónica fue el modelo de quarks relativizado de Godfrey e Isgur, cuyas predicciones lograron reproducir gran parte del espectro hadrónico observado y establecieron un marco que sigue siendo influyente en la actualidad. Sin embargo, el modelo de quarks convencional presenta limitaciones intrínsecas. Algunos enigmas persistentes, como la resonancia $\Lambda(1405)$, escapaban a una interpretación sencilla dentro de este marco y apuntaban a la necesidad de explicaciones alternativas. En las dos últimas décadas, la espectroscopía de hadrones ha vivido un progreso notable (a menudo denominado la "segunda revolución de la física de hadrones"), impulsado por el descubrimiento de numerosos estados que no encajan, o solo de forma forzada, en el modelo tradicional. Estos se conocen colectivamente como *estados exóticos*. Otra frontera destacada de la física hadrónica aborda el comportamiento de la materia fuertemente interactuante en condiciones extremas de densidad bariónica y/o temperatura. La descripción del diagrama de fases de QCD sigue siendo uno de los grandes desafíos abiertos, con implicaciones que abarcan desde el Universo primitivo hasta la estructura de las estrellas de neutrones, además de aportar claves para comprender el confinamiento y la ruptura de la simetría quiral. Esta tesis conecta estas dos líneas de investigación estudiando las propiedades de estados hadrónicos exóticos tanto en el vacío como en los medios densos o calientes de materia fuertemente interactuante.

En el Capítulo 2 analizamos cómo dos estados exóticos relevantes (el $T_{cc}(3875)$ y el $D_{s0}^*(2317)$, en adelante T_{cc} y D_{s0}^*), junto con sus compañeros relacionados por la simetría de espín del quark pesado (HQSS), se modifican en un medio nuclear denso. Estos estados se modelan como moléculas hadrónicas $D^{(*)}D^*$ y $D^{(*)}K$, respectivamente. Tras repasar el marco teórico de la materia nuclear, introducimos los conceptos de autoenergía y funciones espectrales, y explicamos cómo calcularlos mediante teorías de campos efectivas basadas en las simetrías quirales y de quark pesado. Posteriormente estudiamos

la dispersión mesón–mesón en el medio, utilizando interacciones ajustadas para reproducir diferentes probabilidades moleculares en su función de onda. Nuestros resultados muestran que un aumento de la densidad nuclear y de la probabilidad molecular provoca un ensanchamiento de las amplitudes de dispersión y de las funciones espectrales. Además, identificamos una clara asimetría de conjugación de carga (especialmente pronunciada en el D_{s0}^*), que refuerza aún más la dependencia de los resultados con la densidad y la probabilidad molecular. Si estas modificaciones pudieran medirse experimentalmente, constituirían una nueva herramienta para investigar las interacciones mesón–mesón, mesón–nucleón y antimesón–nucleón, así como la estructura interna de estos estados exóticos.

Respecto al acceso experimental a propiedades hadrónicas dependientes de la densidad, el Capítulo 3 estudia la viabilidad de medir tales efectos en el mesón D, un constituyente esencial de los estados exóticos mencionados anteriormente. El análisis se basa en la técnica del *cociente de transparencia*, utilizada con éxito para el mesón η', en la que la partícula de interés se fotoproduce en distintos núcleos A mediante la reacción $\gamma A \to D^+ D^- A'$. La sección eficaz resultante depende tanto de la fotoproducción del mesón D en un nucleón ligado como de su probabilidad de absorción al propagarse por el núcleo. Al normalizar con respecto a la sección eficaz en ^{12}C, se elimina la contribución del mecanismo de producción y se aísla la probabilidad de absorción, que escala aproximadamente con el radio nuclear. Este término de absorción está directamente relacionado con la parte imaginaria de la autoenergía del mesón D en materia nuclear. A partir de un modelo nuclear sencillo y de predicciones teóricas para la autoenergía del D, obtenemos cocientes de transparencia en torno a 0.6 para núcleos pesados. Estos valores sugieren que tales mediciones podrían realizarse de manera realista en futuras instalaciones como el EIC, EicC o una posible actualización de GlueX.

El Capítulo 4 cambia el enfoque de la densidad a la temperatura, con un estudio del estado exótico T_{cc} y de su compañero HQSS en un baño térmico piónico. Se presentan las ideas fundamentales de la *teoría térmica de campos* en el formalismo de *tiempo imaginario* (Matsubara). El análisis se apoya en el modelo de interacción $D^{(*)}D^*$ desarrollado en el Cap. 2, que genera dinámicamente el polo del T_{cc} en la amplitud y permite ajustar la probabilidad molecular. Para ello, se necesitan las autoenergías y funciones espectrales de D y D^* en un medio térmico de piones. Utilizamos resultados obtenidos previamente, aunque hacemos una breve revisión de su cálculo. De forma análoga al caso de medios densos, obtenemos una función espectral del T_{cc} muy dependiente de la probabilidad molecular. Para probabilidades altas, la resonancia se funde a temperaturas cercanas a 100 MeV, mientras que para probabilidades bajas los resultados son extremadamente sensibles a los

detalles de la interacción $D^{(*)}D^*$. Estos hallazgos indican que la información experimental sobre la dispersión $D^{(*)}D^*$ a temperatura finita (como la accesible en RHIC o en el LHC) podría aportar claves importantes sobre la naturaleza molecular del T_{cc} y de su compañero HQSS. Asimismo, combinar estos estudios con posibles medidas de sus propiedades espectrales a densidad finita (por ejemplo, en FAIR) ofrecería restricciones complementarias sólidas sobre su estructura y composición.

Finalmente, en el Capítulo 5 regresamos al espacio libre (vacío) para explorar otra configuración de tipo exótico: los estados ligados de tres cuerpos. Motivados por el descubrimiento del T_{cc} y la interacción atractiva implícita entre los mesones D y D^*, estudiamos la posible existencia de un sistema ligado DND^*. Las interacciones DN y D^*N, ya empleadas en el Capítulo 2 para analizar las funciones espectrales de mesones con encanto en materia nuclear, son revisadas aquí. El estudio se lleva a cabo mediante la aproximación de centro fijo a las ecuaciones de Faddeev, que ofrece un marco accesible para la dinámica de tres cuerpos. Suponiendo que el subsistema D^*N se ligue formando la $\Lambda_c(2940)$ o en la $\Lambda_c(2910)$ (según el espín total del sistema), encontramos estructuras de tipo resonancia en los canales $J^P = 1/2^+$ y $3/2^+$. Resultados similares se obtienen al considerar en su lugar al par DN ligado formando la $\Lambda_c(2765)$. Dentro de las incertidumbres del esquema, estos resultados apoyan la posible existencia de dichos estados. Su confirmación experimental proporcionaría información valiosa sobre las interacciones DN y D^*N, aclarando el papel de la dinámica molecular en el espectro de los estados Λ_c^*.

El trabajo presentado en esta tesis ha dado lugar a la publicación de varios artículos [1–5] (cuatro publicados y uno en revisión), así como a presentaciones en congresos internacionales [6–8].

Resum

La teoria de la Cromodinàmica Quàntica (QCD) és un dels pilars del Model Estàndard de la física de partícules. Aquesta teoria descriu la interacció forta entre quarks i gluons, que son els constituents fonamentals dels hadrons, Un avanç decisiu en el desenvolupament de l'espectroscòpia hadrònica va ser el model de quarks relativitzat de Godfrey i Isgur, les prediccions del qual van reproduir amb èxit bona part de l'espectre hadrònic observat i van establir un marc que continua sent de referència hui en dia. Tanmateix, el model de quarks convencional presenta limitacions intrínseques. Enigmes irresolts, com la ressonància $\Lambda(1405)$, van quedar fora d'una interpretació senzilla dins d'aquest marc i van assenyalar la necessitat d'explicacions alternatives. En les últimes dues dècades, l'espectroscòpia d'hadrons ha experimentat un progrés notable (sovint anomenat la "segona revolució de la física d'hadrons"), impulsat pel descobriment de nombrosos estats que no poden, o només de manera forçada, encaixar dins del model tradicional. Aquests es coneixen col·lectivament com *estats exòtics*. Una altra frontera destacada en la física hadrònica és l'estudi del comportament en condicions extremes de densitat bariònica i/o temperatura de la matèria fortament interactuant. Determinar el diagrama de fases de la QCD continua sent un dels grans reptes oberts del camp, amb implicacions que van des de l'Univers primitiu fins a l'estructura de les estrelles de neutrons, a més d'aportar noves claus per a la nostra comprensió teòrica del confinament i de la ruptura de la simetria quiral. Aquesta tesi ha unit aquestes dues línies d'investigació estudiant les propietats dels estats hadrònics exòtics tant en el buit com en medis densos o calents de matèria fortament interactuant.

En el Capítol 2 hem analitzat com dos estats exòtics prominents (el $T_{cc}(3875)$ i el $D_{s0}^{*}(2317)$), juntament amb els seus companys relacionats per la simetria d'espín de quark pesat (HQSS), es modifiquen en un medi nuclear dens. Aquests estats els hem modelat com a molècules hadròniques $D^{(*)}D^{*}$ i $D^{(*)}K$, respectivament. Després de revisar el marc teòric de la matèria nuclear, hem introduit els conceptes d'autoenergia i funcions espectrals, i hem descrit com es poden calcular mitjançant teories efectives de camps condicionades per les simetries quirals i de quark pesat. A continuació, hem estudiat la dispersió

mesó–mesó al medi, emprant interaccions ajustades per reproduir diferents probabilitats moleculars en la funció d'ona. Els nostres resultats mostren que l'augment de la densitat nuclear i de la probabilitat molecular provoca un eixamplament de les amplituds de dispersió i de les funcions espectrals. A més, hem identificat una marcada asimetria de conjugació de càrrega (especialment intensa per al D_{s0}^*), que reforça encara més la dependència dels resultats amb la densitat i la probabilitat molecular. Si aquestes modificacions es pogueren mesurar experimentalment, constituirien una nova eina per a investigar les interaccions mesó–mesó, mesó–nucleó i antimesó–nucleó, així com l'estructura interna d'aquests estats exòtics.

Pel que fa a l'accés experimental a propietats hadròniques dependents de la densitat, en el Capítol 3, hem estudiat la viabilitat de mesurar aquestes propietats en el mesó D, un constituent fonamental dels estats exòtics esmentats prèviament. L'estudi s'ha basat en la tècnica del *cocient de transparència*, aplicada amb èxit al mesó η', en què la partícula d'interés es fotoproduïx en diversos nuclis A mitjançant la reacció $\gamma A \to D^+ D^- A'$. La secció eficaç resultant depén tant de la fotoproducció del mesó D en un nucleó lligat com de la seua probabilitat d'absorció al propagar-se pel nucli. Quan es normalitza respecte a la secció eficaç en ^{12}C, s'elimina la dependència del mecanisme de producció i s'aïlla la probabilitat d'absorció, que escala aproximadament amb el radi nuclear. Aquest terme d'absorció està directament relacionat amb la part imaginària de l'autoenergia del mesó D en matèria nuclear. Amb un model nuclear senzill i prediccions teòriques per a l'autoenergia del D, hem obtingut cocients de transparència d'aproximadament 0.6 per a nuclis pesats. Aquests valors indiquen que aquestes mesures poden dur-se a terme de manera realista en instal·lacions futures com l'EIC, l'EicC o una possible ampliació de GlueX.

El Capítol 4 trasllada el focus de la densitat a la temperatura, amb un estudi de l'estat exòtic $T_{cc}(3875)$ i del seu company HQSS en un bany tèrmic piònic. Primer, hem presentat les idees bàsiques de la *teoria de camps tèrmics* en el formalisme de *temps imaginari* (Matsubara). L'anàlisi es fonamenta en el model d'interacció $D^{(*)}D^*$ desenvolupat en el Cap. 2, que genera dinàmicament el pol del T_{cc} en l'amplitud i permet ajustar la probabilitat molecular. Per a això, van ser necessàries les autoenergies i funcions espectrals de D i D^* en un medi de pions calents, que hem pres de la literatura després de comentar breument el seu càlcul. En estreta analogia amb el cas d'alta densitat, hem obtingut una funció espectral del T_{cc} molt dependent de la probabilitat molecular. Per a probabilitats elevades, la ressonància es dissol a temperatures d'uns 100 MeV, mentre que per a probabilitats baixes, els resultats son extremadament sensibles als detalls de la interacció $D^{(*)}D^*$. Aquestes troballes suggerixen que la informació experimental sobre la dispersió $D^{(*)}D^*$ a temperatura finita (com la que és accessible en RHIC o al LHC) podria aportar pistes valuoses sobre la naturalesa

molecular del $T_{cc}(3875)^+$ i del seu company HQSS. A més, combinar aquests estudis amb possibles mesures de les seues propietats espectrals a densitat finita (per exemple, en FAIR) proporcionaria restriccions complementàries sòlides sobre la seua estructura i composició.

Finalment, en el Capítol 5 hem tornat a l'espai lliure (buit) per explorar una altra configuració de tipus exòtic: els estats lligats de tres cossos. Motivats pel descobriment del T_{cc} i per la interacció atractiva implícita entre els mesons D i D^*, hem estudiat la possible existència d'un sistema lligat DND^*. Les interaccions DN i D^*N, que havíem emprat prèviament en el Capítol 2 per analitzar les funcions espectrals de mesons amb *charm* en matèria nuclear, han estat revisitades ací. L'estudi s'ha dut a terme mitjançant l'aproximació de centre fix de les equacions de Faddeev, que ofereix un marc accessible per a la dinàmica de tres cossos. Suposant que el subsistema D^*N està lligat formant la $\Lambda_c(2940)$ o la $\Lambda_c(2910)$ (segons l'espín total del sistema), hem trobat estructures de tipus ressonància en els canals $J^P = 1/2^+$ i $3/2^+$. Resultats similars apareixen també quan considerem la parella DN lligada formant la $\Lambda_c(2765)$. Dins de les incerteses del plantejament, aquests resultats donen suport a la possible existència de tals estats. La seua confirmació experimental aportaria informació valuosa sobre les interaccions DN i D^*N, aclarint el paper de la dinàmica molecular en l'espectre dels estats Λ_c^*.

El treball presentat en aquesta tesi ha donat lloc a la publicació de diversos articles [1–4], així com a presentacions en congressos internacionals [6–8].

Contents

1

Introduction

Spectroscopy has played a central role in the development of modern physics, providing crucial insight into the symmetries and underlying dynamics of physical systems. A paradigmatic example is the spectroscopic study of the hydrogen atom, which was instrumental in the birth of quantum mechanics and, later, the formulation of quantum electrodynamics. These advances ultimately paved the way for the Standard Model of particle physics, our most successful framework to date for describing the known elementary particles and their interactions. Among its pillars stands *Quantum Chromodynamics* (QCD), the theory of the strong interaction, which governs the dynamics of quarks and gluons through their color charge and explains the formation of hadrons as bound states of these fundamental constituents.

Beyond the study of hadrons in vacuum, an equally important question concerns their behavior in a strongly interacting medium. Embedding hadrons in nuclear matter or exposing them to high temperatures modifies their masses, widths, and interactions, reflecting the underlying changes in their structure. Such medium effects are not only of theoretical interest but also have direct phenomenological consequences: in nuclear physics, they influence the possible formation of bound states of mesons with nuclei; in astrophysics, they are essential for understanding the equation of state of neutron stars; and in high–energy physics, they play a central role in the characterization of the quark–gluon plasma created in relativistic heavy–ion collisions. This dual perspective—on hadrons as both isolated states and as probes of extreme environments—motivates the two main lines of research followed in this manuscript.

At its core, this thesis focuses on the study of *exotic hadronic states*—configurations beyond the conventional quark–antiquark and three–quark picture—within the theoretical framework of low–energy QCD. Particular attention is given to how such states, exemplified by the $T_{cc}(3875)^+$ and the $D_{s0}^*(2317)$, respond to extreme conditions of nuclear density and temperature.

Their medium modifications provide a unique window into the interplay of the compact and molecular components in their wave function, while their role in the possible formation of three-body bound states opens an additional venue of investigation. To set the stage, the remainder of this introduction offers a brief overview of QCD and highlights the open questions that continue to drive research in this field.

1.1 EFT approaches for QCD at low energies

QCD is formulated as a non-Abelian gauge theory based on the local SU(3) color symmetry. Quarks transform under the fundamental representation, while gluons belong to the adjoint representation and mediate the interaction by carrying color themselves. The non-Abelian character of SU(3) color is intimately related to some of QCD's most distinctive features, such as gluon self-interactions, *asymptotic freedom* at high energies, and *color confinement* at low energies. Whereas asymptotic freedom drives the QCD coupling weak at high energies—making perturbation theory reliable for hard processes—confinement renders the low-energy regime intractable for standard perturbative methods. Understanding hadrons and their interactions therefore requires alternative strategies to standard perturbation theory in order to capture the essential non-perturbative dynamics of QCD at low energies. On the numerical side, Lattice QCD (LQCD) provides a first-principles approach by evaluating (Euclidean) correlators in the path-integral formalism, and has achieved remarkable success in reproducing much of the hadron spectrum. On the analytical side, there are several methods, among which the *effective field theory* (EFT) approach plays a central role.[1] It is within this EFT framework that the present work is situated.

EFTs provide a powerful framework to describe physics in regimes where a full treatment of the underlying dynamics is either unknown or computationally intractable. The central idea is to identify the relevant degrees of freedom at a given energy scale and to construct the most general Lagrangian consistent with the symmetries of the fundamental theory. The unresolved short-distance dynamics is then systematically encoded in a finite set of low-energy constants (LECs).[2] In QCD's low-energy regime, the growth of the strong coupling

[1] Although we contrast EFTs with LQCD here for exposition, there are also lattice-inspired simulations built on EFTs. A prominent example is Nuclear Lattice Effective Field Theory [9, 10], which has been used to compute the structure and spectrum of different nuclei.

[2] Strictly speaking, most low-energy EFTs (e.g., ChPT, HQET, HHChPT) are nonrenormalizable in the traditional sense: loop divergences require an infinite tower of higher-dimensional counterterms. With a power-counting scheme, however, they are renormalizable order by order, so at any fixed order only a finite number of LECs enter. These LECs encode short-distance physics and are fixed by data or by matching to the underlying theory. By contrast, renormalizable gauge theories such as QCD and QED require counterterms only

constant renders perturbation theory unreliable: Green functions receive dominant nonperturbative contributions and a weakly interacting quasi-particle description in terms of quarks and gluons breaks down. It is therefore natural to formulate an EFT in terms of color-singlet hadronic degrees of freedom, with a Lagrangian constrained by QCD's symmetries and with short-distance dynamics absorbed into the LECs. The choice of hadronic fields and the approximate symmetries to be emphasized depend on the energy scale of interest.

A key ingredient in the construction of QCD–motivated EFTs is the presence of a natural hadronic scale, $\Lambda_{\rm QCD} \sim 0.2 - 0.3$ GeV, associated with the onset of confinement and nonperturbative dynamics. This scale allows one to classify quarks into "light" and "heavy" depending on whether their masses are small or large compared to $\Lambda_{\rm QCD}$.[3] The light quarks (u, d, s) satisfy $m_q \ll \Lambda_{\rm QCD}$, while the heavy quarks (c, b, t) fulfill $m_Q \gg \Lambda_{\rm QCD}$. In each case, different approximate symmetries emerge, which constrain the form of the EFT at low energies.

One of the paradigmatic QCD–motivated effective theories is ChPT, built on the approximate chiral symmetry of the QCD Lagrangian. In the limit of vanishing light–quark masses $m_u, m_d, m_s \to 0$ (with $N_f = 3$), the theory enjoys a global $\mathrm{SU}(3)_L \times \mathrm{SU}(3)_R$ symmetry acting separately on left– and right–handed quark fields. However, the QCD vacuum preserves only the vector subgroup $\mathrm{SU}(3)_V$. The axial generators are spontaneously broken and, according to Goldstone's theorem, this produces $N_f^2 - 1 = 8$ massless Goldstone bosons, identified with the pseudoscalar octet $(\pi, K, \bar{K}, \eta_8)$. Because chiral symmetry is only approximate—explicitly broken by the light quark masses—and the $\mathrm{U}(1)_A$ symmetry is anomalous, these states acquire masses and are therefore pseudo–Nambu–Goldstone bosons (with the mass of the singlet η' driven very large by the anomaly). ChPT is the corresponding low–energy EFT describing their interactions, organized as a systematic expansion in external momenta and light–quark masses over the chiral scale $\Lambda_\chi \sim 0.7 - 1$ GeV, with LECs encoding short–distance QCD dynamics [11–14].

An important development in the theoretical implementation of ChPT occurred with the introduction of Unitarized ChPT (UChPT). The central idea is to take a low-order chiral amplitude and unitarize it through the

for operators already present in the Lagrangian, so no new independent parameters appear beyond masses, couplings, and field renormalizations. Despite introducing LECs, EFTs remain predictive because higher-order effects are systematically suppressed by powers of E/Λ, with Λ the hard energy scale of the EFT.

[3] The definition of quark masses is subtle, since quarks are confined and cannot be measured directly. In practice, one adopts a renormalization scheme (typically $\overline{\rm MS}$) and quotes scale–dependent running masses. Here, the classification into light and heavy refers only to their relative size compared to $\Lambda_{\rm QCD}$.

Bethe–Salpeter equation (BSE), thereby re-summing higher-order contributions and restoring exact elastic unitarity of the scattering amplitude, in close analogy with the role of the Schrödinger equation in quantum mechanics. This extension significantly enlarges the energy range of applicability of the theory and has led to striking predictions, such as the two-pole nature of the $\Lambda(1405)$ resonance in $\bar{K}N$ scattering [15–18].

Another approximate symmetry of QCD that becomes especially relevant in the charm and bottom sectors is *heavy–quark spin symmetry* (HQSS) [19, 20]. The key idea is that, in the limit $m_Q \gg \Lambda_{\rm QCD}$ (m_Q being the mass of the heavy quark), the chromomagnetic interactions that flip the heavy quark spin are suppressed as $\Lambda_{\rm QCD}/m_Q$. Consequently, the spin of the heavy quark decouples from the light degrees of freedom, which dominate the hadron's dynamics. This feature is not unique to QCD: in general, the magnetic moment μ associated with a spin S scales as $\mu \propto S/(2m)$, so in the heavy–mass limit $m \to \infty$ spin interactions vanish (as in the hyperfine splitting of hydrogen). For hadrons containing a single heavy quark, HQSS predicts nearly degenerate spin doublets. A paradigmatic example is the pseudoscalar D and vector D^* mesons ($c\bar{q}$, with $\bar{q}$ a light antiquark), which form an HQSS doublet with a splitting of about 140 MeV. For bottom mesons ($\bar{b}q$), the symmetry is even better realized, with the B–B^* gap reduced to about 45 MeV. This situation is depicted in Fig. 1.1, where the mass splittings of the lowest lying strange, charm and bottom mesons are compared. In particular, it is apparent in this figure that this symmetry is not well realized for the light K and K^* mesons.

Beyond spin, the heavy–quark limit also implies an approximate heavy–quark *flavor* symmetry (HQFS), since replacing one heavy quark by another leaves the dynamics unchanged up to $1/m_Q$ corrections. Together, these form the heavy–quark spin–flavor symmetry, which is central to the spectroscopy of hadrons containing heavy quarks.

The formal framework that embodies these ideas is *heavy–quark effective theory* (HQET), developed in the late 1980s and early 1990s, notably by Isgur and Wise [21, 22]. HQET expands the QCD Lagrangian in powers of $1/m_Q$, with HQSS and HQFS exact at leading order and systematically broken at higher orders [19].

In order to describe hadrons that contain both light and heavy quarks, the principles of ChPT and HQET can be combined into a unified framework. This is the basis of *heavy–hadron chiral perturbation theory* (HHChPT) [23–26], where heavy–light mesons are treated as matter fields transforming under both heavy–quark spin–flavor symmetry and the chiral symmetry of the light sector. In this approach, one constructs the most general effective Lagrangian consistent with both sets of symmetries, expanding systematically in derivatives and inverse powers of the heavy–quark mass. HHChPT has been widely used

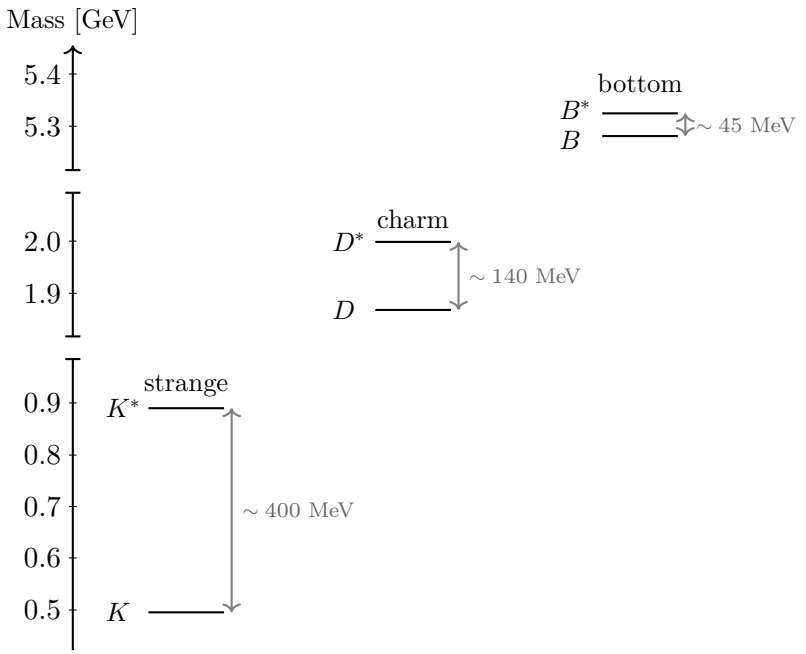

Figure 1.1: Illustration of the approximate HQSS in mesons. In the strange sector, the K–K^* splitting is ~ 400 MeV, showing that HQSS is badly broken. For charmed mesons, the D–D^* splitting is ~ 140 MeV, while for bottom mesons the B–B^* splitting is only ~ 45 MeV. Axis breaks indicate that the absolute masses are not drawn to scale.

to study the interactions of charmed and bottom mesons with pions, kaons, and other Goldstone bosons, providing a controlled EFT framework that links the light and heavy sectors.

It is worth stressing the complementarity between HQET and HHChPT. HQET provides a systematic $1/m_Q$ expansion of QCD for hadrons with a single heavy quark, independent of the details of the light sector, and is thus ideally suited for processes where the dynamics is dominated by the heavy quark itself (e.g. inclusive decays of the heavy hadron or heavy–to–heavy form factors). By contrast, HHChPT is tailored to the low–energy regime where soft Goldstone bosons couple explicitly to heavy–hadron fields, specializing to the study of the interactions among them in the HQSS and chiral limits.

An alternative line of development is the *hidden local symmetry* or *hidden gauge formalism* [27, 28], in which light vector mesons (ρ, K^*, $\bar{K}^*$ ω, ϕ) are introduced as gauge bosons of a hidden local symmetry embedded in the chiral Lagrangian. This framework provides natural interaction terms for vector mesons with pseudoscalars and with themselves, and it has been successfully

extended to include heavy mesons as well [26]. In particular, the hidden gauge approach has been instrumental in describing hadronic molecules dynamically generated by meson–meson or meson–baryon interactions, many of which are prime candidates for exotic hadrons [29–32].

Together, HHChPT and the hidden gauge formalism exemplify how symmetry principles can be combined to construct Lagrangians that capture the interplay between light–quark chiral dynamics and heavy–quark symmetry, providing versatile tools to investigate the spectroscopy and interactions of heavy hadrons in both vacuum and medium. The symmetry–based EFT framework outlined in this section forms the conceptual foundation for the hadron–hadron interactions studied throughout this thesis.

1.2 The quark model and exotic hadrons

In the early 1960s, the rapid discovery of new hadrons led to a proliferation of states that required a unifying principle. A major breakthrough came with the introduction of the *Eightfold Way* by Gell-Mann and, independently, Ne'eman [33, 34]. This classification scheme, based on the approximate SU(3) flavor symmetry of the strong interactions, organized the observed baryons and mesons into multiplets (octets, decuplets, and singlets) according to their spin, parity, and flavor quantum numbers such as isospin and strangeness. Among its most remarkable successes was the prediction of the Ω^- baryon, later discovered in 1964 [35], which completed the baryon decuplet. Shortly after, Gell-Mann and Zweig proposed the quark model [36, 37], which provided a physical interpretation of the Eightfold Way by postulating that hadrons are composed of more fundamental constituents—quarks—transforming as the fundamental triplet representation of SU(3) flavor. While the quark model provided an elegant classification of hadrons, quarks themselves remained hypothetical for several years. Their dynamical nature as real degrees of freedom was not confirmed until the early 1970s, when deep inelastic scattering experiments at SLAC revealed point-like constituents inside the proton, soon identified with quarks [38–40]. Together, these milestones laid the foundation for QCD and cemented it as one of the central pillars of the Standard Model of particle physics.

In the classical quark model, mesons are described as quark–antiquark ($q\bar{q}$) states, while baryons are composed of three quarks (qqq). This simple scheme, introduced in the 1960s, successfully accounted for the observed hadron multiplets and provided an intuitive framework for organizing the spectrum. However, it is now clear that this picture is not the whole story. Experimentally, there exist states that either cannot be accommodated within the classical quark configurations or for which such an assignment is rather unnatural. A

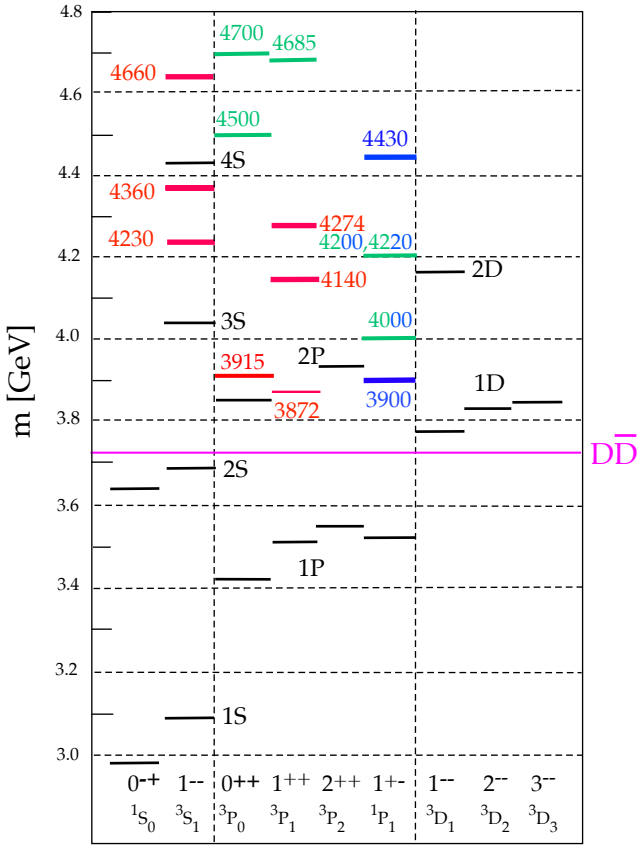

Figure 1.2: Mass spectrum with known $I^G(J^{PC})$ observed in the charmonium region. The $D\bar{D}$ line shows the open charm threshold. The well-known $c\bar{c}$ mesons are shown in black. (The $1\,^1D_2$ η_{c2}, expected around 3800 MeV, has not been seen yet.) The established additional observed states are shown in red, and the states needing confirmation (i.e., omitted from the Summary Tables) are labeled in green. The blue color denotes exotic isovectors. Source: PDG 2024 review [18], Fig. 15.2.

subset even carries genuinely exotic quantum numbers that are inaccessible to conventional $q\bar{q}$ or qqq states. Some examples of these states in the charmonium sector are presented in Fig. 1.2. From the QCD perspective, the only strict requirement is that hadrons form overall color singlets, which in principle allows more complex configurations such as tetraquarks ($qq\bar{q}\bar{q}$), pentaquarks ($qqqq\bar{q}$), glueballs (bound states of gluons), hybrids containing valence gluons, or even hadronic molecules formed by residual interactions between color-singlet clusters. In practice, these labels are not absolute: different internal configu-

rations with the same global quantum numbers can mix. For decades, such exotic structures remained largely speculative, but the recent discovery of a rich spectrum of candidates—many located near two-hadron thresholds—has reignited interest and triggered a lively debate on the true nature of these states.

Of particular historical relevance was the discovery of the $\chi_{c1}(3872)$ (formerly $X(3872)$), first observed by the Belle Collaboration in 2003 in B decays with the final state $J/\psi\,\pi^+\pi^-$ [41]. Its existence has since been firmly established by numerous experiments (BaBar, BESIII, CDF, D0, LHCb) in several production channels, including e^+e^- annihilation, Λ_b decays, and both $\bar{p}p$ and pp collisions. This narrow state ($\Gamma < 1$ MeV) lies right at the $D^0\bar{D}^{*0}$ threshold and decays predominantly into this channel. Its composition is widely believed to be largely molecular in line with predictions dating back to 1991 [42]. Since then, many non-$c\bar{c}$ candidates have been reported above the open-charm threshold, often with quantum numbers consistent with charmonium but incompatible with a pure $c\bar{c}$ interpretation. In addition, isovector (charged) mesons have been observed decaying into $c\bar{c}$ states accompanied by a charged pion or kaon. For instance, the 1^{+-} $T_{c\bar{c}1}(3900)^+$ (formerly $Z_c(3900)^+$) and the $T_{c\bar{c}s1}(4000)^+$ (formerly $Z_{cs}(4000)^-$) cannot be pure charmonia; they are instead consistent with $c\bar{c}u\bar{d}$ and $c\bar{c}s\bar{u}$ configurations, respectively. These states may belong to the same nonet [43, 44], so identifying the missing multiplet members would provide important clues about their underlying structure.

Outside the charmonium sector, an even more remarkable milestone was reached with the observation of the doubly charmed $T_{cc}(3875)^+$ by LHCb [45]. Unlike the $\chi_{c1}(3872)$, whose internal structure can still be debated between a conventional charmonium and an extended molecular configuration (or both), the $T_{cc}(3875)^+$ stands out as one of the clearest indications of a genuine tetraquark-like hadron: its doubly charmed nature necessarily requires a minimal quark content of four valence quarks ($cc\bar{u}\bar{d}$). This exceptionally narrow resonance was observed in the $D^0D^0\pi^+$ invariant-mass spectrum, with a mass $m_{\text{thr}} + \delta m_{\text{exp}}$, where $m_{\text{thr}} = 3875.09\,\text{MeV}$ is the $D^{*+}D^0$ threshold and $\delta m_{\text{exp}} = -360 \pm 40^{+4}_{-0}\,\text{keV}$, and a width of only $\Gamma = 48 \pm 2^{+0}_{-14}\,\text{keV}$ (see Fig. 1.3). Its extreme proximity to the D^0D^{*+} and D^+D^{*0} thresholds strongly favors a hadronic-molecule interpretation [46–64], although compact tetraquark scenarios had been proposed long before its observation [65, 66]. The exceptional clarity of the $T_{cc}(3875)^+$ as a tetraquark-like candidate, together with the intense theoretical debate it has generated, provides a natural motivation for this thesis.

With respect to the charm–strange sector, compelling tetraquark-like state candidates have been also observed. The scalar $D^*_{s0}(2317)^\pm$ was first reported by BaBar in 2003 [67] and soon after confirmed by CLEO together with the axial

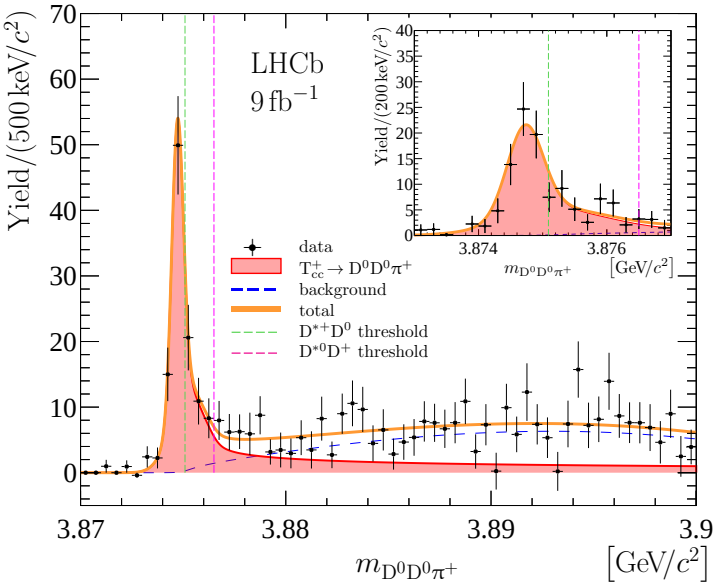

Figure 1.3: Distribution of $D^0D^0\pi^+$ invariant mass where the contribution of the non-D^0 background has been statistically subtracted. Figure taken from Ref. [45].

$D_{s1}(2460)^{\pm}$ [68]. Both resonances lie about 45 MeV below the DK and D^*K thresholds and are extremely narrow, with widths $\lesssim 4$ MeV at 95% C.L. [18]. Their properties raised several puzzles [69]:

1. Their masses are much lower than predicted by the Godfrey and Isgur quark model [70].

2. The splitting between the D_{s1} and D_{s0}^* equals, within a few MeV, the D^*–D mass difference.

3. The strange $D_{s0}^*(2317)$ is lighter than the non-strange $D_0^*(2300)$, contrary to naive quark-mass hierarchy expectations.

These anomalies are naturally explained if the $D_{s0}^*(2317)$ and $D_{s1}(2460)$ are predominantly DK and D^*K bound states, respectively [62, 71, 72], an interpretation further supported by LQCD studies [73–76]. Alternative descriptions in terms of conventional $c\bar{s}$ mesons, tetraquarks, or mixed configurations have also been discussed [77–79], but the molecular picture provides a particularly consistent resolution of the puzzles. As such, the $D_{s0}^*(2317)$, discovered alongside the $\chi_{c1}(3872)$, remains a benchmark case for testing ideas about exotic hadrons and serves as one of the central motivations of this thesis.

Another possible exotic-like configuration is that of bound states of three hadrons. The idea that few-hadron systems might bind through residual strong interactions dates back to the early studies of the deuteron as a two-nucleon bound state, which naturally suggested the existence of more complex multi-body configurations. Theoretical interest in three-body bound states grew with the development of the Faddeev formalism [80] and, later, the fixed-center approximation (FCA) [81], tools designed to address the complexities of three-body dynamics. These methods have since been applied to meson–meson–meson, meson–meson–baryon, and meson–baryon–baryon systems—systems composed of six, seven and eight valence quarks, respectively—leading to predictions of bound or resonant states such as the $\overline{K}NN$ [82], $K\overline{K}N$ [83], $\phi\overline{K}K$ [84], or $\overline{D}DK$ [85] systems. Experimentally, hints of such configurations have been reported in kaonic nuclei [86–88] and in the heavy-flavor sector, though their interpretation remains debated. Today, the study of three-body hadron states is an active line of research, as it provides not only possible new exotic candidates but also valuable insight into the two-body interactions that underlie them.

1.3 Hadronic matter in extreme conditions

The second important topic addressed in this manuscript is that of strongly interacting hadronic matter under extreme conditions of baryon density or temperature. At sufficiently high temperatures and/or baryon densities, hadrons are expected to lose their identity and dissolve into their fundamental constituents, quarks and gluons, forming a new state of matter known as the quark–gluon plasma (QGP). The existence of this deconfined phase was already proposed in the mid–1970s [89, 90], only a few years after the formulation of QCD. Although color confinement forbids the direct observation of isolated quarks and gluons, asymptotic freedom predicts that inter-quark forces weaken at high energies, naturally suggesting a transition from the confined hadronic phase to a deconfined QGP under extreme conditions. Modern LQCD calculations at vanishing baryon density confirm this picture: the transition is a smooth crossover around $T_c \simeq 155$ MeV, accompanied by the approximate restoration of chiral symmetry for the light quarks [91–93]. At larger baryon densities, however, the situation remains far less clear. Lattice methods are hindered by the sign problem, and progress relies on effective models, functional approaches, and perturbative calculations, which suggest the possible existence of a first–order transition line terminating at a critical end point (CEP) (see reviews [94, 95]). The QCD phase diagram may also contain additional regions, such as color–superconducting phases at asymptotically high densities, relevant for the interior of neutron stars. Figure 1.4 summarizes this qualitative picture:

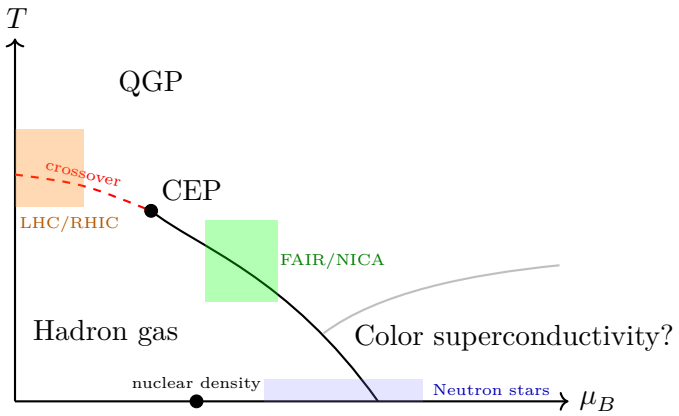

Figure 1.4: Schematic QCD phase diagram in the (T, μ_B) plane. At low baryon density, LQCD predicts a smooth crossover around $T_c \simeq 155$ MeV. At higher densities, effective models suggest a first–order phase transition terminating in a critical end point (CEP). The approximate regions probed by heavy–ion experiments (LHC/RHIC, FAIR/NICA) and by astrophysical observations of neutron stars are also indicated.

the crossover region probed in heavy–ion collisions at the *Relativistic Heavy Ion Collider* (RHIC) and the *Large Hadron Collider* (LHC), the conjectured first–order line at higher densities, and the astrophysical domain explored through neutron–star observations.

From a wider perspective, the study of QCD matter under extreme conditions connects directly to fundamental questions in physics and cosmology. At very high temperatures, the QGP is believed to have filled the Universe during its first microseconds after the Big Bang, before cooling led to the formation of hadrons and, eventually, nuclei. Conversely, the high–density regime, where baryon chemical potentials become large, is of crucial importance for the physics of compact astrophysical objects such as neutron stars. The composition of matter at several times nuclear saturation density—whether in terms of nucleons, hyperons, deconfined quarks, or more exotic degrees of freedom—determines the equation of state that governs the mass–radius relation of neutron stars and plays a central role in the interpretation of multi-messenger signals from neutron-star mergers (see [96–100] for some reviews). Thus, exploring the QCD phase diagram in both temperature and density directions is not only a central goal of hadronic physics, but also provides essential input to cosmology and astrophysics.

As illustrated in Fig. 1.4, the extreme conditions required for QGP formation can be recreated in the laboratory through relativistic heavy-ion collisions

at facilities such as CERN and *Brookhaven National Laboratory* (BNL). In 2000, at the end of the heavy-ion program at the Super Proton Synchrotron (SPS), CERN reported possible evidence for the formation of the QGP in Pb+Pb collisions [101]. The discovery was firmly established a few years later, in 2005, through Au+Au collisions at the RHIC at BNL [102–106]. Recently, the study of the QGP has entered an exciting new era with the heavy-ion program at the LHC, where the dedicated ALICE experiment—together with CMS and ATLAS—provides unprecedented opportunities to probe its properties, from collective flow to jet quenching and quarkonium suppression [107]. Looking ahead, new facilities such as the *Facility for Antiproton and Ion Research* (FAIR, GSI Darmstadt, Germany) [108] and the *Nuclotron-based Ion Collider fAcility* (NICA, JINR Dubna, Russia) aim to extend this exploration toward the high-baryon-density region of the QCD phase diagram.

That high–density frontier, however, remains much more elusive. Even at lower beam energies, as in the RHIC Beam Energy Scan and the upcoming FAIR and NICA programs, the created systems are short–lived and hot, complicating the extraction of equilibrium properties. A central goal of these programs, already pursued at RHIC and to be further explored at FAIR and NICA, is the search for signatures of the conjectured critical end point, though no conclusive evidence has yet been obtained. Complementary information on dense QCD matter comes from astrophysical observations of neutron stars, whose masses, radii, and tidal deformabilities constrain the equation of state at several times nuclear saturation density [109, 110]. An additional and more controlled laboratory probe is provided by mesonic atoms, exotic bound states where a meson replaces an electron in the atomic orbit. Precision spectroscopy of kaonic or pionic atoms, and potentially of heavier systems with open–charm mesons, offers unique access to the meson–nucleon interaction at threshold and thereby constrains in–medium hadron properties [111–119] (see also the reviews [98, 120]). Taken together, heavy–ion experiments, astrophysical data, and mesonic atoms provide complementary windows into the high–density frontier of QCD matter, although a complete understanding of this regime—including the possible existence of color–superconducting phases—remains an outstanding challenge.

From the theoretical point of view, major efforts have been devoted to understanding strongly interacting matter in both the high–temperature (QGP) and high–density (nuclear matter) regimes, which complement one another in the QCD phase diagram. In the density axis, the theoretical study of nuclear matter has a long history, dating back to the early liquid–drop and shell models developed in the mid–20th century to describe bulk nuclear properties and the structure of finite nuclei [121, 122]. The concept of infinite nuclear matter, introduced as a simplified model in which surface effects are neglected, soon

became a cornerstone for understanding the saturation properties of the strong interaction. In the 1950s and 1960s, Brueckner theory and related many–body approaches were formulated to deal with the short–range repulsion of the nucleon–nucleon force [123–125], leading to the first microscopic descriptions of the nuclear equation of state. These early calculations revealed the so–called Coester band problem [126], highlighting the need for three–body forces to reproduce empirical saturation properties.

With the advent of QCD, efforts shifted toward linking these phenomenological models to the underlying theory of strong interactions. Modern approaches now combine effective field theories, such as chiral EFT for nuclear forces [127, 128], with sophisticated many–body methods and inputs from lattice QCD [129–131], providing an increasingly systematic description of nuclear matter across a wide range of densities and isospin asymmetries. This historical trajectory illustrates the progressive refinement from phenomenological models to QCD–motivated frameworks, the latter underpinning much of the present work on hadrons in a dense medium.

On the temperature side, the study of strongly interacting matter has followed a parallel historical path. Early applications of statistical mechanics to hadrons led to the concept of the hadron resonance gas, already in use in the 1960s to describe particle yields in high–energy collisions [132]. The idea of a limiting ("Hagedorn") temperature, beyond which the hadronic description breaks down, was one of the first hints of a new phase of matter. With the advent of QCD, these ideas were placed on a firmer footing: finite–temperature field theory was developed through both real–time and imaginary–time (Matsubara) formalisms [133, 134], providing systematic tools to compute thermal correlators and spectral functions. Numerical LQCD calculations at finite temperature later established the existence of a smooth crossover around $T_c \simeq 155$ MeV [92, 93], where deconfinement and chiral symmetry restoration occur simultaneously.

These advances have shaped our modern understanding of hot QCD matter, from the equation of state to transport properties such as viscosities and diffusion coefficients. In parallel, effective theories and models—including thermal extensions of chiral perturbation theory, unitarized approaches, and quasi-particle models—have been developed to describe hadronic excitations in the medium and their dissolution near T_c. This historical trajectory, much like that of nuclear matter at high density, illustrates the refinement from early thermodynamical models to fully QCD–based approaches, which form the basis for the finite–temperature studies carried out in this thesis.

2

Properties of exotic mesons in nuclear matter

2.1 Introduction

During the last two decades, hadron spectroscopy has been revolutionized by the discovery of a plethora of *exotic* states, which could not be easily accommodated within conventional constituent quark model states. The charmonium-like sector—the so-called XYZ family—has experienced a decisive progress after the pioneering observation of the $\chi_{c1}(3872)$ [41]. Since then, LHCb has expanded the landscape with the discovery of the pentaquark candidates P_c and P_{cs} [135–139], as well as with new exotic mesons, such as the $T_{cs}(2900)$ [140, 141] and the doubly charmed tetraquark-like $T_{cc}(3875)^+$ [45, 142]. These advances have sparked vigorous discussions about their underlying structure, with interpretations ranging from compact multiquark configurations (tetraquarks or pentaquarks) and hadro-quarkonium to loosely bound hadronic molecules, kinematical cusps, or various hybrids of these pictures (see, e.g., Refs. [46, 143–148] for relevant reviews).

As discussed in the Introduction, among these exotic states, the recently discovered $T_{cc}(3875)^+$ has attracted a strong interest from the hadronic community, since it is one of the clearest examples of a state with a minimum quark content of four quarks. This exceptionally narrow resonance was observed in the $D^0D^0\pi^+$ invariant-mass spectrum, with its mass sitting very close to the D^0D^{*+} and D^+D^{*0} thresholds (cf. Fig. 1.3) [45]. This fact strongly favors a hadronic-molecule interpretation [46–64], although a compact tetraquark picture was proposed well before its discovery [65, 66]. In any case, the near-threshold nature of the signal implies that hadronic degrees of freedom must be explicitly included when analyzing experimental data [146].

Further experimental inputs on this state are highly desirable in order to

clarify its nature. In particular, heavy-ion collision femtoscopic correlation functions for the D^0D^{*+} and D^+D^{*0} channels have emerged as promising tools to disentangle relevant dynamical details of its structure. Some analyses have already been carried out for the $T_{cc}(3875)^+$, first with coordinate-space wave functions and potentials in Ref. [149], and more recently using momentum-space interactions in Ref. [150]. Another alternative way to probe the structure of the $T_{cc}(3875)^+$ is to study how it behaves under the extreme densities and temperatures achieved in heavy-ion collisions at RHIC, the LHC, or the forthcoming FAIR facility. Similar investigations have already been carried out for the $\chi_{c1}(3872)$. Using a coalescence model, the ExHIC Collaboration [151–153] showed that treating the $\chi_{c1}(3872)$ as a $D\bar{D}^*$ molecule leads to production yields far exceeding those expected for a compact tetraquark, especially once the hadronic phase is included [154, 155], because molecular configurations induce larger production and absorption cross sections in the hadronic medium. The nature of this exotic state has also been explored with instantaneous coalescence models [156, 157], a statistical hadronization approach [158, 159], and a thermal-rate equation scheme [159], although these studies neglected possible in-medium modifications of the $\chi_{c1}(3872)$ in the hadronic phase. Such medium effects have since been incorporated in calculations that embed the $\chi_{c1}(3872)$ in a hot meson bath [160, 161] and in cold nuclear matter [162]; related QCD sum-rule analyses have examined the mass shifts of heavy exotics such as the $\chi_{c1}(3872)$ and $Z_c(3900)$ [163, 164].

Another extremely relevant tetraquark-like candidate is the $D_{s0}^*(2317)^\pm$, first reported by BaBar in 2003 [67] and soon confirmed by CLEO, together with the $D_{s1}(2460)^\pm$ [68]. Both resonances lie roughly 45 MeV below the DK and D^*K thresholds, respectively, and far below the quark model expectations [70, 165–170]. Both states are isoscalar, with quantum numbers $I(J^P) = 0(0^+)$ for the D_{s0}^* and $0(1^+)$ for the D_{s1}, so their only allowed strong decays are the isospin-violating channels $D_s^{(*)}\pi$, resulting in widths below 4 MeV at 95% C.L. [171].

Similarly to the T_{cc}, numerous theoretical scenarios have been put forward to explain the structure of the $D_{s0}^*(2317)$. Conventional $c\bar{q}$ quark model scenarios [77, 172–177], compact tetraquark $cq\bar{q}\bar{q}$ configurations [78, 178–182], molecular heavy–light meson approaches [71, 72, 143, 183–194], and hybrid pictures combining quark model, tetraquark, and molecular components [79, 195–197] have been considered. Lattice-QCD studies have also been pivotal. Early simulations that used only $c\bar{s}$ interpolators obtained masses above the physical value [198, 199], whereas later calculations that included two-meson operators reproduced the experimental masses of both $D_{s0}^*(2317)$ and $D_0^*(2300)$ resonances [73–75, 200]. The HadSpec Collaboration [76] recently provided a detailed description of the isoscalar DK and $D\overline{K}$ scattering amplitudes and

the $D_{s0}^*(2317)$ pole, in agreement with the unitarized Heavy meson ChPT (HMChPT) framework of Ref. [72]. This latter scheme also reproduces the low-lying lattice levels reported in [201], supporting a two-pole structure in the $D_0^*(2300)$ region, a picture reinforced by the latest HadSpec results [202] and by high-precision LHCb analyses of $B^- \to D^+\pi^-\pi^-$ and $B_s^0 \to \overline{D}^0 K^-\pi^+$ decays [203, 204] interpreted in Ref. [69]. Given this sustained interest, complementary probes, such as femtoscopic correlation functions for the relevant channels, have been proposed in [205–208].

In summary, the internal structure of exotic tetraquark candidates—particularly the $T_{cc}(3875)$ and the $D_{s0}^*(2317)$—has captivated the hadronic community for over two decades, because it challenges the theoretical foundations of the description of the hadron spectrum. In this chapter, we examine how the properties of these states (and their corresponding antiparticles) are modified when they are embedded in nuclear matter for a range of Weinberg compositeness scenarios [209]. The key idea is that the molecular components (D^*D and $\overline{D}^*\,\overline{D}$ for the T_{cc}^+ and $T_{\bar{c}\bar{c}}^-$; DK and $\overline{D}\,\overline{K}$ for the D_{s0}^{*+} and D_{s0}^{*-}, respectively) will be renormalized differently, since the medium induces a charge-conjugation asymmetry. Given the very different meson-nucleon and antimeson-nucleon interactions, especially for the KN and $\overline{K}N$ case, we predict characteristic density-dependent differences between the in-medium spectra of $T_{cc}(3875)^+$ and $D_{s0}^*(2317)^+$ on the one hand, and their antiparticles $T_{\bar{c}\bar{c}}(3875)^-$ and $D_{s0}^*(2317)^-$ on the other—differences that should grow with increasing density. Experimental confirmation of such patterns would strongly support dominant molecular components.[1] A preliminary dense-matter study of the $D_{s0}^*(2317)^+$ (but not of its antiparticle) appears in Ref. [210], while thermal-medium effects on the $D_0^*(2300)$ have been analyzed in Ref. [211] within the NLO-HMChPT framework, finding no particle–antiparticle asymmetry because $D^{(*)}\pi$ and $\overline{D}^{(*)}\pi$ (and likewise $K\pi$ and $\overline{K}\pi$) interactions are identical in the SU(2) limit. Chapter 4 complements the present study on dense matter by exploring how a hot pionic bath, which does not induce charge conjugation asymmetry, affects $T_{cc}(3875)^{\pm}$.

The present chapter is structured as follows: First, in Sect. 2.2 we introduce the concept of nuclear matter and the in-medium nucleon propagator. Next, in Sect. 2.3 we discuss, in a general way, how the properties of any meson change when it is embedded in a dense nuclear medium. In particular, we introduce the important concepts of self-energy and spectral functions, and show the results obtained in the literature for the finite-density modifications of the D, D^* and K mesons (as well as their charge-conjugation partners)—since these are the *building blocks* of the molecular states we study in this Thesis. In Sect. 2.4 we

[1] A density-driven particle–antiparticle asymmetry of this type would likely be different for compact configurations.

analyze how to describe two-meson molecular states in nuclear matter. We first discuss the dynamical generation of such states in vacuum, and introduce the concept of *molecular probability*, and afterwards we describe how the presence of the dense nucleonic medium alters these states, both from the scattering matrix and from the self-energy points of view. In Sects. 2.5 and 2.6, we show and discuss the obtained finite-density results for the T_{cc} and D_{s0}^*, respectively, focusing on the comparison between the two charge-conjugated partners in each case. We also analyze the situation for the respective HQSS partners of both the $T_{cc}(3875)$ and the $D_{s0}^*(2317)$. Finally, we provide our conclusions in Sect. 2.7.

2.2 Brief overview of nuclear matter

This section is based on the classic books by Fetter & Walecka [212], and Mattuck [213]. Let us start by briefly defining what *nuclear matter* is. For this, let us consider the 'semi-empirical mass formula' for the nuclear binding energy by Weizsäcker:

$$E(N,Z) = \underbrace{-a_1 A}_{\substack{\text{nuclear}\\ \text{forces}}} + \underbrace{a_2 A^{2/3}}_{\substack{\text{surface}\\ \text{correction}}} + \underbrace{a_3 Z^2 A^{-1/3}}_{\substack{\text{Coulomb}\\ \text{correction}}} + \underbrace{\tfrac{1}{4} a_4 (N-Z)^2/A}_{\substack{\text{Pauli principle}\\ \text{correction}}}, \tag{2.1}$$

where Z and N are the number of protons and neutrons, respectively, and $A = Z + N$ is the mass number. The different a_i's are parameters that must be fitted to known nuclear masses. In the first term, $-a_1$ represents the binding energy of a single nucleon within the nucleus (i.e., away from the surface), because of the attractive nuclear forces, which is around -15.9 MeV. The remaining terms are corrections to this value arising from, in order of appearance: the existence of the surface of the nucleus, the Coulomb repulsion between protons, and the exclusion principle. Next, let us imagine then a system where there are so many nucleons that the surface correction is negligible, where the Coulomb force is negligible, and where the number of protons is equal to the number of neutrons (total isospin zero). In such a simple system, we would see that the total energy is proportional to the number of nucleons A. This hypothetical system, consisting of a large number of protons and an equal number of neutrons interacting only through nuclear forces, is the usual definition for *nuclear matter*. Furthermore, isotropy is also requested for this system, so that the total spin must be zero. The fact that the system is very large in size—ideally infinite—makes it homogeneous, a property which imposes both total energy and total momentum conservation. However, the presence of this medium breaks Lorentz invariance as it defines a privileged frame, in which the medium is at rest.

When considering a many-body system made out of fermions—like the nucleons in nuclear matter—the most important feature is the appearance

of allowed and forbidden states due to Pauli's exclusion principle. If we consider the fermions to be non-interacting, these allowed/forbidden states can be characterized by a given momentum k_F (the Fermi momentum) and by some temperature through the Fermi-Dirac distribution. However, in nuclear physics, thermal agitation is generally very small compared to the typical energy scale, and thus it can be safely neglected. Then, at zero temperature, we can write the following relation between the density ρ and the Fermi momentum:

$$\rho = \frac{A}{V} = \sum_{\alpha} \int \frac{d^3k}{(2\pi)^3} n_\alpha(\vec{k}) = 4 \int \frac{d^3k}{(2\pi)^3} \Theta\left(k_F - |\vec{k}|\right) = \frac{2}{3\pi^2} k_F^3. \tag{2.2}$$

In Eq. (2.2) $n_\alpha(\vec{k})$ represents the occupation number of the state with spin and isospin characterized by α and momentum $\vec{k}$, which corresponds to the Fermi-Dirac distribution at zero temperature.[2]

2.2.1 Nucleon propagator in nuclear matter

As a simple example of how Pauli blocking modifies the behavior of a Fermi gas even in the absence of interactions, let us examine the nucleon propagator in nuclear matter. We start from the expansion in terms of free Dirac spinors of the nucleon field, written as ($\mathbf{x} = (t, \vec{x})$)

$$\psi_\alpha(\mathbf{x}) = \int \frac{d^3p}{(2\pi)^3} \frac{1}{\sqrt{2\omega_p}} \left[c_\alpha(\vec{p})\, u_\alpha(\vec{p})\, e^{-i\mathbf{p}\cdot\mathbf{x}} + d_\alpha^\dagger(\vec{p})\, v_\alpha(\vec{p})\, e^{i\mathbf{p}\cdot\mathbf{x}} \right], \tag{2.3}$$

where ω_p is the on-shell energy of a nucleon with three–momentum $\vec{p}$, its four-momentum is denoted as $\mathbf{p} = (\omega_p, \vec{p})$. $u_\alpha(\vec{p})$ and $v_\alpha(\vec{p})$ are the Dirac spinors for the particle and antiparticle solutions, and $c_\alpha^{(\dagger)}(\vec{p})$ and $d_\alpha^{(\dagger)}(\vec{p})$ denote the corresponding annihilation (creation) operators. The index α labels the spin and isospin degrees of freedom. These operators obey the following anti-commutation relations:

$$\left\{ c_\beta(\vec{p}),\, c_\alpha^\dagger(\vec{p}\,') \right\} = \left\{ d_\beta(\vec{p}),\, d_\alpha^\dagger(\vec{p}\,') \right\} = (2\pi)^3 \delta(\vec{p} - \vec{p}\,') \delta_{\beta\alpha}, \tag{2.4}$$

[2] Another way to write Eq. (2.2) is

$$\rho = \int d\varepsilon\; g(\varepsilon) n(\varepsilon).$$

where $g(\varepsilon)$ is the degeneracy of the energy level ε, which for a Fermi gas of spin 1/2 and isospin 1/2 particles reads:

$$g(\varepsilon) = 4 \int \frac{d^3k}{(2\pi)^3} \delta\left(\varepsilon - \frac{k^2}{2m}\right).$$

and all the other possible combinations are zero.

We are considering that there is a Fermi sea of nucleons that fills all possible states up to some Fermi momentum k_F. Therefore, the fundamental state of the system is no longer the quantum vacuum $|0\rangle$, but a state $|\Psi_0\rangle$ with a given density of non-interacting particles (a Fermi gas). In this situation, we change the notation:

$$\begin{cases} p > k_F & \rightarrow & c_\alpha(\vec{p}) \equiv a_\alpha(\vec{p}), \\ p < k_F & \rightarrow & c_\alpha(\vec{p}) \equiv b^\dagger_\alpha(\vec{p}), \end{cases} \tag{2.5}$$

where $p \equiv |\vec{p}|$. This notation makes it apparent that the operator $c_\alpha(\vec{p})$, which annihilates a particle, can also be thought of as creating a *hole* when applied with p below the Fermi momentum. Similarly,

$$\begin{cases} p > k_F & \rightarrow & c^\dagger_\alpha(\vec{p}) \equiv a^\dagger_\alpha(\vec{p}), \\ p < k_F & \rightarrow & c^\dagger_\alpha(\vec{p}) \equiv b_\alpha(\vec{p}). \end{cases} \tag{2.6}$$

In other words, $c^\dagger_\alpha(\vec{p})$ can be reinterpreted to destroy a *hole*, and thus becomes $b_\alpha(\vec{p})$ if applied with momentum within the Fermi sea. From the anti-commutation relations of Eq. (2.4) we deduce

$$\left\{a_\beta(\vec{p}),\, a^\dagger_\alpha(\vec{p}\,')\right\} = \left\{b_\beta(\vec{p}),\, b^\dagger_\alpha(\vec{p}\,')\right\} = (2\pi)^3\delta(\vec{p}-\vec{p}\,')\delta_{\beta\alpha} \tag{2.7}$$

while all the other combinations vanish. In particular, we have the following.

$$\begin{aligned} \left\{a_\beta(\vec{p}),\, b_\alpha(\vec{p}\,')\right\} &= \left\{c_\beta(\vec{p})|_{p>k_f},\, c^\dagger_\alpha(\vec{p}\,')|_{p'<k_F}\right\} = (2\pi)^3\delta(\vec{p}-\vec{p}\,')\delta_{\beta\alpha} = 0, \\ \left\{a^\dagger_\beta(\vec{p}),\, b^\dagger_\alpha(\vec{p}\,')\right\} &= \left\{c^\dagger_\beta(\vec{p})|_{p>k_f},\, c_\alpha(\vec{p}\,')|_{p'<k_F}\right\} = (2\pi)^3\delta(\vec{p}-\vec{p}\,')\delta_{\beta\alpha} = 0, \end{aligned} \tag{2.8}$$

due to the fact that $\vec{p}$ and $\vec{p}\,'$ are different by the definition of the operators a and b. With all of these, we can rewrite the field of Eq. (2.3) as

$$\psi_\alpha(\mathbf{x}) = \int \frac{d^3p}{(2\pi)^3}\frac{1}{\sqrt{2\omega_p}}\Bigg\{\Big[n_\alpha(\vec{p})b^\dagger_\alpha(\vec{p}) + (1-n_\alpha(\vec{p}))a_\alpha(\vec{p})\Big]u_\alpha(\vec{p})e^{-i\mathbf{p}\cdot\mathbf{x}} + d^\dagger_\alpha(\vec{p})v_\alpha(\vec{p})e^{i\mathbf{p}\cdot\mathbf{x}}\Bigg\}. \tag{2.9}$$

In the one-particle case, we can create a particle from vacuum and annihilate it from a non-vacuum state. However, in the presence of a Fermi sea, the fundamental difference is that we cannot create particles with energies below the Fermi energy of the sea (alt. we cannot annihilate holes with energy above the Fermi energy). Since there is no Fermi sea of antiparticles, the antiparticle part of the field remains unchanged.

Even for non-interacting nucleons, Pauli blocking still produces a measurable effect on a system with many nucleons. For example, it is well known that the requirement for the total wave function to be antisymmetric yields an expectation value for the distance between two identical particles that is different from the one obtained in the classical, distinguishable particle scenario. If the spatial part of the wave function is antisymmetric, then the separation of the two particles is greater than in the distinguishable case. In contrast, if the spatial part is symmetric, then it is more probable to find the particles closer to each other. This phenomenon is known in the literature as the *exchange force*, as it can be interpreted as some kind of attractive or repulsive interaction between fermions. However, this "force" does not arise from any of the four basic interactions, but from the statistical properties of the system.

From the field in Eq. (2.9) one can compute the Feynman propagator of a nucleon in nuclear matter with the Pauli blocking effects implemented. This results in the expression

$$G_{\beta\alpha}(p^0,\vec{p}) = \frac{1}{2\omega_p}\left\{[1-n_\alpha(p)]\,\frac{\not{\mathbf{p}}' + m_N}{p^0-\omega_p+i\varepsilon} + n_\alpha(p)\frac{\not{\mathbf{p}}' + m_N}{p^0-\omega_p-i\varepsilon} + \frac{\not{\mathbf{p}}'' - m_N}{p^0+\omega_p-i\varepsilon}\right\}\delta_{\beta\alpha}, \quad (2.10)$$

where $\mathbf{p}' = (\omega_p, \vec{p})$ and $\mathbf{p}'' = (\omega_p, -\vec{p})$. In this expression, we can see that the spin and isospin dependence of the propagator, encoded in the α and β quantum numbers, is trivial. The first term in this propagator is associated to particles above the Fermi energy, the second term represents the propagation of holes below the Fermi energy, and the third term describes the propagation of antiparticles. Since there is no a Fermi sea of antiparticles, it is evident that the antiparticle part remains unmodified, as was already noted in the field definition of Eq. (2.9).

The expressions that have been presented here are valid for a system of non-interacting fermions. When considering the interactions between them, their propagators get renormalized and their quasi-particle nature arises.[3]

[3]The concept of *quasi-particle* is commonly used in many-body theory. The physical idea is that when a particle enters a many body system, it interacts strongly with the particles in its vicinity, and the latter create a "cloud" around the original particle. This happens, for example, in the case of a positive ion propagating through water. This positive ion attracts a cloud of negative ions and then propagates (almost freely, although with a different *effective* mass) through the medium. This new system (particle + cloud), which is weakly interacting with other particles, is what is understood as a quasi-particle. Mathematically, quasi-particles can be thought of as a new set of degrees of freedom of the system, chosen in such a way that the interactions among them are minimal. This is the idea behind renormalization in quantum field theory. A more detailed (and stimulating!) discussion on the concept of quasi-particles can be found in the first few chapters of Mattuck's book [213].

Different approximations for the interactions between them lead to different results for the ground-state energy of the system, the nucleon self-energies, and other properties. For example, for low-density nuclear matter, the interaction between nucleons can be approximated by summing up only the contributions from the so-called *ladder diagrams*. This affects the form of the n_α distribution to some degree, typically smoothing out a bit the sharp step function.[4] However, for our purposes, there is no special need to consider these interactions. In reality, if the nuclear matter system is taken to have a density equal to that of heavy nuclei at their center (the so-called *normal nuclear density* $\rho_0 = 0.17$ fm^{-3}), the mean separation between two nucleons is about 2 fm. We can compare this with the interaction range of the strong force, which is given by the inverse mass of the pion and is about $r_{\text{strong}} \sim 1.4$ fm. Since the separation is around 1.5 times the interaction range, one expects that the attractive interaction can be regarded as 'weak', in the sense that the errors introduced by the omission of this interaction will be less than—or comparable to, at most—the systematic uncertainties of other parts of our calculation.

In the following sections, we shall not deal anymore with the well-studied topic of nuclear matter. There are many references in which the properties of this system have been discussed, e.g. in [212, 213]. We will instead switch to the subject of heavy mesons in nuclear matter, which is the main focus of this part of the thesis, and it is necessary to discuss the results that will be shown for the exotic states $T_{cc}(3875)$ and $D_{s0}^*(2317)$ in Sects. 2.5 and 2.6.

2.3 Meson self-energies in nuclear matter

In this section, we address the question of how the properties of mesons change when they are immersed in a dense nuclear medium at zero temperature. For any particle species other than nucleons, the modifications they experience cannot come from Pauli blocking effects due to the presence of a Fermi sea. Instead, the nuclear-matter modifications come from the interactions of the particles with the nucleons in the medium. We illustrate this by discussing first how the propagator changes.

Let Δ_0 be the propagator of a certain meson M in the free space—that is, in vacuum,

$$\Delta_0(p^0, \vec{p}) = \frac{1}{(p^0)^2 - \vec{p}^2 - m_M^2 + i\varepsilon}, \tag{2.11}$$

where m_M is the mass of the meson. We will represent this free propagation as

[4] It can be shown that the interactions between the particles cannot completely remove the discontinuity of the zero-temperature step function distribution. What they do is reduce its magnitude to some value < 1. Therefore, the Fermi surface exists even for an interacting system at zero-temperature (see Sect. 11.3 of Ref. [213]).

a dashed line in Feynman diagrams. In the presence of the nuclear medium, there will be some non-zero probability—or, in quantum terms, some *probability amplitude*—that it will scatter with one of the nucleons. We shall represent this interaction as a square, and the associated vertex will be parameterized with a function t^{MN}. The free propagation of the nucleon, with which the meson interacts, will be represented by a solid line. Up to first order in perturbation theory, the only possible diagram will be given by the one represented in Fig. 2.1. At higher orders, it is possible to draw many more diagrams that contain more than one vertex $-it^{MN}$ and more than one nucleon loop. Depending on which diagrams are kept and which are neglected, different approximations to the interaction between the meson M and the nucleons can be built.[5] The physical interpretation of the diagram in Fig. 2.1 is that the meson M *knocks out* a nucleon N from the ground-state with momentum $q < k_f$ and knocks it *back in* instantly. This process is known as *forward scattering*. Although at first sight the meson's momentum appears unchanged by the collision—suggesting no net effect—the process nevertheless *produces a genuine change*. This *change* will be parameterized by a new *effective mass* and *decay width*, as we shall see.

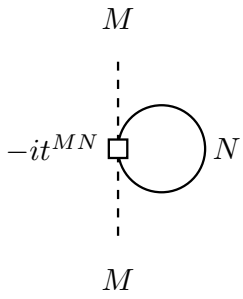

Figure 2.1: Bubble diagram for the forward scattering of a meson M on a nucleon N (increasing time taken in the up direction).

The diagram of Fig. 2.1 can be translated into an integral using the standard set of Feynman rules (e.g., see Table 9.1 in Ref. [213]), and thus one can directly evaluate the amplitude using the in-medium propagator for the nucleon in Eq. (2.10). For a meson M with a four-momentum $\mathbf{p} = (p^0, \vec{p})$, this integral

[5]Some of these approximations are historically important, and they are given a name. Examples are the Hartree approximation, which considers only forward-scattering diagrams like the one shown in Fig. 2.1, or the Hartree-Fock, which also considers exchange diagrams (only possible with identical particles), etc.

reads

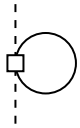

$$= \left[i\Delta_0(p^0,\vec{p})\right]^2 (-1) \int \frac{d^4q}{(2\pi)^4}\, iG^N(q^0,\vec{q})[-it^{MN}\left(p^0+q^0,\vec{p}+\vec{q}\right)] \quad (2.12)$$

where q^0 and $\vec{q}$ are the energy and the three-momentum of the nucleon (respectively) running inside the loop. Note the extra (-1) factor arising from the closed fermion loop. We shall leave the spin structure of this amplitude aside for now, and will come back to it in Sect. 2.3.3. Factoring out the external propagators of the M meson, we are left with the following quantity:

$$-\int \frac{d^4q}{(2\pi)^4} G^N(q^0,\vec{q})\; t^{MN}\left(p^0+q^0,\vec{p}+\vec{q}\right). \quad (2.13)$$

This integral has a divergent vacuum contribution and a non-divergent density-dependent contribution, stemming from the vacuum and in-medium parts of the nucleon propagator G^N of Eq. (2.10), respectively. In the non-relativistic limit, we can write the nucleon propagator as

$$G^N(q^0,\vec{q}) = \overbrace{\frac{1}{q^0-\omega_q+i\varepsilon} - \frac{1}{q^0+\omega_q-i\varepsilon}}^{\text{vacuum part}}$$
$$\underbrace{+\,n(q)\left(\frac{1}{q^0-\omega_q-i\varepsilon} - \frac{1}{q^0-\omega_q+i\varepsilon}\right)}_{\text{in-medium part}}. \quad (2.14)$$

In the evaluation of the diagram of Fig. 2.1 we will only keep the density-dependent part, which will introduce the nuclear medium modifications to the meson propagator. Consider now the customary prescription

$$\frac{1}{x-x_0\mp i\varepsilon} = \mathrm{PV}\frac{1}{x-x_0} \pm i\pi\delta(x-x_0), \quad (2.15)$$

with PV denoting the principal value of the integral. With this, we can simplify the density-dependent part of nucleon propagator, obtaining

$$G^N(q^0,\vec{q}) = \frac{1}{q^0-\omega_q+i\varepsilon} - \frac{1}{q^0+\omega_q-i\varepsilon} + 2\pi i\, n(q)\delta(q^0-\omega_q). \quad (2.16)$$

Introducing now the in-medium part of the nucleon propagator into the expression of Eq. (2.13) and integrating over q^0, one finds

$$-\int \frac{d^4q}{(2\pi)^4} n(q) 2\pi i \delta(q^0 - \omega_q) t^{MN}\left(p^0 + q^0, \vec{p} + \vec{q}\right)$$

$$= -i \int \frac{d^3q}{(2\pi)^3} n(q)\; t^{MN}\left(p^0 + \omega_q, \vec{p} + \vec{q}\right),$$

and therefore, the lowest-order in-medium meson self-energy reads

$$-i\Pi(p^0, \vec{p}) = -i \int_{q<k_F} \frac{d^3q}{(2\pi)^3}\, t^{MN}\left(p^0 + E_N\left(\vec{q}^{\,2}\right), \vec{p} + \vec{q}\right). \tag{2.17}$$

Note that this quantity is actually independent of the direction of $\vec{p}$. However, in our notation, we choose to keep the vector symbol ($\vec{}$) to avoid any possible confusion with the four-momentum (denoted here by a bold letter).

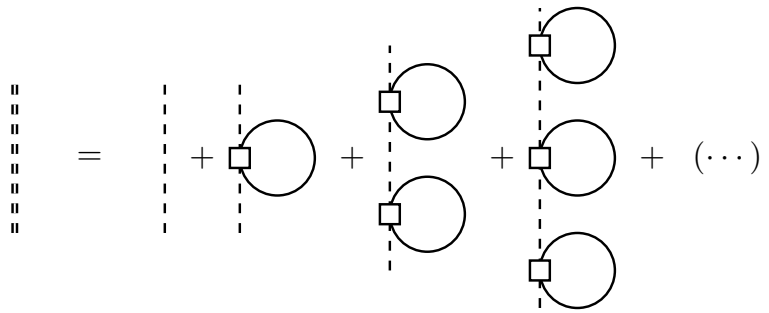

Figure 2.2: Dressed propagator of the meson M in the nuclear medium.

In order for the total probability to add up to one—or, in other words, for elastic unitarity to be fulfilled—we need to consider that there is some probability amplitude that the meson M scatters with two, three, or more nucleons one after another. These processes will be less probable than the one presented in Fig. 2.1, but will nonetheless contribute to the total probability amplitude. One can draw Feynman diagrams describing these processes and sort them in ascending numbers of loops, and then proceed to their sum, as in Fig. 2.2. The sum of all these amplitudes is usually referred to as the *dressed* or *renormalized* propagator of the M meson, and we shall represent it with a double dashed line, and with the function Δ_ρ, where ρ is the nucleon density. We can translate the diagrams of Fig. 2.2 into equation form and write

$$\Delta_\rho = \Delta_0 + \Delta_0\Pi\Delta_0 + \Delta_0\Pi\Delta_0\Pi\Delta_0 + \Delta_0\Pi\Delta_0\Pi\Delta_0\Pi\Delta_0 + \cdots. \tag{2.18}$$

Given that the loop identified with $\Pi(p^0, \vec{p})$ in Eq. (2.17) can be factored out on every diagram in the infinite series of Fig. 2.2, or equivalently on every term of Eq. (2.18), the series can be rewritten as a geometric series. Applying

the well-known result for the sum of a geometric series, one ends up with the standard *Dyson's equation* for the dressed propagator of the meson M:

$$\Delta_\rho(p^0,\vec{p}) = \frac{1}{[\Delta_0(p^0,\vec{p})]^{-1} - \Pi(p^0,\vec{p})}. \tag{2.19}$$

The quantity $\Pi(p^0,\vec{p})$ of Eq. (2.17) is known as the *(irreducible) self-energy* of M.[6] Since the self-energy is, in general, a complex quantity, it will introduce a certain mass shift and a width to the meson M inside of the nuclear medium, defined by the following equation

$$(m_M^\rho)^2 = m_M^2 + \Pi\left(m_M^\rho,\vec{0}\right). \tag{2.20}$$

This equation for m_M^ρ is, in practical terms, difficult to solve. Given that the quantity m_M^ρ will generally be a complex quantity, one would need to define the self-energy for complex values of its energy variable. However, we can get a first approximation of m_M^ρ by setting the energy argument of Π to be the mass of the meson in the vacuum, m_M. Since the self-energy (both real and imaginary parts) will be small compared to the mass of the M meson—otherwise, the whole formalism of quasi-particles would be meaningless—we can write

$$m_M^\rho \simeq m_M + \frac{\Pi(m_M,\vec{0})}{2m_M}. \tag{2.21}$$

The quantity $\Pi(p^0,\vec{p})/2m_M$ is often referred to as *optical potential*. From this equation, we find that, as a first approximation, the mass of the meson is shifted by an amount given by

$$\Delta m_M^\rho = \frac{\text{Re }\Pi(m_M,\vec{0})}{2m_M}, \tag{2.22}$$

and that it develops a width given by

$$\frac{\Gamma_M}{2} = -\frac{\text{Im }\Pi(m_M,\vec{0})}{2m_M}. \tag{2.23}$$

The self-energy also introduces a modification to the field normalization (the factor 1 appearing in the numerator of the propagator), which is often written in quantum field theory textbooks as Z. We will discuss the value of this normalization parameter in the following sections.

It is important to stress that the self-energy $\Pi(p^0,\vec{p})$ defined in Eq. (2.17) incorporates only the effects of the nuclear medium. In particular, it arises

[6] The term *irreducible self-energy* indicates that the diagram cannot be separated into two independent parts. In contrast, a reducible contribution, such as the $\Delta_0\Pi\Delta_0\Pi\Delta_0$ term in Eq. (2.18), can be decomposed into two successive Π insertions.

from the interactions of the meson with the *real nucleons* of the Fermi sea, and does not include the vacuum self-energy generated by virtual nucleon loops. In the absence of a medium, the nucleon Fermi momentum vanishes, the integral in Eq. (2.17) is zero, and the propagator reduces to the free form $\Delta_0(p^0, \vec{p})$, whose physical mass already contains the vacuum self-energy contribution through renormalization. Since this contribution is absorbed in the parameters of the effective Lagrangian—notably the M-meson mass and its coupling to nucleons—the self-energy of Eq. (2.17) appearing in the in-medium propagator of Eq. (2.19) accounts exclusively for observable modifications induced by the nuclear environment.

2.3.1 Computing the self-energy

In the previous section, we have seen that the self-energy of Eq. (2.17) is the key quantity that defines how the propagator of a meson changes when it is embedded in a nuclear medium. However, we have not given many details about how to actually compute this quantity, beyond giving a general expression for it. Although it may appear to be a rather simple computation, this is really not the case. In particular, the meson-nucleon interaction, parameterized by the function t^{MN}, will also depend on the density. As it turns out, the equation for the density-dependent self-energy of Eq. (2.17) represents a self-consistent equation to determine the meson in-medium spectral properties. This has been studied in many works in the literature, e.g. see Refs. [214–216]). Since we will be using the results from the mentioned references, we will briefly discuss these calculations in this section.

Let us assume some interaction kernel, namely v^{MN}, describing the two-body interaction in $S-$wave of the M meson with a nucleon. This interaction is usually derived from an appropriate EFT such as ChPT or HHChPT. We will go into more details of this interaction when discussing the specific mesons that we consider for our calculations (D, D^* and K) in the following sections. Using this interaction, one can obtain a first approximation to the meson self-energy by inserting it as the interaction vertex that we denoted as t^{MN} in Eq. (2.17). However, this turns out to be not a very good approximation for the cases studied in this thesis, mainly because of two reasons. On the one hand, an interaction coming from perturbation theory cannot produce any dynamically generated states, such as bound states or resonances. This is because these states correspond to poles in the scattering amplitude, and the power expansion taken in usual perturbation theory cannot diverge for any given order (it can only diverge when summing up an infinite set of terms). In other words, the appearance of dynamically generated states breaks the convergence of perturbation theory near the regions where these states appear. On the other hand, the linear $v^{MN}\rho$ approximation for the optical-potential

is not realistic in the sense that it does not include higher order finite-density modifications.

In order to generate dynamical states when dealing with standard quantum field theory in vacuum, one possible method is to solve the Bethe-Salpeter equation (BSE) for the (unitarized) T matrix. In the finite-density scenario, we can employ the same scheme and write within the on-shell approximation[7]

$$t_\rho^{MN}(P^0,\vec{P}) = \frac{v^{MN}(\sqrt{s})}{1 - v^{MN}(\sqrt{s}) g_\rho^{MN}(P^0,\vec{P})}. \tag{2.24}$$

In this equation $g_\rho^{MN}(P^0,\vec{P})$ is the in-medium meson-nucleon loop function, $\mathbf{P} = (P^0,\vec{P})$ the total meson-nucleon four-momentum and $s = \mathbf{P}^2$ is the invariant mass of the system.[8] Eq. (2.24) can be represented diagrammatically as shown in Fig. 2.3.

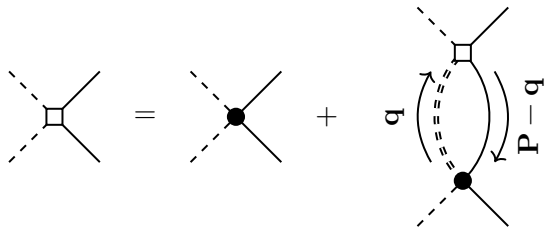

Figure 2.3: Diagrammatic representation of the BSE for the unitarized amplitude in the nuclear medium. The white square and the black dot represent t_{MN} and v_{MN}, respectively. The four-momenta involved in the loop are presented in bold (increasing time taken in the up direction).

The unitarized amplitude of Eq. (2.24) differs from the vacuum one only in the meson-nucleon loop function,[9] defined as

$$g_\rho^{MN}(P^0,\vec{P}) = i\int_\Lambda \frac{d^4q}{(2\pi)^4}\, \Delta_\rho^M(q^0,\vec{q}) G_\rho^N(P^0-q^0,\vec{P}-\vec{q}). \tag{2.25}$$

[7]Despite its seemingly crude nature, the on–shell factorization of the Bethe–Salpeter equation provides an accurate description of the unitarized T–matrix [217, 218]. The justification lies in the fact that off–shell contributions merely renormalize the interaction kernel, and their effects can be absorbed into suitable choices of the renormalization scale and/or of the higher order counter-terms.

[8]In Eq. (2.24), we express v^{MN} in terms of the invariant mass s, but the loop-function g^{MN} in terms of the individual components of the total four-momentum $\mathbf{P}$. This is in order to explicitly show that, although the potential v^{MN} is a Lorentz-invariant quantity, the finite-density loop function g_ρ^{MN} is not, due to the fact that the nuclear medium breaks Lorentz covariance.

[9]Actually, one can also consider density corrections to the meson-nucleon interaction and going beyond the potential v^{MN}, but these corrections are shown to be subdominant.

In this equation, we label the propagators of the meson and the nucleon with the superscripts M and N, respectively. Furthermore, since the loop integral is divergent, it is necessary to regularize it appropriately. The chosen regulator is a three-momentum cutoff Λ,[10] whose value is fixed by requiring that the vacuum ($\rho = 0$) results reproduce some known experimental quantities—e.g. in $\overline{K}$–nucleon scattering, the results reproduce the double-pole structure of the $\Lambda(1405)$. Once the vacuum loop function has been regularized, it is possible to implement the density-dependent modifications without the cutoff dependence, since these modifications are finite. Let us show mathematically what we just stated. It is possible to write the finite-density meson-nucleon loop function as

$$g_\rho^{MN}(P^0, \vec{P}) = g_0^{MN}(\sqrt{s}) + \tilde{g}_\rho^{MN}(P^0, \vec{P}), \tag{2.26}$$

On the one hand, the vacuum loop function in the previous expression —$g_0^{MN}(\sqrt{s})$— is divergent and it is regulated with the cutoff, fixed as we discussed before. On the other hand, the $\tilde{g}_\rho^{MN}$ term, which is given by

$$\tilde{g}_\rho^{MN}(P^0, \vec{P}) = i \int_\Lambda \frac{d^4q}{(2\pi)^4} \left[\Delta_\rho^M(q^0, \vec{q}) G_\rho^N(P^0 - q^0, \vec{P} - \vec{q}) - \Delta_0^M(q^0, \vec{q}) G_0^N(P^0 - q^0, \vec{P} - \vec{q})\right], \tag{2.27}$$

is not divergent. Therefore, there is no need to use any regulator, and we can safely set $\Lambda \to \infty$.[11]

Let us now analyze the density-dependent meson-nucleon loop function. The propagator of the nucleon inside the loop (G_ρ^N) is the same as that given in Eq. (2.10). The density effects on this propagator arise only from Pauli blocking, and not from the interactions of the nucleon with the other nucleons of the Fermi sea. The in-medium meson propagator (Δ_ρ^M) was given in Eq. (2.18), and depends on the MN interaction of Eq. (2.24) through the self-energy $\Pi(p^0, \vec{p})$ (recall Eq. (2.17)). Therefore, we see that Eqs. (2.24) and (2.17) constitute a coupled system of integral equations for the density-dependent self-energy $\Pi(p^0, \vec{p})$ and the scattering amplitude t_ρ^{MN}:

$$\begin{cases} \Pi(p^0, \vec{p}) = \displaystyle\int_{q<k_F} \frac{d^3q}{(2\pi)^3}\, t_\rho^{MN}(p^0 + E_N(\vec{q}^{\,2}), \vec{p} + \vec{q}), \\ \left[t_\rho^{MN}(p^0, \vec{p})\right]^{-1} = [t_0^{MN}(\sqrt{s})]^{-1} - \tilde{g}_\rho^{MN}(p^0, \vec{p}). \end{cases} \tag{2.28}$$

[10] The cutoff prescription for the regularization of the loop function, together with the on-shell factorization of the BSE, have been shown to be appropriate for the description of finite-density effects (see footnote 32 in Sect. 2.6.1).

[11] In practice, when computing $\tilde{g}_\rho^{MN}$ numerically, one needs to cut the integral at some point. One can choose some Λ' large enough so that $\tilde{g}_\rho^{MN}$ is effectively independent of changes in the value of this Λ'.

In practice, this system is solved using a self-consistent numerical algorithm: one first computes an initial self-energy $\Pi^{(1)}$ from the vacuum scattering amplitude t_0^{MN}; this $\Pi^{(1)}$ yields the first in-medium loop correction $\tilde{g}_\rho^{MN,(1)}$ and, in turn, the density-dependent amplitude $t_\rho^{MN,(1)}$. Feeding $t_\rho^{MN,(1)}$ back into the calculation produces an improved self-energy $\Pi^{(2)}$. The cycle is then repeated until Π and t_ρ^{MN} stabilize, a convergence that in practice is reached after only a few iterations.

2.3.2 The spectral function

The *spectral density function*, or simply spectral function, is a quantity—closely related to the self-energy, as we shall see—that describes the properties of quasi-particles. The idea is similar to that of the Fourier transform of a time-dependent function $f(t)$, which decomposes the original function into the sum of its components for different frequencies ω. Let us consider the free propagator for the meson M of Eq. (2.11), which in coordinate space can be written as

$$i\Delta_0(t,\vec{x}) = \theta(t)\int \frac{d^3q}{(2\pi)^3}\frac{1}{2\omega_q}e^{-i(\omega_q t-\vec{q}\cdot\vec{x})} + \theta(-t)\int \frac{d^3q}{(2\pi)^3}\frac{1}{2\omega_q}e^{i(\omega_q t-\vec{q}\cdot\vec{x})}. \quad (2.29)$$

where θ represents the step function and ω_q is the energy of the meson with a three-momentum $\vec{q}$. The first term corresponds to the particle part, while the second term yields the antiparticle one. Now, let us consider the in-medium meson propagator and introduce a spectral decomposition by adding an extra integral over some ω variable, so that

$$\begin{aligned} i\Delta_\rho(t,\vec{x}) = \theta(t)\int_0^\infty d\omega \int \frac{d^3q}{(2\pi)^3} S_M(\omega,\vec{q};\rho)e^{-i(\omega t-\vec{q}\cdot\vec{x})} \\ + \theta(-t)\int_0^\infty d\omega \int \frac{d^3q}{(2\pi)^3} S_{\overline{M}}(\omega,\vec{q};\rho)e^{i(\omega t-\vec{q}\cdot\vec{x})}, \end{aligned} \quad (2.30)$$

We have introduced two new functions—S_M for the particle part and $S_{\overline{M}}$ for the antiparticle one—that will encode the density dependence of the propagator. These are precisely the *spectral functions*.[12] It is clear from the expression in Eq. (2.30) that, in order to reproduce the free propagator, one has

$$S_M(\omega,\vec{q};\rho=0) = S_{\overline{M}}(\omega,\vec{q};\rho=0) = \frac{\delta(\omega-\omega_q)}{2\omega_q}. \quad (2.31)$$

[12] Alternatively, the spectral function can also be understood in the following way: $S_M(\omega,\vec{q};\rho)$ is the *probability density* that, if we insert a meson M with a three-momentum $\vec{q}$ into the many-body system (characterized by density ρ), then we measure its energy to be ω. A detailed discussion on this can be found in Appendix H of Ref. [213].

That is, in the free space, the spectral function is just a Dirac delta peaking at the energy corresponding to a meson with momentum $\vec{q}$. However, when considering the meson inside of a dense medium, these spectral functions depart from the delta-like shape shown previously. In general, for a given density and a three-momentum $\vec{q}$, the spectral function (as a function of the energy variable ω) will no longer peak at $\omega = \omega_q$, and it will develop some width—that is, there will be some nonzero spread of energies contributing to the ω integration in Eq. (2.30). Therefore, the energy will no longer be a well-defined quantity for M (or $\overline{M}$)—or in other words, M ($\overline{M}$) will no longer be a stationary state of the problem, and there will be some non-zero probability of it decaying to other states. Note also that, in principle, the forms of S_M and $S_{\overline{M}}$ may be different. This depends on whether the interactions of the M and $\overline{M}$ mesons with the particles of the medium are different.

Let us now transform the density-dependent propagator in the time-space variables to the energy-momentum variables (which are the interesting ones in scattering problems). When done, it reads as follows.

$$\Delta_\rho^M(p^0,\vec{p}) = \int_0^\infty d\omega \left(\frac{S_M(\omega,\vec{p};\rho)}{p^0 - \omega + i\varepsilon} - \frac{S_{\overline{M}}(\omega,\vec{p};\rho)}{p^0 + \omega - i\varepsilon} \right) \tag{2.32}$$

This expression is the usual form of the so-called *Källén-Lehmann spectral representation* of the propagator. Its interpretation is similar to what we discussed for the space-time propagator. It is easily seen that, by setting both spectral functions to the normalized delta of Eq. (2.31), one recovers the usual expression for the free propagator in the energy-momentum space.

The self-energy of the meson M and its spectral function are related through the following identity

$$S_M(p^0,\vec{p};\rho) = -\frac{1}{\pi}\text{Im }\Delta_\rho^M(p^0,\vec{p}) = -\frac{1}{\pi}\frac{\text{Im }\Pi(p^0,\vec{p})}{|(p^0)^2 - \vec{p}^2 - m_M^2 - \Pi(p^0,\vec{p})|^2}. \tag{2.33}$$

This identity holds for the particle component of M (we have $p_0 > 0$). For the antiparticle component, the spectral function reads

$$S_{\overline{M}}(p^0,\vec{p};\rho) = -\frac{1}{\pi}\text{Im }\Delta_\rho^M(-p^0,\vec{p}). \tag{2.34}$$

These relations can be easily checked by inserting them into Eq. (2.32). Through these equations, it is clear that the self-energy and spectral functions encode the same information about how the dense medium affects the properties of the meson M. In fact, it is possible to write the spectral representation of Eq. (2.32) in a more compact way. Extending the definition of the spectral function to negative energies such that

$$\tilde{S}_M(p^0,\vec{p};\rho) = \begin{cases} S_M(p^0,\vec{p};\rho) & p^0 > 0, \\ -S_{\overline{M}}(-p^0,\vec{p};\rho) & p^0 < 0, \end{cases} \tag{2.35}$$

we can write

$$\Delta_\rho^M(p^0,\vec{p}) = \int_{-\infty}^{\infty} d\omega \frac{\tilde{S}_M(\omega,\vec{p};\rho)}{p^0 - \omega + \text{sign}(\omega)\ i\varepsilon}. \tag{2.36}$$

We now turn to the interpretation of the spectral functions. The spectral function can be usually approximated around the quasiparticle peak by a relativistic Breit–Wigner distribution,[13]

$$S(E,\vec{0};\rho) \sim \frac{\kappa}{\left(E^2 - M^2\right)^2 + M^2\Gamma^2}, \tag{2.37}$$

where M and Γ are parameters characterizing, respectively, the position of the maximum and the full width at half maximum of the distribution, and κ is a normalization constant.

For the case of S_M, these parameters can be expressed approximately as (cf. Eq. (2.33))

$$M^2 = m_M^2 + \Delta m_M^\rho = m_M^2 + \text{Re}\ \Pi(m_M,\vec{0}), \tag{2.38}$$

$$M\Gamma = -\text{Im}\ \Pi(m_M,\vec{0}). \tag{2.39}$$

Thus, the parameter M corresponds to the quasi-particle mass, while Γ represents its width. In this way we recover, in approximate form, the same expressions for the in-medium mass shift and width of the meson M that were previously obtained from the self-energy corrections to the propagator, Eqs.(2.22) and (2.23).

2.3.3 Self-energy in spin and isospin basis

Up to this point, our discussion of the self-energy of the meson M has assumed that the particles involved are both scalar and isoscalar, in order to simplify the notation. However, we are well aware that nucleons have spin and isospin equal to 1/2, while the meson M will typically have spin 0 or 1, and some isospin structure as well. In this section, we discuss this issue.

Let us start by studying the spin structure of the self-energy. We will assume that the meson M has a total spin and z component of spin given by the quantum numbers (s, s_z). Similarly, for the nucleon N, its spin will be characterized by the pair (r, r_z). We will work for a general r, and only at the end of our calculation we will set the nucleon spin quantum number to 1/2. Having a general expression will also allow us to apply the self-energy (iso)spin decomposition in the case of finite temperature, which will be studied at the end of Sect. 4.3.2.

[13] Also referred to as the Cauchy or Lorentzian distribution.

The scattering amplitude will be given by

$$\langle s, s'_z, r, r'_z | t | s, s_z, r, r_z \rangle. \tag{2.40}$$

In this discussion, we will ignore the momentum dependence of the scattering amplitude. Inserting now a change of basis for the sum of the two spins, we can write

$$\langle s, s'_z, r, r'_z | t | s, s_z, r, r_z \rangle = \sum_{J',M'} \sum_{J,M} \langle J'M' | s, s'_z, r, r'_z \rangle \langle JM | s, s_z, r, r_z \rangle \langle J', M' | t | J, M \rangle, \tag{2.41}$$

where $\langle JM | j_1 m_1 j_2 m_2 \rangle$ are the Clebsch-Gordan coefficients for the sum of the j_1 and j_2 spins to give the total spin J. Owing to the Wigner-Eckart theorem and the fact that we assume that the amplitude is S wave—so that it conserves total spin, or in other words, t is a spin singlet—we see that

$$\langle J', M' | t | J, M \rangle = t^{(J)} \delta_{J'J} \delta_{M'M}, \tag{2.42}$$

where $t^{(J)} \equiv \langle J || t || J \rangle$ ins the reduced matrix-element. Therefore, we can simplify the expression for the change of basis in Eq. (2.41) and write it as

$$\langle s, s'_z, r, r'_z | t | s, s_z, r, r_z \rangle = \sum_{J,M} \langle JM | s, s'_z, r, r'_z \rangle \langle JM | s, s_z, r, r_z \rangle t^{(J)}. \tag{2.43}$$

Now, in the nucleon loop appearing in the self-energy, we have to sum over all possible third components of spin. Therefore, we will have to calculate

$$\sum_{r_z} \langle s, s'_z, r, r_z | t | s, s_z, r, r_z \rangle = \sum_{r_z} \sum_{J,M} \langle JM | s, s'_z, r, r_z \rangle \langle JM | s, s_z, r, r_z \rangle t^{(J)}. \tag{2.44}$$

Taking into account that the Clebsch-Gordan coefficients $\langle JM | j_1 m_1 j_2 m_2 \rangle$ are zero if $m_1 + m_2 \neq M$, we can simplify this expression as:

$$\sum_{r_z} \langle s, s'_z, r, r_z | t | s, s_z, r, r_z \rangle = \delta_{s'_z, s_z} \sum_{r_z} \sum_{J} \left(\langle J, s_z + r_z | s, s_z, r, r_z \rangle \right)^2 t^{(J)}. \tag{2.45}$$

In fact, this preceding equality is independent of the value chosen for s_z.

Let us now particularize Eq. (2.45) for our case of interest. In the following sections, we will deal with D mesons and kaons, which are pseudoscalar states. We will also be interested in the D^* mesons, which are spin vectors. Then, let us consider a spin 1/2 nucleon ($r = 1/2$), and assuming that the meson is a pseudoscalar ($s = 0$), then we find

$$\sum_{r_z} \langle 0, 0, 1/2, r_z | t | 0, 0, 1/2, r_z \rangle = 2 t^{(J=1/2)}. \tag{2.46}$$

In turn, for a vector meson ($s = 1$) we have

$$\sum_{r_z} \langle 1, s'_z, 1/2, r_z | t | 1, s_z, 1/2, r_z \rangle = \delta_{s'_z, s_z} \left(\frac{2}{3} t^{(J=1/2)} + \frac{4}{3} t^{(J=3/2)} \right). \tag{2.47}$$

This completes the spin decomposition analysis.

We shall now investigate the isospin case. Actually, since the isospin and spin are completely equivalent, the reasoning in isospin space runs parallel to the spin case. Again, since the amplitude t is isospin symmetric—or in other words, an isospin singlet—we arrive at an expression analogous to that of Eq. (2.45). For our cases of interest, which are the charmed D mesons and the kaons, we see that all of them are isodoublets. Then, let us assume a meson with isospin $1/2$ and third component i_z. For the nucleon, we know that it is an isodoublet, and we shall name its third component by t_z. Following the same steps as in the spin case, one can readily write

$$\sum_{t_z} \langle 1/2, i'_z, 1/2, t_z | t | 1/2, i_z, 1/2, t_z \rangle = \delta_{i'_z, i_z} \left(\frac{1}{2} t^{(I=0)} + \frac{3}{2} t^{(I=1)} \right). \tag{2.48}$$

Now, considering both the spin and isospin structure of the amplitude at the same time, we arrive at the formulas

$$\Pi^{MN} = \int_{q<k_F} \frac{d^3q}{(2\pi)^3} \left(t^{(S=1/2, I=0)} + 3t^{(S=1/2, I=1)} \right) \tag{2.49}$$

for a pseudoscalar meson M with isospin $1/2$ (like the D or K mesons), and

$$\Pi^{M^*N} = \int_{q<k_F} \frac{d^3q}{(2\pi)^3} \left(\frac{1}{3} t^{(J=1/2, I=0)} + t^{(J=1/2, I=1)} + \frac{2}{3} t^{(J=3/2, I=0)} + 2t^{(J=3/2, I=1)} \right) \tag{2.50}$$

for a vector meson M^* with isospin $1/2$ (like the D^* mesons). In Eqs. (2.49) and (2.50) we have omitted the trivial dependence of the self-energy on the spin and isospin indices of the meson $M^{(*)}$, as well as the energy-momentum dependence on both Π and the amplitudes t, which is the same as that shown in Eq. (2.28).

2.3.4 $D^{(*)}$, $\overline{D}^{(*)}$, K and $\overline{K}$ self-energies in nuclear matter

In this section, we present and analyze the results for the self-energies of the charmed D and D^* mesons, and of kaons and antikaons. The results for the K and $\overline{K}$ and $D^{(*)}$ and $\overline{D}^{(*)}$ spectral functions in the nuclear medium were obtained in Ref. [214] and Refs. [215, 216, 219], respectively.

$D^{(*)}$ and $\overline{D}^{(*)}$ spectral functions

Let us start with the charmed mesons. Before showing the results for the spectral functions, we briefly discuss the model that was used in Refs. [215, 216, 219] for the $D^{(*)}$−nucleon and $\overline{D}^{(*)}$−nucleon interactions. Since the channels of interest involve the charmed pseudoscalar and vector mesons, HQSS needs to be implemented in the effective interaction. In order to do this, the authors consider an extension of the Weinberg-Tomozawa (WT) Lagrangian, which is symmetric in SU(3)−flavor (actually it is chiral $\mathrm{SU}(3)_L \times \mathrm{SU}(3)_R$), to the $\mathrm{SU}(6)_{\mathrm{lsf}} \times$ HQSS spin-flavor symmetry group (the subscript "lsf" denotes light quark spin–flavor symmetry).

Under SU(8) spin-flavor symmetry, the potential matrix elements (tree-level amplitudes) can be written as[14]

$$v_{ab}^{IJSC}(\sqrt{s}) = D_{ab}^{IJSC}\,\frac{\sqrt{s}-M}{2f^2}\left(\sqrt{\frac{E+M}{2M}}\right)^2, \tag{2.51}$$

where the labels $IJSC$ denote the total isospin, angular momentum, strangeness, and charm quantum numbers of the meson-baryon system. The quantities M and E in the above equation represent the common mass and the center-of-mass energy of the baryons within the corresponding SU(8) representation, respectively. The coefficient D_{ab}^{IJSC} is a matrix in the coupled-channel space, with a and b indexing the channels, and f is the weak decay constant of the mesons.

However, the $SU(8)$ spin-flavor symmetry is strongly broken in nature. For example, the pion and the D meson, which are part of the same multiplet under this symmetry, exhibit significantly different masses. To account for this symmetry breaking, the authors break this symmetry down to SU(6) × HQSS in the open-charm sectors and incorporate the physical hadron masses in the tree-level interaction of Eq. (2.51), as well as in the computation of the kinematic thresholds for the various channels. Additionally, they include corrections for the differences in decay constants between non-charmed and charmed pseudoscalar and vector mesons. Taking these effects into account, they rewrite the tree-level amplitudes as

$$v_{ab}^{IJSC}(\sqrt{s}) = D_{ab}^{IJSC}\,\frac{2\sqrt{s}-M_a-M_b}{4f_a f_b}\sqrt{\frac{E_a+M_a}{2M_a}}\sqrt{\frac{E_b+M_b}{2M_b}}, \tag{2.52}$$

where now different masses $M_{a(b)}$, CM energies $E_{a(b)}$, and decay constants $f_{a(b)}$ are taken, depending on the channels a, b. For further details, the reader can consult Ref. [215].

[14] The spinor normalization $\bar{u}u = \bar{v}v = 1$ has been used for the expression in Eq. (2.51), as well as the convention $V = -\mathcal{L}$.

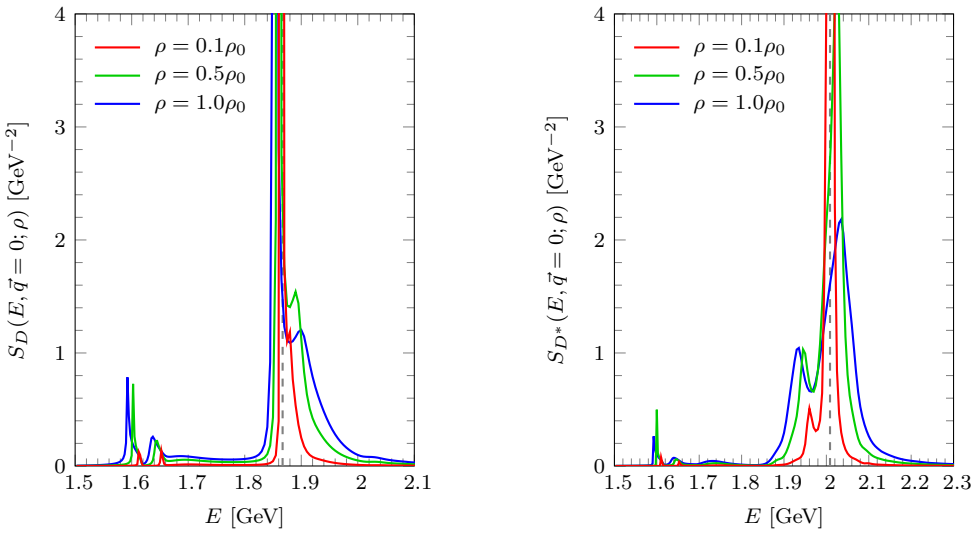

Figure 2.4: Spectral functions of the D (left) and D^* (right) mesons at zero three-momentum ($\vec{q} = 0$), plotted as a function of the charm meson energy E, for three nuclear densities: $\rho = 0.1\rho_0$, $0.5\rho_0$, and ρ_0, with $\rho_0 = 0.17\,\text{fm}^{-3}$. The dashed lines are located at the mass of the corresponding meson in vacuum.

Using the formula in Eq. (2.52), and employing the self-consistent unitarization scheme presented in Sect. 2.3.1, one can arrive at the results for the D, D^*, $\overline{D}$, and $\overline{D}^*$ spectral functions presented in Fig. 2.4. For zero density, the spectral functions would correspond to Dirac deltas peaking at the mass of the different charmed mesons, which are represented by a dashed line in the plots. As density increases, one observes a general broadening of the spectral functions, as well as some shift in the peak position, as was discussed when studying the spectral function in Sec. 2.3.2. However, it is clear that the Lorentzian approximation given in Eq. (2.37) is not valid in the energy ranges plotted, as several other peak structures appear in every plot. These peak structures correspond to the so-called *resonance-hole excitations*.

We will comment on the nature of the resonance-hole excitations. These excitations occur for energies of the (off-shell) M meson such that the invariant mass of the MN system is near the mass of some resonance in any of the appropriate spin-isospin channels. As occurs when studying the meson-nucleon cross section, the presence of these resonances enhances the shape of the spectral function, producing peaks. However, in the many-body conceptual frame, since the nucleons filling the Fermi sea are not of interest, one does not speak of MN resonances, but of the M meson decaying to a resonance-hole pair. From the reaction point of view, instead of having $MN \to X$, with X being the resonance

of interest, one writes $M \to XN^{-1}$, N^{-1} representing the creation of a hole in the Fermi sea. This is why the structures appearing in the spectral function of the M mesons are called resonance-hole excitations.

J	I	SU(8) state	Couples mainly to	Exp. candidate
$\frac{1}{2}$	0	$\Lambda_c(2595)$	D^*N	$\Lambda_c(2595)$
	1	$\Sigma_c(2556)$	$D^*\Delta$	—
		$\Sigma_c(2823)$	DN, D^*N and $D^*\Delta$	—
		$\Sigma_c(2868)$	DN, D^*N and $D^*\Delta$	—
$\frac{3}{2}$	0	$\Lambda_c(2660)$	$\Sigma_c^*\pi$	$\Lambda_c(2625)$
		$\Lambda_c(2941)$	D^*N	$\Lambda_c(2940)$[a]
	1	$\Sigma_c(2554)$	$D\Delta$ and $D^*\Delta$	—
		$\Sigma_c(2902)$	D^*N	$\Sigma_c(2800)$

[a] At the time the original work of Ref. [215] was published, there was no experimental confirmation of the quantum numbers of the $\Lambda_c(2940)$. As of the year 2025, it is listed in the PDG as $I(J^P) = 0(3/2^-)$ [18].

Table 2.1: List of resonances which couple to the DN and D^*N channels, as predicted by the SU(6) × HQSS spin-flavor model used in Ref. [215]. The states are classified by their spin J and isospin I quantum numbers. The main channels to which each resonance couples are given, as well as their possible experimental counterpart.

In the sector where the DN and D^*N amplitudes are involved, the SU(6) × HQSS model predicts eight resonances, which are listed here in Table 2.1 (for additional details about these states, see [220]). In the spectral function of the D meson, two peaks can be observed at the lower end of the energy spectrum (around $E = 1.6$ GeV). These peaks correspond to the $\Sigma_c(2556)$ and the $\Lambda_c(2595)$ states. Near the quasi-particle peak of the D meson—which is the highest one, obeying the real part of the equation for the renormalized mass, Eq. (2.20)—the $\Sigma_c(2823)$ resonance appears. This resonance is modified by the nearby $\Sigma_c(2868)$ state, and both of them are found to have an attractive effect on the DN threshold. For the D^* state, the quasi-particle peak is shifted toward higher energies and mixes with the $\Lambda_c(2941)$ resonance. On the left-hand side of the quasi-particle peak, the structure appearing there is the result of a mixing between the $\Sigma_c(2868)N^{-1}$ and $\Sigma_c(2902)N^{-1}$ excitations (N^{-1} representing a nucleon *hole*). Other resonance-hole states are also visible in the low-energy part of the plot, such as $\Sigma_c(2554)N^{-1}$.

Let us now briefly analyze the self-energies of the anti-charmed mesons $\overline{D}$ and $\overline{D}^*$, which are plotted in Fig. 2.5. In the $\overline{D}$ self-energy, one can recognize a resonance-hole structure very close to the quasi-particle peak. Given the quark

content of the anti-charmed mesons—$\bar{c}q$, with q a light quark—the resulting resonances from the interaction with nucleons must have a minimum of five valence quarks.[15] Therefore, this structure, namely $\theta(2805)$, is a loosely bound pentaquark with $I = 0$, $J = 1/2$ near the DN threshold, which is found to strongly couple to the DN and D^*N channels [221]. On the other hand, the $\overline{D}^*$ self-energy shows a mixing of the quasi-particle peak with several resonance-hole states. These states, among others, are described in Ref. [221].

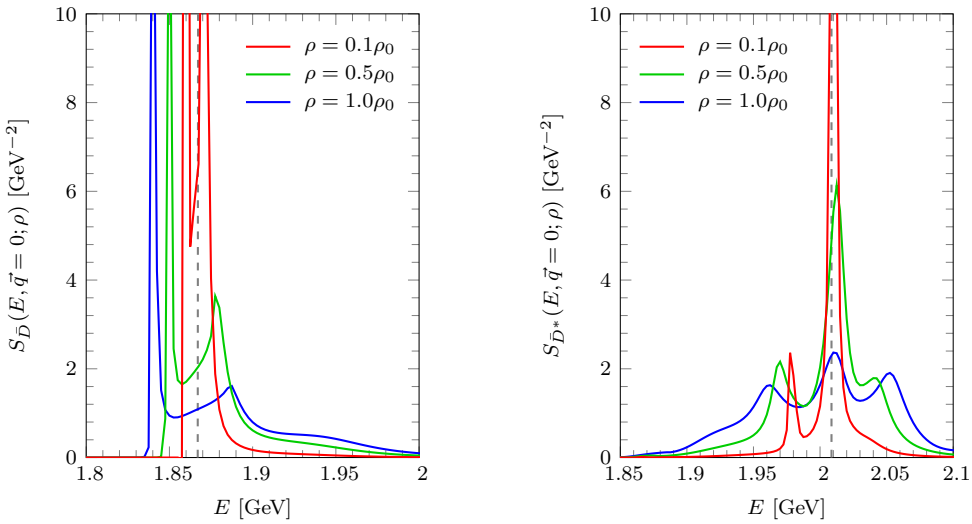

Figure 2.5: Spectral functions of the $\overline{D}$ (left) and $\overline{D}^*$ (right) mesons at zero three-momentum ($\vec{q} = 0$), plotted as a function of the anti-charm meson energy E, for three nuclear densities: $\rho = 0.1\rho_0$, $0.5\rho_0$, and ρ_0. The dashed lines are located at the mass of the corresponding meson in vacuum.

The appearance of these pentaquark-like resonant structures in the $\overline{D}^{(*)}N$ amplitudes is a feature of the SU(6) $\times$ HQSS spin-flavor model. Other models—for example, the SU(4) WT model of Ref. [222], or the $t-$channel vector exchange model of Ref. [223]—find a smooth and repulsive behavior for these amplitudes. In either way, the fact remains that the interaction with nucleons of the anti-charmed $\overline{D}$ and $\overline{D}^*$ mesons is very different from that of the charmed D and D^* mesons. This asymmetry, which can be regarded as a breaking of charge-conjugation symmetry by the presence of the nuclear Fermi sea, will have profound effects on the density dependence of the $T_{cc}(3875)^+$, as we shall see.

[15] This was not the case for the charmed mesons with quark content $c\bar{q}$, as the light antiquark can annihilate one of the light quarks of the nucleon.

K and $\overline{K}$ spectral functions

Let us now switch our attention to the self-energies that the kaon and anti-kaon develop when embedded in dense nuclear matter. These self-energies were computed in Ref. [214] using the lowest-order chiral perturbation theory Lagrangian that couples the octet of light pseudoscalar mesons to the octet of $1/2^+$ baryons. The coupled-channels tree-level amplitude (potential), in this case, reads

$$v^s_{ab} \;=\; -C_{ab}\,\frac{1}{4f^2}\,(2\sqrt{s}-M_{B_a}-M_{B_b})\,\sqrt{\frac{M_{B_a}+E_a}{2M_{B_a}}}\,\sqrt{\frac{M_{B_b}+E_b}{2M_{B_b}}}\,. \tag{2.53}$$

In this expression, M_{B_a} and E_a are the mass and energy of the baryon in the channel 'a', respectively, while $\sqrt{s}$ is the CM energy and C_{ab} represents the coefficients of the matrix in the coupled-channels space. In addition, f is the meson decay constant, which is taken as $f = 1.15 f_\pi$ to correctly describe the experimental characteristics of the low energy $\overline{K}N$ scattering and in particular to reproduce the properties of the $\Lambda(1405)$ resonance [214].

Using the potential given in Eq. (2.53), the amplitudes are unitarized, and the self-energies for the different species are computed in a self-consistent manner, similar to the formalism presented in Sec. 2.3.1. However, in this case, the computation incorporates the S- and P-waves of the kaon-nucleon interaction and takes into account Pauli blocking effects for the intermediate baryons as well as their self-energies. The authors also take into account finite-temperature modifications, taking the precaution that the $T \to 0$ limit is correct. This makes the computation more complex than the one presented in this thesis and can be reviewed in Ref. [214]. We will not dive any deeper into the details of the calculation and will limit ourselves to present and analyze the results for the zero-temperature density-dependent spectral functions for the kaon and the anti-kaon.

For the kaon self-energy, we approximate it by the free-space spectral function (Dirac delta), shifted to an energy $E^{\rm qp}$ which depends on the nucleon density. We write

$$S_K(E,\vec{q};\rho) \approx \frac{\delta\left(E - E^{\rm qp}(\vec{q};\rho)\right)}{2E^{\rm qp}(\vec{q};\rho)}. \tag{2.54}$$

which is justified in light of the fact that the KN interaction is very weak in ChPT, so the medium effects for the kaon are expected to be very small. This approximation was also used in Ref. [214], and it was found that the kaon spectral function was well described by this zero-width distribution. In the left plot of Fig. 2.6, we show the kaon quasi-particle energy ($E^{\mathbf{qp}}$) introduced in Eq. (2.54) as a function of the modulus of the three momentum, for four different nuclear densities. As we can see, there is a slight modification of the

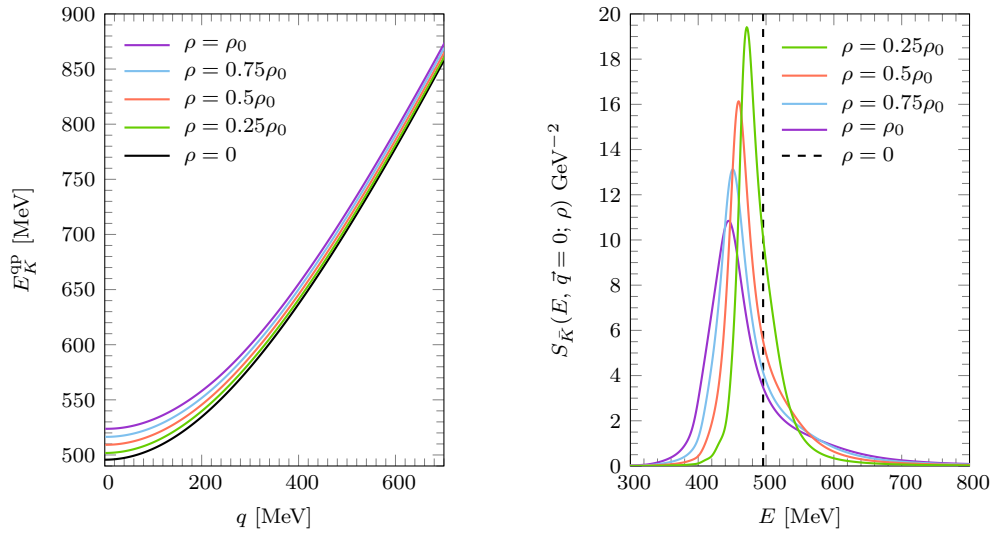

Figure 2.6: Left panel: Kaon quasi–particle energy $E^{\rm qp}$ [Eq. (2.54)] as a function of the kaon three-momentum magnitude $q = |\vec{q}|$ for several nuclear densities, expressed in units of $\rho_0 = 0.17\,\text{fm}^{-3}$. Right panel: Energy dependence of the $\overline{K}$ spectral function at zero three-momentum ($\vec{q} = 0$) for various densities.

in-medium mass for the kaon toward higher energies. However, this difference becomes less relevant as the momentum increases. The width of the K spectral function is negligible.

The $\overline{K}$ self-energy is represented in the right plot of Fig. 2.6. In this case, one observes a general broadening of the spectral function, as well as a shift of the quasi-particle mass towards lower energies—in contrast with the kaon, whose mass shifted to higher energies. Unlike the case of the D mesons, there are no apparent peaks due to the presence of resonance-hole excitations. However, in this channel, the two resonances which form the double pole structure of the $\Lambda(1405)$ are dynamically generated, and their presence produces both the shift and the broadening of the $\overline{K}$ spectral function, as thoroughly discussed in Refs. [112, 214, 224].

We have discussed the modification of the properties of the $D^{(*)}$ and $\overline{D}^{(*)}$ mesons, as well as of kaons and anti-kaons, when they are embedded in a dense nuclear medium. We are now in a position to analyze the in-medium scattering and interaction of these mesons. This will be done in the next section. Once we have presented the formalism for the scattering of two mesons in the nuclear medium, we will discuss the results obtained for the $T_{cc}(3875)$ and the $D_{s0}^*(2317)$ exotic states.

2.4 Two-meson scattering in nuclear matter

In this section, we discuss how the two-meson scattering amplitude is changed when these mesons are inside of a nuclear medium at zero temperature. We also discuss how the properties of the dynamically generated states are modified. First, we review the formalism used in free space to dynamically generate a state in the S wave dispersion of two mesons.

2.4.1 Dynamical state generation in vacuum

We begin by considering some X state as a generic two-meson S-wave loosely bound molecule characterized by quantum numbers $I(J^P)$. Later, we will specify X to represent the T_{cc} or the D^*_{s0}, corresponding to DD^* and DK hadron-pairs with quantum numbers $0(1^+)$ and $0(0^+)$, respectively. For now, however, we shall keep the notation general.

Although spin symmetry is exact—that is, the Hamiltonian does not mix states with different values of the total angular momentum[16]—isospin symmetry is approximate. Isospin-breaking effects arise because the particles within an isospin multiplet have unequal masses. As a result, the kinetic term in the Hamiltonian no longer respects isospin symmetry, and the thresholds for producing pairs of particles are shifted accordingly. These effects can be taken into account, as was done in Ref. [52] for the case of the T_{cc}. In this thesis, we do not consider them and we always work in the *isospin limit*, assuming equal masses for mesons within the same isospin multiplet, set to their average value. For example, in the case of the D mesons we shall take $m_D = (m_{D^0} + m_{D^+})/2$.

Then, under the assumption of exact isospin symmetry, the problem of two-meson scattering can be treated as a simple single-channel process, with well-defined quantum numbers $I(J^P)$. We consider two families of potentials to describe the scattering processes, which can be regarded as the tree-level amplitude derived from an effective Lagrangian. We choose the following parameterizations[17]

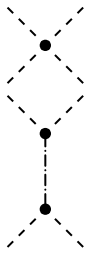

$$\equiv -iV_A, \qquad V_A(s) = C + Ds, \tag{2.55a}$$

$$\equiv -iV_B, \qquad V_B(s) = \frac{1}{C' + D's}, \tag{2.55b}$$

[16] In particular, if we assume a purely S-wave interaction, then it does not mix states with different total spin.

[17] In the diagrams of Eqs.(2.55a) and (2.55b) the direction of increasing time is taken upward. Thus, V_B represents an s-channel exchange of some bare state.

with $C^{(\prime)}$ and $D^{(\prime)}$ two LECs for each of the two different families of potentials. These LECs should be fixed to reproduce some known features of the unitarized amplitude, as we will show below.

Once the interaction kernel V (general notation for V_A or V_B) has been defined, the amplitude can be unitarized by solving the BSE, as was done in Sect. 2.3.1 when computing the self-energy of a meson in the nuclear medium. The unitarized amplitude reads[18]

$$T(s) = \left[V^{-1}(s) - \Sigma_0(s)\right]^{-1}, \tag{2.56}$$

where $\Sigma_0(s)$ is the two-meson vacuum loop function, defined as

$$\Sigma_0(s) = i \int \frac{d^4q}{(2\pi)^4} \Delta_0^M(P-q)\Delta_0^{M'}(q). \tag{2.57}$$

where the function Δ_0^M is the vacuum M meson propagator, and $\mathbf{P}$ is the total four-momentum of the system, with $s = \mathbf{P}^2$. Since the loop function is ultraviolet divergent, we need to renormalize it. We employ, as we have done before in this document, a cutoff Λ in momentum space. The cutoff-dependent two-meson vacuum loop function reads (see second erratum of [225])

$$\begin{aligned}\Sigma_0(s) = \frac{1}{32\pi^2}\Bigg\{ &-\frac{\Delta}{s}\log\frac{M_1^2}{M_2^2} + \frac{\nu}{s}\Bigg[\log\frac{s-\Delta+\nu\sqrt{1+\frac{M_1^2}{\Lambda^2}}}{-s+\Delta+\nu\sqrt{1+\frac{M_1^2}{\Lambda^2}}} \\ &+ \log\frac{s+\Delta+\nu\sqrt{1+\frac{M_2^2}{\Lambda^2}}}{-s-\Delta+\nu\sqrt{1+\frac{M_2^2}{\Lambda^2}}}\Bigg] + 2\frac{\Delta}{s}\log\frac{1+\sqrt{1+\frac{M_1^2}{\Lambda^2}}}{1+\sqrt{1+\frac{M_2^2}{\Lambda^2}}} \\ &- 2\log\left[\left(1+\sqrt{1+\frac{M_1^2}{\Lambda^2}}\right)\left(1+\sqrt{1+\frac{M_2^2}{\Lambda^2}}\right)\right] + \log\frac{M_1^2M_2^2}{\Lambda^4}\Bigg\},\end{aligned} \tag{2.58}$$

where

$$\Delta = M_2^2 - M_1^2, \qquad \nu = \sqrt{\left[s-(M_1+M_2)^2\right]\left[s-(M_1-M_2)^2\right]}, \tag{2.59}$$

and M_1, M_2 are the meson masses. The ν quantity can also be rewritten as

$$\nu = \sqrt{\lambda(s, M_1^2, M_2^2)} \tag{2.60}$$

where $\lambda(x,y,z)$ is the Källén (or triangular) function, and is related to the center-of-mass momentum as $k = \nu/2\sqrt{s}$.

[18] We use capital letters to denote the two–meson T–matrix and potential, in contrast to the lowercase notation employed for the meson–nucleon case in Eq. (2.24).

Now, let us assume that there is some X state in the MM' scattering amplitude, appearing as a bound state below the threshold. Then, the scattering amplitude will have a pole in the physical Riemann sheet, and can be written in the vicinity of the pole as

$$T(s) = \frac{g_0^2}{s - m_0^2} + \cdots \tag{2.61}$$

where m_0 is the mass of the state X and g_0^2 its coupling to the meson pair MM'. From the amplitude, one can obtain m_0 and g_0 as

$$T^{-1}(m_0^2) = 0, \qquad \frac{1}{g_0^2} = \left.\frac{dT^{-1}(s)}{ds}\right|_{s=m_0^2}. \tag{2.62}$$

Reversing this argument, if one knows m_0 and g_0^2, one can determine the scattering amplitude near the pole. This is precisely the logic we follow. Since there are only two LECs in our parameterization of the potential (for each family), we can exactly solve Eq. (2.62) for $C^{(\prime)}$ and $D^{(\prime)}$ in terms of m_0 and g_0^2. For the $A-$type potential, we find the following expressions:

$$C = \frac{1}{\Sigma_0(m_0^2)} + \frac{1 + g_0^2\Sigma_0'(m_0^2)}{g_0^2\Sigma_0^2(m_0^2)}m_0^2, \qquad D = -\frac{1 + g_0^2\Sigma_0'(m_0^2)}{g_0^2\Sigma_0^2(m_0^2)}, \tag{2.63}$$

where

$$\Sigma_0'(m_0^2) \equiv \left.\frac{d\Sigma_0(s)}{ds}\right|_{s=m_0^2}. \tag{2.64}$$

On the other hand, for the LECs appearing in the B family of potentials, we find

$$C' = \Sigma_0(m_0^2) - \frac{1 + g_0^2\Sigma_0'(m_0^2)}{g_0^2}m_0^2, \qquad D' = \frac{1 + g_0^2\Sigma_0'(m_0^2)}{g_0^2}. \tag{2.65}$$

Note that $C^{(\prime)}$ and $D^{(\prime)}$ depend on the cutoff Λ through the loop function, so that the renormalization group equation

$$\frac{d}{d\Lambda}(V^{-1} - \Sigma_0) = 0 \tag{2.66}$$

is fulfilled. In this way, the mass and coupling of the X state are cutoff independent.

2.4.2 Molecular probability

We now discuss the concept of molecular probability, which will be central to the discussion of our results. This concept was first introduced by Weinberg in Ref. [209], and was later reinterpreted in the work of [226]. We will briefly discuss two simple scenarios considered in the latter reference to illustrate the concept of molecular probability.

We work in the non-relativistic quantum mechanics framework, and start by considering the two-meson contact potential in S wave, separable in momentum space

$$\langle \vec{p}\,'|V|\vec{p}\rangle = v\,\Theta(\Lambda - p')\Theta(\Lambda - p), \tag{2.67}$$

where $p \equiv |\vec{p}|$ is the center-of-mass momentum of the two particles, and v is some constant parameter. For a potential of this form, the Lippmann-Schwinger equation (LSE) leads to a simple algebraic equation for the scattering amplitude.[19]

$$\langle \vec{p}\,'|T|\vec{p}\rangle = t(E)\,\Theta(\Lambda - p')\Theta(\Lambda - p), \qquad t(E) = \frac{v}{1 - vG(E)} \tag{2.68}$$

In the previous equation, G is the non-relativistic two-meson loop function

$$G(E) = \int_{p<\Lambda} d^3p \frac{1}{E - m_1 - m_2 - \frac{p^2}{2\mu}}, \tag{2.69}$$

with m_1 and m_2 the masses of the involved mesons and μ the reduced mass of the system. If this simple parameterization for the t matrix presents a bound state, a pole at some energy m below threshold, then the coupling of this state to the two-meson channel can be obtained as[20]

$$\frac{1}{g^2} = \left.\frac{dt^{-1}(E)}{dE}\right|_{E=m} = -\left.\frac{dG}{dE}\right|_{E=m} \quad \rightarrow \quad 1 = -g^2 G'(m). \tag{2.71}$$

[19] In this context we use the term LSE rather than BSE to emphasize that the discussion is set within nonrelativistic quantum mechanics, as opposed to the relativistic framework employed in the rest of this chapter.

[20] The normalization of the quantum mechanics T–matrix, potential and two-meson propagator loop function differs from the non-relativistic reduction of the quantum field theory ones, which have been used extensively in this chapter,—by some factors in the single-channel case. The relation between them are

$$V^{\rm QFT} = 32\pi^3\mu\sqrt{s}\,V, \qquad T^{\rm QFT} = 32\pi^3\mu\sqrt{s}\,T, \qquad G^{\rm QFT} = \frac{G}{32\pi^3\mu\sqrt{s}}. \tag{2.70}$$

In these relations, the 'QFT' superscript denotes the quantum-field-theoretical quantities, while their corresponding quantum mechanics counterparts do not have any superscript. These relations are derived by comparing the imaginary parts of both loop functions and then taking into account that the product VG needs to be dimensionless.

which allows to interpret $P = -g^2 G'(m)$ as the probability that the state with mass m is a molecule composed of the two interacting hadrons.

Let us now consider a scenario where many channels are involved. We start from a separable potential of the form of Eq. (2.67), where now the constant v is taken to be a $N \times N$ square matrix, with N being the number of channels involved. If the resulting T matrix has a singularity at a given energy m, then the couplings are defined as

$$g_i g_j = \lim_{E \to m} (E - m) t_{ij}(E), \tag{2.72}$$

where the ij subscripts denote the matrix element of the T matrix in the coupled channel space. In this scenario, it is possible to show that the normalization of the wave function of the bound state with mass m implies

$$\langle \psi | \psi \rangle = \sum_{i=1}^{N} |\langle \phi_i | \psi \rangle|^2 = 1, \tag{2.73}$$

where $|\phi_i\rangle$ represents the state of the system in channel i. By solving the time-independent Schrödinger equation for the state $|\psi\rangle$ with energy m, one can determine the coefficients $\langle \phi_i | \psi \rangle$ to be

$$|\langle \phi_i | \psi \rangle|^2 = -g_i^2 G_i'(m), \tag{2.74}$$

where G_i' represents the derivative of the loop function in channel i. The quantity of Eq. (2.74) is precisely the probability of the channel i in the bound state wave-function.[21] Taking the previous equations together, we can write

$$\sum_{i=1}^{N} P_i = \sum_{i=1}^{N} \left[-g_i^2 G_i'(m) \right] = 1, \tag{2.75}$$

which is the generalization to N channels of the extremely simple formula of Eq. (2.71).

Let us return to the single-channel case, considering now an energy-dependent potential.

$$\langle \vec{p}\,' | V | \vec{p} \rangle = v(E)\, \Theta(\Lambda - p')\Theta(\Lambda - p). \tag{2.76}$$

In this case, the on-shell factorization of the LSE still yields

$$t(E) = \frac{v(E)}{1 - v(E)G(E)} \tag{2.77}$$

[21] One may be alerted by the minus sign appearing in Eq. (2.74). If the quantity $|\langle \phi_i | \psi \rangle|^2$ is to be interpreted as a probability, it should be strictly positive. This is not a problem since, for a given m below the i threshold, $G_i'(m)$ is actually a negative real number. On the other hand, g_i^2 is a positive real quantity because the pole is on the real axis of the first Riemann sheet.

Applying in this case the formula for the probability that the state with mass m is measured as a state in channel 1—the only channel available since we are in a single-channel approach—yields

$$P = -g^2 G'(m)^2 \neq 1 \tag{2.78}$$

since then by definition of the coupling

$$\frac{1}{g^2} = \left.\frac{dt^{-1}}{dE}\right|_{E=m} = \left.\left(\frac{dv^{-1}}{dE} - \frac{dG}{dE}\right)\right|_{E=m}, \quad \rightarrow \quad g^2 \left.\frac{dv^{-1}}{dE}\right|_{E=m} + P = 1. \tag{2.79}$$

In light of the previous equation, we see that there is now an extra contribution to the normalization of the state from the energy dependence of the potential. This contribution accounts for other degrees of freedom which are not explicitly considered in the two-hadron effective potential $v(E)$(e.g. the exchange of additional states, etc..) We shall interpret

$$P = -g^2 G'(m) \tag{2.80}$$

as the probability that the state $|\psi\rangle$ is a two-meson $(m_1 - m_2)$ molecule, while $1 - P$ would be the probability weight of other (non-)molecular degrees of freedom. Assuming that the thresholds for other two-body channels are far away from the mass m of the bound state, $Z \equiv 1 - P$ will parameterize the probability that the state is actually a *genuine* degree of freedom of the theory, that is, a compact quark state, whose properties are modified by the meson cloud. We will return below to this discussion by analyzing the form of the energy-dependent potential families considered in the following sections.

Although we identify P with the molecular probability, this interpretation calls for some caution. In order shed some extra light into this topic, some discussion on the Weinberg compositeness concept and further developments are in order here. In Ref. [209] the experimental values for the scattering length (a) and effective range (r) from the proton-neutron scattering were used by Weinberg to show evidence that the deuteron is composite. However, this does not follow from the evaluation of the so-called compositeness P, defined as $P = 1 - Z = 1/\sqrt{1 + 2r/a}$. This expression gives the meaningless result of $P = 1.68 > 1$ for the molecular probability [227–230], as one would naively infer from Ref. [209]. The key token for the deuteron compositeness is the fact that r is small and positive on the order of the range $\sim m_\pi^{-1}$ of the proton-neutron interaction, as Weinberg indicated, rather than large and negative. Therefore, any conclusion about the nature of an exotic state based solely on the calculation of P can be misleading, as it neglects corrections of $O(1/\gamma_b)$, with $\gamma_b = \sqrt{-2\mu E_b}$ the binding momentum. Here, μ and $E_b (< 0)$ are the reduced mass of the hadron pair and the binding energy (e.g. $E_b = -2.2\,\text{MeV}$

for the deuteron), respectively. Several later works have worked out different applications, re-derivations, re-interpretations, and extensions of Weinberg's compositeness relations [62, 226–246], but so far there is no clear consensus on how to apply these relations to determine the compositeness or elementariness of specific states, in particular if they are not bound.

Note that despite Z being defined as a bare-state probability in Eq. (18) of Ref. [209], it is not fully observable as the bare compact QCD states are not physical, and the effects produced by the interacting hadron cloud should be considered. Indeed, Z is a renormalization field factor [209, 227] (as we will see in Sect. 2.4.4), being scheme and even a regularization-dependent quantity. However, in the weak binding limit ($\gamma_b \ll \beta$, with $1/\beta$ providing an estimate of the interaction range corrections) and for two particle $S-$wave scattering, the quantity Z is dominated by a term obtained from the residue of the two-hadron scattering amplitude $f(E)$ at the physical pole $E = E_b$ [209, 227]. Given that the latter is the effective coupling of the bound state to the continuum channel, a measurable quantity, this model-independent contribution to Z becomes a valuable measure of the compositeness. The scheme and scale-dependent terms of Z, for instance those analytic in E, have to be fixed by some renormalization condition, but importantly they are suppressed by a factor of the order $\mathcal{O}(\gamma_b/\beta)$ [209, 227]. More specifically, in the weak binding limit

$$P = 1 - Z \simeq \frac{\mu \hat{g}^2}{\gamma_b} + O\left(\gamma_b/\beta\right), \qquad \hat{g}^2 = \lim_{E \to E_b} (E_b - E) f(E)\,. \tag{2.81}$$

The above equation shows how the effective coupling $\hat{g}^2$, although it does not fully determine the sub-leading contributions $\mathcal{O}(\gamma_b/\beta)$ to Z, provides most of the molecular probability $P = 1 - Z$. This will be the scheme followed in this work. Further discussion and references can be found in Ref. [62].

Returning to the QFT language used in the discussion of the previous section on the generation of a dynamical state in vacuum (Sect. 2.4.1), we define in this case

$$P_0 = -g_0^2 \Sigma_0'(m_0^2) \tag{2.82}$$

where now the derivative of the loop function is taken with respect to $s = E^2$.[22] We denote the molecular probability "P_0" in this case to make it apparent that it is defined from the coupling and loop function in vacuum. This definition will remain as-is when considering the finite-density effects.

[22] The definition of Eq. (2.82) is consistent with Eq. (2.81). The couplings $\hat{g}$ and g_0 differ due to the difference of normalization between the scattering amplitudes f and T used in Eqs. (2.81) and (2.56), respectively. In addition, note that for a shallow bound state, the leading term of $\frac{\partial \Sigma_0(s)}{\partial s}\Big|_{s=m_0^2}$ is proportional to $1/\gamma_b$.

In terms of the molecular probability P_0, the two families of potentials read

$$V_A(s) = \frac{1}{\Sigma_0(m_0^2)} + \frac{\Sigma_0'(m_0^2)}{\left[\Sigma_0(m_0^2)\right]^2}\frac{1-P_0}{P_0}(s-m_0^2), \tag{2.83a}$$

$$V_B^{-1}(s) = \Sigma_0(m_0^2) - \Sigma_0'(m_0^2)\frac{1-P_0}{P_0}(s-m_0^2). \tag{2.83b}$$

In these expressions, it is already apparent that in the $P_0 \to 1$ limit, the two families of potentials behave as

$$\lim_{P_0\to 1} V_A = \lim_{P_0\to 1} V_B = \frac{1}{\Sigma_0(m_0^2)} = \text{const.} \tag{2.84}$$

This result is in line with our previous discussion that energy dependence on the potential reflects the appearance of additional degrees of freedom.

2.4.3 Dynamical state generation in nuclear matter

Now we take into account the effect that the dense nuclear medium has on the T matrix. In order to do so, we incorporate the density dependence in the propagators of the two mesons, leaving their interaction unchanged.[23] The in-medium BSE reads

$$T^{-1}(s;\rho) = V(s) - \Sigma(s;\rho), \tag{2.85}$$

where the density-dependent two-meson loop function is

$$\Sigma(s;\rho) = i\int \frac{d^4q}{(2\pi)^4}\Delta^M(E-q^0,\vec{P}-\vec{q};\rho)\Delta^{M'}(q^0,\vec{q};\rho), \tag{2.86}$$

with E the total energy and $\vec{P}$ the total three-momentum of the hadron pair. As we discussed earlier, the introduction of the nuclear medium breaks Lorentz invariance. Therefore, both the in-medium loop function $\Sigma(s;\rho)$ and the in-medium T matrix $T(s;\rho)$ should actually depend on E and $\vec{P}$ separately. However, we will derive results only for the case where the center of mass of the two-meson pair is at rest in the medium rest frame—that is, for $\vec{P}=\vec{0}$. In this frame, we can simply name $s=E^2$, so as to make the notation simple and similar to that of the vacuum case.

One can now introduce the spectral decomposition of the meson propagators,

$$\Delta^M(q^0,\vec{q}) = \int_0^\infty d\omega \left(\frac{S_M(\omega,\vec{q};\rho)}{q^0-\omega+i\varepsilon} - \frac{S_{\overline{M}}(\omega,\vec{q};\rho)}{q^0+\omega-i\varepsilon}\right), \tag{2.87}$$

[23] As it was discussed before when dealing the meson self-energy in a dense medium—see Eq. (2.24)—density modifications in the interaction kernel are considered as sub-leading ones.

and performing the q^0 integration in Eq. (2.86), one obtains

$$\Sigma(s;\rho) = \int_\Lambda \frac{d^3q}{(2\pi)^3} \int_0^\infty d\omega \int_0^\infty d\omega' \left(\frac{S_M(\omega,\vec{q};\rho) S_{M'}(\omega',\vec{q};\rho)}{E-\omega-\omega'+i\varepsilon} - \frac{S_{\overline{M}}(\omega,\vec{q};\rho) S_{\overline{M}'}(\omega',\vec{q};\rho)}{E+\omega+\omega'-i\varepsilon} \right) \quad (2.88)$$

In this expression, we have already set $\vec{P}=0$. In order to regularize the UV divergent loop of Eq. (2.88), we introduce a sharp cutoff Λ.[24] It is possible to write the density-dependent loop function in an alternative way, which is convenient for performing its numerical calculation. With a change of variables $\omega \to \Omega = \omega + \omega'$, we can write the loop function as follows,

$$\Sigma(s=E^2\,;\,\rho) = \frac{1}{2\pi^2} \int_0^\infty d\Omega \left(\frac{f_{MM'}(\Omega\,;\,\rho)}{E-\Omega+i\varepsilon} - \frac{f_{\overline{M}\overline{M}'}(\Omega\,;\,\rho)}{E+\Omega-i\varepsilon} \right), \quad (2.89)$$

where the auxiliary function $f_{MM'}$ is defined as

$$f_{MM'}(\Omega;\,\rho) = \int_0^\Lambda dq\, q^2 \int_0^\Omega d\omega\; S_M\left(\omega,\,|\vec{q}|;\,\rho\right) S_{M'}\left(\Omega-\omega,\,|\vec{q}|;\,\rho\right). \quad (2.90)$$

Additional details of the computation of this loop function, which is one of the main objects of this thesis, are provided in Appendix A.

Once the density-dependent two-meson loop has been determined, one can describe how the properties of the dynamical X state are modified.[25] Let us first focus on how the medium density modifies the pole position and the coupling when considering the $A-$type potential of Eq. (2.83a) as the kernel of the BSE. The density-dependent pole position, which we shall name $m(\rho)$, will be given by a zero in the inverse amplitude:

$$0 = T_A^{-1}(m_\rho^2;\rho) = V_A^{-1}(m_\rho^2) - \Sigma(m_\rho^2;\rho) \quad (2.91)$$

This leads to the following implicit equation for m_ρ:

$$m_\rho^2 = m_0^2 - \frac{P_0}{1-P_0} \frac{1}{\Sigma_0'(m_0^2)} \left[\Sigma_0(m_0^2) - \frac{\left[\Sigma_0(m_0^2)\right]^2}{\Sigma(m_\rho^2;\rho)} \right]. \qquad \text{(type } A\text{)} \quad (2.92)$$

[24] In principle, finite density effects are cutoff independent, as discussed when analyzing the finite-density meson-nucleon loop function of Eq. (2.25). However, in our formalism we kept the cutoff even for the finite-density modifications to the loop. This can result in some artifacts, which we expect will be small

[25] Recall that, ultimately, this X state will represent either the $T_{cc}(3875)$ or the $D_{s0}^*(2317)$ states (or their heavy quark spin partners).

The in-medium coupling can be derived from the density-dependent T matrix through the definition

$$\frac{1}{g_\rho^2} = \left.\frac{dT^{-1}(s;\rho)}{ds}\right|_{s=m_\rho^2}, \tag{2.93}$$

yielding, after using the equation (2.92) for m_ρ, the following

$$\frac{1}{g_\rho^2} = -\left[\frac{\Sigma(m_\rho^2;\rho)}{\Sigma_0(m_0^2)}\right]^2 \frac{1-P_0}{P_0}\Sigma_0'(m_0^2) - \Sigma'(m_\rho^2;\rho). \qquad \text{(type } A\text{)} \tag{2.94}$$

Using now the type$-B$ potential as the kernel of the BSE, one can derive in the same way the expressions for the in-medium mass and coupling of the X state,

$$m_\rho^2 = m_0^2 - \frac{1}{\Sigma_0'(m_0^2)}\frac{P_0}{1-P_0}\left[\Sigma(m_\rho^2;\rho) - \Sigma_0(m_0^2)\right], \qquad \text{(type } B\text{)} \tag{2.95}$$

$$\frac{1}{g_\rho^2} = -\frac{1-P_0}{P_0}\Sigma_0'(m_0^2) - \Sigma'(m_\rho^2;\rho). \qquad \text{(type } B\text{)} \tag{2.96}$$

Comparing the expressions for the $A-$ and $B-$type potentials, we see that they are equivalent when one can approximate $\Sigma(m_\rho^2;\rho)/\Sigma_0(m_0^2) \simeq 1$, that is, for small in-medium modifications.

We have arrived at an expression for the density-dependent coupling of the X state to the two-meson channel, as well as an implicit equation for the density-dependent mass. Although this is one way of writing the solution to the problem we were tackling, in practice it is not a useful one. More specifically, the resolution of the implicit equation for the in-medium renormalized mass m_ρ would require knowledge of the finite-density two-meson loop function for complex values of its argument (of m_ρ) and it is not evident how to perform an analytic continuation to the complex plane of the loop function of Eq. (2.88). The fact that m_ρ will be complex can be easily seen by approximating this mass in the medium by the vacuum mass in the self-consistent equation. Taking, for example, the expression of m_ρ arising from the B potential, one finds

$$m_\rho^2 = m_0^2 - \frac{1}{\Sigma_0'(m_0^2)}\frac{P_0}{1-P_0}\left[\Sigma(m_0^2;\rho) - \Sigma_0(m_0^2)\right]. \tag{2.97}$$

Since $\Sigma(m_0^2;\rho)$ can (and will) have an imaginary part even for energies below threshold, m_ρ will become complex.

Given that the problem of determining the value of m_ρ—or in other words the pole position—is difficult, we shall focus in determining the density-dependent scattering amplitude $T(s;\rho)$ on the real axis. From the lineshapes obtained, we will infer the medium modifications of the mass and width of the state. We will also explore in Sect. 2.4.7 an approximate method to determine the position of the pole.

2.4.4 Self-energy formalism and relation to the T–matrix scheme

In this subsection, we investigate the modification of the properties of a given state X, which couples to a two-meson channel, in a dense nuclear medium. The discussion runs parallel to what was studied at the beginning of Sec. 2.3 when dealing with the meson self-energies. However, there is a key difference, which is the fact that the X state is dressed by the nuclear medium only through its coupling to the two-meson channel, and we do not take into account any *direct* dressing in the X propagator. This is appropriate for instance to describe the medium-properties of a charmonium-like ($c\bar{c}$) state as the $X(3872)$, since one expects the $XN \to XN$ coupling to be small. However, this exotic resonance is successfully described as a $(D\bar{D}^* + hc)$ molecule [226], and therefore its line-shape in a dense medium should be strongly affected by the density-dependent self-energies that the $D^{(*)}$ and $\bar{D}^{(*)}$ mesons acquire.

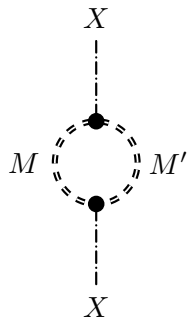

Figure 2.7: Self-energy diagram for the X state coupling to mesons M and M'. The black dots represent the bare coupling $\hat{g}$, and the double dashed lines correspond to the MM' loop function dressed with the nucleons of the system (time taken in the vertical direction).

Let us start by considering a preexisting *bare* X state with mass $\hat{m}$ and coupling $\hat{g}$ to a given two-meson channel. In free space, the irreducible self-energy of the X state due to its coupling to the two mesons (see Fig. 2.7) can be written as

$$-i\Pi_0^{(X)}(s) = [-i\hat{g}][i\Sigma_0(s)][-i\hat{g}] \quad \Rightarrow \quad \Pi_0^{(X)}(s) = \hat{g}^2\Sigma_0(s), \tag{2.98}$$

where Σ_0 is the two-meson loop function in vacuum. Upon resummation of all the possible insertions of the self-energy, one ends with the dressed propagator for the X:

$$\Delta_0^{-1}(s) = \hat{\Delta}^{-1}(s) - \Pi_0^{(X)}(s) \tag{2.99}$$

where

$$\hat{\Delta}^{-1}(s) = s - \hat{m}^2 + i\varepsilon \tag{2.100}$$

is the bare X propagator. From this formula, one defines the physical mass of the X state in vacuum as

$$m_0^2 = \hat{m}^2 + \Pi_0^{(X)}(m_0^2) = \hat{m}^2 + \hat{g}^2\Sigma_0(m_0^2). \tag{2.101}$$

Since the loop function is, in principle, divergent, so too will be the bare mass $\hat{m}$, such that the physical mass m_0 is finite. Furthermore, the renormalized coupling is given by

$$g_0^2 = \hat{g}^2 Z_0 \tag{2.102}$$

with Z_0 the field renormalization factor,

$$\frac{1}{Z_0} = \left.\frac{d\Delta_0^{-1}(s)}{ds}\right|_{s=m_0^2} = 1 - \hat{g}^2\Sigma_0'(m_0^2). \tag{2.103}$$

One can invert the relation between $\hat{g}^2$ and g_0^2

$$g_0^2 = \frac{\hat{g}^2}{1 - \hat{g}^2\Sigma_0'(m_0^2)} \quad \rightarrow \quad \hat{g}^2 = \frac{g_0^2}{1 + g_0^2\Sigma_0'(m_0^2)}, \tag{2.104}$$

and inserting this into the definition of the field normalization factor yields

$$Z_0 = \frac{1}{1 - \hat{g}^2\Sigma_0'(m_0^2)} = 1 + g_0^2\Sigma_0'(m_0^2) = 1 - P_0, \tag{2.105}$$

with P_0 the molecular probability defined in Eq. (2.82). From this last relation, and given the interpretation of P_0, the meaning of the Z_0 factor is clear: It represents the probability that the state is a pure "bare" state, in contrast to having a molecular nature in the two-meson channel considered.

Let us now consider a dense nucleon medium that renormalizes the meson propagators. Proceeding exactly as in the vacuum case, we find the renormalized mass and coupling

$$m_\rho^2 = \hat{m}^2 + \Pi_\rho^{(X)}(m_\rho^2) = \hat{m}^2 + \hat{g}^2\Sigma(m_\rho^2;\rho), \tag{2.106}$$

$$g_\rho^2 = \frac{\hat{g}^2}{1 - \hat{g}^2\Sigma'(m_\rho^2;\rho)}. \tag{2.107}$$

Since the bare $\hat{m}$ and $\hat{g}^2$ are potentially divergent quantities, it is more useful to rewrite the previous expressions in terms of the finite m_0^2 and g_0^2, using the relations of Eqs. (2.101) and (2.104). This results in the following expressions:

$$m_\rho^2 = m_0^2 + \frac{g_0^2}{1 + g_0^2\Sigma_0'(m_0^2)}\left[\Sigma(m_\rho^2;\rho) - \Sigma_0(m_0^2)\right], \tag{2.108}$$

$$g_\rho^2 = \frac{g_0^2}{1 - g_0^2 \left[\Sigma'(m_\rho^2;\rho) - \Sigma_0'(m_0^2)\right]}. \tag{2.109}$$

In terms of the molecular probability, these relations read

$$m_\rho^2 = m_0^2 - \frac{1}{\Sigma_0'(m_0^2)} \frac{P_0}{1-P_0} \left[\Sigma(m_\rho^2;\rho) - \Sigma_0(m_0^2)\right], \tag{2.110}$$

$$g_\rho^2 = -\frac{1}{\frac{1-P_0}{P_0}\Sigma_0'(m_0^2) + \Sigma'(m_\rho^2;\rho)}. \tag{2.111}$$

Note that from the previous expressions we have $m_\rho \to m_0$ and $g_\rho^2 \to g_0^2$ in the limit $\rho \to 0$.

Comparing these last equations with those that were obtained using the T–matrix formalism in Sect. 2.4.3, we see that they are completely equivalent to the case where the type$-B$ potential was used—see Eqs. (2.95) and (2.96). This should be expected, as the type$-B$ potential can be expressed as

$$V_B(s) = \frac{\hat{g}^2}{s - \hat{m}^2} \tag{2.112}$$

using the relations between the vacuum and the bare parameters that were derived in this section. This shows that this interaction is generated by the exchange of a bare state X. The only difference between the self-energy formalism presented here and the T–matrix presented in the previous section is the choice of the asymptotic state (the state that is placed in the nuclear medium). In this section, this asymptotic state is the bare X, while in Sect. 2.4.3 we considered the two mesons as asymptotic states. Aside from this minor difference, both formalisms are completely equivalent in this case. On the other hand, the type$-A$ interaction is not of the form of an explicit exchange of any bare state in the $s-$channel. It can be understood as a purely molecular contact interaction plus some energy dependence coming from a Taylor expansion around the physical vacuum pole of contributions arising from the exchange of some genuine bare quark-model states.

2.4.5 Spectral functions in the self-energy and T–matrix formalisms

In the previous subsection, we found that the dressed propagator for the X state in nuclear matter can be expressed as

$$\Delta(s;\rho) = \frac{1}{s - \hat{m}^2 - \Pi_\rho^{(X)}(s)} = \frac{1}{s - m_0^2 - \left[\Pi_\rho^{(X)}(s) - \Pi_0^{(X)}(m_0^2)\right]}, \tag{2.113}$$

where we define

$$\tilde{\Pi}^{(X)}(s;\rho) = \Pi_{\rho}^{(X)}(s) - \Pi_{0}^{(X)}(m_0^2) = \hat{g}^2\left[\Sigma(s;\rho) - \Sigma_0(m_0^2)\right] \tag{2.114}$$

as the contribution to the self-energy of the X coming from the nuclear medium. What we call $\tilde{\Pi}^{(X)}$ is analogous to what we were referring to as Π when studying the meson self-energies in Sect. 2.3. That is, $\tilde{\Pi}^{(X)}$ is a quantity that contains only the effects of the nuclear medium—so that when ρ tends to zero, we have $\tilde{\Pi}^{(X)} \to 0$. We can now use the definition given in Eq. (2.33) for the spectral function in terms of the propagator.

$$S^{(X)}(s;\rho) = -\frac{1}{\pi}\text{Im }\Delta(s;\rho). \tag{2.115}$$

It is also possible to define the X spectral function from the two-meson T–matrix point of view. Let us start by considering the potential V_B as the kernel to derive the T–matrix, since in this case we have shown that the results are equivalent to those arising from the self-energy formalism. We have

$$\begin{aligned} &T_B^{-1}(s;\rho) = V_B^{-1}(s) - \Sigma(s;\rho) \\ \to \quad &T_B^{-1}(s) = \frac{s-\hat{m}^2}{\hat{g}^2} - \Sigma(s;\rho) = \frac{s-\hat{m}^2-\hat{g}^2\Sigma(s;\rho)}{\hat{g}^2} = \frac{\Delta^{-1}(s;\rho)}{\hat{g}^2}. \end{aligned} \tag{2.116}$$

For the specific form V_B of the potential, we obtain that T_B and the X state propagator only differ in the normalization, given by the bare coupling. This motivates the definition

$$S^{(X)}(s;\rho) = -\frac{1}{\pi}\text{Im }\frac{T(s;\rho)}{\hat{g}^2} \tag{2.117}$$

which will be exactly equal to the self-energy of Eq. (2.115) for the T–matrix computed using V_B as the kernel, and will only be approximately equal in the region around the X vacuum-mass m_0 when using any other potential that produces the same pole as V_B in the free space. In particular, for the case of V_A, which can be rewritten in terms of the bare coupling, we have

$$V_A(s) = \frac{1}{\Sigma_0(m_0^2)} - \frac{1}{\hat{g}^2\Sigma_0^2(m_0^2)}(s-m_0^2), \tag{2.118}$$

so that the T–matrix can be approximated in a region around the vacuum pole mass m_0 as

$$T_A^{-1}(s;\rho) = \left[\frac{1}{\Sigma_0(m_0^2)} - \frac{1}{\hat{g}^2\Sigma_0(m_0^2)}(s-m_0^2)\right]^{-1} - \Sigma(s;\rho)$$

$$= \left[\Sigma_0(m_0^2) + \frac{1}{\hat{g}^2}(s - m_0^2) + \mathcal{O}\left(\frac{(s-m_0^2)^2}{\hat{g}^4}\right)\right] - \Sigma(s;\rho)$$
$$= \frac{\Delta^{-1}(s;\rho)}{\hat{g}^2} + \mathcal{O}\left(\frac{(s-m_0^2)^2}{\hat{g}^4}\right). \quad (2.119)$$

This expansion is completely general and can be applied to any T-matrix. From Eq. (2.119) it follows that, for a generic potential, the definition of the spectral function of the X in terms of the two-meson scattering T-matrix coincides with that obtained from the renormalized propagator only if the X state couples sufficiently strongly to the two-meson channel. The required strength of this coupling depends on the energy range under consideration—through the numerator of the higher-order terms in Eq. (2.119)—and is characterized by the density-dependent width of the X state, $\Gamma^{(X)}$:

$$\hat{g}^2 \gg m_0 \Gamma^{(X)}(\rho). \quad (2.120)$$

Expressing the bare coupling in terms of the molecular probability yields

$$\hat{g}^2 = -\frac{1}{\Sigma_0'(m_0^2)} \frac{P_0}{1 - P_0}, \quad (2.121)$$

so that the condition in Eq. (2.120) translates into requiring a sufficiently large value of P_0, i.e. close to unity.

2.4.6 Analysis of the limiting values for the molecular probability

It is interesting to study the limiting cases $P_0 \to 0$ (purely compact state) and $P_0 \to 1$ (purely molecular state).[26] Let us start with the purely compact scenario. In this case, one has

$$g_0^2 = -\frac{P_0}{\Sigma_0(m_0^2)} \to 0, \quad (2.122)$$

and through Eq. (2.104), necessarily $\hat{g}^2 \to 0$. This means that the X state does not couple to the two-meson channel, and therefore it does not get renormalized by the mesons. From the propagator point of view,

$$\Delta(s;\rho) = \frac{1}{s - m_0^2 - \hat{g}^2\left[\Sigma(s;\rho) - \Sigma_0(m_0^2)\right]}$$

[26] We do not consider states with $P_0 > 1$, although physical examples exist for which the molecular probability evaluated as in Eq. (2.82) results in a value greater than one, most famously the deuteron [209] (see discussion in Sect. 2.4.2).

$$= \frac{Z_0}{Z_0(s-m_0^2) - g_0^2\left[\Sigma(s;\rho) - \Sigma_0(m_0^2)\right]} \to \frac{1}{s - m_0^2 + i\varepsilon}, \quad (2.123)$$

and therefore it holds true that $\hat{m} = m_0 = m_\rho$. In the T–matrix approach, in either the type A or B scenarios, it is also found that $g^2(\rho) \to 0$. This signals that the T–matrix is not fit for describing the X state in this scenario, since the coupling is zero and therefore the X cannot be dynamically generated in the two-meson scattering amplitude. This can also be seen in the fact that the potentials need to become singular at the vacuum mass of the X, with $V'(m_0^2) \sim 1/P_0 \to \infty$.

Considering now the purely molecular case, we have that both the A and B potentials become equal and constant, cf. (2.84). The T–matrix takes the form

$$T(s;\rho) = \frac{1}{\Sigma_0(m_0^2) - \Sigma(s;\rho)} \quad (2.124)$$

and the in-medium mass is related to the vacuum mass, independently of the potential used, through

$$\Sigma_0(m_0^2) - \Sigma(m_\rho^2;\rho) = 0, \quad (2.125)$$

with the in-medium coupling being

$$g_\rho^2 = -\frac{1}{\Sigma'(m_\rho^2;\rho)}. \quad (2.126)$$

Analyzing the situation from the self-energy point of view, we see that the propagator of Eq. (2.123) becomes null—except when $s = m_\rho^2$, when both the numerator and the denominator are zero—as $P_0 \to 1$ and $Z_0 \to 0$. However, with the usual field renormalization, one can remove the factor Z_0 from the numerator. This results in the following propagator:

$$Z_0^{-1}\Delta(s;\rho) = \frac{1}{Z_0(s-m_0)^2 - g_0^2\left[\Sigma(s;\rho) - \Sigma_0(m_0^2)\right]}. \quad (2.127)$$

Even in this form, as Z_0 goes to zero, the vacuum part of the propagator vanishes, and we are simply left with the part originating from the self-energy $\tilde{\Pi}^{(X)}$. This is because there is no bare compact state in this limit, and the pole structure is generated only from the two-meson loop function contribution. We can check that in this limit,

$$\hat{g}^2 = \frac{g_0^2}{Z_0} \to \infty, \qquad \hat{m}^2 = m_0^2 - \hat{g}^2\Sigma_0(m_0^2) \to \infty. \quad (2.128)$$

The result holds even when regularizing the loop function Σ_0.

2.4.7 Effective loop function

In the last two paragraphs of Sect. 2.4.3 we pointed out that the exact determination of the pole of the unitarized amplitude in the finite-density scenario was a difficult task, given that it would require the analytic continuation to the complex plane of the density-dependent two-meson loop function $\Sigma(s;\rho)$. To perform this analytic continuation for complex values of s is not straightforward. In this subsection, we present an approximate method that allows us to search for poles in the complex plane and that will be used in our study of the T_{cc}^{+}.

The physical motivation for this method is that we can approximately understand the two-meson loop function in the nuclear medium as arising from the now unstable mesons, whose masses in the medium are shifted toward complex values. Although the spectral functions of the mesons may have a rich structure due to the presence of resonance-hole excitations, as is the case for D and D^*, this structure is *mostly* washed out when the integration over the energy variables of the spectral functions is calculated in the in-medium loop function; cf. Eq. (2.88). Therefore, one can approximately account for the density effects on the mesons by just the modification of their masses $M_1 \to M_1^{\text{eff}}(\rho)$ and $M_2 \to M_2^{\text{eff}}(\rho)$, and therefore write

$$\Sigma(s;\rho) \simeq \Sigma_0\left(s; M_1^{\text{eff}}(\rho), M_2^{\text{eff}}(\rho)\right). \tag{2.129}$$

The function $\Sigma_0\left(s; M_1^{\text{eff}}(\rho), M_2^{\text{eff}}(\rho)\right)$ is just the analytic formula for the relativistic two-meson loop function of Eq. (2.58), where we have replaced the masses of the mesons in vacuum, M_1 and M_2, by their effective masses in the nuclear medium, $M_1^{\text{eff}}(\rho)$ and $M_2^{\text{eff}}(\rho)$. Since Σ_0 already has an analytic expression, its analytic continuation to complex values of s is straightforward, and therefore it is easy to look for the poles of the T–matrix in the complex plane by numerically solving the following equation for the complex variable z:

$$T^{-1}(z) = V^{-1}(z) - \Sigma_0\left(z; M_1^{\text{eff}}(\rho), M_2^{\text{eff}}(\rho)\right) = 0. \tag{2.130}$$

Next, we discuss the values we shall take for $M_1^{\text{eff}}(\rho)$ and $M_2^{\text{eff}}(\rho)$. Contrary to what one might expect, we do not take these masses from their respective spectral functions. We fix these values by fitting Σ_0 to the known function $\Sigma(s;\rho)$ on the real axis. That is why we speak of *effective masses*, since they do not necessarily correspond to their values dependent on the nuclear density. We parameterize the density-induced changes on the effective masses as

$$M_1^{\text{eff}}(\rho) = M_1 + \Delta M(\rho) - i\frac{\Gamma(\rho)}{2}, \tag{2.131}$$

$$M_2^{\text{eff}}(\rho) = M_2 + \Delta M(\rho) - i\frac{\Gamma(\rho)}{2}. \tag{2.132}$$

Although, in principle, the mass changes induced by density are different for each of the $D^{(*)}$ and $\bar{D}^{(*)}$ mesons, we take them to be the same and describe them only with the two parameters ΔM and Γ. In this way, we reduce the number of free parameters used in the fit and, as we will see, we find a good enough description of the original loop function $\Sigma(s;\rho)$, as shown for the D^*D loop function in Fig. 2.17 of Sect. 2.5.5.

2.5 Finite density results for the $T_{cc}(3875)$

In this section, we particularize the formalism that was presented in Sect. 2.4 to the case of the $T_{cc}(3875)^+$ and its antiparticle, the $T_{\bar{c}\bar{c}}(3875)^-$. Then, we show the obtained results for these exotic states, as well as make some predictions for their HQSS partners.

2.5.1 Review of the formalism applied to the T_{cc}

We start by considering the $T_{cc}(3875)^+$ as a D^*D state with isospin and spin-parity quantum numbers $I(J^P) = 0(1^+)$. Therefore, we assume that T_{cc}^+ is an isoscalar state, with only a minor isospin breaking that arises from the different masses of the channels involved, as we detail below. This is consistent with the experimental analyses of [45, 52, 142], where no peak was observed in the isospin $I = 1$ channel D^+D^{*+}.

As was already mentioned at the start of Sect. 2.4, we consider a HQET interaction, which is diagonal in the isospin basis, and only take into account the $S-$wave contribution since $T_{cc}(3875)^+$ is located almost at the DD^* threshold. The relation between isospin and particle bases is[27]

$$|DD^*, I = 1\rangle = -\frac{1}{\sqrt{2}}\left(|D^{*+}D^0\rangle + |D^{*0}D^+\rangle\right), \tag{2.133}$$

$$|DD^*, I = 0\rangle = -\frac{1}{\sqrt{2}}\left(|D^{*+}D^0\rangle - |D^{*0}D^+\rangle\right), \tag{2.134}$$

In the particle basis $\{D^{*+}D^0,\, D^{*0}D^+\}$, the interaction, which is not diagonal, reads

$$\mathcal{V} = \frac{1}{2}\begin{pmatrix} V_1 + V_0 & V_1 - V_0 \\ V_1 - V_0 & V_1 + V_0 \end{pmatrix}, \tag{2.135}$$

[27] Note that there is a global "$-$" sign in this change of basis which does not affect the overall results. This "$-$" sign comes from the isospin convention $|\bar{d}\rangle = -|\frac{1}{2}, +\frac{1}{2}\rangle$, $|\bar{u}\rangle = |\frac{1}{2}, -\frac{1}{2}\rangle$, which implies for the charmed mesons $|D^0\rangle = |c\bar{u}\rangle = |\frac{1}{2}, -\frac{1}{2}\rangle$, $|D^+\rangle = |c\bar{d}\rangle = -|\frac{1}{2}, +\frac{1}{2}\rangle$. There is no sign difference for anticharmed mesons $|\bar{D}^0\rangle$ and $|D^-\rangle$.

where V_0 and V_1 are effective contact interactions in the isospin 0 and isospin 1 channels, respectively. The BSE in this coupled-channel approach reads

$$\mathcal{T}^{-1}(s) = \mathcal{V}^{-1} - \mathcal{G}(s)\,, \tag{2.136}$$

where the diagonal matrix $\mathcal{G}(s)$ is constructed from the two-meson loop functions,

$$\mathcal{G}(s) = \begin{pmatrix} \Sigma_{D^{*+}D^0}(s) & 0 \\ 0 & \Sigma_{D^{*0}D^+}(s) \end{pmatrix}\,. \tag{2.137}$$

Isospin-breaking effects enter the unitarized T–matrix through the kinetic terms of the different two-meson loop functions, due to the mass splitting between the charged and neutral D mesons. However, when taking the exact isospin limit, in which $m_D = (m_{D^+} + m_{D^0})/2$ and similarly for the vector mesons $m_{D^*} = (m_{D^{*+}} + m_{D^{*0}})/2$, the loop function becomes proportional to the identity

$$\mathcal{G}(s) = \mathbb{I}_{2\times 2}\Sigma_0(s). \tag{2.138}$$

In this equation, the vacuum loop function Σ_0 is given in Eq. (2.58), particularizing the masses M_1 and M_2 to m_D and m_{D^*}. Therefore, in Eq. (2.136) the isospin channels decouple, and we can solve their $T-$matrices independently. This is precisely what we do in this study. In order to regularize Σ_0, we take a three-momentum sharp cutoff $\Lambda = 700$ MeV, and we will take the same cutoff for both the vacuum and the nuclear-density dependent loops.

We take the $I = 0$ amplitude and for the interaction kernel we use the A and B families of $S-$wave potentials presented in Eqs. (2.83a) and (2.83b). Since we work in the isospin limit, we cannot take m_0 to be the physical mass of the T_{cc}. Instead, we take a binding energy with respect to the isospin-symmetric DD^* threshold of $E_B = m_D + m_{D^*} - m_0 = 0.8$ MeV. This value is motivated by the analysis performed in the isospin limit in Ref. [52]. With the m_0 parameter already fixed, we consider several scenarios for the molecular probability P_0 ranging from 0 to 1. We show the resulting potentials in Fig. 2.8.

In Fig. 2.8 it is apparent that both families of potentials can be substantially different. However, there are some remarks that can be made. Firstly, we see that the value of the potential and of its first derivative at $s = m_0^2$ is the same for both the A and B families.

$$V_A(m_0^2) = V_B(m_0^2) = \frac{1}{\Sigma_0(m_0^2)}, \tag{2.139a}$$

$$V_A'(m_0^2) = V_B'(m_0^2) = -\frac{1}{\hat{g}^2\left[\Sigma_0(m_0^2)\right]^2}. \tag{2.139b}$$

This is a direct result of the definition of the LECs by fixing the pole position and the value of the coupling, recall Eqs. (2.62). It is clear from the plots of

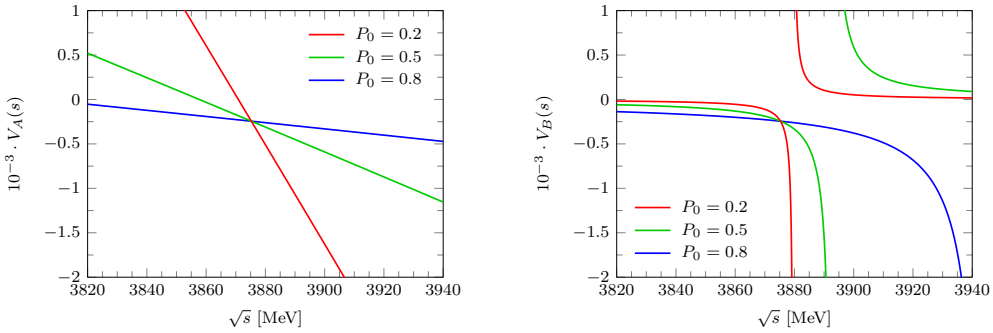

Figure 2.8: Plot of V_A (left-hand side) and V_B (right-hand side) potentials of Eqs. (2.83a) and (2.83b) as a function of the invariant mass $\sqrt{s}$ for different values of the molecular probability P_0.

Fig. 2.8 that both potentials become singular at $\sqrt{s} = m_0$ if $P_0 \to 0$, and both become very similar around $\sqrt{s} = m_0$ when $P_0 \to 1$. All these features were already noted when discussing the limiting cases of P_0 in Sect. 2.4.6. Therefore, a similar qualitative behavior of the unitarized amplitude should be expected in the A and B scenarios when considering a value for P_0 close to unity, while some important differences may arise for small molecular probabilities.

2.5.2 Nuclear medium results for the $T_{cc}(3875)^+$

In this section, we first discuss the in-medium DD^* loop function and show some results for the density-dependent $T-$matrices, computed using V_A or V_B as kernels of the BSE. After that, we present equivalent results for the spectral functions within the self-energy formalism.

In-medium amplitude

Now, we examine the results we have obtained for the $I(J^P) = 0(1^+)$ D^*D amplitude inside of the nuclear medium $|T(E;\rho)|^2$ [Eq. (2.85)]. We plot different quantities as functions of the energy E of the D^*D pair in the nuclear medium rest frame ($\vec{P} = \vec{0}$). Note that $E \equiv \sqrt{s}$ in the notation of the previous sections, first introduced in Sect. 2.4.3. First, we show in Fig. 2.9, results for the in-medium D^*D loop function. To better interpret the density modifications to the loop function, we rewrite the T–matrix in the medium, first shown in Eq. (2.85), as

$$T^{-1}(s\,;\,\rho) = V_{\text{eff}}^{-1}(s\,;\,\rho) - \Sigma_0(s\,)\,, \tag{2.140a}$$
$$V_{\text{eff}}^{-1}(s\,;\,\rho) = V^{-1}(s) + \delta\Sigma(s\,;\,\rho)\,, \tag{2.140b}$$

where $\delta\Sigma(s\,;\,\rho) = [\Sigma_0(s) - \Sigma(s\,;\,\rho)]$. In this new expression, the medium corrections are incorporated into the effective potential V_{eff}, while the two-meson loop is that of the vacuum. This will be used in order to infer whether the nuclear medium induces an effective attractive or repulsive behavior on the two-meson interaction.

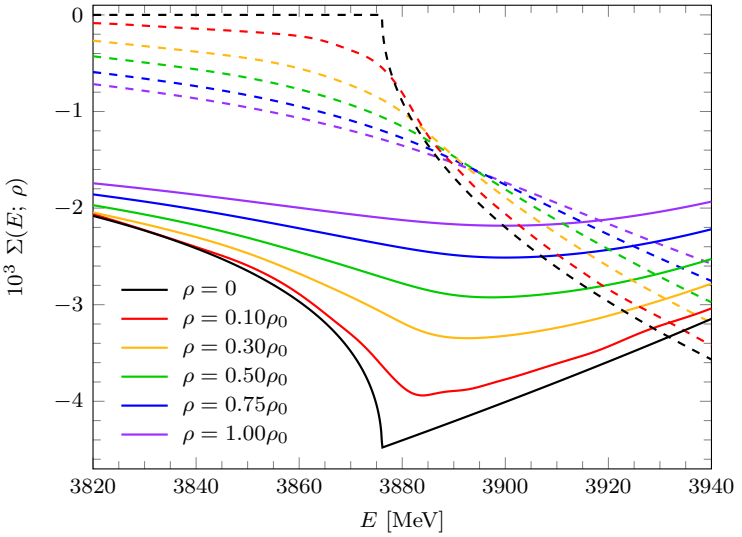

Figure 2.9: D^*D loop function for various values of the nuclear matter density ρ as a function of the D^*D pair energy E in the c.m. frame. The solid and dashed lines stand for the real and imaginary parts, respectively. A three-momentum cutoff $\Lambda = 700$ MeV is implemented for its regularization.

We are now ready to examine the loop function in the medium $\Sigma(E;\,\rho)$, presented in Fig. 2.9 for various values of the nuclear density ρ ranging from zero to ρ_0, with $\rho_0 = 0.17$ fm^{-3} the normal nuclear matter density. On the one hand, regarding the imaginary part (dashed lines), we see that the unitarity cut, which sharply begins at the D^*D threshold in vacuum, becomes smoothed as the density increases. Additionally, we observe that the loop function develops an imaginary part even for energies below the threshold. This occurs because the D and D^* mesons acquire a certain width, determined by their spectral functions, when they are placed within the medium. As we have already discussed, this width is the result of the interactions between the D and D^* mesons and nucleons, which lead to inelastic processes (for example $DN \to \Lambda_c^*$) and therefore to the decay of the D and D^* mesons in the medium. On the other hand, the real part (solid lines) also flattens with increasing densities and shifts toward a larger, less negative value, so $\text{Re}\,\delta\Sigma(s\,;\,\rho) < 0$. Invoking now the definition of V_{eff}, this means that $\text{Re}\,V_{\text{eff}}^{-1}(s;\rho) \leq V^{-1}(s)$. This would imply

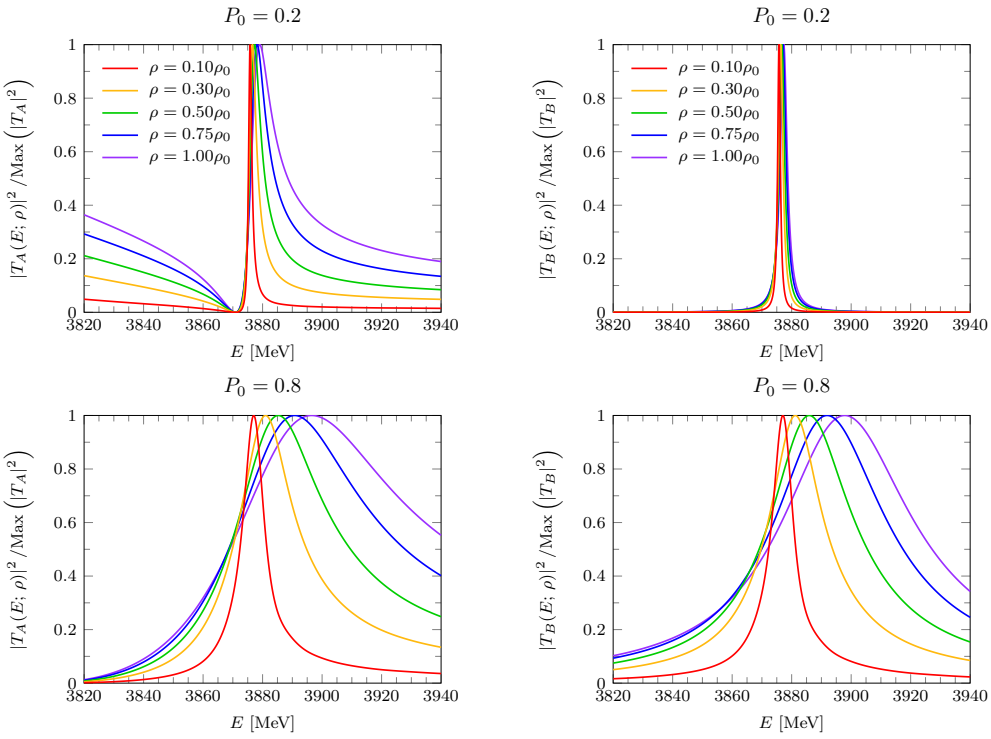

Figure 2.10: Squared modulus of the D^*D amplitudes obtained by solving the BSE using the $V_A(s)$ (left column) and $V_B(s)$ (right column) potentials, as a function of the center-of-mass energy E, for several values of the nuclear density ρ (different line colors) and for two values of the molecular probability P_0 ($P_0 = 0.2$ in the top row and 0.8 in the bottom row). Note that the amplitudes have been normalized to be one at their maximum.

that the effect of the medium is to generate repulsion in the D^*D interaction. However, one has to take this claim with caution, since the imaginary part of the density-dependent loop is sizable, so that V_{eff}^{-1} will also have a large imaginary part, which we cannot neglect.

After calculating the modified D^*D loop function $\Sigma(E;\rho)$, the D^*D T–matrix in nuclear medium can be derived from the $T_{cc}(3875)^+$ mass and its D^*D probability (m_0 and P_0) in vacuum, as previously discussed. We consider two families of $T-$matrices, namely T_A and T_B, derived from the $V_A(E)$ and $V_B(E)$ potentials, respectively, and different values of the molecular probability P_0.

In Fig. 2.10 we present the squared modulus of the T_A (left column) and T_B (right column) amplitudes for different densities, considering two values for

the molecular probability $P_0 = 0.2$ (top row) and 0.8 (bottom row). In order to better compare between the different density scenarios considered, we have normalized the squared amplitudes to be one at the maximum of the T_{cc} peak. When comparing the amplitude computed using the $V_A(E)$ potential and the one obtained from the $V_B(s)$ potential, we conclude that for high values of the molecular D^*D component, the predictions of both potentials are very similar. This was expected since in the limit $P_0 \to 1$ both potentials are very similar in the region of energies around $s = m_0^2$, as was already discussed when analyzing Fig. 2.8. For small values of P_0 ($P_0 = 0.2$ in the upper plots), both potentials are very different, leading to distinct $T-$matrices in the medium, despite giving rise to the same mass (m_0) and coupling (g_0^2) in the free space. This can be easily understood since the A potential presents a zero very close to m_0, while V_B has a pole near m_0. These features produce great distortions on their respective $T-$matrices.

Comparing the density dependence of the in-medium $T-$matrices for small and large P_0 cases, we find that the medium effects are significantly larger for the scenarios where a high molecular probability is considered. This is natural, since density corrections affect the T_{cc} only through its coupling to the DD^* channel in our model. For large values of P_0, the width increases significantly with density, and the peak position is shifted to higher energies. When considering a small molecular component, the changes to the $T_{cc}(3875)^+$ become less important and, as mentioned before, the $T-$matrices differ depending on the used potential. The amplitudes deduced from $V_A(E)$ show the zero that this type of potential has below m_0, with the position of the zero being independent of the nuclear density, as discussed in Ref. [162]. However, the amplitude below and above this zero shows a clear dependence on the density. In contrast, when using the $V_B(E)$ interaction, we basically observe the peak induced by the bare pole present in the potential. In this case, the in-medium effects are even smaller than when considering the $V_A(E)$ potential, and for $P_0 = 0.2$ the amplitude is almost density independent. Considering these important differences between the low and high P_0 scenarios, any experimental input on $|T(E;\rho)|^2$, in particular for energies around m_0, could shed light on the dynamics of the interacting D^*D pair.

In-medium self-energy and spectral function

We shall now analyze the density-induced modifications to the T_{cc}^+ from the equivalent self-energy point of view. The functional dependence of the T_{cc}^+ self-energy in the energy and density variables is equivalent to that of the two-meson in-medium loop function. The only difference is an overall normalization factor, given by the bare coupling $\hat{g}$, and a shift to the real part given by $\Sigma_0(m_0^2)$, cf.

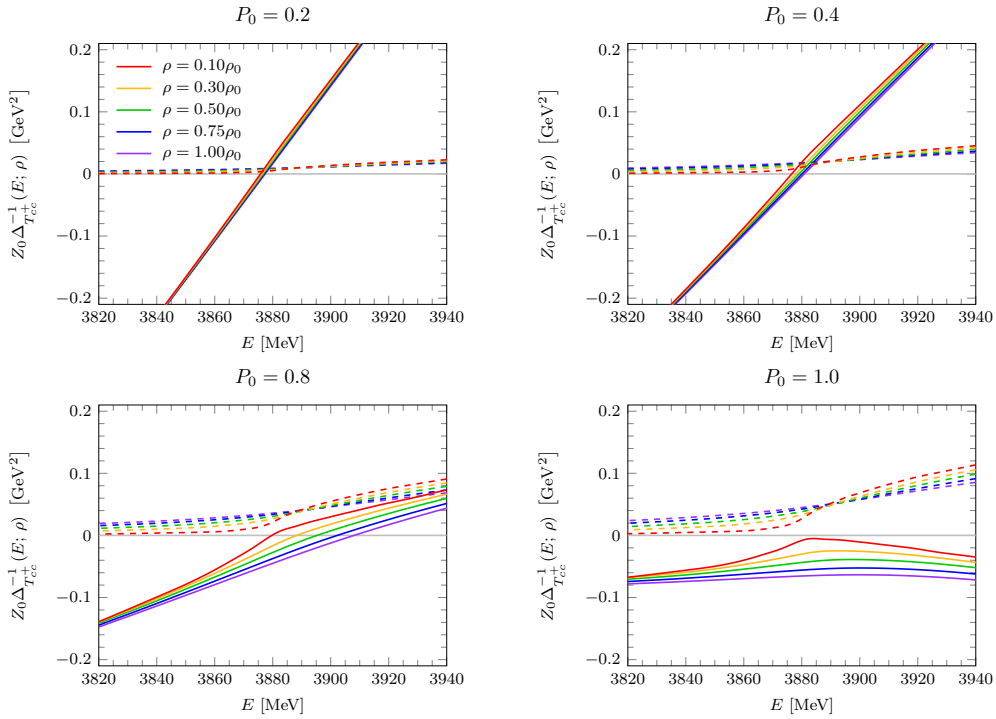

Figure 2.11: Plots of the inverse of the propagator of the $T_{cc}(3875)^+$ as a function of the center-of-mass energy E for different values of the nuclear density ρ (different colors on the graphs) and for different values of the molecular probability P_0 on each graph. The solid (dashed) lines correspond to the real (imaginary) parts of the propagator. Also note that the propagator has been conveniently normalized with a Z_0 factor.

Eq. (2.114). Thus, we find it redundant to plot $\tilde{\Pi}^{(T^+_{cc})}$, as it is extremely similar to the function of Fig. 2.9.

It is more interesting to analyze the density behavior of the T^+_{cc} propagator. In Fig. 2.11 we plot the inverse of the T^+_{cc} propagator for several densities (different line colors) considering four molecular probabilities. We divide the propagator by the field renormalization constant Z_0 in order for it not to be null in the $P_0 \to 1$ limit. For zero molecular probability, this propagator is just the vacuum propagator of the T^+_{cc}, which does not have an imaginary part, and whose inverse real part is linear in s, vanishing for $s = m_0^2$. For increasing values of P_0, the propagator has an increasing contribution from $\tilde{\Pi}^{(T^+_{cc})}$. This produces a nonzero imaginary part, and shifts the position of the zero in the

real part. The position of this zero defines the quasi-particle mass:[28]

$$\text{Re } \Delta^{-1}_{T^+_{cc}}(m_{\text{qp}};\rho) = 0. \tag{2.141}$$

The position of the quasi-particle mass is not significantly affected by the density for small molecular probabilities (see the plots corresponding to $P_0 = 0.2$ and 0.4), it is markedly shifted toward higher values with increasing density in the $P_0 = 0.8$ scenario. At a specific molecular probability value between 0.9 and 1, m_{qp} approaches infinity, resulting in no solutions for the mass of the quasi-particle for $P_0 = 1$. This signals the fact that, for high enough molecular probabilities, it stops making sense to talk about the renormalization of a bare preexisting T^+_{cc} core. The linear behavior on s of the inverse propagator is "overwritten" by the self-energy contribution, and one can no longer discuss the presence of a T^+_{cc} quasi-particle. In the limiting case of $P_0 = 1$, the inverse propagator is completely determined by the T^+_{cc} self-energy. Therefore, the plot in the lower right corner of Fig. 2.11 simply represents the $\tilde{\Pi}^{(T^+_{cc})}$ self-energy part.

In Fig. 2.12 we present the results for the T^+_{cc} spectral function. We consider both the genuine spectral function defined from the T^+_{cc} propagator—equivalent to the one originating from the T_B amplitude as discussed in the formalism—in the right column, as well as the spectral function arising from the imaginary part of the T_A amplitude, shown in the left column. The two rows of this figure correspond to the molecular probabilities of 0.2 and 0.8. For small molecular probabilities, the lineshapes of both spectral functions are quite different, since one can hardly define a spectral function coming from the two-body D^*D scattering amplitude in this case. Again, it is inferred from these graphs that for a low value of P_0 there is little effect arising from the dense nuclear medium. In the high molecular component scenario, both pictures give comparable results and produce a much larger T^+_{cc} width, which increases with density. One can observe in these plots that the position of the quasi-particle mass, linked to the position of the peak in the spectral functions, shifts toward higher energies, as we have already noted by looking at the inverse propagator.

2.5.3 Nuclear medium results for the $T_{\bar{c}\bar{c}}(3875)^-$

We will now discuss the results for the charge-conjugated partner of the $T_{cc}(3875)^+$, namely the $T_{\bar{c}\bar{c}}(3875)^-$. We will refer to this state as $T^-_{\bar{c}\bar{c}}$ for short. The comparison between both charge-conjugation partners was an important novelty in the work of Ref. [1] as compared with the previous analysis of the

[28] Recall that we are always taking the system to be at rest in the nuclear-matter rest frame. If the T^+_{cc} had some nonzero three-momentum, we would talk about *the quasi-particle energy* instead.

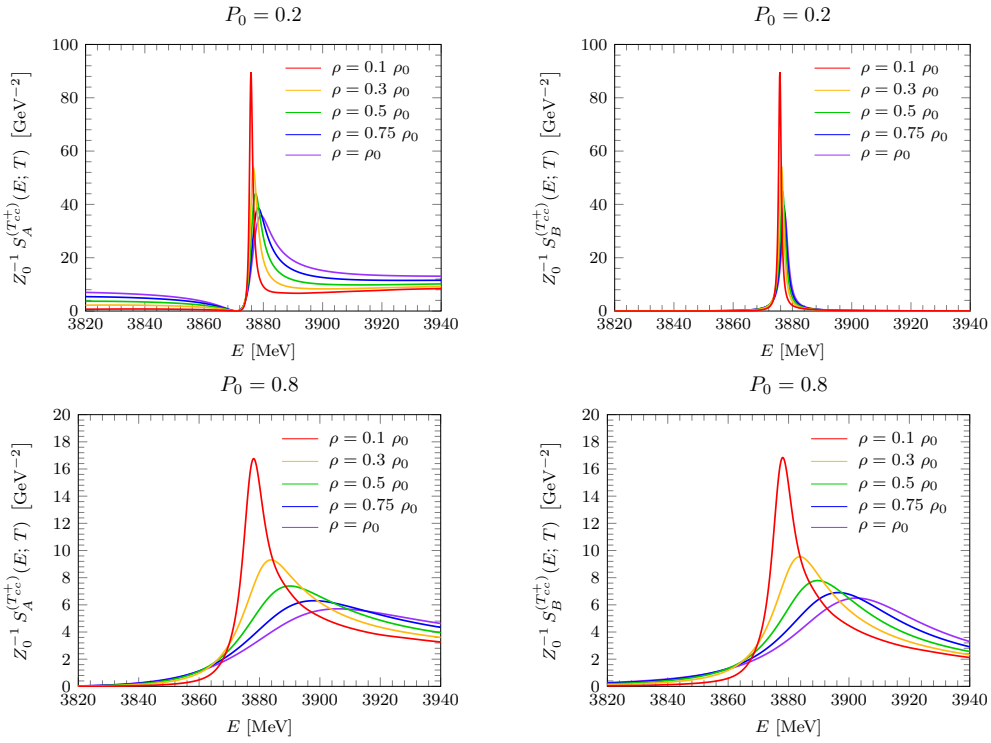

Figure 2.12: Spectral function of the T_{cc}^+, obtained from the T_A (left column) or the $T_B(s)$ (right column) amplitudes, with the latter being equivalent to the spectral function obtained directly from the propagator. These spectral functions are displayed as function of the center-of-mass energy E, for several values of the nuclear density ρ (different line colors) and for two values of the molecular probability P_0 ($P_0 = 0.2$ and 0.8 in the top and bottom rows, respectively). The spectral functions have been divided by the field normalization factor Z_0.

$\chi_{c1}(3872)$ in the nuclear medium of [162]. Due to charge-conjugation symmetry, the $T_{\bar{c}\bar{c}}(3875)^-$ has the same vacuum mass m_0 and coupling g_0^2 as the T_{cc}^+. In the free space, the description of the $T_{\bar{c}\bar{c}}^-$ runs parallel to that of the T_{cc}^+, but taking into account that now this state couples to the $I(J^P) = 0(1^+)$ $\overline{D}^*\overline{D}$ two-meson channel. However, the presence of the dense nuclear medium breaks this symmetry, and the $T_{\bar{c}\bar{c}}^-$ will no longer have the same mass and coupling as its charge-conjugation sibling, the T_{cc}^+.

When considering the $T_{\bar{c}\bar{c}}^-$ in dense nuclear matter, the anticharmed $\overline{D}$ and $\overline{D}^*$ mesons will get renormalized by the medium. As we already noted when discussing their spectral functions, the changes produced by the nuclear medium

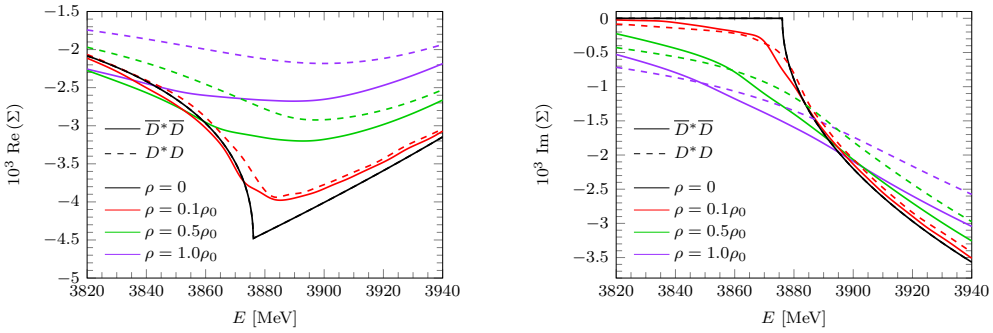

Figure 2.13: Real (left) and imaginary (right) parts of the $\overline{D}^*\overline{D}$ (solid lines) and D^*D (dashed lines) loop functions. We show results for different values of the nuclear medium density as a function of the c.m. energy of the meson pair.

to the $\overline{D}$ and $\overline{D}^*$ will be different from those produced to their charge-conjugated partners D and D^*, cf. Figs. 2.4 and 2.5. This is because the nucleons of the Fermi sea interact very differently with the charmed or anticharmed mesons. The $\overline{D}^*\overline{D}$ in-medium loop function—which we will denote as $\overline{\Sigma}(s;\rho)$—using now the $\overline{D}^*$ and $\overline{D}$ spectral functions, is

$$\overline{\Sigma}(E^2\,;\,\rho) = \frac{1}{2\pi^2}\int_0^\infty d\Omega\left(\frac{f_{\overline{D}\overline{D}^*}(\Omega\,;\,\rho)}{E-\Omega+i\varepsilon} - \frac{f_{DD^*}(\Omega\,;\,\rho)}{E+\Omega-i\varepsilon}\right), \tag{2.142}$$

and we find different density patterns as compared with the D^*D in-medium loop of Eq. (2.89). This can be seen in Fig. 2.13, where we present a comparison of the real (left-hand plot) and imaginary (right-hand plot) parts of the $\overline{D}^*\overline{D}$ (solid lines) and D^*D (dashed lines) loop functions for several values of the nuclear density ρ (line colors). The real and imaginary parts of the loop functions $\overline{D}^*\overline{D}$ and D^*D are the same in vacuum ($\rho = 0$) as required by charge-conjugation symmetry, which ensures that the pairs of $\overline{D}^*\overline{D}$ and D^*D mesons have the same masses. However, when considering a density different from zero (even as small as $0.1\,\rho_0$), notable differences appear between the two loop functions. Similarly to Eq. (2.140) of our analysis of the D^*D loop function, we can also define for the in-medium $\overline{D}^*\overline{D}$ pair an effective potential $\overline{V}_{\rm eff}(s\,;\,\rho)$. Since the free space terms are equal, it follows that

$$\overline{V}^{-1}_{\rm eff}(s\,;\,\rho) - V^{-1}_{\rm eff}(s\,;\,\rho) = \frac{V_{\rm eff}(s\,;\,\rho) - \overline{V}_{\rm eff}(s\,;\,\rho)}{V_{\rm eff}(s\,;\,\rho)\overline{V}_{\rm eff}(s\,;\,\rho)} = \Sigma(s\,;\,\rho) - \overline{\Sigma}(s\,;\,\rho) \tag{2.143}$$

Examining the real part of the loop function at the various densities displayed in Fig. 2.13, one sees that the $\overline{D}^*\overline{D}$ curves consistently lie below the corresponding D^*D ones, a separation that is most pronounced below threshold.

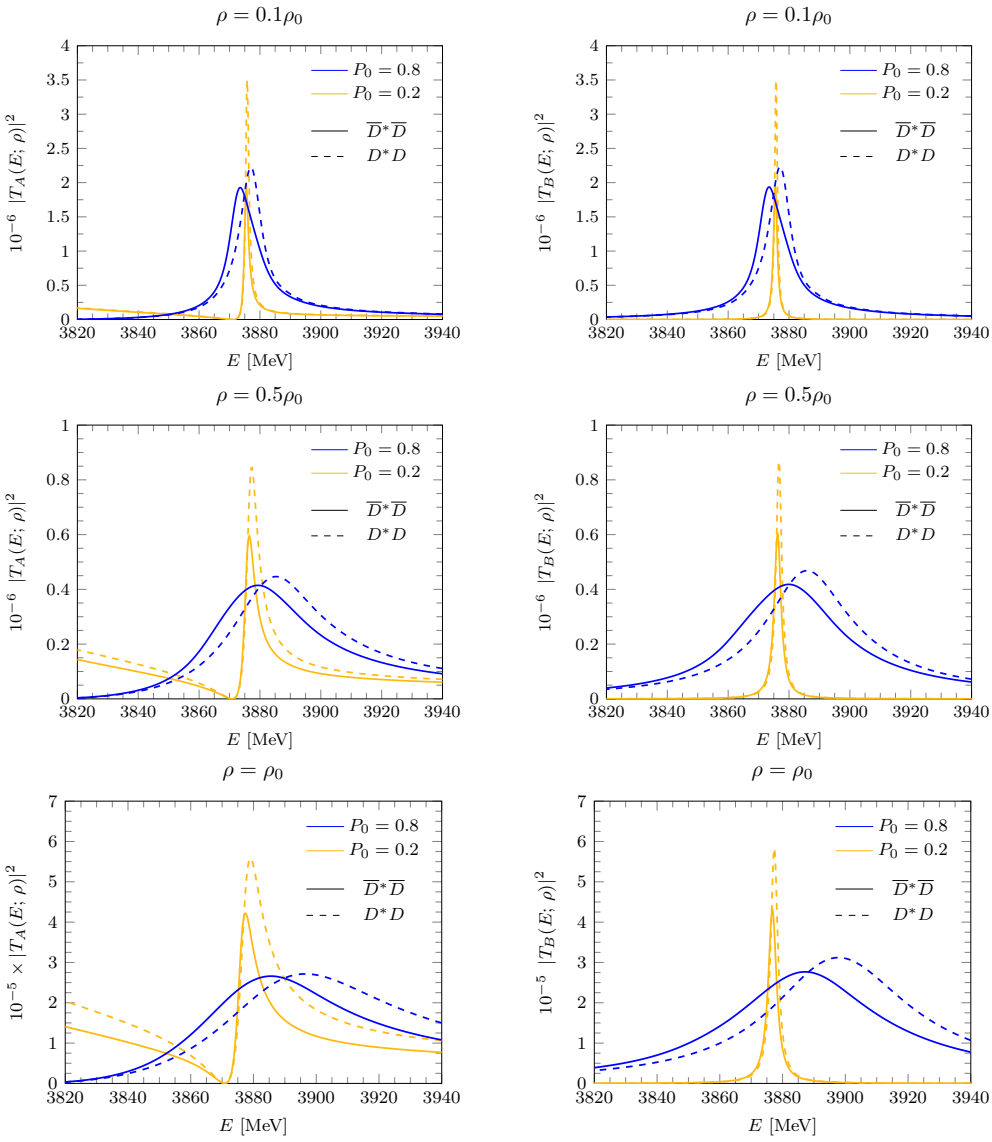

Figure 2.14: In medium $\overline{D}^*\overline{D}$ (solid lines) and D^*D (dashed lines) modulus square amplitudes obtained by solving the BSE using the $V_A(s)$ (left) and $V_B(s)$ (right) potentials, for vacuum molecular probabilities $P_0 = 0.2$ (orange) and $P_0 = 0.8$ (blue), and for different nuclear densities ρ.

Because the real part of the $\overline{D}^*\overline{D}$ loop function for all densities is more negative than its D^*D counterpart, it follows that $\mathrm{Re}\left[\Sigma(s\,;\,\rho) - \overline{\Sigma}(s\,;\,\rho)\right] > 0$. Consequently, taking into account the previous remark together with Eq.(2.143), one

concludes that the medium induces a generally more repulsive interaction for the T_{cc}^{+} than for the $T_{\bar{c}\bar{c}}^{-}$. Therefore, we should anticipate that the T_{cc}^{+} will be generated at higher energies than the $T_{\bar{c}\bar{c}}^{-}$. Turning to the imaginary part for the $T_{\bar{c}\bar{c}}^{-}$ case, it is of the same order as the shift in the real part across all densities, and thus cannot be ignored—just as was observed for the T_{cc}^{+} in Sect. 2.5.2. Moreover, the density-dependent imaginary part of the $\overline{D}^{*}\overline{D}$ loop varies with energy more abruptly than its $D^{*}D$ counterpart. As a result, for energies below the two-meson threshold, one finds $|\mathrm{Im}, \overline{\Sigma}| < |\mathrm{Im}, \Sigma|$, whereas well above threshold, the inequality reverses, $|\mathrm{Im}, \overline{\Sigma}| > |\mathrm{Im}, \Sigma|$. Near—but still below—the vacuum threshold, the imaginary parts of the two loop functions approach one another. Even so, deciding whether the $T_{\bar{c}\bar{c}}^{-}$ or the T_{cc}^{+} ends up with a larger width remains impossible, because the width depends on the energy at which each state is produced for a given density, and those production energies are expected to differ. Should both states be created close to the two–meson threshold, their widths may well turn out to be similar, since in that region the imaginary parts of the respective loop functions are nearly identical.

Figure 2.14 displays several panels with the modulus squared of the in-medium T-matrices for $\overline{D}^{*}\overline{D}$ (solid curves) and $D^{*}D$ (dashed curves). In every case, the BSE equation is solved with the corresponding density-dependent two-meson loop, using either the type A kernel (left column) or the type B kernel (right column). Three densities are examined—$0.1\rho_0$ (top), $0.5\rho_0$ (middle), and ρ_0 (bottom)—and for each density two molecular probabilities are considered, $P_0 = 0.2$ (orange) and $P_0 = 0.8$ (blue). The width of the $T_{\bar{c}\bar{c}}^{-}$ peak increases as the density increases, an effect that becomes more pronounced at larger P_0, mirroring the behavior already observed for T_{cc}^{+} in Sect. 2.5.2. The relative position and width of the $T_{\bar{c}\bar{c}}^{-}$ and T_{cc}^{+} peaks depend jointly on P_0 and the density. Specifically, for sufficiently high molecular probability and density, the $T_{\bar{c}\bar{c}}^{-}$ maximum always appears at a lower energy than the T_{cc}^{+} maximum. At small P_0 and low density, this separation is hardly visible, as anticipated. Regarding the widths, the $T_{\bar{c}\bar{c}}^{-}$ state tends to be narrower than the T_{cc}^{+} once both P_0 and the density are large, although this difference is less striking than the shift in the peak positions and is difficult to discern directly in Fig. 2.14. Overall, the two states respond quite differently inside nuclear matter, and their properties prove highly sensitive to the molecular probability assigned in free space.

2.5.4 Nuclear medium results for the HQSS partner of the $T_{cc}(3875)$: the $T_{cc}^{*}(4016)$

As discussed in Sect. 1.1, HQSS arises in the limit $m_Q \gg \Lambda_{\mathrm{QCD}}$, where spin–dependent interactions of the heavy quark are suppressed. As a consequence,

hadrons containing a heavy quark appear in nearly degenerate spin doublets, such as the pseudoscalar D and vector D^* mesons, split by about 140 MeV, or the B and B^* mesons, with a smaller gap of roughly 45 MeV.

Theoretically, the T_{cc}^+—understood as a $I(J^P) = 0(1^+)$ D^*D state—also has an HQSS partner in the $I(J^P) = 0(1^+)$ D^*D^* channel. We will refer to this state as $T_{cc}^*(4016)$. This state has been studied in several theoretical works [52, 53, 247], although no experimental confirmation is currently available. Similarly to the case of the lowest-lying charmed mesons, where the mass splitting is $m_{D^*} - m_D \sim m_\pi$, one also expects in this case that the mass difference between the T_{cc} and the T_{cc}^* will be of about the mass of the pion. That is, the binding energy of the T_{cc}^* with respect to the D^*D^* threshold will be similar to the binding energy of the T_{cc} with respect to the D^*D threshold. In fact, due to the modification of the reduced mass of the system, the binding energy of the T_{cc}^* with respect to the D^*D^* threshold is theoretically found to be slightly larger than that of the T_{cc} with respect to the D^*D threshold—around 1.5 MeV depending on the regularization scale [162], which is to be compared with the binding of 0.8 MeV of the T_{cc}. In our calculation, we shall fix again the potential parameters in order to produce a T_{cc}^* pole in the free-space D^*D^* scattering amplitude at some given energy m_0^*. We will study the dependence of the results by varying the chosen value for m_0^* to be within the binding energy range $E_B^* \in [0.8, 1.6]$ MeV ($E_B^* = 2m_{D^*} - m_0^*$).

The density effects are incorporated through the corresponding loop function:

$$\Sigma^*(E\,;\,\rho) = \frac{1}{2\pi^2}\int_0^\infty d\Omega \left(\frac{f_{D^*D^*}(\Omega\,;\,\rho)}{E - \Omega + i\varepsilon} - \frac{f_{\overline{D}^*\overline{D}^*}(\Omega\,;\,\rho)}{E + \Omega - i\varepsilon} \right), \tag{2.144}$$

which only involves in this case the heavy-light vector mesons. In Fig. 2.15 we compare the results obtained for the D^*D^* loop with the DD^* loop previously shown in Fig. 2.9. We consider several densities and plot the real part (left-hand plot) and the imaginary part (right-hand plot) of both functions with respect to the on-shell center-of-mass momentum $k = \sqrt{2\mu(E - E_{\rm th})}$ for the corresponding channel, with μ the reduced mass and $E_{\rm th}$ the production threshold of either the D^*D or the D^*D^* channel.

We observe in this case that the two loop functions do not coincide in vacuum. This is because they correspond to different channels, where particles with different masses are involved. As an example, we study the imaginary parts of both vacuum loop functions, given by

$$\text{Im}\ \Sigma_0(s) = -\frac{k(s)}{8\pi\sqrt{s}}, \tag{2.145}$$

with k the on-shell center of mass momentum of the considered system. For small k, we can approximate this function by a straight line, resulting in the

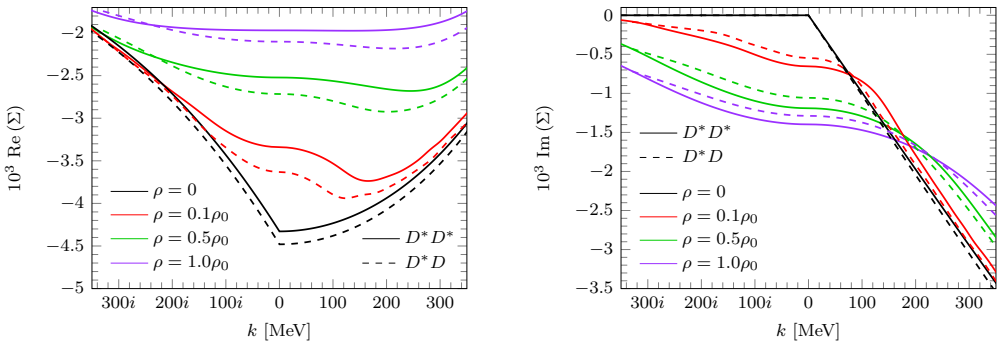

Figure 2.15: Real (left-hand side) and imaginary (right-hand side) parts of the D^*D^* (solid lines) and D^*D (dashed lines) scattering loop functions (Σ^* and Σ, respectively) for different values of the nuclear medium density ρ. Since the thresholds for the D^*D and D^*D^* channels are different, we plot the two loops as functions of the magnitude of the center-of-mass three-momentum k.

following results for the D^*D and D^*D^* loops, respectively:

$$\begin{aligned} \text{Im}\,\Sigma_0(s) &\simeq -\frac{k(s)}{8\pi(m_D + m_{D^*})}, \\ \text{Im}\,\Sigma_0^*(s) &\simeq -\frac{k(s)}{8\pi(m_{D^*} + m_{D^*})}, \end{aligned} \qquad k \ll m_D. \tag{2.146}$$

These lines have slightly different slopes, characterized by the sum of the masses of the particles in each channel. This slope difference is clearly visible in the right-hand plot of Fig. 2.15. One can analyze the real part in the same way, and the difference between both functions can be shown to depend on the masses of the particles involved in each channel, as well as the chosen value for the cutoff. With increasing density, the differences between the D^*D and the D^*D^* loops become increasingly more notable, arising from the different DN and D^*N interactions.

Next, we show some results for the in-medium D^*D^* scattering amplitude, using the V_A and V_B potentials, where the LECs are chosen to produce a pole in the first Riemann sheet below the threshold, with a binding energy between 0.8 and 1.6 MeV, and with a molecular probability P_0. The binding energy interval considered produces a band of different solutions, which can be taken as a measure of the systematic uncertainty arising from the HQSS part of our model.[29] These results are presented in Fig. 2.16.

[29]There are other sources of systematic uncertainties in the calculation, as the truncation of the effective theory, or the determination of the cutoff-dependent real part of the finite density loop function.

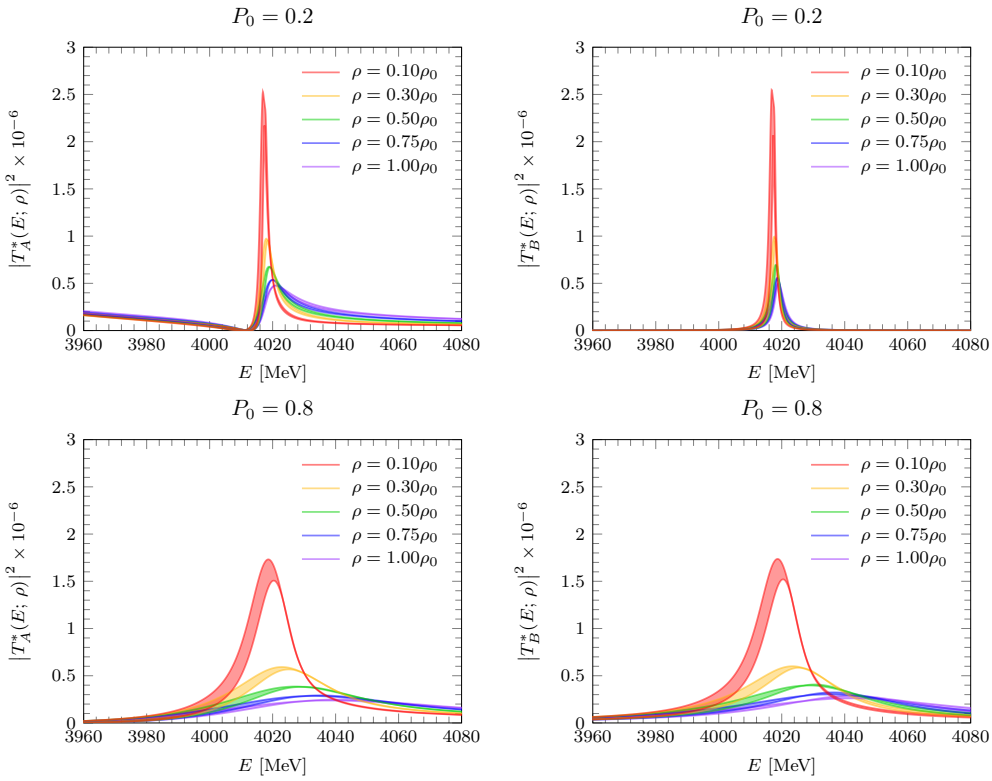

Figure 2.16: Squared modulus of the D^*D^* amplitudes obtained by solving the BSE using the $V_A(s)$ potential (left column) and the $V_B(s)$ potential (right column), as a function of the center-of-mass energy E, for several values of the nuclear density ρ (different line colors) and for two values of the molecular probability P_0 ($P_0 = 0.2$ in the top row and 0.8 in the bottom row). The bands cover the solutions corresponding to taking the T^{*+}_{cc} binding energy to be in the interval [0.8, 1.6].

The amplitudes in this figure show a similar behavior to that found for the D^*D case. Again, density effects are more notable for a high value of the molecular probability. The specific shape of the scattering amplitude is strongly dependent on the potential family for a small value of P_0, while for P_0 close to 1 these differences become very minor. The interval considered for the binding energy of T^{*+}_{cc} produces a band of uncertainty which is negligible compared to density effects. Therefore, one can qualitatively describe the behavior of the T^{*+}_{cc} taking its binding to be any of the values considered. In what follows, we will choose a value for the binding energy of 0.8 MeV.

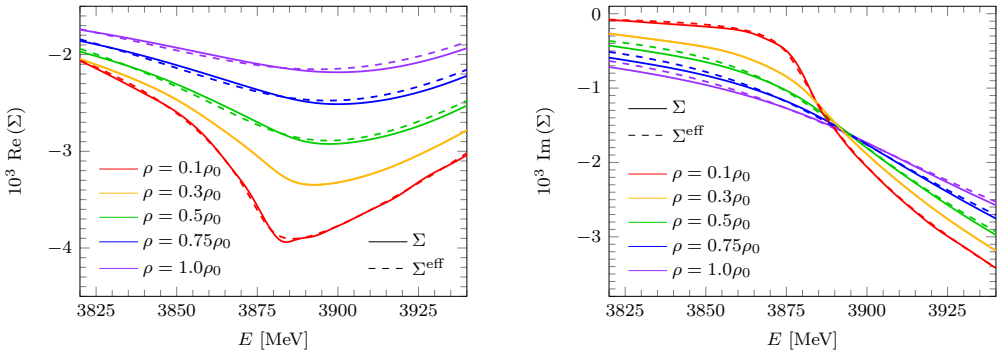

Figure 2.17: Real (left) and imaginary (right) parts of the exact density-dependent loop function (solid lines) and the fitted effective loop function (dashed lines) for the D^*D meson pair.

2.5.5 Poles in the complex plane

In this section, we adopt the approximation of Eq.(2.129) for the different in-medium loop functions considered—that is, the D^*D, $\overline{D}^*\overline{D}$, D^*D^* and $\overline{D}^*\overline{D}^*$ loop functions. As was discussed in Sect. 2.4.7, we take the analytic formula for the loop function in vacuum and fit the (complex) values for the masses of the mesons in order to reproduce the exact finite-density loop function. In Fig. 2.17 we show a comparison between the effective loop function obtained (dashed lines) and the original one for the case of D^*D scattering. We can see that there is a very good agreement between the original finite-density loop function and the effective one. A similar good agreement is also obtained for the rest of the channels, and the results of the various fits are shown in Table 2.2.

Once the effective analytic loop functions have been determined, we can evaluate the amplitudes on the whole s complex plane, exploring several densities ρ and vacuum probabilities P_0. A systematic search reveals a pole on the first Riemann sheet (as defined in Ref. [162]), situated away from the real axis. This does not violate the analyticity of the full scattering T–matrix of the process. The fact that we find poles away from the real axis on the first Riemann sheet is produced by our effective treatment of the many-body channels $D^*DN \to D^*DN'$ and $\overline{D}^*\overline{D}N \to \overline{D}^*\overline{D}N'$, included in the effective loop. The resulting complex poles are shown in Fig. 2.18. There we plot, for several densities (varying line colors) the pole trajectories (dashed lines) obtained from varying P_0 from 0 (common upper end of every trajectory, on the real axis) to 1 (lower end of every trajectory, with $\text{Im}(E) < 0$). In zigzag lines we also present the location of the unitarity cut of the effective loop functions,

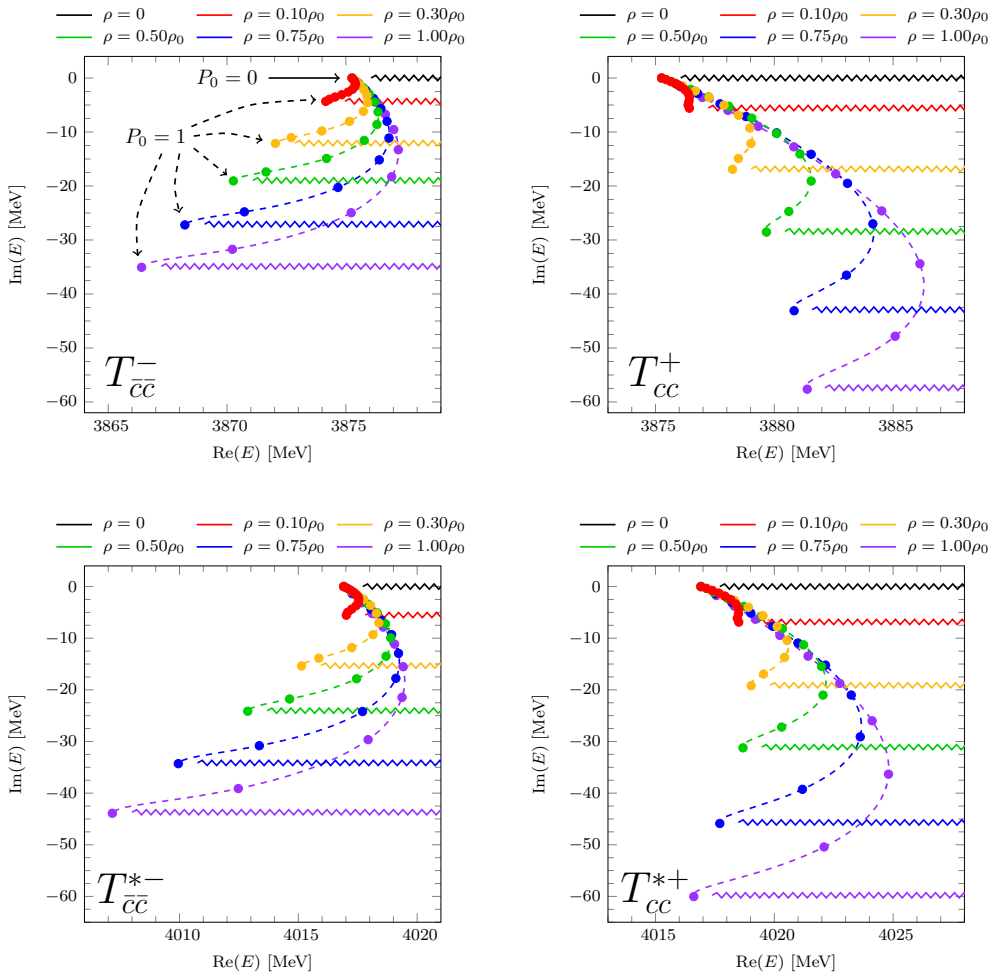

Figure 2.18: Top: Complex pole positions of the $T_{\bar{c}\bar{c}}(3875)^-$ (left) and the $T_{cc}(3875)^+$ (right) for different values of the density (ρ) and vacuum molecular probabilities (P_0) obtained using the potential $V_A(s)$. Different line colors represent different densities, while the continuous dashed lines correspond to results obtained by running P_0 from 0 (upper end) to 1 (lower end). The points in these lines correspond to steps in the molecular probability of $\Delta P_0 = 0.1$. The zigzag lines represent the unitarity cut of the effective loop function $\Sigma_0\left(s; M_1^{\rm eff}(\rho), M_2^{\rm eff}(\rho)\right)$ for different densities, as detailed in Sect. IIIB of Ref. [162]. Bottom: Same as the top plots, but for the $T^*_{\bar{c}\bar{c}}(4016)^-$ (left) and the $T^*_{cc}(4016)^+$, heavy quark spin partners of the $T_{\bar{c}\bar{c}}(3875)^-$ and the $T_{cc}(3875)^+$.

D^*D			$\overline{D}^*\overline{D}$		
ρ/ρ_0	ΔM [MeV]	$\Gamma/2$ [MeV]	ρ/ρ_0	ΔM [MeV]	$\Gamma/2$ [MeV]
0.10	0.58	2.8	0.10	−0.55	2.2
0.30	1.48	8.4	0.30	−1.61	6.0
0.50	2.19	14.2	0.50	−2.48	9.5
0.75	2.77	21.5	0.75	−3.50	13.5
1.00	3.03	28.7	1.00	−4.41	17.4

D^*D^*			$\overline{D}^*\overline{D}^*$		
ρ/ρ_0	ΔM [MeV]	$\Gamma/2$ [MeV]	ρ/ρ_0	ΔM [MeV]	$\Gamma/2$ [MeV]
0.10	0.79	3.4	0.10	0.05	2.8
0.30	1.05	9.6	0.30	−0.88	7.7
0.50	0.88	15.5	0.50	−2.01	12.0
0.75	0.39	22.8	0.75	−3.48	17.1
1.00	−0.16	29.9	1.00	−4.85	21.9

Table 2.2: Table of the parameters ΔM and $\Gamma/2$ (given in MeV) describing the meson masses modification of the effective loop function for D^*D scattering (upper left-hand side), $\overline{D}^*\overline{D}$ scattering (upper right-hand side), D^*D^* scattering (lower left-hand side) and for $\overline{D}^*\overline{D}^*$ scattering (lower right-hand side). For the fits, 51 points of the original loop were sampled in a symmetric interval of 120 MeV around the respective thresholds of the D^*D and D^*D^* channels.

which gets displaced away from the real axis for complex values of the meson masses.

The results presented in Fig. 2.18 reinforce the conclusions drawn previously. For zero molecular probability, we see that the pole is not affected by the density of the medium, staying at the corresponding vacuum mass m_0. With increasing density and molecular probabilities, all poles are driven toward the complex plane, developing a significant width. For $P_0 = 1$, the poles fall to the left of the unitarity cut of the effective loop with the corresponding density. This is due to the fact that, since the potential is real, the effective loop function must also be real for the T–matrix to present a pole. This occurs below the threshold, which is now located in the complex plane. In the $P_0 = 1$ case, the

width of the corresponding state is given by the sum of the effective widths of the mesons, given by the parameter Γ in Table 2.2. Comparison of the upper panels of Fig. 2.18 shows that the nucleonic medium drives the T_{cc}^{+} and $T_{\bar{c}\bar{c}}^{-}$ poles along clearly distinct trajectories in the (ρ, P_0) plane. Typically, the T_{cc}^{+} becomes broader than the $T_{\bar{c}\bar{c}}^{-}$, while its effective mass shifts to higher energies, whereas the $T_{\bar{c}\bar{c}}^{-}$ moves to lower energies relative to their free-space position. A similar situation is found when comparing the HQSS partners of the bottom panels, with the $T_{\bar{c}\bar{c}}^{*-}$ moving to lower energies and getting a smaller width than the T_{cc}^{*+}. Furthermore, the HQSS partners seem to be slightly more affected by the nuclear medium than the $T_{c\bar{c}}^{\pm}$ states. The experimental measurement of these density patterns would provide valuable information on the complex dynamics of the T_{cc}^{+} tetraquark state discovered by LHCb.

2.6 Finite density results for the $D_{s0}^{*}(2317)$

We dedicate this section to the study of the $D_{s0}^{*}(2317)^{+}$, as well as its charge conjugation and HQSS partners, in nuclear matter. For this, we must first discuss the main specific features of the $S-$wave $D^{(*)}K$ and $\overline{D}^{(*)}\overline{K}$ scattering formalism. Because the present study addresses Goldstone boson–charmed meson scattering—not charmed meson–charmed meson interactions—we must relate our interaction kernel to the amplitudes derived in *Heavy-Meson Chiral Perturbation Theory*.[30] First, we will discuss the modifications of the general formalism that was presented in Sect. 2.4. Then, we will show the results obtained, comparing them with what has already been shown for the T_{cc} and partners in Sect. 2.5.

2.6.1 Review of the formalism applied to the D_{s0}^{*} case

Vacuum amplitude and matching of the effective potentials to HM-ChPT

The $D_{s0}^{*}(2317)^{+}$ ($D_{s0}^{*}(2317)^{-}$) is modeled in vacuum as a bound state in the $I(J^P) = 0(0^+)$ DK ($\overline{D}\overline{K}$) amplitude. We work again in the isospin limit, taking $m_D = (m_{D^+} + m_{D^0})/2$ and $m_K = (m_{K^+} + m_{K^0})/2$.[31] In this case, similar to what was shown for the case of the T_{cc} in Sect. 2.5.1, both isospin channels decouple, and we are left with a single-channel BSE for the isoscalar T–matrix.

[30] HMChPT is the restriction to the single heavy-meson sector of HHChPT, first discussed in the Introduction, Chap. 1.

[31] We omit explicit $D_s\eta$ coupled-channel effects, since its threshold sits about 150 MeV above the DK one; any modest influence it may have near the $D_{s0}^{*}(2317)$ can be safely absorbed through a retuning of the low-energy constants (cf. Refs. [236, 248–250]).

For the DK ($\overline{D}\overline{K}$) loop function we take the cutoff regulator Λ to be 700 MeV—the same one that we used in our study of $D^*D^{(*)}$ scattering amplitudes. For the interaction kernel, we consider again the two families of potentials first presented in Eqs. (2.83a) and (2.83b). The parameters of both potential families are fixed by choosing a value for the molecular probability $P_0 \in [0,1]$, and taking the mass of D_{s0}^* in vacuum to be $m_0 = 2317.8$ MeV, as listed on the PDG [18]. Using the physical mass for the D_{s0}^* while taking the unphysical isospin symmetric masses for the D and K mesons is not consistent. However, given that the binding energy of the D_{s0}^* is about 45 MeV—much larger in this case than for the T_{cc}—we expect that using the physical mass of the D_{s0}^* instead of the unphysical mass in the isospin limit will not significantly affect the final results and conclusions.

Although we are parameterizing the interaction kernel in the same manner as we did when studying the D^*D scattering, the interaction among charmed mesons and light goldstone bosons originates from a different effective theory, namely HMChPT. The LO S-wave, isoscalar DK interaction obtained in HMChPT is [191]

$$V_{\chi\mathrm{LO}}(s) = \frac{-3s + 2m_K^2 + 2m_D^2 + (m_D^2 - m_K^2)^2/s}{4f^2}, \tag{2.147}$$

with $f \simeq 93\,\mathrm{MeV}$. Reference [194] employed this LO kernel—unitarized through the on-shell BSE equation—to connect the $D_{s0}^*(2317)$ to the enhancements observed just above threshold in the D^0K^+ and $\overline{D}^0K^-$ invariant-mass spectra measured by BaBar in the decays $B^+ \to \overline{D}^0 D^0 K^+$ and $B^0 \to D^- D^0 K^+$ [251], as well as by LHCb in $B_s \to \pi^+ \overline{D}^0 K^-$ [204]. This analysis revealed a pole at $2315 \pm 17\,\mathrm{MeV}$ with a molecular probability of $70^{+6}_{-10}\%$. Whereas Ref. [194] fixed the ultraviolet behavior through a subtraction constant fitted to those spectra, in the present work we adopt a sharp momentum cutoff, which is more convenient for implementing nuclear-medium effects.[32] Both renormalization prescriptions are equivalent, and we reproduce the results of [194] in the kinematic region of interest with a cutoff $\Lambda = 875 \pm 85\,\mathrm{MeV}$ (cf. Eq. (52) of Ref. [255]).

The connection of the HMChPT potential with the V_A- or V_B-type potentials can be made by taking a power expansion of $V_{\chi LO}$ (type A) or $V_{\chi LO}^{-1}$ (type B) in the vicinity of the position of the $D_{s0}^*(2317)$ pole. However, we will still fix the LECs of the V_A and V_B potentials from the values of m_0 and P_0, rather than matching them directly to the $V_{\chi LO}$ potential. In Fig. 2.19,

[32] This choice is consistent with the calculations of the $D^{(*)}$, $\overline{D}^{(*)}$ and $\overline{K}$ spectral functions in a medium of Refs. [214–216, 219] and, in combination with the on-shell BSE, has already provided an excellent description of kaonic-atom data via the resulting antikaon–nucleus optical potential [214, 252–254]. We do not expect off-shell contributions to significantly affect the main conclusions of this work.

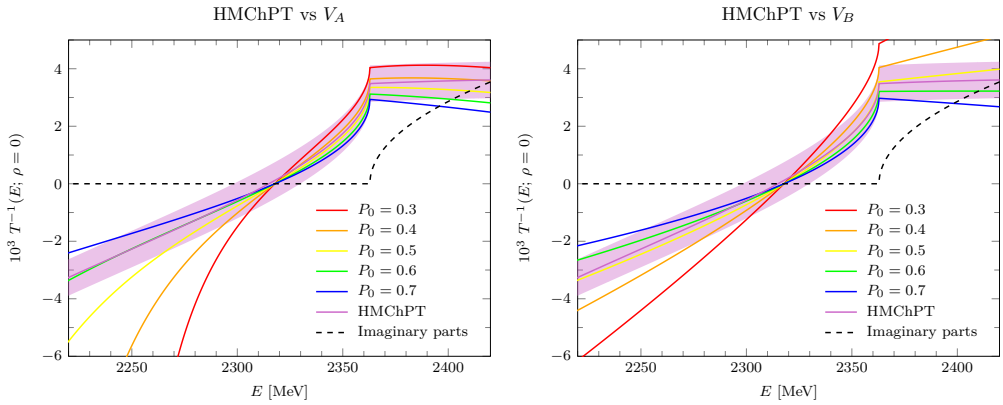

Figure 2.19: Real parts of the free-space $S-$wave isoscalar DK inverse amplitudes obtained using the LO HMChPT scheme followed in Ref. [194] (magenta band) and the V_A (left panel) and V_B (right panel) families of potentials (Eqs. (2.83a) and (2.83b) respectively), adjusted for different $D^*_{s0}(2317)$ molecular probabilities (P_0), as functions of the center of mass energy (E) of the DK pair. The band of the HMChPT result accounts for the uncertainty on the subtraction constant fitted in Ref. [194] to the combined BaBar and LHCb mass distributions. The imaginary part (black dashed line) of the inverse amplitude for real E ($= \sqrt{s}$) is the same independently of the potential and of the used regularization method, as it is derived from unitarity, i.e. $\mathrm{Im}[T^{-1}(s)] = -\mathrm{Im}[\Sigma_0(s)] = \theta\left(s-(m_D+m_K)^2\right)\lambda^{1/2}(s,m_D^2,m_K^2)/(16\pi s)$, with θ and λ the step and Källen functions, respectively.

we present a comparison of the vacuum inverse $T-$matrices derived from the A and B potentials—both determined by $m_0 = 2317.8$ MeV and for several values of P_0—and from the $V_{\chi LO}$ potential. For the regularization of the loop function when computing the T–matrix using $V_{\chi LO}$ as the kernel, we use the dimensional regularization scheme of Ref. [194], in particular, employing the same subtraction constant fitted in that reference instead of the sharp cutoff used elsewhere in this manuscript. We see that the LO HMChPT result in the region of interest around the $D^*_{s0}(2317)$ mass ($2280\,\mathrm{MeV} < E < 2390\,\mathrm{MeV}$) is reasonably well reproduced using both the V_A and V_B families of potentials and molecular probabilities between 0.5 and 0.7.

DK and $\overline{D}\overline{K}$ scattering in isospin-symmetric nuclear matter

Now we focus on the modifications of the T amplitude introduced by the DK and $\overline{D}\overline{K}$ loop functions, $\Sigma(s;\rho)$ and $\overline{\Sigma}(s;\rho)$, respectively, computed in a nuclear environment. As we have mentioned before, the dense nuclear medium breaks

charge-conjugation symmetry, and as a consequence, the scattering amplitudes of DK and $\overline{D}\overline{K}$ will no longer be the same. Furthermore, we expect large asymmetries in this case (as compared with the T_{cc}) since, as we saw in Sect. 2.3, the spectral functions for the kaon—which is approximately a Dirac delta—and the antikaon—showing a large broadening due to the excitation of states such as the $\Lambda(1405)$—are radically different.

We make use again of Eq. (2.89) in order to compute the two-meson loop function in the nuclear medium. However, there is now a simplification as compared with the case of two charmed mesons. This simplification lies in the fact that the kaon spectral function is extremely narrow and can be approximated by a Dirac delta function (recall Eq. (2.54) of Sect. 2.3). In terms of the Dirac delta approximation for the kaon spectral function, we can simplify the expression for the auxiliary function f_{DK} which enters into the computation of the in-medium loop function. This yields

$$f_{DK}(\Omega;\rho) = \int_0^\Lambda dq\, q^2 \frac{S_D(\Omega - E_{\rm qp}^{(K)}, |\vec{q}\,|;\rho)}{2E_{\rm qp}^{(K)}} \,, \tag{2.148}$$

which reduces in one the number of integrals needed, as compared with the expression of Eq. (2.90).

Finally, we can define an effective density-dependent potential, including the effects of the in-medium loop functions, in the same way presented when analyzing the T_{cc}, cf. Eqs. (2.140).

$$T^{-1}(s;\rho) = V_{\rm eff}^{-1}(s;\rho) - \Sigma_0(s)\,, \tag{2.149a}$$
$$V_{\rm eff}^{-1}(s;\rho) = V^{-1}(s) + \delta\Sigma(s;\rho)\,, \tag{2.149b}$$
$$\delta\Sigma(s;\rho) = \Sigma_0(s) - \Sigma(s;\rho)\,, \tag{2.149c}$$

The density behavior of the effective potential will allow us to discuss how the nuclear environment effectively changes the interaction between the two mesons. In the $\overline{D}\overline{K}$ case, we analogously define the effective potential resulting now from the charge-conjugated loop function $\overline{\Sigma}$. Since at zero density both loops are equal, both effective potentials are related as

$$\overline{V}_{\rm eff}^{-1}(s;\rho) - V_{\rm eff}^{-1}(s;\rho) = \Sigma(s;\rho) - \overline{\Sigma}(s;\rho)\,. \tag{2.150}$$

The HQSS partner of the $D_{s0}^*(2317)$: the $D_{s1}(2460)$

Just as the vector D^* lies roughly one pion mass above the pseudoscalar D, the isoscalar axial meson $D_{s1}(2460)$ ($J^P = 1^+$) sits about m_π higher in energy than its scalar partner $D_{s0}^*(2317)$ ($J^P = 0^+$). This near-degeneracy is commonly interpreted as evidence that the two states form a HQSS doublet, whose light degrees of freedom carry isospin $I = 0$ and spin–parity $s_\ell^P = 1/2^+$ [197].

Within our approach, the $D_{s1}(2460)^+$ is dynamically generated from the isoscalar S-wave D^*K interaction. HQSS then implies that the $I(J^P) = 0(0^+)$ DK and $I(J^P) = 0(1^+)$ D^*K amplitudes are identical once the pseudoscalar D mass is replaced by the vector D^* mass and the difference between the DK and D^*K thresholds has been taken into account. Only small HQSS breaking corrections enter the coefficients of the potentials V_A and V_B, reflecting the difference between the splittings $m_{D_{s1}(2460)} - m_{D^*_{s0}(2317)}$ and $m_{D^*} - m_D$. Density effects are incorporated by evaluating the in-medium D^*K and $\overline{D}^*\overline{K}$ loop functions in the same way as described in Sect. 2.4.3.

2.6.2 Nuclear medium results for the D^*_{s0} and partners

In this section, we examine how nuclear matter modifies the $D^{(*)}K$ and $\overline{D}^{(*)}\,\overline{K}$ loop functions and the corresponding squared moduli of the scattering amplitudes in the $I(J^P) = 0(0^+)$ and $0(1^+)$ channels, where the $D^*_{s0}(2317)$ and $D_{s1}(2460)$ poles are located. Since many of the findings are qualitatively similar to what was found in Sect. 2.5 for the T_{cc} in nuclear matter, we shall now focus on the main observations and conclusions for the case at hand, not entering into as many details as we did in Sect. 2.5.

Figure 2.20 shows the line shapes of the $\overline{D}\,\overline{K}$ (solid curves) and DK (dashed curves) loop functions for densities from $\rho = 0$ up to normal nuclear matter density, $\rho_0 = 0.17$ fm^{-3}. Charge–conjugation symmetry forces both loop functions to coincide at $\rho = 0$; yet, as the density grows, the real [left panel of Fig. 2.20] and imaginary [right panel of Fig. 2.20(b)] parts of $\Sigma(s;\rho)$ and $\overline{\Sigma}(s;\rho)$ drift apart markedly. The resulting charge–conjugation asymmetry—that is, the difference between the DK and $\overline{D}\overline{K}$ curves—is considerably larger than the D^*D versus $\overline{D}^*\,\overline{D}$ pattern reported in Sect. 2.5.2 for the $T_{cc}(3875)^+$ and $T_{\bar{c}\bar{c}}(3875)^-$ tetraquarks.

Inspecting the loop functions in the vicinity of the vacuum D^*_{s0} pole ($E \simeq$ 2320 MeV) reveals two key features. First, the imaginary part of the $\overline{D}\,\overline{K}$ loop exceeds that of the DK loop, so we expect that the in-medium D^{*-}_{s0} develops a larger width than the D^{*+}_{s0}. This broadening originates from the sizeable width acquired by the antikaon quasi-particle peak in matter (cf. Fig. 2.6), whereas the kaon peak retains its sharp structure.

Second, in the same energy window, the real part of the $\overline{D}\,\overline{K}$ loop is significantly more negative than its DK counterpart. Via Eq. (2.150) one finds

$$\mathrm{Re}\big(\overline{V}^{-1}_{\mathrm{eff}}\big) - \mathrm{Re}\big(V^{-1}_{\mathrm{eff}}\big) \;>\; 0, \tag{2.151}$$

which, if the imaginary parts of the effective potentials are momentarily neglected, implies that V_{eff} is more repulsive than $\overline{V}_{\mathrm{eff}}$. As a consequence, the D^{*+}_{s0} pole is driven to higher energies relative to the D^{*-}_{s0} pole. We emphasize

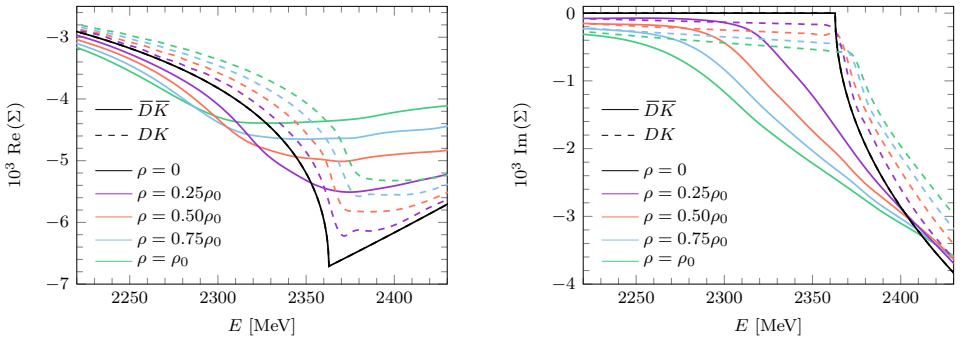

Figure 2.20: Real (left) and imaginary (right) parts of the $\overline{D}\overline{K}$ (solid lines) and DK (dashed lines) loop functions. We show results for different values of the nuclear medium density (in units of $\rho_0 = 0.17$ fm^{-3}) as a function of the center of mass energy of the heavy light-Goldstone meson pair. Figure taken from Ref. [2].

that omitting the imaginary part is an approximation, especially for the $\overline{D}\,\overline{K}$ channel, where it is not negligible.

The in-medium behavior of the D^*K and $\overline{D}^*\,\overline{K}$ loop functions follows almost the same density pattern as the DK and $\overline{D}\,\overline{K}$ cases, so we omit the corresponding plots. The qualitative conclusions are unchanged. The main differences are (i) the vacuum threshold now lies at $E = m_{D^*} + m_K$ and (ii) the imaginary part in matter is somewhat larger, owing to the slightly stronger D^*N and $\overline{D}^*N$ interactions. Even so, the kaon and antikaon spectral functions continue to dominate the overall shape of the loop functions.

We now focus on the in-medium amplitudes for the $D^{(*)}K$ and $\overline{D}^{(*)}\overline{K}$ channels. Figure 2.21 displays $|T|^2$ obtained with the V_A interaction and two molecular probabilities, $P_0 = 0.2$ and $P_0 = 0.8$. These choices represent two opposite scenarios, the larger value reproducing approximately the HMChPT result of Ref. [194] (see discussion on the previous subsection 2.6.1). We consider the densities $\rho = 0.5\,\rho_0$ (top panels) and $\rho = \rho_0$ (bottom panels). Calculations with the V_B interaction lead to almost indistinguishable curves for both molecular contents, differing only slightly in the resonance tails.[33]

The left-hand panels of Fig. 2.21 show the isoscalar–scalar $I(J^P) = 0(0^+)$ amplitudes for the DK and $\overline{D}\,\overline{K}$ channels—corresponding to the D_{s0}^{*+} and D_{s0}^{*-} states—plotted with dashed and solid curves, respectively. We see that these states, which were bound in vacuum, acquire a finite width once embedded in

[33]The similarity between the V_A and V_B results is greater here than in the $\chi_{c1}(3872)$ (Ref. [162]) or $T_{cc}(3875)^+$ (Sect. 2.5 and also Ref. [1]) analyses because the $D_{s0}^*(2317)^\pm$ is much more deeply bound.

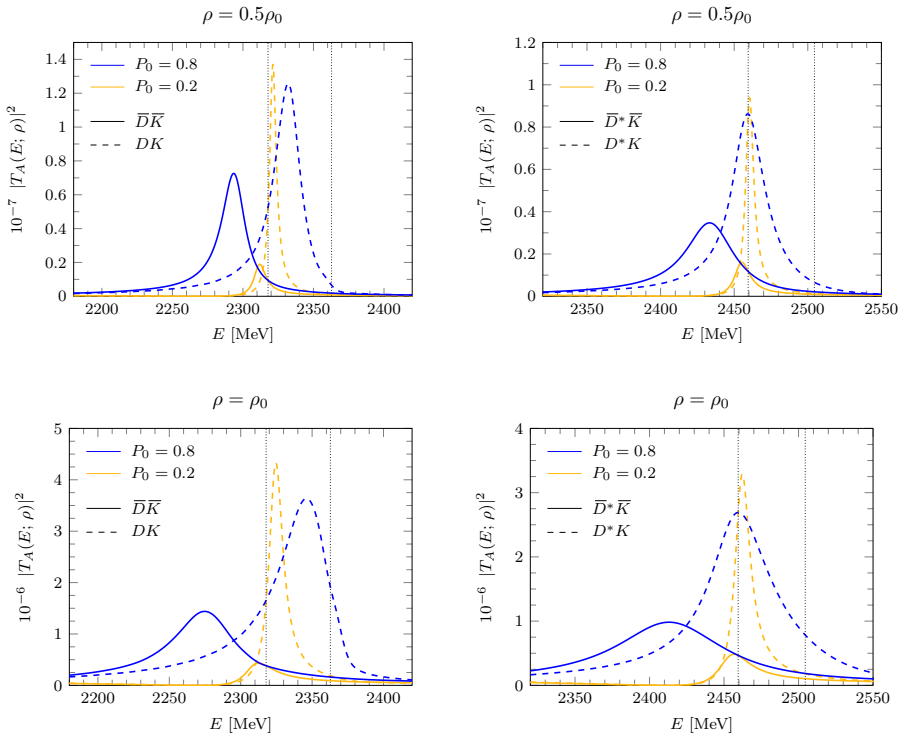

Figure 2.21: Left panels: In-medium $\overline{D}\overline{K}$ (solid lines) and DK (dashed lines) modulus squared amplitudes obtained by solving the BSE using the $V_A(s)$ potential, for vacuum molecular probabilities $P_0 = 0.2$ (orange) and $P_0 = 0.8$ (blue), and for nuclear densities $\rho = 0.5\rho_0$ (top) and $\rho = \rho_0$ (bottom). Right panels: Same as left panels but for $\overline{D}^*\overline{K}$ (solid lines) and D^*K (dashed lines) modulus square amplitudes. In all plots the dotted vertical lines correspond, from left to right, to the vacuum $D_{s0}^*(2317)^\pm$ or $D_{s1}(2460)^\pm$ mass and $D^{(*)}K$ ($\overline{D}^{(*)}\overline{K}$) threshold.

nuclear matter, the broadening being more pronounced in the high-molecular probability scenario. As density and P_0 increase, the D_{s0}^{*+} peak shifts markedly to higher energies, while the D_{s0}^{*-} peak moves to lower energies—much more so than for the T_{cc}^+ and $T_{\bar{c}\bar{c}}^-$. This trend, anticipated from the real part of the effective potential, persists in the shown amplitudes, where the imaginary parts of the loop functions are included. For every density and molecular content considered, the D_{s0}^{*-} develops a larger width than the D_{s0}^{*+}, a difference that stems primarily from the contrasting in-medium renormalization of kaon and antikaon propagators.

The right-hand panels of Fig. 2.21 display the isoscalar–axial $I(J^P) = 0(1^+)$

amplitudes for D^*K and $\overline{D}^*\,\overline{K}$, corresponding to the D_{s1}^+ and D_{s1}^- poles. Although their overall medium evolution resembles that of the scalar partners, two differences stand out. First, both axial states acquire noticeably larger widths, a consequence of the slightly stronger D^*N and $\overline{D}^*N$ interactions predicted by the model of Refs. [220, 256]. Second, the D_{s1}^+ peak does not move upward in energy as the D_{s0}^{*+} does. Taken together, these effects make the in-medium line shapes of D_{s1}^+ and D_{s1}^- less distinct than those of the D_{s0}^{*+}–D_{s0}^{*-} pair across all density and molecular-probability scenarios considered.

Similar conclusions can be drawn for the behavior of the $D_{s0}^*(2317)^\pm$ states (and their HQSS partners) in the nuclear medium from their self-energy, spectral functions, and pole positions in the s complex plane. All of these quantities signal a strong charge conjugation asymmetry in nuclear matter, which is strongly dependent on the molecular component of these states. Showing all these different plots here, as was done for the case of the T_{cc}, would not add any additional points to the discussion, so we end this results section here.

2.7 Conclusions

In this chapter, we have carried out a unified and comparatively detailed exploration of the in-medium behavior of two different families of heavy exotic candidates that are dynamically generated as poles in unitarized S-wave two-meson amplitudes. Firstly, we have analyzed in a general way how the individual mesons are modified when embedded in a dense nuclear medium, and explained the self-consistent procedure used for the computation of their self-energies and spectral functions. Then, we have discussed how the two-meson scattering matrix is modified in nuclear matter, considering all the density dependence in the dressed two-meson loop functions. We have shown how two families of energy-dependent interactions, both consistent with HQSS yet differing in their analytic structure, allow us to vary the molecular probability associated to these states. We have applied this formalism to the study of finite-nuclear density effects on the tetraquark-like $T_{cc}(3875)$ and $D_{s0}^*(2317)$ states, together with their HQSS partners. In general terms, the resulting trajectories of the poles in the complex energy plane reveal a pronounced sensitivity to both the density of the nuclear medium and the degree of molecular compositeness.

The first part of the study focuses on the $T_{cc}(3875)^+$ and its antiparticle $T_{\bar{c}\bar{c}}(3875)^-$, which we model as isoscalar D^*D and $\overline{D}^*\overline{D}$ molecules, respectively. The medium effects are incorporated by dressing the charmed mesons with the self-consistent spectral functions of Refs. [215, 216, 219]. When the molecular component dominates, the T_{cc}^+ experiences a strong broadening accompanied by an upward mass shift, whereas the $T_{\bar{c}\bar{c}}^-$ becomes only moderately wider and

is driven downward in energy. These opposite trends are due to the appreciable difference between the attractive $D^{(*)}N$ interaction and the comparatively weaker $\overline{D}^{(*)}N$ counterpart. Using HQSS, we have extended the calculation to the HQSS partners $T^*_{cc}(4016)^+$ and $T^*_{\bar{c}\bar{c}}(4016)^-$ generated in D^*D^* and $\overline{D}^*\overline{D}^*$ scattering. Owing to the stronger D^*N coupling, the medium modifications are amplified in this $J^P = 1^+$ sector, yet the qualitative particle–antiparticle asymmetry persists.

The second part of the chapter addresses the strange–charm systems $D^*_{s0}(2317)^\pm$ and $D_{s1}(2460)^\pm$. These states are produced dynamically from isoscalar $D^{(*)}K$ and $\overline{D}^{(*)}\overline{K}$ amplitudes whose free-space kernels reproduce their empirical masses with different Weinberg compositeness probabilities. The embedding in nuclear matter is performed by dressing not only the charmed mesons but also the kaons and antikaons with their respective self-energies, thereby capturing the marked disparity between the attractive $\overline{K}N$ interaction and the weakly repulsive KN channel. This disparity breaks charge-conjugation symmetry in a spectacular fashion: already at half nuclear saturation density the spectral distribution of the $D^*_{s0}(2317)^+$ is pushed to higher energies and becomes significantly narrower, while its antiparticle migrates to lower energies and develops a much broader Breit-Wigner-like profile, with the two lineshapes barely overlapping when the molecular probability is large. A similar pattern emerges for the HQSS partners $D_{s1}(2460)^\pm$, although the resonances are globally wider because the underlying D^*N and $\overline{D}^*N$ interactions are stronger than their pseudoscalar counterparts. In any case, kaon-antikaon dynamics within the nuclear medium remains the driving mechanism behind the pronounced particle–antiparticle asymmetry.

Taken together, these results demonstrate that the magnitude—and possibly the sign—of the density-induced mass and width shifts are closely related to two ingredients: the hadron-molecular content of the state and the difference in the strength of meson and anti-meson interactions with nucleons. Consequently, precision measurements of the in-medium spectral functions of the $T_{cc}(3875)$ and the $D^*_{s0}(2317)$ states, e.g. in relativistic heavy-ion collisions at the *Compressed Baryonic Matter* (CBM) experiment at FAIR or in fixed-target $\bar{p}$–nucleus experiments at PANDA, would provide a stringent experimentally driven test of their internal structure. Confirming the predicted mass shifts and widths would strongly support a dominant molecular configuration, whereas a milder or qualitatively different behavior would favor the compact tetraquark interpretation. In addition, such data would offer valuable constraints on the not well-known self-energies of kaons, antikaons and open-charm mesons in dense nuclear matter, thereby closing the feedback loop between exotic-hadron spectroscopy and the physics of the hadronic medium.

3

On the measurement of the D meson width in nuclear matter with the transparency ratio

3.1 Introduction and motivation

In Chapter 2 we have analyzed how two tetraquark–like candidates—the doubly charmed T_{cc} and the charmed–strange D_{s0}^*—are modified as they propagate through nuclear matter. Our main conclusion is that, if the predicted density patterns could be observed experimentally—in particular the charge–conjugation asymmetry induced by the medium—they would provide a novel probe of the internal structure of these exotic states. Both T_{cc} and D_{s0}^* are, *a priori*, compatible with both compact tetraquark and hadronic molecular interpretations, though their proximity to two–meson thresholds strongly favors the latter. Medium effects may offer additional discrimination: hadronic molecules, being loosely bound systems of two hadrons, are expected to be more fragile in nuclear matter than genuine tetraquark states, whose color–driven binding is comparatively stronger. While we have provided theoretical predictions for the in–medium modifications of these states, their experimental verification remains an important challenge.

To probe how nuclear density affects a given state, one must design an experiment in which the state propagates through nuclear matter. Such a medium exists naturally in two contexts: neutron stars and atomic nuclei. The former, however, is far beyond the reach of controlled laboratory experiments, leaving atomic nuclei as the practical environment in which these effects can be studied. For the case of light mesons, many methods have been put forward to study the meson–nucleus interaction, e.g. scattering of pions and kaons with

nuclei, or mesonic atoms [257, 258]. These particular studies were possible because pion and kaon beams are available. However, for the vast majority of particles there exist no beams, rendering the experimental investigation of their in-medium properties much more difficult. Examples of such particles are η and η'. Nevertheless, the determination of the $\eta-$ and $\eta'-$nucleus interaction and the possibility of the existence of $\eta^{(\prime)}-$nucleus bound states have been experimentally investigated [259–268].

One of the available experimental methods for determining the nuclear properties of particles is known as *transparency ratio*, first proposed in Ref. [269]. In this method, a highly energetic photon is sent toward a nucleus target, so that it interacts with one of the nucleons and produces the hadron whose finite nuclear density properties are to be determined. This method was conceived to determine the width of antiprotons ($\bar{p}$) in the nuclear medium. Although $\bar{p}$ beams are available, the measurement of the $\bar{p}$ absorption in nuclei was not useful, since the $p\bar{p}$ annihilation probability is so large that the $\bar{p}-$nucleus cross section is roughly πR^2, with R the radius of the nucleus—that is, nearly all antiprotons are absorbed in such a scenario. The insensitivity of this experiment to the $\bar{p}$ width in the nuclear medium stimulated the proposal of an alternative method. The idea was to produce the antiprotons *inside* the nucleus, rather than measuring the absorption from a $\bar{p}$ beam. In this approach, a beam of photons—that can reach all parts of the nucleus with negligible absorption—is used to produce an antiproton inside the nucleus, and then the probability that it leaves the nucleus without being absorbed is determined. Subsequently, by measuring the $\bar{p}$ production in different nuclei, it is possible to determine the $\bar{p}$ width. This method has become popular and has been used to determine the properties in the medium of different particles [270–278]. In Ref. [274] the transparency ratio technique was applied to the reaction $\gamma A \to \eta' A'$ (A and A' representing the initial and final nuclei), comparing η' production on ^{12}C, ^{40}Ca, ^{93}Nb and ^{208}Pb. In order to suppress possible contributions from multinucleon processes, the production rates were normalized to that of ^{12}C.

Although it would be highly desirable to measure the properties of T_{cc} or D_{s0}^* in the nuclear medium, the transparency ratio is actually not suitable for this task, since there are some kinematic restrictions—due to energy and momentum conservation—that render it unusable. Basically, in order to produce very massive particles from a photon-nucleon collision one needs a very energetic photon, which is an important challenge on the experimental side. Furthermore, if we consider the minimum energy that the photon needs to produce this heavy particle, which would produce it at rest in the center-of-mass frame, then in the laboratory (LAB) frame—where the nucleus is at rest—the heavy particle is boosted to a very high momentum. This is not desirable for two reasons: First, the probability density per unit length for the absorption of the

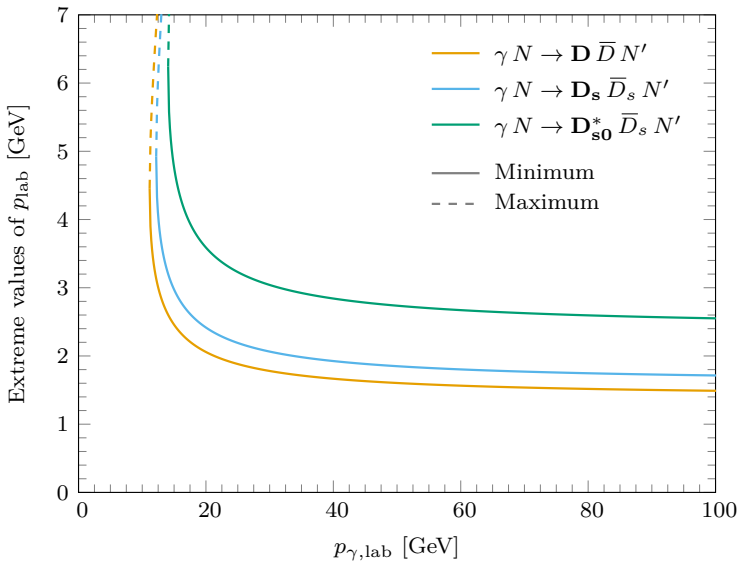

Figure 3.1: Minimum (solid line) and maximum (dashed line) values of the three-momentum with which the $D^*_{s0}(2317)$ (green line), the D_s (blue line) and the isospin-symmetric D (orange line) mesons are produced (through the photoproduction reactions given in the legend of the plot) in the LAB frame, as a function of the photon-energy.

heavy particle inside of the nucleus is inversely proportional to the magnitude of its three-momentum (we will show this in the next sections). Therefore, the higher the momentum of the particle, the less sensitive the method becomes to its in-medium width. Second, the theoretical determination of the finite nuclear density self-energies at high three-momentum is unreliable because of the presence of momentum cutoffs—or any general renormalization scale—in the calculation. Therefore, it is desirable that the particle subject to the finite-nuclear-density study is produced with a minimum momentum in the LAB frame. For this, however, one needs an even more energetic photon.

This situation is illustrated in the plot of Fig. 3.1. There, we consider the photoproduction of several charmed mesons, including the $D^*_{s0}(2317)$, off a nucleon N. The reactions considered are

$$\gamma N \to \mathbf{D^*_{s0}}\,\overline{D}_s\,N', \tag{3.1a}$$

$$\gamma N \to \mathbf{D_s}\,\overline{D}_s\,N', \tag{3.1b}$$

$$\gamma N \to \mathbf{D}\,\overline{D}\,N'. \tag{3.1c}$$

In order to conserve the charm and strangeness quantum numbers, a corresponding anti-meson also needs to be produced. In Fig. 3.1 we plot the

minimum three-momentum (in solid lines) that the mesons marked in bold get in the LAB frame, as a function of the photon energy. As we can see, the greater the mass of the produced charmed meson, the higher the minimum photon energy needed to produce it, marked by the leftmost end of each of the displayed curves. Furthermore, the minimum LAB momentum decreases with growing $p_{\gamma,\mathrm{lab}}$, but saturates at some value. For the case of the D^*_{s0}, this value is around 2.6 GeV. This momentum is very large compared to the maximum momentum available in the theoretical predictions, of about 1 GeV. Furthermore, the photon energies required to produce the D^*_{s0} with this momentum are about 50 GeV, which are unrealizable in any present or planned future experiments. The T_{cc} case—though not treated explicitly—would be even less favorable, due to its larger mass. It is now clear that the transparency ratio is not suitable, at least at the present time, for measuring the nuclear-density modifications to these states.

However, the situation is different for a lighter meson, such as the D mesons. The photon energies required for producing a D meson with momentum below 2 GeV are around 20 GeV. These energies can be achieved by future experiments such as the EIC or the EicC. Given this more hopeful scenario, our aim in this section is to study in more depth the feasibility of this measurement, providing some theoretical predictions. Although the nuclear medium properties of D mesons have been extensively studied theoretically in the literature [1, 2, 162, 210, 215, 222, 279–286], the experimental observation of these theoretical results remains an unexplored field. The study presented in this chapter aims to propose a method based on the use of the nuclear transparency ratio. We investigate the following reaction:

$$\gamma A \to D^+ D^- A', \tag{3.2}$$

where A represents a nuclear target. We will consider ^{12}C, ^{40}Ca, ^{93}Nb and ^{208}Pb—the same nuclei that were used in the investigation of the nuclear density properties of the η' in Ref. [274]. We will base our results on the theoretical predictions for the D meson nuclear-density-dependent self-energy obtained in Ref. [215]. This study is of a prospective character, and some approximations will be made. We shall test the robustness of some of the approximations considered in order to strengthen our main conclusion, which will be on the feasibility of this measurement. When the experiment is eventually carried out, improvements to the calculation can be taken into account, some of which we mention at the end of the chapter.

This chapter is organized as follows. In Sect. 3.2 we define the transparency ratio and present the formalism used for its evaluation. In Sect. 3.3, we show the main result of this work and discuss some improvements to the evaluation of the transparency ratio to test their robustness. In Sect. 3.4 we draw our

conclusions on the feasibility of this measurement.

3.2 Computing the D^+ transparency ratio

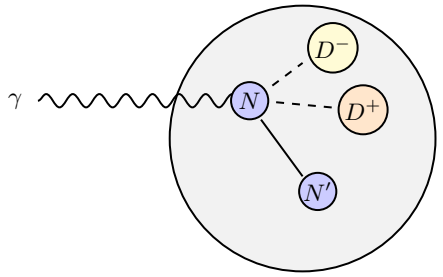

Figure 3.2: Schematic picture of the process considered for the $\gamma A \to D^+ D^- A'$ reaction.

A schematic picture of the photoproduction of a $D\overline{D}$ pair from a nucleon inside a given nucleus—which is the key process defining the transparency ratio—is given in Fig. 3.2. This process takes place in two steps. Firstly, the photon γ scatters on a nucleon N inside the nucleus—characterized by some mass number A—producing as a result D^+ and D^- mesons, and a recoiling nucleon N'. Secondly, the D mesons propagate inside the nucleus, and there is some nonzero probability that they are absorbed by the nuclear medium (that is, that they undergo inelastic scattering with one of the other nucleons), this probability being governed by the imaginary part of their self-energy. The complete cross section for the production of a D meson off a nucleus through the reaction

$$\gamma N \to D^+ D^- N' \tag{3.3}$$

consists of the combination of these two steps. We refer to this cross section as σ_A.

Now, in the usual definition of the transparency ratio, one normalizes σ_A by A times the production cross section off a nucleon, which we shall name σ_N.[1]

$$\bar{T} = \frac{\sigma_A}{A\sigma_N}. \tag{3.4}$$

By construction, this quantity will be very sensitive to the absorption part of the D mesons and not so sensitive to the details of their production. However, there can be contributions to σ_A arising from multistep processes leading to the

[1] Alternatively, it is also common to normalize σ_A with respect to the production cross section off the deuteron.

same final state D^+D^-N'. In order to reduce the impact of such processes in the evaluation of the transparency ratio, we normalize the result to that of the ^{12}C nucleus.

$$T = \frac{\sigma_A/A}{\sigma_{12}/12}. \tag{3.5}$$

This was also done in the study of the η' transparency ratio of Ref. [274], as already mentioned in the introduction.

With this, we have presented our definition for the transparency ratio T, which depends on the mass number of the target nuclei, A. However, a further comment is in order here. We have chosen to study the D^+ meson instead of the D^-. This is because the photoproduction of the D^- could take place through several two-body final states such as $\gamma N \to D^-(\Lambda_c, \Sigma_c, \dots)$. For the D^+, since its quark content is $c\bar{d}$, any two-body channel should proceed through the creation of pentaquark-like resonances, which have not been observed.

3.2.1 Survival probability of the D^+ in a nucleus

We start by computing the survival probability of the D^+ meson in the nucleus once it has been produced off a nucleon, which corresponds to the *second step* in the nucleus cross section σ_A introduced previously. First, we need to define a model for the density profile of the different nuclei considered. As a starting point, we take a very simple picture for the nuclei, assuming a sphere of constant density $\rho_0 = 0.17$ fm^{-3}.

$$\rho(r) = \begin{cases} \rho_0, & |\vec{r}| \leq R, \\ 0, & |\vec{r}| > R, \end{cases} \qquad R = \left(\frac{3A}{4\pi\rho_0}\right)^{\frac{1}{3}}. \tag{3.6}$$

We refer to this model as "*hard-sphere*" nucleus. In this density parameterization, we compute the radius of each nucleus (R) from ρ_0 and the mass number A. We will study the overall impact that this simplistic representation of the nuclei has on the final results by considering more realistic harmonic oscillator or two-parameter Fermi distributions for the different nuclei in Sect. 3.3.1.

With the density profile of the nuclei defined, we now evaluate the absorption probability of the D^+ meson inside the nucleus. We know that the probability density per unit time that a given particle decays is

$$\frac{dP}{dt} = \frac{1}{\Gamma} \tag{3.7}$$

where Γ is the width of the particle. As we already found in Eq. (2.23), this decay width can be related to the imaginary part of the self-energy through the following approximate expression.

$$\Gamma \simeq \frac{\mathrm{Im}\,\Pi(m_D, \vec{p} = \vec{0}; \rho)}{m_D}. \tag{3.8}$$

where m_D is the mass of the D meson, $\vec{p}$ its three-momentum, and ρ is the density of the nuclear medium. Note that this previous relation was found for zero three-momentum. We now aim to generalize this expression for Γ to the case of $p > 0$.

The energy p^0 corresponding to a D meson with three-momentum $\vec{p}$ is determined by the pole of the renormalized propagator—cf. (2.18), so that

$$(p^0)^2 - \vec{p}^2 - m_D^2 - \Pi(p^0, \vec{p}; \rho) = 0. \tag{3.9}$$

This p^0 energy will be complex, and its real and imaginary parts will be given by

$$p^0 = E_{\text{qp}} - i\frac{\Gamma}{2}, \tag{3.10}$$

where E_{qp} is the quasiparticle energy. Isolating now the real and imaginary parts of Eq. (3.9) we write the following system of equations for E_{qp} and Γ:

$$E_{\text{qp}}^2 - \frac{\Gamma^2}{4} - \vec{p}^2 - m_D^2 - \text{Re}\,\Pi(E_{\text{qp}} - i\Gamma/2, \vec{p}; \rho) = 0, \tag{3.11a}$$

$$-E_{\text{qp}}\Gamma - \text{Im}\,\Pi(E_{\text{qp}} - i\Gamma/2, \vec{p}; \rho) = 0. \tag{3.11b}$$

Similarly to what was discussed in Sect. 2.3 when studying the meson self-energy in a general way, an exact solution to these equations is difficult to find, as one would need to evaluate the self-energy Π for complex values of its energy argument. However, we can extract a first-order approximation to the solution of this system of coupled equations by setting $\Gamma = 0$ everywhere except in the left term in the imaginary part equation (3.11b). In more detail, we can solve

$$\tilde{E}_{\text{qp}}^2 - \vec{p}^2 - m_D^2 - \text{Re}\,\Pi(\tilde{E}_{\text{qp}}, \vec{p}; \rho) = 0 \tag{3.12}$$

for $\tilde{E}_{\text{qp}}$, and then use this value to determine the width via

$$\tilde{\Gamma} = -\frac{\text{Im}\,\Pi(\tilde{E}_{\text{qp}}, \vec{p}; \rho)}{\tilde{E}_{\text{qp}}}. \tag{3.13}$$

Taking the D spectral functions that were determined in [215] for a nuclear density of $\rho_0 = 0.17\ \text{fm}^{-3}$, we obtain the approximate value for the quasiparticle energy, which is plotted in the left panel of Fig. 3.3 (orange line). For reference, we also show in blue the relativistic free-space energy of the meson. Using the obtained values of $\tilde{E}_{\text{qp}}$ as a function of the modulus of the three-momentum, we can now evaluate the imaginary part of the self-energy to obtain a first approximation of $\tilde{\Gamma}$. The line shape obtained for $\text{Im}\,\Pi$ as a function of the momentum is shown in the right panel of Fig. 3.3.

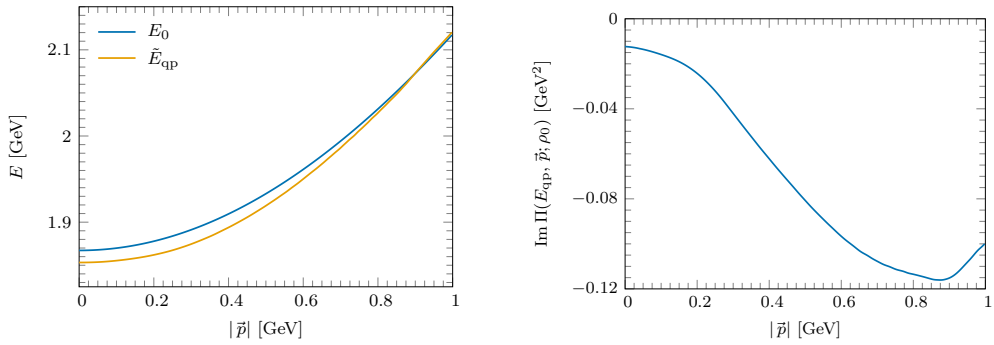

Figure 3.3: Left panel: Plot of the relativistic free-space D meson energy $E_0 = \sqrt{m_D^2 + \vec{p}^2}$ (blue line) and of the D quasiparticle energy obtained from solving Eq. (3.12) (orange line), as functions of the D meson three-momentum in the nucleus rest-frame (LAB frame). Right panel: Plot of the imaginary part of the self-energy evaluated at the quasiparticle energy for normal nuclear density, as a function of the D meson three momentum.

In the work of Ref. [215] the spectral functions for the D mesons were determined up to a three-momentum of $|\vec{p}| = 1$ GeV. However, as we discussed in Sect. 3.1, in our calculation the minimum momentum with which the D mesons are produced is around 1.5 GeV, depending on the energy of the incident photon; cf. Fig. 3.1. Therefore, some sort of extrapolation is needed. In the prospective character of this work, we shall take a constant extrapolation, with

$$\mathrm{Im}\,\Pi \simeq -0.1\ \mathrm{GeV}^2 = \mathrm{const.} \tag{3.14}$$

This constant value is of the order of magnitude of the results shown in the right panel of Fig. 3.3. However, we will study the impact that reducing this constant value has on the final results.

Up to this point, we have presented how the width of a state is related with the differential probability that the state decays *per unit time*, and how one can estimate this width from the imaginary part of the self-energy. However, in our evaluation, we need the differential decay probability *per unit length*. This quantity is related to the one from Eq. (3.7) as

$$\frac{dP}{dl} = \frac{dP}{dt}\frac{dt}{dl} = \frac{1}{\Gamma}\frac{1}{v} \simeq -\frac{\mathrm{Im}\,\Pi}{Ev} = -\frac{\mathrm{Im}\,\Pi}{p}. \tag{3.15}$$

To arrive at the previous expression, we have used the relativistic formula for the velocity $v = p/E$. Actually, the quantity we are interested in is the probability that the D meson leaves the nucleus without being absorbed. This survival

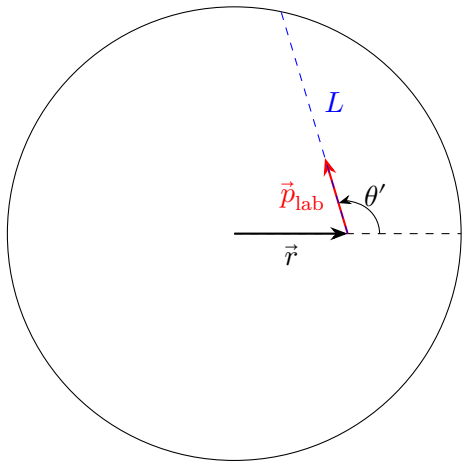

Figure 3.4: Diagrammatic representation of the nucleus in the hard-sphere model, together with the $\vec{r}$ and $p_{\rm lab}$ vectors, the angle θ' between them, and the distance L.

probability, which we name S, is given by[2]

$$S(\vec{r},\vec{p}_{\rm lab};\rho) = \exp\left[-\int_{\vec{r}'} \frac{-{\rm Im}\,\Pi\left(E_{\rm qp},p_{\rm lab};\rho(\vec{r}')\right)}{p_{\rm lab}} dl\right] \tag{3.18}$$

where $\vec{r}$ represents the point inside the nucleus where the D^+ meson is produced, and the trajectory of the D^+ in its way out of the nucleus is parametrized in terms of l as

$$\vec{r}' = \vec{r} + l\frac{\vec{p}_{\rm lab}}{p_{\rm lab}} \tag{3.19}$$

with $\vec{p}_{\rm lab}$ the three-momentum of the D^+ meson in the LAB frame, and $p_{\rm lab}$ its modulus.

For the hard-sphere nuclear model, for which the density is given by Eq. (3.6), the integral of Eq. (3.18) can be easily evaluated analytically. This

[2]This expression for the survival probability arises from

$$S(l+dl) = S(l)\left[1 - \frac{dP}{dl}dl\right], \tag{3.16}$$

where $[1-\frac{dP}{dl}dl]$ represents the probability that the D meson is not absorbed in a distance dl. This equation can be rewritten as

$$\frac{dS}{dl} = -\frac{dP}{dl}S(l), \tag{3.17}$$

which yields the usual exponential decay law for a constant decay probability dP/dl. The solution will not be exponential for a general dependence of dP/dl on l.

results in

$$S_{\rm HS}(\vec{r},\vec{p}_{\rm lab};\rho) = \exp\left[\frac{{\rm Im}\,\Pi\left(E_{\rm qp},p_{\rm lab};\rho_0\right)}{p_{\rm lab}}\int_{\vec{r}'} dl\right] = \exp\left[\frac{{\rm Im}\,\Pi\left(E_{\mathbf{qp}},p_{\rm lab};\rho_0\right)}{p_{\rm lab}}L\right], \quad (3.20)$$

where the remaining integral is just the length L of the straight line that connects $\vec{r}$ with the surface of the nucleus in the direction of $\vec{p}_{\rm lab}$. Due to rotational symmetry, this quantity depends only on the distance between the point where the D^+ is created and the center of the nucleus, r (taking the origin of coordinates at the center of the nucleus); and on the angle between $\vec{r}$ and $\vec{p}_{\rm lab}$, which we name θ'. A diagram presenting $\vec{r}$, $\vec{p}_{\rm lab}$, θ' and L is presented in Fig. 3.4. The expression for L can easily be found to yield[3]

$$L(r,\theta') = \sqrt{R^2 - r^2\sin^2\theta'} - r\cos\theta'. \quad (3.21)$$

For a more realistic density distribution in the nucleus, e.g. harmonic oscillator or two-parameter Fermi distributions, the integral of Eq. (3.18) will be more complex, and we shall solve it numerically.

This concludes our calculation of the survival probability of the D^+ meson inside the nucleus once it has been produced. We will next deal with the production cross section of the D^+ meson, as well as present the phase-space integration of the three-body final state.

3.2.2 Nucleon cross section and phase space evaluation

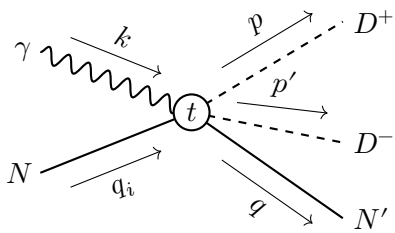

Figure 3.5: Schematic diagram for the process $\gamma N \to D^+D^-N'$, indicating the different momentum labels.

We now consider the photoproduction of the D^+D^- pair off a nucleon, ignoring for the moment the role of the nucleus, and in particular the absorption

[3]This can be done by squaring Eq. (3.19), taking $(\vec{r}')^2 = R^2$ and solving for l.

of the D^+ meson. In Fig. 3.5 we show a schematic diagram of this process, indicating the momentum label corresponding to each particle. The cross section for this process will be given by

$$\sigma_N = \frac{1}{4m_N\left|\vec{k}_{\rm lab}\right|}\int\frac{d^3q}{(2\pi)^3}\frac{1}{2E(q)}\int\frac{d^3p}{(2\pi)^3}\frac{1}{2\omega(p)}\int\frac{d^3p'}{(2\pi)^3}\frac{1}{2\omega(p')} \times 4m_N^2\left|t\right|^2(2\pi)^4\delta^4(\mathbf{k}+\mathbf{q_i}-\mathbf{p}-\mathbf{p}'-\mathbf{q}). \quad (3.22)$$

In this previous expression, m_N is the mass of the nucleon, and

$$\left|\vec{k}_{\rm lab}\right| = \frac{\sqrt{\lambda(s,m_N^2,0)}}{2m_N} = \frac{s-m_N^2}{2m_N} \quad (3.23)$$

is the momentum of the photon in the LAB frame (λ being the Källén function), where the nucleus is at rest. $E(q)$ represents the energy of the final nucleon, and ω represents the energy of either the D^+ or the D^- mesons. In our notation, we use bold letters (e.g., $\mathbf{p}$) to denote the four-momenta, while three-momenta are represented with the standard vector notation ($\vec{p}$). The modulus of a three-momentum is represented by a simple letter (p). In addition, a factor $4m_N^2$ arising from the field normalization of the nucleons has been added to render the squared modulus of the T–matrix element—represented by $|t|^2$—dimensionless.

After integrating the energy-momentum conservation deltas and performing a change of variables (details for this integration are given in Appendix B), we can write this cross section as

$$\sigma_N = \frac{m_N^2}{(s-m_N^2)\sqrt{s}}\frac{1}{32\pi^4}\int_{m_{\rm inv}^{\rm min}}^{m_{\rm inv}^{\rm max}} pp'\,dm_{\rm inv}\int_{-1}^{1}d\cos\theta\int_0^{2\pi}d\phi\;|t|^2. \quad (3.24)$$

In this simplified expression, p represents the momentum of the D^+ in the γN center of mass frame, parametrized as

$$\vec{p} = p\begin{pmatrix}\sin\theta\cos\phi\\ \sin\theta\sin\phi\\ \cos\theta\end{pmatrix}, \qquad p = \frac{\sqrt{\lambda(s,m_D^2,m_{\rm inv}^2)}}{2\sqrt{s}}, \quad (3.25)$$

$$\omega(p) = \frac{s+m_D^2-m_{\rm inv}^2}{2\sqrt{s}}, \quad (3.26)$$

where the θ and ϕ angles are taken with respect to the direction of the momentum of the incident photon $\vec{k}$, which is taken along the z axis

$$\vec{k} = k\begin{pmatrix}0\\0\\1\end{pmatrix}, \qquad k = \frac{1}{2\sqrt{s}}(s-m_N^2) \quad \text{(center of mass frame)}, \quad (3.27)$$

$$k_{\text{lab}} = \frac{1}{2m_N}(s - m_N^2) \quad \text{(LAB frame)}. \tag{3.28}$$

In addition, m_{inv} is the invariant mass associated to the $D^- N'$ pair (with N' the nucleon emitted in $\gamma N \to D^+ D^- N'$). The integration limits for m_{inv} are[4]

$$m_{\text{inv}}^{\text{min}} = m_{D^-} + m_N, \tag{3.31a}$$
$$m_{\text{inv}}^{\text{max}} = \sqrt{s} - m_{D^+}. \tag{3.31b}$$

We explicitly distinguish m_{D^-} and m_{D^+} to indicate which final–state particle we are referring to. Lastly, we define p' to be the three-momentum of the D^- meson in the ND^- rest frame. This is given by

$$p' = \frac{\sqrt{\lambda\left(m_{\text{inv}}^2, m_{D^-}^2, m_N^2\right)}}{2m_{\text{inv}}}, \tag{3.32}$$

which is the usual relativistic formula for the center-of-mass three-momentum of a two-particle system (cf. Eq. (2.60) replacing $s \to m_{\text{inv}}^2$).

In summary, in Eq. (3.24) we have presented the cross section for the photoproduction of the $D^+ D^-$ pair off a nucleon. Although this expression depends on the transition matrix element $|t|^2$, when taking the transparency ratio—recall Eqs. (3.4) and (3.5)—the features arising in the different cross sections due to $|t|^2$ will mostly cancel. In other words, we expect the dependence of the transparency ratio on the features of the scattering amplitude to be residual. Then, we shall approximate it to be constant.

$$|t|^2 \sim \text{const.} \tag{3.33}$$

In Sect. 3.3.1 we will improve on this assumption by considering a strong momentum dependence in $|t|^2$.

[4]The lower limit follows from the fact that the minimum invariant mass corresponds to a null relative three-momentum in the ND^- rest frame. The maximum value is derived from the definition of the total invariant mass s

$$s = (P_{ND^-} + p_{D^+})^2, \tag{3.29}$$

where P_{ND^-} the total four-momentum of the ND^- pair and p_{D^+} is the four momentum of the D^+. Then, for a fixed s, the maximum value of $m_{\text{inv}}^2 = P_{ND^-}^2$ is obtained when the ND^+ pair and the D^+ meson have zero relative three-momentum in the center of mass frame, so that

$$s = m_{\text{inv}}^2 + m_{D^+}^2 + 2m_{\text{inv}} m_{D^+}. \tag{3.30}$$

3.2.3 Photoproduction cross section off a nucleus

We now focus on the D^+ photoproduction off a nucleon lying inside a nucleus. The basic building block is the cross section of Eq. (3.24), but now we have to take into account the nucleon density in the nucleus and the survival probability of the D^+ in nuclear matter.

In the local density approach, the differential cross section (per unit volume) for the D^+ production off a nucleon will be proportional to the nucleon density at the point $\vec{r}$ where the photon impinges:[5]

$$\frac{d\sigma}{dV} \propto \rho(\vec{r})|t|^2. \tag{3.34}$$

Furthermore, we also need to consider the survival probability of the D^+ meson, given in Eq. (3.18). Taking both of these considerations into account, the total cross section for the photoproduction of the D^+ meson off a nucleus now reads as follows.

$$\sigma_A = \frac{m_N^2}{(s-m_N^2)\sqrt{s}} \frac{1}{32\pi^4} \int_{m_{\rm inv}^{\rm min}}^{m_{\rm inv}^{\rm max}} pp' dm_{\rm inv} \int_{-1}^{1} d\cos\theta \int_0^{2\pi} d\phi \int d^3r \\ \rho(\vec{r})|t|^2 \exp\left[\int_{\vec{r}'} \frac{{\rm Im}\,\Pi\left(E_{\mathbf{qp}}, p_{\rm lab}; \rho(\vec{r}')\right)}{p_{\rm lab}} dl\right]. \tag{3.35}$$

This expression is simplified in the hard-sphere nuclear model, where the density distribution is a step function:

$$\sigma_A^{\rm HS} = \frac{m_N^2}{(s-m_N^2)\sqrt{s}} \frac{1}{32\pi^4} \int_{m_{\rm inv}^{\rm min}}^{m_{\rm inv}^{\rm max}} pp' dm_{\rm inv} \int_{-1}^{1} d\cos\theta \int_0^{2\pi} d\phi \int_{r<R} d^3r \\ \rho_0|t|^2 \exp\left[\frac{{\rm Im}\,\Pi\left(E_{\mathbf{qp}}, p_{\rm lab}; \rho_0\right)}{p_{\rm lab}} L(r,\theta')\right]. \tag{3.36}$$

At this point, in order to evaluate the cross section of Eq. (3.36), it only remains to define the integration over $\vec{r}$ and the quantity $p_{\rm lab}$, which corresponds to the momentum of the D^+ meson in the LAB frame, where the nucleus is at rest. The position vector $\vec{r}$ is taken as

$$\vec{r} = r \begin{pmatrix} \sin\tilde{\theta}\cos\tilde{\phi} \\ \sin\tilde{\theta}\sin\tilde{\phi} \\ \cos\tilde{\theta} \end{pmatrix}. \tag{3.37}$$

[5] For the sake of clarity, we omit in this formula extra differentials associated to the momentum coordinates of the produced particles.

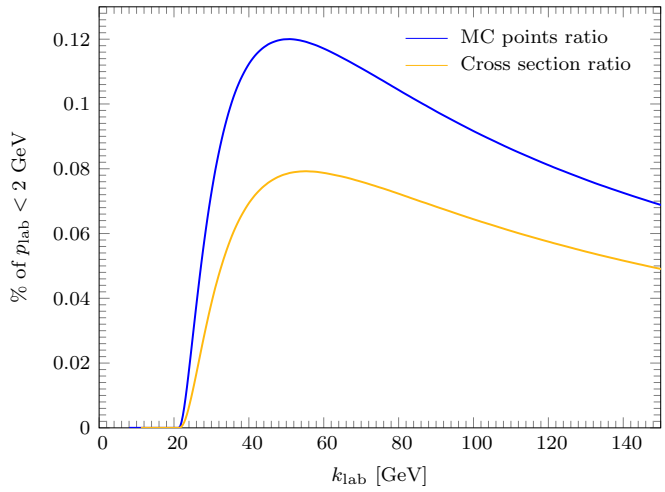

Figure 3.6: Percentage of D^+ mesons with $p_{\rm lab} < 2$ GeV as a function of the photon momentum in the LAB frame, estimated using two different methods. The blue line corresponds to the the fraction of sampled points in the Monte Carlo integration for which $p_{\rm lab} < 2$ GeV. The orange line is computed taking the ratio of the nucleon cross section including the $p_{\rm lab} < 2$ GeV condition, divided by the total nucleon cross section computed in the full available phase space.

However, given the symmetry of this setup, the integration over the $\tilde{\phi}$ angle is redundant, and we can safely add a factor 2π to Eq. (3.36) and take $\tilde{\phi} = 0$.

Lastly, to obtain $\vec{p}_{\rm lab}$ from $\vec{p}$ we perform a boost from the γN center-of-mass frame—where the initial nucleon N has momentum $\vec{q}_i = -\vec{k}$—to the LAB frame—where N is at rest ($\vec{q}_{i,\rm lab} = \vec{0}$).[6] This boost is given by the general formula of Ref. [287]:

$$\vec{p}_{\rm lab} = \left[\left(\frac{E(q_i)}{m_N} - 1\right)\frac{\vec{p}\cdot\vec{q}_i}{|\vec{q}_i|^2} - \frac{\omega(p)}{m_N}\right]\vec{q}_i + \vec{p}. \tag{3.38}$$

Once $\vec{p}_{\rm lab}$ has been obtained, one can easily compute the angle θ' needed to evaluate $L(r,\theta')$ from

$$\cos\theta' = \frac{\vec{r}\cdot\vec{p}_{\rm lab}}{r p_{\rm lab}}. \tag{3.39}$$

[6] In the LAB frame—defined as the nucleus rest frame—we set the nucleon's initial momentum to zero. Although this neglects its statistical (Fermi) motion inside the nucleus, the approximation is expected to be excellent because the D^+ photoproduction threshold requires a photon with very large momentum $\vec{k}$.

With this, we are now in a position to calculate the transparency ratio of Eq. (3.5). However, before proceeding with the results, we shall make some remarks about the photon energies needed for this process, extending the discussion that was first presented in Sect. 3.1, in particular in Fig. 3.1. The minimum value of $\sqrt{s}$ for γN_i is

$$(\sqrt{s})_{\min} = m_N + m_{D^-} + m_{D^+} \simeq 4.678 \text{ GeV}, \tag{3.40}$$

which corresponds to a photon momentum $k \simeq 11.17$ GeV (see Fig. 3.1). We can use the general boost of Eq. (3.38) to obtain the minimum p_{lab}. This minimum occurs when the D^+ meson's center-of-mass momentum is maximal and antiparallel to the incoming photon momentum.

$$\vec{p} = \frac{\sqrt{\lambda[s, m_D^2, (m_{\text{inv}}^{\min})^2]}}{2\sqrt{s}} \begin{pmatrix} 0 \\ 0 \\ -1 \end{pmatrix}. \tag{3.41}$$

Using this previous expression, together with the fact that in the center-of-mass frame $\vec{q}_i = -\vec{k}$, one can easily evaluate the minimum value of the D^+ momentum in the LAB frame. The value for the modulus of this momentum turns out to be

$$p_{\text{lab}}^{\min} = -\frac{E(q_i)}{m_N} p + \frac{\omega(p)}{m_N} q_i. \tag{3.42}$$

As discussed in Sect. 3.1, we find that for values of s close to the D^+D^-N' threshold the minimum momentum of the D^+ in the LAB frame is of the order of 3 GeV. For growing s, $p_{\text{lab}}^{\min}$ tends to the asymptotic value

$$\lim_{s\to\infty} p_{\text{lab}}^{\min} = \frac{m_D^2 - m_N^2}{2m_N} = 1.387 \text{ GeV}. \tag{3.43}$$

This behavior can also be observed in the plot of Fig. 3.1.

As we already mentioned in the Introduction, producing a D^+ meson with a high LAB momentum is not desirable for two reasons:

1. The absorption probability is suppressed by p_{lab}, cf. Eq. (3.18).
2. The theoretical calculation of Ref. [215] for the imaginary part of the D^+ self-energy in the nuclear medium is available up to 1 GeV.

Due to these reasons and given the minimum p_{lab} shown in Eq. (3.43), we select momenta $p_{\text{lab}} < 2$ GeV. We expect that including this momentum filter in the experiment should improve its efficiency. We can then estimate the photon energy that maximizes the fraction of D^+ that are produced with a LAB momentum below 2 GeV. This estimate is obtained in two ways: 1) by

a Monte Carlo integration of the phase space in Eq. (3.36), computing the fraction of sampled points for which $p_{\rm lab} < 2$ GeV (blue line);[7] and 2) by taking the ratio of the nucleon cross section—cf. (3.24)—restricted to $p_{\rm lab} < 2$ GeV to the total nucleon cross section evaluated over the entire phase space. We see a qualitative agreement between both evaluations, although the latter method produces a result which is roughly 0.7 that of the former. In any case, from the shape of both momentum distributions we see that the optimal photon momentum in the LAB frame is $k_{\rm lab} \simeq 50$ GeV, which corresponds to a γN invariant mass of $\sqrt{s} \simeq 10$ GeV. We therefore perform our transparency–ratio calculations at this energy.

3.3 Predictions for the D^+ transparency ratio

In this section, we discuss the results for the transparency ratio for the D^+ mesons—shown in Fig. 3.7—as a function of the mass number of the nucleus A. We consider three constant values for the imaginary part of the self-energy of the D^+: $\mathrm{Im}\,\Pi = -0.1$ GeV^2 (red, solid), -0.05 GeV^2 (blue, dashed), and -0.025 GeV^2 (green, dotted)—the latter two being half and one quarter of the value of Eq. (3.14), respectively—to test the sensitivity of $T(A)$ to the absorption part of the nuclear cross section.

For $\mathrm{Im}\,\Pi = -0.1$ GeV^2, $T(A)$ departs markedly from unity, indicating that a measurement of this observable should be sensitive to the D^+ width in the nuclear medium. An analogous sensitivity was observed in η' photoproduction on nuclei [274], where the data implied an in–medium width at $\rho = \rho_0$ of

$$\Gamma_{\eta'} = -\,\mathrm{Im}\,\Pi_{\eta'}/E_{\eta'} \simeq 15 \sim 25 \text{ MeV}.$$

Reducing the magnitude of $\mathrm{Im}\,\Pi$ to -0.05 or -0.025 GeV^2 shifts $T(A)$ closer to 1, yet it remains clearly below unity, showing that values smaller than those inferred in Ref. [215] would still be experimentally observable.

However, there are some caveats to these results. In our calculation, we have assumed that $\mathrm{Im}\,\Pi$ is dominated by genuine absorption (where the D^+ disappears) and that quasielastic $D^+N \to D^+N'$ is subleading. This holds in the calculations of Ref. [215], where the main contributions to $\mathrm{Im}\,\Pi$ arise from $DN \to \pi\Sigma_c$, $\pi\Lambda_c$, $K\Xi_c$, and D^*N. However, this may not be the case when considering other DN interaction models. In order to suppress possible contributions from quasi-elastic scattering, we propose the following filter, which could be applied in future studies when actual data is available.

Kinematically, the large photon energies produce D^+D^-N in a tight forward cone in the LAB frame. However, if a D^+ undergoes a quasielastic collision,

[7] The blue line in Fig. 3.6 corresponds to the result shown in Fig. 2 of Ref. [3]. The orange line was not considered in that reference.

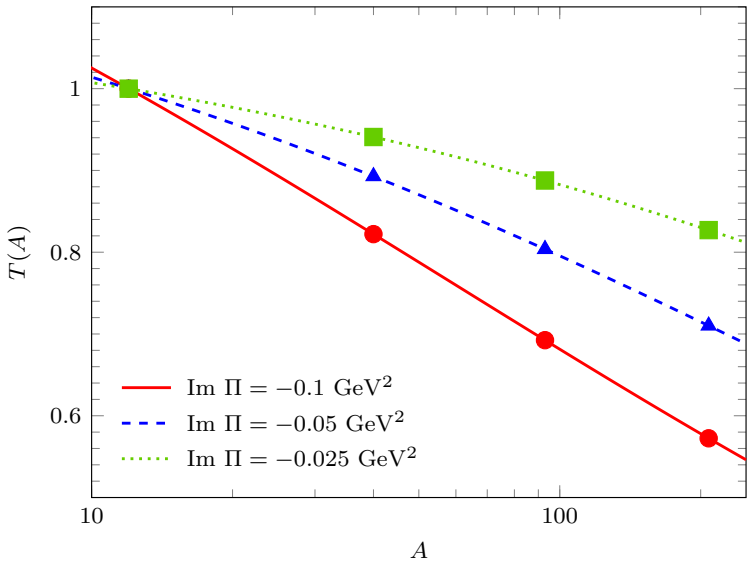

Figure 3.7: Transparency ratio of Eq. (3.5), normalized to ^{12}C as a function of the mass number of nuclei. The three lines show the transparency ratio calculated with different values of Im Π. The points (circles, triangles and squares) in the figure indicate the results for ^{12}C, ^{40}Ca, ^{93}Nb, and ^{208}Pb.

$D^+N \to D^+N'$, its direction spreads and the final D^+ is no longer as forward–peaked as the primary one. Therefore, an additional forward angle filter on the detected D^+ would suppress quasi-elastic events, effectively selecting those that did not interact and allowing the absorptive part of the in-medium self-energy to be better isolated. A similar argument applies to primary D^+ with $|\vec{p}_{\rm lab}| > 2$ GeV that lose energy through quasi-elastic scattering. In a further step, one could account for photon shadowing at the experimental energy, which is expected to be much smaller than the strong absorption suffered by D mesons [274].

In addition, easily implemented refinements of the transparency ratio calculation are possible. First, one may use realistic (e.g., two-parameter Fermi model) density profiles for each nucleus. This changes the evaluation of the integral in Eq. (3.18), requiring an explicit ρ–dependence of the imaginary part of the D^+ self-energy. Second, since the assumption of a constant scattering amplitude $|t|^2$ can be thought of as rather crude, we shall introduce its dominant energy dependence. In the next section, we incorporate these corrections into the nuclear cross section of Eq. (3.35) and reassess the transparency ratio to test the robustness of the results shown in Fig. 3.7.

3.3.1 Improved density profiles and momentum-dependent photoproduction

In order to derive the results for the D^+ transparency ratio shown in Fig. 3.7, some approximations were used. Among them, we assumed a constant density profile for the different nuclei and did not consider any energy or momentum dependence on the D^+ photoproduction amplitude. These approximations were made under the argument that the transparency ratio is not very sensitive to the details of the production or the shape of the nucleus, but rather to the absorption of the D^+ meson. However, in this section, we shall test the validity of this assumption, using more realistic density profiles for the different nuclei, as well as the main energy dependence on the photoproduction amplitude.

Let us start by considering the improved density profiles for the different nuclei. Following Refs. [274, 288, 289], we take a two-parameter Fermi model for the ^{40}Ca, ^{93}Nb and ^{208}Pb, given by

$$\rho_{\rm 2pF}(r) = \frac{\tilde{\rho}_0}{1+\exp\left(\frac{r-R}{a}\right)}. \tag{3.44}$$

This density distribution depends on two parameters with length dimensions, R and a, and a normalization constant $\tilde{\rho}_0$ which is chosen so that

$$\int d^3r\, \rho_{\rm 2pF}(r) = A \tag{3.45}$$

for the different nuclei (with A their mass number). The different parameters used for each nucleus are presented in Table 3.1.

Nucleus	R [fm]	a [fm]	$\tilde{\rho}_0$ [fm^{-3}]
^{40}Ca	3.51	0.563	0.176
^{93}Nb	4.87	0.573	0.169
^{208}Pb	6.62	0.549	0.160

Table 3.1: Numerical constants of the two-parameter Fermi model for ^{40}Ca, ^{93}Nb, ^{208}Pb. Taken from Ref. [288] (see also [289]).

For the case of ^{12}C, we use a harmonic oscillator model, with the expression for the density profile being in this case as follows.

$$\rho_{\rm HS}(r) = \tilde{\rho}_0 \left(1 + c\left(\frac{r}{R}\right)^2\right) e^{-(r/R)^2}. \tag{3.46}$$

The c and R parameters are taken to be [289]

$$c = 1.082 \text{ [dimensionless]}, \qquad R = 1.692 \text{ fm}, \tag{3.47}$$

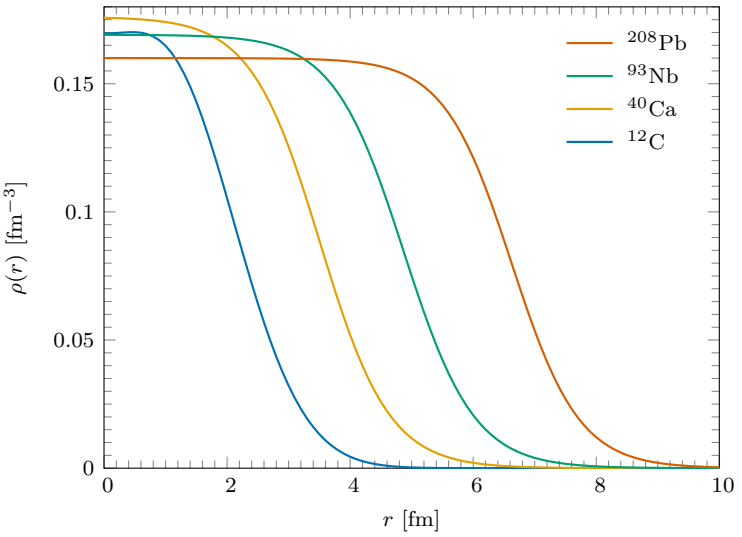

Figure 3.8: Density profiles of the different nuclei considered (in different colors) as a function of the radial coordinate r, extracted from Ref. [288].

while $\tilde{\rho}_0$ is again computed from the normalization of the density distribution,

$$\tilde{\rho}_0 = \int d^3r \; \rho_{\rm HS}(r) = 12. \tag{3.48}$$

Its value is found to be $\tilde{\rho}_0 = 0.170$ fm^{-3}.

In Fig. 3.8, we plot the different density profiles for the four nuclei considered. These shapes are more realistic than the simple step functions of Eq. (3.6). When taking these density distributions into account, the integration of the absorption probability through the path that the D^+ meson follows on its way out of the nucleus—cf. Eq. (3.18)—has to be done with more care. Taking the imaginary part of the D^+ self-energy to be proportional to the density (which is true for small enough values of the density), we now write the survival probability of the D^+ meson as

$$S(\vec{r},\vec{p}_{\rm lab};\rho) = \exp\left[\int_{\vec{r}'} \frac{{\rm Im}\,\Pi\left(E_{\mathbf{qp}},p_{\rm lab};\rho_0\right)\frac{\rho(r')}{\rho_0}}{p_{\rm lab}} dl\right]. \tag{3.49}$$

In this expression, $\rho(r')$ represents one of the different density profiles previously introduced for the various nuclei, and r' is the distance from the center of the nucleus to the point of the trajectory of the D^+ meson, parametrized in terms of l through Eq. (3.19) (taking the origin of coordinates at the center of the nucleus). Since there is no easy analytical expression for the integral in this case, we perform it numerically using a Gauss-Legendre algorithm.

Next, we will include some momentum dependence in the photoproduction amplitude. Although the result of the nuclear cross section is greatly affected by the functional form of this amplitude, we expect that the effect on the final result for the transparency ratio will be small, since both the numerator and denominator of Eq. (3.5) will be affected in a similar way. However, we shall test this assertion here.

In Ref. [290], the authors compute the amplitude for the $\gamma p \to D^+ D^{*-} p$ and other related processes, evaluating its dependence on momentum and angular variables. In order to probe whether the transparency ratio is sensitive to changes in the amplitude, we do not consider it necessary to include all the different variables. We shall implement only the amplitude dependence on the variable $t' = (\mathbf{q_i} - \mathbf{q})^2$ ($\mathbf{q_i}$ and $\mathbf{q}$ being the four-momentum of the initial and final nucleons, respectively), which leads to the largest variation in the cross section—a reduction of two orders of magnitude from $t' \simeq 0$ to $t' \simeq -1$ GeV^2. Considering any other variables would unnecessarily complicate the calculation. Therefore, we now assume

$$|t|^2 = |t_0|^2 \exp\left[\log(10^{-2})\,\frac{t'}{-1\ \text{GeV}^2}\right]. \tag{3.50}$$

When considering this new momentum dependence on the amplitude, we need to revise the phase space integration of Eq. (3.35). Due to the dependence of t' on the angle between $\vec{q}_i$ and $\vec{q}$, we need to consider the integration over the $\vec{q}$ angles explicitly (not just a factor 4π). If we evaluate the $\vec{p}'$ ($\vec{p}'$ being the momentum of the D^- meson) and $\vec{q}$ integration in the $D^- N'$ rest frame (as detailed in Appendix B), where $\vec{p}' = -\vec{q}$, we can instead integrate the angles of the $\vec{p}'$ momentum.

$$4\pi \to \int_{-1}^{+1} d\cos\tilde{\theta}' \int_0^{2\pi} d\tilde{\phi}', \qquad \vec{p}' = p' \begin{pmatrix} \sin\tilde{\theta}'\cos\tilde{\phi}' \\ \sin\tilde{\theta}'\sin\tilde{\phi}' \\ \cos\tilde{\theta}' \end{pmatrix}. \tag{3.51}$$

Besides, since the $\vec{q}$ momentum is taken in the $D^- N'$ rest frame, in order to evaluate t' we need to boost $\vec{q}_i$ from the γN rest frame—where $\vec{q}_i = -\vec{k}$ with $\vec{k}$ the photon momentum; and the $D^- N'$ pair has momentum $-\vec{p}$, with $\vec{p}$ the momentum of the D^+ meson—to the $D^- N'$ rest frame. This boost is given by

$$\vec{q}_{i,\text{boost}} = -\left[\left(\frac{E_{D^- N'}(p^2)}{m_{\text{inv}}} - 1\right)\frac{\vec{p}\cdot\vec{k}}{p^2} - \frac{E_N(k^2)}{m_{\text{inv}}}\right]\vec{p} - k. \tag{3.52}$$

In this expression, we have

$$E_{D^- N'}(p^2) = \sqrt{m_{\text{inv}}^2 + p^2} \qquad E_N(k^2) = \sqrt{m_N^2 + k^2}, \tag{3.53}$$

with m_{inv} the invariant mass of the $D^- N'$ system. Now we are in position to evaluate the momentum transfer squared, which results in the following expression.

$$t' = (\mathbf{q_i} - \mathbf{q})^2 = 2m_N^2 - 2E_N(q^2_{i,\text{boost}})\sqrt{m_N^2 + p'^2} - 2\vec{q}_{i,\text{boost}} \cdot \vec{p}'. \tag{3.54}$$

With all this considerations, the nuclear cross section is now written as

$$\begin{aligned}\sigma_A = & \frac{m_N^2}{(s - m_N^2)\sqrt{s}} \frac{1}{64\pi^4} \\ & \times \int_{m_{\text{inv}}^{\min}}^{m_{\text{inv}}^{\max}} pp' dm_{\text{inv}} \int_{-1}^{1} d\cos\theta \int_0^{2\pi} d\phi \int_{-1}^{1} d\cos\tilde{\theta}' \int_0^{2\pi} d\tilde{\phi}' \int_{-1}^{+1} d\cos\tilde{\theta} \int dr r^2 \\ & \times \rho(r)|t_0|^2 \exp\left[4.6 \frac{t'}{1\ \text{GeV}^2}\right] \exp\left[\int_{\vec{r}'} \frac{\text{Im}\,\Pi\left(E_{\mathbf{qp}}, p_{\text{lab}}; \rho_0\right) \frac{\rho(r')}{\rho_0}}{p_{\text{lab}}} dl\right].\end{aligned} \tag{3.55}$$

In order to evaluate the seven integrals of this expression, we use a Monte Carlo integration method, selecting again the points for which p_{lab} is smaller than 2 GeV. For the integral in the exponential defining the survival probability of the D^+ meson, we use the Gauss-Legendre quadrature.

Transparency ratio results including the previous improvements

In Fig. 3.9 we present a comparison of the transparency ratio, including the previously discussed improvements to the nuclear density profiles and the production amplitude (green squares), with the original transparency ratio of Fig. 3.7 for $\text{Im}\,\Pi = -0.1$ GeV^2 (red line). For reference, we also include as blue points the results of the transparency ratio obtained when considering only the improved density profiles, and no momentum dependence on the photoproduction amplitude. The green squares have some attached error bands, which indicate the uncertainty coming from the Monte Carlo integration method. These statistics are computed by repeating the evaluation of the integral twenty times, taking for each evaluation a different random seed to initialize the random number generator. Then, the green squares correspond to the mean value of the results obtained for each of the seeds, while the error bands represent their standard deviation. The Monte Carlo integration errors in the original calculation (red curve) and in the variant that accounts only for the density correction (blue circles) are negligible; therefore, we do not include them.

Although minor differences appear between the different cases considered in Fig. 3.9, the overall behavior remains essentially unchanged: for ^{208}Pb the deviation is approximately 5%, and only slightly larger for ^{40}Ca and

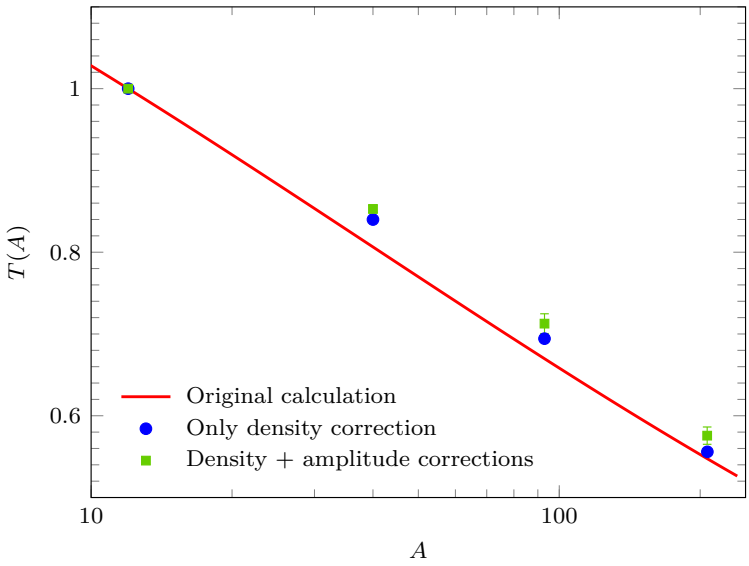

Figure 3.9: *Green squares*: results for the transparency ratio to ^{12}C using realistic densities with Im Π = Im $\Pi(\tilde{\rho}_0)\rho(r)/\tilde{\rho}_0$ and Im $\Pi(\tilde{\rho}_0) = -0.1$ GeV^2, as well as the momentum dependence of the D^+D^- photoproduction amplitude. The error bands in this case indicate the uncertainties of the Monte Carlo integration method. *Blue circles*: results obtained when only the changes in the nuclear density are considered. *Red solid line*: result of Fig. 3.7 for Im $\Pi = -0.1$ GeV^2 with the simplified treatment.

^{93}Nb. Further variations arising from different momentum dependencies of the $\gamma N \to D^+D^-N'$ amplitude should therefore be minimal. This corroborates the conclusion of [274] that the transparency ratio is largely insensitive to the details of the production mechanism. Our tests show that the modest shifts visible in Fig. 3.9 stem mainly from the use of realistic nuclear density profiles, while refinements of the transition amplitude itself play a secondary role.

Regarding experimental feasibility, the GlueX facility at Jefferson Lab can deliver photons with energies up to roughly 12 GeV [291]. Although this exceeds the 11.2 GeV threshold for D^+D^- production, it is insufficient to create slow D^+ mesons with laboratory momenta below 2 GeV; Fig. 3.6 shows that a photon energy close to 21 GeV is required. A possible future upgrade of the JLab electron beam to 22 GeV [292] would open that kinematic window, although with limited statistics. Looking further ahead, future machines will comfortably reach the energies needed for $\gamma A \to A'\, D^+D^-$ and enhance the yield of low-momentum D^+ mesons. The US Electron-Ion Collider (EIC) is expected to achieve electron-proton center-of-mass energies up to 100 GeV [293], while

China's EicC plans electron-nucleus collisions in the $10 \sim 15$ GeV range [294]. To our knowledge, the reaction proposed here offers the first realistic avenue for directly measuring the in-medium width of the D meson.

3.4 Conclusions

We have investigated the feasibility of extracting the in-medium width of the D mesons through nuclear transparency measurements. The process considered is $\gamma A \to D^+ D^- A'$, driven at the nucleon level by $\gamma N \to D^+ D^- N'$, where N denotes a bound nucleon. Once produced, the D^+ is tracked, and the probability that it leaves the nucleus without being absorbed is evaluated. Our integration scheme for the total nuclear cross section is designed so that observables of interest—such as the fraction of D^+ mesons escaping with a given momentum, the emission angles, or the invariant masses of the unobserved D^- and N'—are obtained with ease.

The calculation employs the imaginary part of the D^+ in-medium self-energy from Ref. [215]. Because these self-energy results are available only up to $p \simeq 1$ GeV. whereas the produced mesons carry at least 1.4 GeV, we restrict our sample to D^+ mesons detected with $p_{D^+} < 2$ GeV. By scanning the photon energy, we find that the fraction of mesons in this momentum window peaks for a photon energy in the laboratory frame of $k_{\rm lab} \simeq 50$ GeV. The resulting transparency ratios, normalized to ^{12}C, fall to about 0.6 for heavy nuclei such as ^{208}Pb—a substantial suppression that should be clearly measurable. Suitable photon beams will be available at forthcoming facilities such as the EIC and EicC, or at an upgraded GlueX.

To keep the study transparent, we have adopted several simplifying assumptions. We also outline possible refinements to our calculations that can be adjusted to the relevant photon energies and experimental constraints once a concrete setup is defined. For the present exploratory stage, we have demonstrated both the feasibility of the measurement and the kinematic conditions that can optimize the sensitivity to the theoretically predicted D^+ self-energy.

4

Exotics at finite temperature: study of the T_{cc}

4.1 Introduction

The structure of the T_{cc} has been an object of great interest among the hadronic community. As already discussed, on the one hand, numerous studies support the molecular interpretation of this state [46–64, 295–299], largely motivated by its proximity to the D^0D^{*+} and D^+D^{*0} thresholds. On the other hand, a compact tetraquark configuration has also been proposed, even prior to its experimental observation [65, 66, 300–303]. However, the proximity of the state to the D^0D^{*+} and D^+D^{*0} thresholds strongly suggests that hadronic degrees of freedom must be explicitly considered for a reliable interpretation of experimental data [147, 246, 304].

Given the current interest in the $T_{cc}(3875)^+$, ongoing research aims at identifying the scenarios in which its internal structure and properties can be most clearly revealed. Recent progress includes studies that employ lattice QCD to generate and analyze the nature of the state [61, 305–310], as well as investigations based on femtoscopic correlation functions [149, 150, 311].

Another venue to explore the nature of the $T_{cc}(3875)^+$ is to study its behavior under the extreme density and temperature conditions achieved at facilities such as the RHIC, the LHC, and the future FAIR. In Ref. [156], the production of exotic tetraquarks T_{QQ} ($Q = c, b$) was analyzed in Pb+Pb collisions at the LHC within a quark coalescence framework, yielding production rates an order of magnitude lower than previously estimated. In Ref. [312], the centrality dependence, rapidity distributions, transverse momentum spectra, and elliptic flow of the $T_{cc}(3875)^+$ (and possible isospin partners) were investigated at LHC energies using the *A Multi-Phase Transport* (AMPT) model with coalescence. This study reported a strong enhancement of the T_{cc} yield in Pb+Pb relative to

pp collisions, comparable to $\chi_{c1}(3872)$ in central events, but with a significantly stronger suppression towards peripheral collisions. Furthermore, Ref. [313] employed the coalescence model for Pb+Pb collisions at $\sqrt{s_{NN}} = 5.02$ TeV, concluding that the T_{cc} could be interpreted either as a compact multiquark configuration or as a loosely bound molecular state composed of charmed mesons.

With the aim of exploring the finite-density regime relevant to the CBM experiment at FAIR, in Chapter 2 we investigated the properties of the $T_{cc}(3875)^+$ and $T_{\bar{c}\bar{c}}(3875)^-$, together with their HQSS partners, in nuclear matter. This study highlighted the characteristic density dependence of this particle–antiparticle pair under the assumption of small or large molecular component in these tetraquark-like states. In the present chapter, our focus shifts from density to temperature: we study the behavior of the $T_{cc}(3875)^+$ and its HQSS partner, the $T_{cc}(4016)^{*+}$, in the hot environment produced in heavy-ion collisions at RHIC and the LHC. In what follows, we shall adopt the molecular perspective as a working hypothesis, while keeping in mind the possible interplay with compact tetraquark components. However, we shall not consider direct temperature effects on these tetraquark components.

The production of loosely bound hadronic molecules in a hot plasma is, at first sight, counterintuitive. Since the plasma temperature can greatly exceed the binding energy of such states, one would naturally expect them to dissociate almost instantaneously through scattering with other particles. Nevertheless, experiments demonstrate that these molecular states are indeed produced in heavy-ion collision (HIC) experiments and appear to emerge from a hadron gas whose temperature is orders of magnitude larger than their binding energy [314]. Moreover, thermodynamical analyses, such as the study in Ref. [315], indicate that the production yield of these states remains nonzero even in the limit where their binding energy tends to zero.

In this chapter, we investigate hadrons at finite temperature, with emphasis on the exotic $T_{cc}(3875)^+$ and its HQSS partner, $T^*_{cc}(4016)$. Sect. 4.2 introduces the imaginary-time formalism (ITF), which provides the statistical basis for thermal field theory. Sect. 4.3 addresses two-meson scattering in a hot medium, presenting the finite-temperature loop function together with the D and D^* spectral functions of Refs. [211, 316]. Finally, Sect. 4.4 applies this formalism to analyze the spectral properties of $T_{cc}(3875)^+$ and $T^*_{cc}(4016)^+$ in a hot pion bath, while Sect. 4.5 summarizes the main conclusions.

4.2 Thermal Systems in Imaginary Time

Standard Quantum Field Theory is typically formulated at zero temperature, an approximation that is adequate in many contexts, such as nuclear systems,

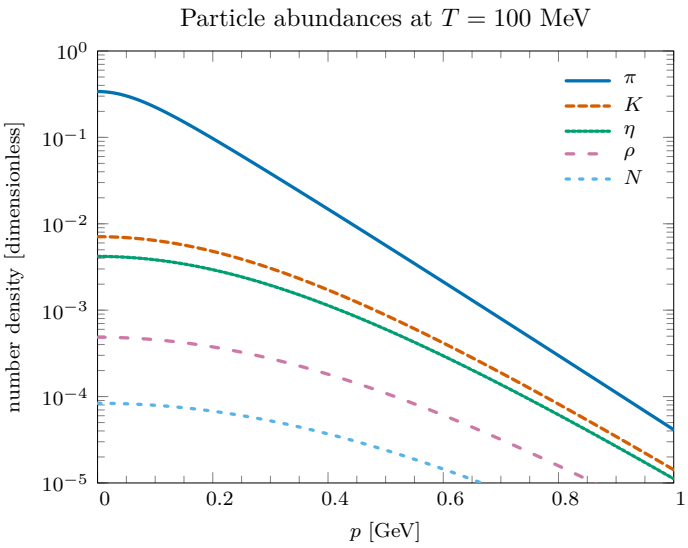

Figure 4.1: Number density of several hadrons in a hot medium at $T = 150$ MeV, as a function of the modulus of their three-momentum p.

where the characteristic energy scales far exceed ordinary thermal energies. There are, however, situations in which temperature effects play a central role. Two paradigmatic examples are cosmology, which probes the extremely hot conditions of the early universe, and the hot quark-gluon plasma produced in HICs. In such cases, a modified theoretical framework is required: *Thermal Quantum Field Theory* (often abbreviated as *Thermal Field Theory*) or *Finite-Temperature Field Theory*.

The idea of connecting temperature with microscopic motion predates kinetic theory itself. Philosophers such as Francis Bacon [317] speculated on this relation, which was later formalized within the kinetic theory of gases. Maxwell's derivation of the velocity distribution [318] provided the first rigorous statistical link between temperature and kinetic energy, a concept that remains central today: temperature characterizes the statistical distribution of particles over accessible energy states. This statistical foundation extends naturally to quantum systems, where fermions (half-integer spin) obey the Fermi–Dirac distribution and bosons (integer spin) follow the Bose–Einstein distribution. Figure 4.1 illustrates these distributions for several hadronic species in a medium at $T = 150$ MeV, showing how the number density of heavier particles is increasingly suppressed.

In this section we present the basic concepts of thermal field theory, with particular emphasis on the *Imaginary-Time Formalism* (ITF). Pioneered by Matsubara [133], the ITF provides the foundation of equilibrium thermal field

theory. Its main advantage lies in its close similarity to zero-temperature QFT: standard perturbative and diagrammatic techniques can be applied with only minor modifications. The essential difference is that time is analytically continued to imaginary values and compactified to the finite interval $[0, \beta]$, with $\beta = 1/k_B T$ (k_B being the Boltzmann constant and T the temperature). In the energy domain this compactification leads to a discrete set of frequencies, the so-called *Matsubara frequencies*. The main features of the ITF will be discussed in detail in the following sections.

Shortly after the development of Matsubara's approach, Kubo [319] and Martin and Schwinger [320] formulated the Kubo–Martin–Schwinger (KMS) condition, which expresses a fundamental relation between thermal propagators in equilibrium. Further advances were made by Keldysh [321], who introduced a complementary real-time formalism. Together, these developments established the modern framework of thermal field theory.

The discussion in this chapter draws primarily on Chap. 14 of Mattuck's textbook [213], which focuses on fermionic systems. We begin by reviewing the statistical foundations of temperature and particle distributions, and then proceed to introduce the Imaginary-Time Formalism and its main features.

4.2.1 From $T = 0$ to finite temperature

Consider a system composed of many interacting particles. We denote by $|\Psi_i\rangle$, with $i = 0, 1, 2, \ldots$, the energy eigenstates of the corresponding Hamiltonian. At $T = 0$, the system occupies its lowest-energy state, namely the many-body *vacuum* in occupation-number formalism, $|\Psi_0\rangle$. For finite temperature ($T > 0$), however, the system is no longer restricted to the ground state but instead has a finite probability of being found in excited states.[1] The probability of finding the system in the excited state $|\Psi_i\rangle$ is given by

$$\mathcal{P}_i = \frac{e^{-\beta(E_i - \mu N_i)}}{\sum_n e^{-\beta(E_n - \mu N_n)}} = \frac{\rho_i}{Z}, \tag{4.1}$$

where E_i is the energy of the state $|\Psi_i\rangle$, N_i is its particle number, and μ is the chemical potential, defined as the energy required to remove a particle from the system. The denominator of Eq. (4.1), Z, is the "grand partition function"; and the numerator, ρ_i, is the "grand distribution function". We work in the *grand canonical ensemble* since, in the occupation number formalism, the number of particles N of the system is not fixed. It is useful to define the distribution operator—often referred to as the *density matrix*—as

$$\hat{\rho} = e^{-\beta(\hat{H} - \mu \hat{N})}, \tag{4.2}$$

[1] A similar situation arises when external potentials are applied.

where $\hat{H}$ is the Hamiltonian of the system, and $\hat{N}$ is the number operator. In terms of the distribution operator, we can write the probabilities of Eq. (4.1) as

$$\mathcal{P}_i = \frac{\langle \Psi_i | \hat{\rho} | \Psi_i \rangle}{\sum_n \langle \Psi_n | \hat{\rho} | \Psi_n \rangle} = \frac{\rho_i}{\operatorname{tr} \hat{\rho}}, \tag{4.3}$$

where tr represents the *trace* of an operator.

The thermal expectation value of some $\hat{O}$ operator is then obtained as

$$\langle \hat{O} \rangle = \frac{\operatorname{tr}\left(\hat{O}\hat{\rho}\right)}{\operatorname{tr} \hat{\rho}} = \sum_n \mathcal{P}_n \langle \Psi_n | \hat{O} | \Psi_n \rangle , \tag{4.4}$$

which corresponds to a weighted average of the expectation value of the operator over all possible energy eigenstates of the system. For convenience, we shall adopt the shorthand notation $\langle \hat{O} \rangle$ to denote such thermal expectation values.[2]

Note that the trace in Eqs. (4.3) and (4.4) uses the exact interacting many-body system state vectors $\{|\Psi_i\rangle\}$. These states are typically difficult to determine. Nevertheless, since the trace is basis independent, one can instead choose the more accessible eigenstates of the non-interacting many-body system, which we name $\{|\Phi_i\rangle\}$. On this basis, Eq. (4.4) reads

$$\langle \hat{O} \rangle = \frac{\sum_{n,m} \langle \Phi_n | \hat{O} | \Phi_m \rangle \langle \Phi_m | \hat{\rho} | \Phi_n \rangle}{\sum_n \langle \Phi_n | \hat{\rho} | \Phi_n \rangle}. \tag{4.5}$$

In the next section, we shall present how the single-particle propagator—one of the main building blocks of perturbation theory—changes when considering the thermal effects. In what follows, we will drop the hat ($\hat{}$) symbols off operators to make the notation lighter.

4.2.2 The finite-temperature propagator for a non-interacting particle in imaginary time formalism

At zero temperature, the Feynman propagator for a fermion is defined as

$$G(k, t_2 - t_1; T = 0) = -i \langle \Psi_0 | T\{c_k(t_2) c_k^\dagger(t_1)\} | \Psi_0 \rangle \tag{4.6}$$

where $T\{\}$ is Wick's time-order operator.[3]

[2] An alternative convention defines the *normalized* density operator as $\hat{\rho} = e^{-\beta(\hat{H} - \mu\hat{N})}/Z$, which satisfies $\operatorname{tr} \hat{\rho} = 1$. In that case, probabilities are written as $\mathcal{P}_i = \langle \Psi_i | \hat{\rho} | \Psi_i \rangle$, and expectation values take the simpler form $\langle \hat{O} \rangle = \operatorname{tr}(\hat{O}\hat{\rho})$. Both conventions are equivalent, but we shall adopt in this chapter the unnormalized one as done in [213].

[3] For fermions, the time-ordering operator introduces a factor (-1) each time two operators are permuted. For bosons, no such factor appears.

To generalize this expression to finite temperature, the ground-state expectation value must be replaced by a thermal average over all energy states, weighted by their corresponding probabilities, as discussed in Sect. 4.2.1. This leads to

$$G(k, t_2 - t_1; T) = -i\langle T\{c_k(t_2)c_k^\dagger(t_1)\}\rangle = -i\frac{\text{tr}\left[T\{c_k(t_2)c_k^\dagger(t_1)\}\rho\right]}{\text{tr}\,\rho}. \tag{4.7}$$

However, this form is not suitable for diagrammatic perturbation theory. Thus, it is customary to introduce a modified propagator[4]

$$\mathcal{G}(k, \tau_2 - \tau_1) = -\langle T\{c_k(\tau_2)c_k^\dagger(\tau_1)\}\rangle \tag{4.8}$$

where the creation and annihilation operators evolve according to[5]

$$O(\tau) = e^{(H-\mu N)\tau} O e^{-(H-\mu N)\tau} \tag{4.9}$$

with O representing any operator, and

$$0 < \tau_1,\, \tau_2 < \beta, \quad \tau \text{ real.} \tag{4.10}$$

As we shall justify in the following, it is possible to expand diagrammatically the modified propagator $\mathcal{G}$ presented Eq. (4.8). Notice that $\mathcal{G}$ can be obtained from the temperature-dependent G function by making the following replacements:

$$\begin{aligned} H &\to H - \mu N \\ it &\to \tau \end{aligned} \tag{4.11}$$

so that since τ is real, t will be imaginary. In this sense, $\mathcal{G}$ is known as the *imaginary time propagator*—and this framework is known as *Imaginary Time Formalism* (ITF).

Two remarks are worth noting here. First, the time-ordering operator in Eq. (4.8) orders the operators such that τ decreases from left to right. Second, the analytic continuation that relates $\mathcal{G}$ to the thermal propagator G corresponds to a Wick rotation, as represented in Fig. 4.2. This continuation allows one to extract physical information from calculations carried out in imaginary time.

Let us now briefly comment on why the function $\mathcal{G}$ can be expanded as a series of diagrams, in close analogy with the vacuum propagator. The key point is that the distribution operator satisfies the relation

$$\frac{\partial \rho}{\partial \beta} = -(H - \mu N)\rho \qquad \text{(Bloch's equation)}. \tag{4.12}$$

[4] In this definition an overall factor of i is omitted, following the conventions of Refs. [212, 213]. We also suppress the explicit temperature label for notational simplicity.

[5] As is common in scattering theory, we work in the interaction picture, so that operators evolve with the free Hamiltonian.

This follows directly by differentiating the definition of ρ given in Eq. (4.2). Equation (4.12) closely resembles the time-dependent Schrödinger equation, which is precisely the equation solved by the zero-temperature propagator,[6]

$$i\frac{\partial\psi}{\partial t} = H\psi \qquad \text{(Schrödinger's equation)}. \tag{4.13}$$

The correspondence between these two equations is clear. This suggests that by performing the replacements $H \to H - \mu N$ and $t \to -i\tau$ everywhere, it is possible to build a finite-temperature perturbation theory based on the Bloch equation in a similar way to the zero-temperature perturbation theory, which is based on the Schrödinger equation. In particular, if the replacements are made in the zero-temperature propagator G, the resulting $\mathcal{G}$ can be expanded in a series of diagrams which are very similar to the zero-temperature series. One can also construct a new set of Feynman rules for these diagrams, which are found for the fermionic case in Table 14.1 of Mattuck's book [213].[7]

We shall now discuss some properties of the $\mathcal{G}$ function. Firstly, the variables τ_1, τ_2 are restricted to the interval $(0, \beta)$, so that their difference $\tau = \tau_2 - \tau_1$ is restricted to $-\beta < \tau < \beta$. This restriction is needed because $\mathcal{G}$ is only guaranteed to converge in that interval. To illustrate this, we first consider the $\tau > 0$ case and introduce the shifted Hamiltonian $\tilde{H} = H - \mu N$. Starting from the definition of the imaginary time propagator, we write

$$\begin{aligned}
\mathcal{G}(k,\tau) &= -\frac{1}{Z}\mathrm{tr}\,\rho c_k(\tau)c_K^\dagger(0) = -\frac{1}{Z}\sum_i \langle\Psi_i|e^{-\beta\tilde{H}}e^{+\tau\tilde{H}}c_k e^{-\tau\tilde{H}}c_k^\dagger|\Psi_i\rangle \\
&= -\frac{1}{Z}\sum_{i,j}\langle\Psi_i|e^{-\beta\tilde{H}}e^{+\tau\tilde{H}}c_k e^{-\tau\tilde{H}}|\Psi_j\rangle\langle\Psi_j|c_k^\dagger|\Psi_i\rangle \\
&= -\frac{1}{Z}\sum_{i,j} e^{(-\beta+\tau)\tilde{E}_i}e^{-\tau\tilde{E}_j}\langle\Psi_i|c_k|\Psi_j\rangle\langle\Psi_j|c_k^\dagger|\Psi_i\rangle,
\end{aligned} \tag{4.14}$$

where we have inserted a complete set of eigenstates $\{|\Psi_i\rangle\}$ of $\tilde{H}$, and we have denoted $\tilde{E}_i \equiv E_i - \mu N_i$. Now, since the values for $\tilde{E}_{i,j}$ can be arbitrarily large, we can guarantee that the sum is finite if the exponents are negative, so we have conditions $-\beta + \tau < 0$ and $-\tau < 0$ that yield $0 < \tau < \beta$. One can make a similar argument for the $\tau < 0$ case, which yields the conditions $-\beta - \tau < 0$ and $\tau < 0$, thus $-\beta < \tau < 0$. Taking everything into account, we have $\tau \in (-\beta, \beta)$, which is the result introduced previously.

An additional property of the (fermion) boson imaginary time propagator is that it obeys (quasi-)periodic boundary conditions on the interval $(-\beta, \beta)$:

$$\textbf{Fermions}: \qquad \mathcal{G}^F(k,\tau) = -\mathcal{G}^F(k,\tau+\beta) \qquad \text{for} \qquad -\beta < \tau < 0, \tag{4.15}$$

[6] In this section we are working in the non-relativistic quantum mechanics framework.

[7] Note that we have not used the Fermi-Dirac statistics to define the imaginary time propagator $\mathcal{G}$, so that this definition should be valid for both fermions and bosons.

$$\textbf{Bosons}: \quad \mathcal{G}^B(k,\tau) = +\mathcal{G}^B(k,\tau+\beta) \qquad \text{for} \qquad -\beta < \tau < 0. \tag{4.16}$$

We can easily prove this using $\mathrm{tr}\, AB = \mathrm{tr}\, BA$. For the fermion imaginary time propagator (we have $\tau < 0$),

$$\begin{aligned}\mathcal{G}^F(k,\tau) &= -\frac{1}{Z}\mathrm{tr}\, e^{-\beta\tilde{H}} T\{c_k(\tau)c_k^\dagger(0)\} = \frac{1}{Z}\mathrm{tr}\, e^{-\beta\tilde{H}} c_k^\dagger(0)c_k(\tau) \\ &= \frac{1}{Z}\mathrm{tr}\, c_k(\tau)e^{-\beta\tilde{H}}c_k^\dagger(0) = \frac{1}{Z}\mathrm{tr}\, e^{-\beta\tilde{H}}e^{+\beta\tilde{H}}c_k(\tau)e^{-\beta\tilde{H}}c_k^\dagger(0) \\ &= \frac{1}{Z}\mathrm{tr}\, e^{-\beta\tilde{H}}c_k(\tau+\beta)c_k^\dagger(0) = -\mathcal{G}^F(k,\tau+\beta). \end{aligned} \tag{4.17}$$

For bosons, given that the time-ordering operator does not change the sign of the product, we have

$$\begin{aligned}\mathcal{G}^B(k,\tau) &= -\frac{1}{Z}\mathrm{tr}\, e^{-\beta\tilde{H}} T\{a_k(\tau)a_k^\dagger(0)\} = -\frac{1}{Z}\mathrm{tr}\, e^{-\beta\tilde{H}} a_k^\dagger(0)a_k(\tau) \\ &= -\frac{1}{Z}\mathrm{tr}\, a_k(\tau)e^{-\beta\tilde{H}}a_k^\dagger(0) = -\frac{1}{Z}\mathrm{tr}\, e^{-\beta\tilde{H}}e^{+\beta\tilde{H}}a_k(\tau)e^{-\beta\tilde{H}}a_k^\dagger(0) \\ &= -\frac{1}{Z}\mathrm{tr}\, e^{-\beta\tilde{H}}a_k(\tau+\beta)a_k^\dagger(0) = \mathcal{G}^B(k,\tau+\beta). \end{aligned} \tag{4.18}$$

Since τ is restricted to the finite interval $(-\beta,\beta)$, the propagator does not admit a Fourier integral decomposition as in the zero-temperature case. Instead, it is taken to be periodic in imaginary time, repeating itself in intervals of 2β from $-\infty$ to $+\infty$. As a consequence, the propagator can be expressed as a Fourier series with discrete frequencies associated with the variable τ.

$$\mathcal{G}(k,\tau) = \frac{1}{\beta}\sum_{n=-\infty}^{+\infty} \mathcal{G}(k,\omega_n)e^{-i\omega_n\tau}, \tag{4.19}$$

$$\mathcal{G}(k,\omega_n) = \frac{1}{2}\int_{-\beta}^{+\beta} d\tau\, \mathcal{G}(k,\tau)e^{i\omega_n\tau}, \tag{4.20}$$

$$\omega_n = \frac{n\pi}{\beta}. \tag{4.21}$$

The ω_n discrete frequencies are known as *Matsubara frequencies*.

Given the (quasi-)periodic conditions for the fermion and boson imaginary-time propagators that were presented in Eqs. (4.15), (4.16), we find that for fermions only odd frequencies are realized (the Fourier coefficients $\mathcal{G}(k,\omega_n)$ for the even frequencies are zero), while for bosons only even frequencies appear.

$$\begin{aligned}\textbf{Fermions}: \quad \omega_n^F &= \frac{(2n+1)\pi}{\beta} \\ \textbf{Bosons}: \quad \omega_n^B &= \frac{(2n)\pi}{\beta} \end{aligned} \qquad n = 0, \pm1, \pm2, \ldots \tag{4.22}$$

We can see this using Eq. (4.20)

$$\begin{aligned}\mathcal{G}(k,\omega_n) &= \frac{1}{2}\int_{-\beta}^{+\beta} d\tau\ \mathcal{G}(k,\tau)e^{i\omega_n\tau} \\ &= \frac{1}{2}\int_{-\beta}^{0} d\tau\ \mathcal{G}(k,\tau)e^{i\omega_n\tau} + \frac{1}{2}\int_{0}^{+\beta} d\tau\ \mathcal{G}(k,\tau)e^{i\omega_n\tau} \\ &= \frac{1}{2}\int_{-\beta}^{0} d\tau\ \left[\pm\mathcal{G}(k,\tau+\beta)\right] e^{i\omega_n\tau} + \frac{1}{2}\int_{0}^{+\beta} d\tau\ \mathcal{G}(k,\tau)e^{i\omega_n\tau} \\ &= \frac{1}{2}\int_{0}^{\beta} d\tau'\ \left[\pm\mathcal{G}(k,\tau')\right] e^{i\omega_n(\tau'-\beta)} + \frac{1}{2}\int_{0}^{+\beta} d\tau\ \mathcal{G}(k,\tau)e^{i\omega_n\tau} \end{aligned} \tag{4.23}$$

Using the general formula for ω_n we have

$$\omega_n(\tau-\beta) = \frac{n\pi}{\beta}(\tau-\beta) = \omega_n\tau - n\pi \tag{4.24}$$

thus,

$$\begin{aligned}&\frac{1}{2}\int_{0}^{\beta} d\tau\ \left[\pm\mathcal{G}(k,\tau)\right] e^{i\omega_n(\tau-\beta)} + \frac{1}{2}\int_{0}^{+\beta} d\tau\ \mathcal{G}(k,\tau)e^{i\omega_n\tau} \\ &\quad= \frac{1}{2}\int_{0}^{\beta} d\tau\ \left[\pm\mathcal{G}(k,\tau)\right] e^{i\omega_n\tau}e^{-in\pi} + \frac{1}{2}\int_{0}^{+\beta} d\tau\ \mathcal{G}(k,\tau)e^{i\omega_n\tau} \\ &\quad= \frac{1}{2}\int_{0}^{\beta} d\tau\ (-1)^n\left[\pm\mathcal{G}(k,\tau)\right] e^{i\omega_n\tau} + \frac{1}{2}\int_{0}^{+\beta} d\tau\ \mathcal{G}(k,\tau)e^{i\omega_n\tau} \\ &\quad= 0 \text{ if } \begin{cases} n \text{ odd, boson.} \\ n \text{ even, fermion.} \end{cases}\end{aligned} \tag{4.25}$$

From this, Eq. (4.22) follows immediately.

Moreover, once the particle statistics (fermionic or bosonic) are specified—and thus the corresponding Matsubara frequencies are fixed—the (quasi-)periodic boundary conditions allow the imaginary-time domain to be restricted to the interval $(0,\beta)$, as illustrated in Fig. 4.2. No additional physical information is contained in any other imaginary-time interval.

We shall now take a look at the explicit form of the imaginary time propagator for finite-temperature fermion and boson systems. In the fermion case, writing explicitly the time-ordering operator in terms of the Heavyside step function θ, we have

$$\mathcal{G}^F(k,\tau) = -\frac{1}{Z}\sum_i \langle\Phi_i|e^{-\beta\tilde{H}}\left[\theta(\tau)\ c_k(\tau)c_k^\dagger(0) - \theta(-\tau)\ c_k^\dagger(0)c_k(\tau)\right]|\Phi_i\rangle$$

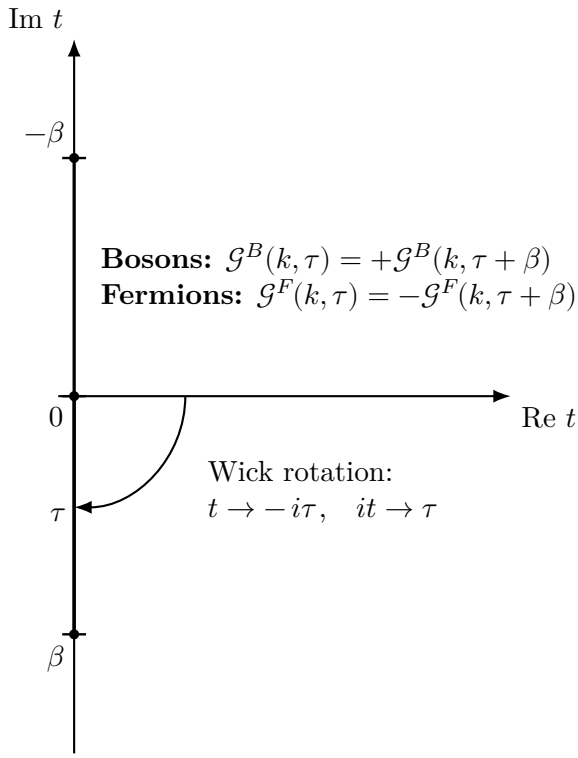

Figure 4.2: Wick rotation from real time t to imaginary time $\tau = it$. In the imaginary-time formalism, the time direction is compactified to $\tau \in [0, \beta]$ with periodic (bosons) or antiperiodic (fermions) boundary conditions.

$$= -\frac{1}{Z}\sum_i \langle\Phi_i|e^{-\beta\tilde{H}}\left[\theta(\tau)\ e^{\tau\tilde{H}}c_k e^{-\tau\tilde{H}}c_k^\dagger - \theta(-\tau)\ c_k^\dagger e^{\tau\tilde{H}}c_k e^{-\tau\tilde{H}}\right]|\Phi_i\rangle. \quad (4.26)$$

Given that

$$e^{\tau\tilde{H}}c_k e^{-\tau\tilde{H}}|\Phi_i\rangle = e^{-\tau(\epsilon_k-\mu)}c_k|\Phi_i\rangle, \quad (4.27)$$

we find

$$\begin{aligned}\mathcal{G}^F(k,\tau) = -\frac{1}{Z}\sum_i (\rho_0)_i \Big[&\theta(\tau)\ e^{-\tau(\epsilon_k-\mu)}\langle\Phi_i|c_k c_k^\dagger|\Phi_i\rangle \\ &- \theta(-\tau)\ e^{-\tau(\epsilon_k-\mu)}\langle\Phi_i|c_k^\dagger c_k|\Phi_i\rangle\Big] \\ = -\Big[&\theta(\tau)\ e^{-\tau(\epsilon_k-\mu)}\langle c_k c_k^\dagger\rangle - \theta(-\tau)\ e^{-\tau(\epsilon_k-\mu)}\langle c_k^\dagger c_k\rangle\Big]. \quad (4.28)\end{aligned}$$

Now, in this previous expression, the following thermal expectation values have appeared.

$$\langle c_k c_k^\dagger\rangle = \langle 1 - N_k\rangle \equiv f_k^+, \qquad \langle c_k^\dagger c_k\rangle = \langle N_k\rangle \equiv f_k^-. \quad (4.29)$$

These correspond to the number density of particles and holes at finite temperature, which are described by the Fermi-Dirac distribution in the case of fermions.[8]

$$f_k^+ = \frac{1}{e^{-\beta(\epsilon_k-\mu)}+1}, \tag{4.30a}$$

$$f_k^- = \frac{1}{e^{\beta(\epsilon_k-\mu)}+1}. \tag{4.30b}$$

With these distributions, the imaginary time fermion propagator is written as

$$\mathcal{G}^F(k,\tau) = -\left[\theta(\tau)f_k^+ - \theta(-\tau)f_k^-\right] e^{-\tau(\epsilon_k-\mu)}. \tag{4.31}$$

Even though in order to operate with this quantity it is convenient to work with imaginary time, we shall perform a Wick rotation and come back to the standard thermal propagator (defined for real values of the time and energy variables) for some paragraphs in order to better interpret it. This results in the following expression:

$$G^F(k,t;T) = -i\left[\theta(t)f_k^+ - \theta(-t)f_k^-\right] e^{-it(\epsilon_k-\mu)}. \tag{4.32}$$

This propagator can also be cast in the energy-momentum space as[9]

$$G^F(k,\epsilon;T) = \frac{f_k^+}{\epsilon-(\epsilon_k-\mu)+i\varepsilon} + \frac{f_k^-}{\epsilon-(\epsilon_k-\mu)-i\varepsilon}. \tag{4.33}$$

The particle part of this propagator—the part with positive time t in Eq. (4.32)—is multiplied by the f_k^+ distribution, while the hole part—with negative time t in Eq. (4.32)—is multiplied by the f_k^- distribution. It is in this sense that f_k^+ describes the particle distribution, while f_k^- describes the hole distribution.

It is interesting to compare the result in Eq. (4.31) with the zero-temperature propagator, given by the following expressions.[10]

$$G^F(k,t,T=0) = -i\left[\theta(t)\theta(\epsilon_k-\epsilon_F) - \theta(-t)\theta(\epsilon_F-\epsilon_k)\right] e^{-i\epsilon_k t}, \tag{4.34}$$

[8]The Fermi–Dirac and Bose–Einstein distributions follow directly from evaluating the thermal averages of creation and annihilation operators in occupation number formalism, using their respective (anti)commutation relations. A detailed derivation can be found in Sect. 14.2 of Ref. [213].

[9]In this expression, we have included the standard positive infinitesimal ε, not to be confused with the energy variable ϵ.

[10]One may also compare the zero-temperature propagator of Eq. (4.34) to that of the nucleon propagator in a dense medium of Eq. (2.10), presented in Sect. 2.2.1. The differences between the nucleon propagator of Eq. (2.10) and the fermion propagator of Eq. (4.34) are only due to the relativistic nature of Eq. (2.10).

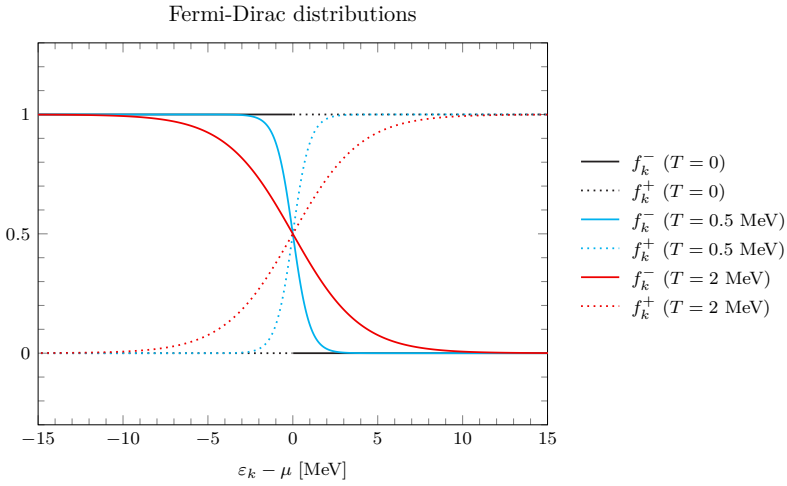

Figure 4.3: Fermi-Dirac distributions for holes (f^-) and particles (f^+) considering different temperatures.

$$G^F(k, \epsilon, T = 0) = \frac{\theta(\epsilon_k - \epsilon_F)}{\epsilon - \epsilon_k + i\varepsilon} + \frac{\theta(\epsilon_F - \epsilon_k)}{\epsilon - \epsilon_k - i\varepsilon}. \tag{4.35}$$

When comparing the finite-temperature with the zero-temperature propagators, we see that aside from the shift in energy by μ, the essential effect of the temperature is to smooth the θ step functions into the f_k^+ and f_k^- Fermi distributions, respectively. This makes it so that, at finite temperature, a particle can propagate with an energy below the Fermi energy, and a hole can propagate with an energy above the Fermi energy. This is not possible in the zero-temperature case, due to the presence of the sharp step functions. The softening of the particle and hole step functions can be observed in Fig. 4.3.

For a bosonic system, the computation is analogous—except for some sign differences—and we can steadily arrive to the following expression for the finite-temperature imaginary time boson propagator:

$$\mathcal{G}^B(k, \tau) = -\left[\theta(\tau) b_k^+ + \theta(-\tau) b_k^-\right] e^{-\tau(\epsilon_k - \mu)}. \tag{4.36}$$

Here, the b_k^+ and b_k^- appear, defined as

$$b_k^+ = -\frac{1}{e^{-\beta(\epsilon_k - \mu)} - 1}, \tag{4.37a}$$

$$b_k^- = \frac{1}{e^{\beta(\epsilon_k - \mu)} - 1}. \tag{4.37b}$$

These are the particle and hole Bose-Einstein distributions. The imaginary-time propagator of Eq. (4.36) translates into the following thermal propagator:

$$G^B(k, t, T) = -i\left[\theta(t) b_k^+ + \theta(-t) b_k^-\right] e^{-i(\epsilon_k - \mu)t}, \tag{4.38}$$

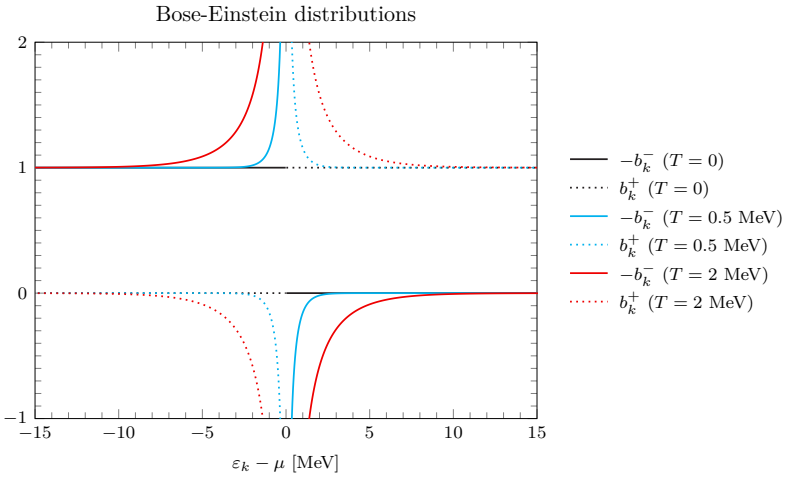

Figure 4.4: Bose-Einstein distributions for holes (b^-) and particles (b^+) considering different temperatures.

$$G^B(k, \epsilon, T) = \frac{b_k^+}{\epsilon - \epsilon_k + i\varepsilon} - \frac{b_k^-}{\epsilon - \epsilon_k - i\varepsilon}. \tag{4.39}$$

This propagator again mainly differs from the corresponding zero-temperature boson propagator—which, since we are working in the non-relativistic quantum mechanics framework, is identical to the fermion one presented in Eq. (4.34)—in the different distributions b_k^+ and b_k^-. We compare different temperature scenarios for the Bose distribution in Fig. 4.4

Some remarks on the interpretation of fermion and boson particle/hole distributions are in order. At first sight, the functions f_k^- and b_k^- appear to represent the number densities of particles populating the many-body ground state at finite temperature. However, in the literature (cf. Ref. [213]), these functions are more naturally regarded as *hole* distributions: they indicate the regions in momentum space where holes can be created and propagate. Conversely, f_k^+ and b_k^+ are interpreted as *particle* distributions, specifying where additional particles may propagate. This viewpoint becomes evident upon inspection of the propagators in Eqs. (4.40) and (4.41), and it is consistent with the general particle–hole picture in many-body physics, where the already occupied momentum states are treated implicitly.

In the case of nuclear matter at zero temperature (see Sect. 2.2.1), the distinction between particles and holes was tied to the Fermi momentum: creation and annihilation operators were defined according to whether they acted on states above or below the Fermi surface. This simple separation, however, breaks down at finite temperature, since the sharp Fermi surface

disappears. In this regime, one can create a hole (i.e., annihilate a particle) even in states above the Fermi energy, or create a particle (i.e., annihilate a hole) in states below it. As a result, both particles and holes may coexist in the same momentum state. This behavior is illustrated Figs. 4.3 and 4.4.

In the following subsections, we shall consider an interacting theory, so that the propagators will be modified by these interactions. Although the thermal propagators that have been shown are the ones with physical meaning, they are not fit for perturbation theory, as was discussed in the first paragraphs of this section. Then, we return to the imaginary-time propagators, and compute their explicit form in the (k, ω_n)−space, which will be of great utility in the following computations.

We start by considering the Fourier transform of the fermion propagator of Eq. (4.23). As was shown in Eq. (4.25), only odd frequencies give a nonzero result. Also, as discussed before, due to the quasi-periodic conditions one can easily take the integration from the $(-\beta, \beta)$ interval to the $(0, \beta)$ interval. Taking this into account, we can write

$$\begin{aligned}\mathcal{G}^F(k,\omega_n^F) &= \int_0^\beta d\tau\, \mathcal{G}^F(k,\tau)\, e^{i\omega_n^F\tau} \\ &= -\int_0^\beta d\tau\, f_k^+\, e^{(i\omega_n^F-\epsilon_k+\mu)\tau} \\ &= -\frac{1}{e^{-\beta(\epsilon_k-\mu)}+1}\,\frac{e^{(i\omega_n^F-\epsilon_k+\mu)\tau}}{i\omega_n^F-\epsilon_k+\mu}\Bigg|_{\tau=0}^{\tau=\beta} = \frac{1}{i\omega_n^F-\epsilon_k+\mu}.\end{aligned} \tag{4.40}$$

We find a very simple result, extremely similar to the vacuum propagator in energy-momentum space, but replacing the energy variable by the imaginary and discrete fermionic Matsubara frequencies $i\omega_n^F$. We can perform a similar calculation for the boson case, obtaining

$$\mathcal{G}^B(k,\omega_n^B) = \frac{1}{i\omega_n^B-\epsilon_k+\mu}. \tag{4.41}$$

Notice how this simple expression is equivalent to that of the fermion propagator, the only difference being the bosonic Matsubara frequencies.

In this section we have analyzed in detail the propagators of bosons and fermions at finite temperature within the imaginary-time formalism (ITF). These propagators, particularly in energy–momentum space, provide the basic building blocks for the developments of the following sections, and will serve as our starting point.

We make two additional remarks. First, the expressions for the thermal propagators given in Eqs. (4.40) and (4.41) were derived in the context of the non-relativistic Schrödinger equation. In what follows, however, we shall mainly

deal with relativistic bosons (such as pions) described by the Klein–Gordon equation. The generalization to this case is straightforward: the ITF propagators differ from their zero-temperature counterparts only in that the continuous energy variable is replaced by discrete Matsubara frequencies (multiplied by the imaginary unit). This replacement remains valid in relativistic quantum mechanics, and thus the relativistic propagators in ITF are obtained in complete analogy.

Second, the discreteness of the Matsubara frequencies, cf. Eq. (4.22), modifies the structure of the Feynman rules at finite temperature. In particular, the energy integral associated with each internal line becomes an infinite sum over Matsubara frequencies.

$$\int \frac{d^4k}{(2\pi)^4} \longrightarrow \frac{1}{\beta}\sum_n \int \frac{d^3k}{(2\pi)^3}. \tag{4.42}$$

In the following subsection, we discuss the standard techniques employed to evaluate these sums, which will play a central role in the calculation of meson self-energies and two-meson loop functions.

4.2.3 The Matsubara frequency summation

The Matsubara frequency summation is the sum over the Matsubara frequencies that appears when evaluating diagrams with internal loops in thermal field theory within the ITF. These sums are typically of the form

$$\frac{1}{\beta}\sum_n F(i\omega_n) \tag{4.43}$$

with F some analytic function and ω_n the Matsubara frequencies. We show here how to perform this sum.

The first step consists in analytically continuing $F(\omega)$ to the entire complex ω-plane. This can be conveniently achieved by using the Källén-Lehmann spectral representation, which is a special case of dispersion relations applied to two-point functions. The key idea is then to apply *Poisson's formula*, which allows one to relate the discrete sum to a contour integral.[11]

$$\frac{1}{\beta}\sum_n F(i\omega_n) = \frac{1}{2\pi i}\oint_C d\omega F(\omega)g(\omega). \tag{4.44}$$

In this expression, we have introduced the auxiliary function $g(\omega)$, which is chosen to present poles on the imaginary ω axis at the Matsubara frequencies

[11] Poisson's summation formula, derived from Cauchy's residue theorem, is valid provided that the function F is analytic on the imaginary axis.

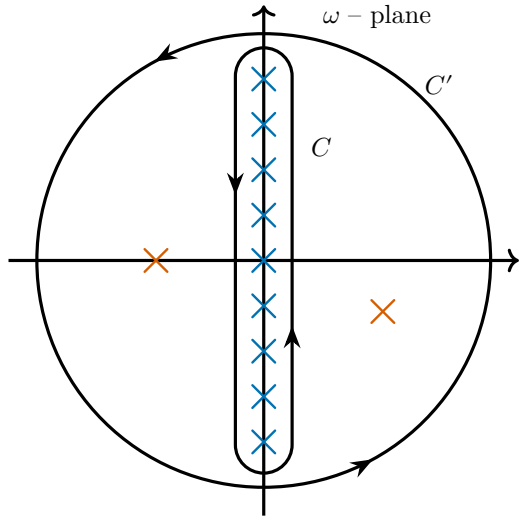

Figure 4.5: Contours used for a finite-temperature calculation. Blue crosses represent the poles presented by the auxiliary function $g(\omega)$ at the Matsubara frequencies. Orange crosses represent other singularities that arise from $F(\omega)$.

that we are considering, either fermionic or bosonic,

$$\textbf{fermion:} \qquad g^F(\omega) = -\frac{1}{e^{\beta\omega}+1} = -f^-(\omega), \tag{4.45}$$

$$\textbf{boson:} \qquad g^B(\omega) = \frac{1}{e^{\beta\omega}-1} = b^-(\omega). \tag{4.46}$$

and the contour C surrounds the imaginary axis. In Fig. 4.5, we represent this situation, showing the poles of the $g(\omega)$ function—that is, the Matsubara frequencies—as blue crosses ($\times$), as well as the contour C around the imaginary axis. It can be steadily checked using Cauchy's residue theorem that with these auxiliary functions, Eq. (4.44) is fulfilled. Also note that the expressions of the auxiliary functions $g(\omega)$ coincide (except for a global sign in the fermion case) with the Fermi or Bose *hole* distributions—cf. Eqs. (4.30b) and (4.37b)—replacing $\epsilon_k - \mu \to \omega$.[12]

Apart from the singularities arising from $g(\omega)$, the original function $F(\omega)$ will have singularities of its own. Consider now the contour C' presented in Fig. 4.5. Using again the residue theorem, we see that the integral around C' will be equal to the sum of the residues from the blue poles on the imaginary axis—that is, equal to the contour integral around C—plus the residues from the $F(\omega)$ function, presented in orange. Since the integral around C' tends to

[12] Alternatively, the $g(\omega)$ functions can also be chosen as the *particle* distributions.

zero as the radius of this contour grows to infinity, we have

$$\oint_{C'} d\omega F(\omega)g(\omega) = 0 = \oint_{C} d\omega F(\omega)g(\omega) + 2\pi i \sum \begin{array}{l}\text{Residues of } F(\omega)g(\omega) \\ \text{at poles of } F(\omega).\end{array} \tag{4.47}$$

From this relation, and taking into account Eq. (4.44), we obtain a simple formula for evaluating the Matsubara frequency sum.

$$\frac{1}{\beta}\sum_n F(i\omega_n) = -\sum \begin{array}{l}\text{Residues of } F(\omega)g(\omega) \\ \text{at poles of } F(\omega).\end{array} \tag{4.48}$$

4.3 Two-meson scattering at finite temperature: The T_{cc} case

Having established the ITF framework, we now proceed to the study of DD^* scattering in a hot medium, which constitutes the central focus of this chapter. To set the stage, we briefly recall the formalism previously employed to describe the T_{cc} in a dense nuclear medium. As will become evident, this framework can be largely extended to the finite-temperature case, with the principal modification arising from the thermal two-meson loop function, which differs from its dense nuclear-medium counterpart in Sect. 2.5. We therefore begin with a concise review of the formalism before turning to its application at finite temperature.

We start by considering a D^*D single-channel S-wave interaction kernel in the $I(J^P) = 0(1^+)$ channel, where the $T_{cc}(3875)$ state appears. The effective field theory that governs the DD^* interaction is consistent with HQSS and is diagonal on the isospin basis. Taking a Taylor expansion of this effective interaction (type A) or its inverse (type B) around the T_{cc}^+ mass in free space, which we name m_0, yields the following families of potentials.

$$V_A(s) = C_1 + C_2\,(s - m_0^2)\,, \tag{4.49a}$$

$$V_B(s) = \left[C_1' + C_2'\,(s - m_0^2)\right]^{-1}\,. \tag{4.49b}$$

In these expressions, s is the total invariant mass squared of the system, and the quantities C_1' and C_2' are low-energy constants. The unitarization of the scattering amplitude is performed using the BSE in the on-shell scheme,

$$\mathcal{T}^{-1}(s) = V^{-1}(s) - \Sigma_0(s), \tag{4.50}$$

where $\Sigma_0(s)$ is the vacuum DD^* loop function—cf. Eq. (2.58)—taken in the exact isospin limit, where $m_D = (m_{D^+} + m_{D^0})/2$ (and similarly for the charmed vector mesons D^{*+} and D^{*0}).

The two LECs of each potential family are fixed by imposing that the vacuum amplitude presents a bound state at an invariant mass squared m_0^2 with molecular probability P_0. The invariant mass is taken to be

$$m_0 = m_D + m_{D^*} - 0.8 \text{ MeV}, \tag{4.51}$$

which corresponds to the mass of the $T_{cc}(3875)$ in the exact isospin limit [52]. The molecular probability P_0 is related to the coupling g_0^2 of the bound state to the DD^* channel through [209, 226]

$$P_0 = -g_0^2 \Sigma'(m_0^2), \tag{4.52}$$

a relation that was discussed in Sect. 2.4.2. Once the $C_1^{(\prime)}$ and $C_2^{(\prime)}$ LECs have been fixed, the two families of potentials take the form presented in Eqs. (2.83a) and (2.83b).

We now introduce the temperature-dependent modifications to the T–matrix. Starting from the BSE in the on-shell approximation, the temperature dependence enters through the dressing of the DD^* mesons in the intermediate loop, while the interaction kernel is kept identical to the vacuum case:[13]

$$\mathcal{T}^{-1}(E, \vec{P}; T) = V^{-1}(s) - \Sigma(E, \vec{P}; T). \tag{4.53}$$

Here, E and $\vec{P}$ denote the total energy and three-momentum of the system (recall that Lorentz invariance is broken in the medium), and $s = E^2 - \vec{P}^2$. As in the nuclear matter study, we work in the rest frame of the medium, setting $\vec{P} = \vec{0}$. The essential difference with respect to the finite-density BSE lies in the loop function: instead of the density-dependent DD^* loop, we must now evaluate the thermal two-meson loop $\Sigma(E, \vec{P}; T)$. Its explicit form, which will be derived in the ITF framework below in section 4.3.1, reads

$$\begin{aligned}\Sigma(E, \vec{P} = 0; T) = &\int \frac{d^3q}{(2\pi)^3} \int_0^\infty d\omega \int_0^\infty d\omega' \, S_D(\omega, |\vec{q}|) \, S_{D^*}(\omega', |\vec{q}|) \\ &\times \Bigg\{ [1 + b^-(\omega, T) + b^-(\omega', T)] \left(\frac{1}{E - \omega - \omega' + i\varepsilon} - \frac{1}{E + \omega + \omega' + i\varepsilon} \right) \\ &+ [b^-(\omega, T) - b^-(\omega', T)] \left(\frac{1}{E + \omega - \omega' + i\varepsilon} - \frac{1}{E - \omega + \omega' + i\varepsilon} \right) \Bigg\}. \end{aligned} \tag{4.54}$$

In this expression, the Bose–Einstein distributions $b^-(\omega, T)$, introduced in the previous section, enter explicitly. The real part of this loop is divergent and is

[13] Here, the T–matrix is denoted by the calligraphic $\mathcal{T}$ to avoid confusion with the temperature T.

regularized, as in the finite-density analysis of Sect. 2.5, with a three-momentum cutoff $\Lambda = 700$ MeV.

The computation of Eq. (4.54) requires the D and D^* spectral functions in a hot medium. These functions incorporate both statistical corrections and the dressing of the heavy mesons due to their interaction with the thermal environment. In this work, we employ the spectral functions obtained in Refs. [211, 316], derived from the interaction of $D^{(*)}$ mesons with a thermal pion bath. For completeness, the derivation of the corresponding self-energies within ITF is summarized in Sect. 4.3.2, from which the spectral functions follow directly via Eq. (2.33). Finally, we note that at finite temperature the $D^{(*)}$ and $\bar{D}^{(*)}$ spectral functions coincide, since the interaction with light mesons is the same for particles and antiparticles in the isospin limit. This fact has been used in writing the loop of Eq. (4.54). Additional details on the evaluation of the thermal DD^* loop function are given in Appendix C.

Once the thermal loop function and thus the T–matrix have been computed, the spectral function of the T_{cc} can be defined directly from the T–matrix as

$$S(E,\vec{P};T) = -\frac{1}{\pi}\frac{\mathrm{Im}\,\mathcal{T}(E,\vec{P};T)}{\hat{g}^2}, \tag{4.55}$$

with $\hat{g}^2$ the bare coupling of the T_{cc} to the DD^* channel. This bare coupling is related to the vacuum coupling g_0^2 and molecular probability P_0 through,

$$\hat{g}^2 = \frac{g_0^2}{Z_0} = -\frac{1}{\Sigma_0'(m_0^2)}\frac{P_0}{1-P_0}. \tag{4.56}$$

As discussed in Sect. 2.4.5, this definition is, in the case of the V_B interaction kernel, completely equivalent to the usual one in terms of the propagator,

$$S(E,\vec{P};T) = -\frac{1}{\pi}\mathrm{Im}\;\Delta^{(T_{cc})}(E,\vec{P};T) \tag{4.57}$$

For a general interaction kernel, the spectral function arising from the T–matrix through Eq. (4.55) is similar to the usual definition only in the energy region around the vacuum mass of the T_{cc}. For reference, the renormalized propagator of the T_{cc} in a hot medium reads

$$\Delta^{(T_{cc})}(E,\vec{P};T) = \left[E^2 - \vec{P}^2 - \tilde{\Pi}^{(T_{cc})}\right]^{-1}, \tag{4.58}$$

where the T_{cc} self-energy is described by

$$\tilde{\Pi}^{(T_{cc})} = \hat{g}^2\left[\Sigma(E,\vec{P};T) - \Sigma_0(m_0^2)\right]. \tag{4.59}$$

These formulas are equivalent to the density-dependent expressions first presented in Eqs. (2.113) and (2.114).

In both the DD^* amplitude and the T_{cc} spectral function, the temperature dependence enters entirely through the two-meson loop function. In the following section, we derive this loop within the ITF, which provides the foundation for the subsequent analysis.

4.3.1 Two–meson loop function in Imaginary Time Formalism

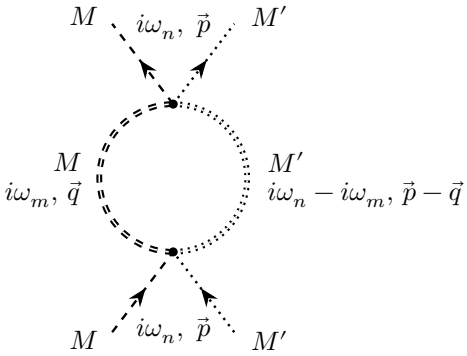

Figure 4.6: Diagram representing the two-meson loop function in the ITF (with imaginary time increasing upwards). The double internal lines indicate dressed propagators in the thermal medium.

In this section, we address the finite-temperature two-meson loop function within the ITF. Our goal is to derive a general expression that will serve as a common building block in two contexts: first and foremost, in the unitarization of the DD^* scattering amplitude at finite temperature [Eq. 4.53]; and second, in the evaluation of the charmed-meson self-energies (Sect. 4.3.2).

The two-meson loop diagram shown in Fig. 4.6 can be evaluated using the ITF Feynman rules (see Table 14.1 of Ref. [213]). Its contribution is given by[14]

$$\mathcal{G}^{MM'}(i\omega_n, \vec{p}) = -\frac{1}{\beta}\sum_m \int \frac{d^3q}{(2\pi)^3}\, \Delta_M(i\omega_m, \vec{q})\, \Delta_{M'}(i\omega_n - i\omega_m, \vec{p} - \vec{q}). \quad (4.60)$$

To perform the Matsubara sum, it is convenient to rewrite the propagators in terms of their Källén–Lehmann spectral representation. Using the compact form introduced in Eq. (2.36), the loop function takes the form

$$\mathcal{G}^{MM'}(i\omega_n, \vec{p}) = -\frac{1}{\beta}\sum_m \int \frac{d^3q}{(2\pi)^3} \int d\omega_1 \int d\omega_2$$

[14] As discussed in Fetter and Walecka [212] (pp. 271–275), a minus sign arises from the additional insertion of the interaction kernel when solving the BSE. This convention differs from that in Mattuck [213] (pp. 249–252), where the extra sign is not included.

$$\times \frac{S_M(\omega_1,\vec{q})}{i\omega_m-\omega_1}\,\frac{S_{M'}(\omega_2,\vec{p}-\vec{q})}{i\omega_n-i\omega_m-\omega_2}. \quad (4.61)$$

The function

$$F(\omega)=\frac{S_M(\omega_1,\vec{q})\,S_{M'}(\omega_2,\vec{p}-\vec{q})}{(\omega-\omega_1)(i\omega_n-\omega-\omega_2)} \quad (4.62)$$

exhibits poles at $\omega=\omega_1$ and $\omega=i\omega_n-\omega_2$. Applying the summation formula of Eq. (4.48), and choosing the Bose–Einstein hole distribution $g(\omega)=b^-(\omega)$ as the auxiliary function—which ensures the correct treatment of bosonic Matsubara poles—one obtains

$$\mathcal{G}^{MM'}(i\omega_n,\vec{p})=\int\frac{d^3q}{(2\pi)^3}\int d\omega_1\int d\omega_2$$
$$\times S_M(\omega_1,\vec{q})S_{M'}(\omega_2,\vec{p}-\vec{q})\left[\frac{b^-(\omega_1)}{i\omega_m-\omega_1-\omega_2}+\frac{b^-(i\omega_n-\omega_2)}{i\omega_n-\omega_1-\omega_2}\right]. \quad (4.63)$$

To further simplify this expression, we make use of the fact that the bosonic Matsubara frequency is proportional to an even integer, so that

$$b^-(\omega_2-i\omega_n)=\frac{1}{e^{\beta\omega_2}e^{-i\beta\omega_n}-1}=\frac{1}{e^{\beta\omega_2}-1}=b^-(\omega_2). \quad (4.64)$$

Furthermore, from Eqs. (4.37a) and (4.37b) it is easily seen that

$$b^-(-\omega)=-b^+(\omega)=-\left[1+b^-(\omega)\right]. \quad (4.65)$$

Using these two properties, we can write the imaginary-time propagator as

$$\mathcal{G}^{MM'}(i\omega_n,\vec{p})=\int\frac{d^3q}{(2\pi)^3}\int d\omega_1\int d\omega_2$$
$$\times\left[1+b^-(\omega_1)+b^-(\omega_2)\right]\frac{S_M(\omega_1,\vec{q})\,S_{M'}(\omega_2,\vec{p}-\vec{q})}{i\omega_n-\omega_1-\omega_2}. \quad (4.66)$$

Thus, in this formalism, the Bose–Einstein statistical factors naturally emerge from the use of the auxiliary distribution $g(\omega)$ in the Matsubara summation.

Starting from the imaginary-time loop function of Eq. (4.66), the corresponding real-time expression is obtained by performing a Wick rotation of the external energy variable. The result reads

$$G^{MM'}(p^0,\vec{p})=\int\frac{d^3q}{(2\pi)^3}\int d\omega_1\int d\omega_2$$
$$\times\left[1+b^-(\omega_1)+b^-(\omega_2)\right]\frac{S_M(\omega_1,\vec{q})\,S_{M'}(\omega_2,\vec{p}-\vec{q})}{p^0-\omega_1-\omega_2+\mathrm{sign}(p^0)\,i\varepsilon}. \quad (4.67)$$

Equation (4.67) constitutes the general result for the two-meson propagator in a hot medium. To proceed further, it is useful to separate the energy integrations into positive- and negative-energy contributions, thereby distinguishing between particle and antiparticle contributions:

$$\int_{-\infty}^{+\infty} d\omega_1 = \int_{-\infty}^{0} d\omega_1 + \int_{0}^{\infty} d\omega_1 = \int_{0}^{\infty} d(-\omega_1) + \int_{0}^{\infty} d\omega_1. \tag{4.68}$$

Employing the relation of Eq. (4.65), together with the definition of the compact spectral function $\tilde{S}$ introduced in Eq. (2.35), one arrives at the expression

$$\begin{aligned} G^{MM'}(p^0,\vec{p}) = & \int \frac{d^3q}{(2\pi)^3} \int_0^\infty d\omega_1 \int_0^\infty d\omega_2 \\ & \times \Bigg\{ [1 + b^-(\omega_1) + b^-(\omega_2)] \\ & \times \left(\frac{S_M(\omega_1,\vec{q})\, S_{M'}(\omega_2,\vec{p}-\vec{q})}{p^0 - \omega_1 - \omega_2 + i\varepsilon} - \frac{S_{\overline{M}}(\omega_1,\vec{q})\, S_{\overline{M}'}(\omega_2,\vec{p}-\vec{q})}{p^0 + \omega_1 + \omega_2 + i\varepsilon} \right) \\ & + [b^-(\omega_1) - b^-(\omega_2)] \\ & \times \left(\frac{S_{\overline{M}}(\omega_1,\vec{q})\, S_{M'}(\omega_2,\vec{p}-\vec{q})}{p^0 + \omega_1 - \omega_2 + i\varepsilon} - \frac{S_M(\omega_1,\vec{q})\, S_{\overline{M}'}(\omega_2,\vec{p}-\vec{q})}{p^0 - \omega_1 + \omega_2 + i\varepsilon} \right) \Bigg\}, \end{aligned} \tag{4.69}$$

valid for positive p^0.[15]

The real part of Eq. (4.69) is divergent and requires regularization, for which we employ a sharp momentum cutoff as in previous chapters. The imaginary part, on the other hand, is finite.

Although Eq. (4.69) was written by explicitly distinguishing between the particle and antiparticle spectral functions, this separation is unnecessary at finite temperature. In a hot medium, the mesons $M^{(\prime)}$ and their antiparticles $\overline{M}^{(\prime)}$ interact in the same way with the surrounding pion bath.[16] As a result, the corresponding spectral functions coincide, and the two-meson loop can be expressed in the simplified form

$$G^{MM'}(p^0,\vec{p}) = \int \frac{d^3q}{(2\pi)^3} \int_0^\infty d\omega_1 \int_0^\infty d\omega_2\, S_M(\omega_1,\vec{q})\, S_{M'}(\omega_2,\vec{p}-\vec{q})$$

[15] This expression should be compared with the nuclear-density two-meson propagator of Eq. (2.88). As expected, both coincide in the limit $b^- \to 0$, corresponding to zero temperature.

[16] The $M\pi$ and $\overline{M}\pi$ interactions are the same due to pions and antipions belonging to the same isospin multiplet.

$$\times \Bigg\{ [1 + b^-(\omega_1) + b^-(\omega_2)] \left(\frac{1}{p^0 - \omega_1 - \omega_2 + i\varepsilon} - \frac{1}{E + \omega_1 + \omega_2 + i\varepsilon} \right)$$

$$+ [b^-(\omega_1) - b^-(\omega_2)] \left(\frac{1}{p^0 + \omega_1 - \omega_2 + i\varepsilon} - \frac{1}{E - \omega_1 + \omega_2 + i\varepsilon} \right) \Bigg\}. \quad (4.70)$$

The imaginary part of the two-meson loop can be expressed as

$$\mathrm{Im}\, G^{MM'}(p^0, \vec{p}) = -\pi \int \frac{d^3q}{(2\pi)^3} \int_0^\infty d\omega_1 \int_0^\infty d\omega_2\, S_M(\omega_1, \vec{q})\, S_{M'}(\omega_2, \vec{p} - \vec{q})$$

$$\times \Bigg\{ \mathrm{sign}(p^0)\, [1 + b^-(\omega_1) + b^-(\omega_2)] \Big[\delta(\omega_2 - (p^0 - \omega_1)) - \delta(\omega_2 + (p^0 + \omega_1)) \Big]$$

$$+ \mathrm{sign}(p^0)\, [b^-(\omega_1) - b^-(\omega_2)] \Big[\delta(\omega_2 - (p^0 + \omega_1)) - \delta(\omega_2 + (p^0 - \omega_1)) \Big] \Bigg\}. \quad (4.71)$$

For positive external energy p^0, the delta function $\delta(\omega_2 + p^0 + \omega_1)$ never contributes, since its argument cannot vanish. After integrating over ω_2, the result becomes

$$\mathrm{Im}\, G^{MM'}(p^0, \vec{p}) = -\frac{1}{2\pi} \int q^2\, dq$$

$$\times \Bigg\{ \int_0^{p^0} d\omega\ \left[1 + b^-(\omega) + b^-(p^0 - \omega) \right] S_M(\omega, \vec{q})\, S_{M'}(p^0 - \omega, \vec{p} - \vec{q})$$

$$+ \int_0^\infty d\omega\ \left[b^-(\omega) - b^-(p^0 + \omega) \right]$$

$$\times \Big[S_M(\omega, \vec{q})\, S_{M'}(p^0 + \omega, \vec{p} - \vec{q}) + S_{M'}(\omega, \vec{p} - \vec{q})\, S_M(p^0 + \omega, \vec{q}) \Big] \Bigg\}. \quad (4.72)$$

The first contribution in Eq. (4.72) corresponds to the usual *unitarity cut*, now modified by the thermal population factors $b^-(\omega)$ that account for the presence of particles in the heat bath. The second contribution, however, has no counterpart at zero temperature: it is generated exclusively by the medium and is referred to as the *Landau cut*. This term is particularly important in the subthreshold region, where it provides an additional source of imaginary part to the two-meson propagator.

Since the objective of this chapter is to evaluate the DD^* thermal loop function, it is essential to determine the corresponding D and D^* spectral

functions at finite temperature. These spectral functions, in turn, are directly determined by the in-medium self-energies of the charmed mesons. The following subsection is therefore devoted to their introduction and discussion.

4.3.2 D and D^* self energies

In this section, we shall apply the ITF presented in Sect. 4.2 to describe the properties of heavy mesons—in particular of the D and D^*—when they are embedded in a hot medium. We will introduce the formalism and results for the temperature-dependent charmed-meson spectral functions that were obtained in Refs. [211, 316] and thoroughly discussed in Ref. [322]. The spectral functions obtained in these references serve as the starting point in our calculation.

Meson self-energy in Imaginary Time Formalism

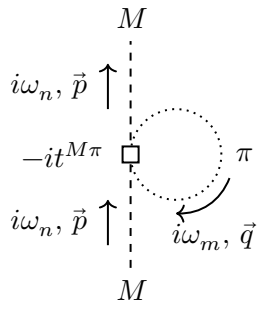

Figure 4.7: Self-energy diagram for an M meson in the presence of a hot bath of pions in ITF (increasing imaginary time taken in the up direction).

We start by considering the irreducible self-energy of a meson M in the presence of a hot bath of pions, which are the dominant light-meson species in a hot hadronic medium, cf. Fig. 4.1. The diagram representing this self-energy is shown in Fig. 4.7.

Within the ITF framework, the self-energy is obtained by applying the corresponding Feynman rules to the diagram shown in Fig. 4.7 (cf. Table 14.1 of Mattuck's book [213]). The resulting expression is

$$\Pi(i\omega_n, \vec{p}) = -\frac{1}{\beta}\sum_m \int \frac{d^3q}{(2\pi)^3}\, \Delta_\pi(i\omega_m, \vec{q})\; t^{M\pi}(i\omega_m + i\omega_n, \vec{q}+\vec{p})\,, \qquad (4.73)$$

where Δ_π denotes the pion propagator and $t^{M\pi}$ the unitarized $M\pi$ T–matrix.[17]

[17]Here we denote the T–matrix with a lowercase t in order to distinguish it from the DD^* T–matrix presented in Eq. (4.50). Similarly, lowercase letters are used in this case for the $M\pi$ potential and the $M\pi$ loop.

As in the case of the two-meson loop discussed earlier, it is convenient, prior to performing the Matsubara frequency sum, to rewrite both the pion propagator and the T-matrix in terms of their spectral representations. The latter takes the form

$$t^{M\pi}(i\omega,\vec{p}) = -\frac{1}{\pi}\int_{-\infty}^{+\infty} d\omega' \, \frac{\mathrm{Im}\, t^{M\pi}(\omega',\vec{p})}{i\omega-\omega'}. \tag{4.74}$$

Substituting these representations into Eq. (4.73), the self-energy becomes

$$\Pi(i\omega_n,\vec{p}) = \frac{1}{\pi\beta}\sum_m \int \frac{d^3q}{(2\pi)^3}\int_{-\infty}^{+\infty} d\omega_1 \, \frac{\tilde{S}_\pi(\omega_1,\vec{q})}{i\omega_m-\omega_1} \times \int_{-\infty}^{+\infty} d\omega_2 \, \frac{\mathrm{Im}\, t^{M\pi}(\omega_2,\vec{q}+\vec{p})}{i\omega_m+i\omega_n-\omega_2}. \tag{4.75}$$

In contrast to Eq. (4.73), the pole structure of the summed function is now explicit. After analytic continuation $i\omega_m \to \omega$, the poles are located at

$$\omega = \omega_1, \qquad\qquad \omega = \omega_2 - i\omega_n. \tag{4.76}$$

Using the Matsubara summation formula derived in the previous section, and choosing the Bose-Einstein hole distribution $g(\omega) = b^-(\omega)$ as the auxiliary function, one finally obtains

$$\Pi(i\omega_n,\vec{p}) = \frac{1}{\pi}\int \frac{d^3q}{(2\pi)^3}\int_{-\infty}^{+\infty} d\omega_1 \int_{-\infty}^{+\infty} d\omega_2 \times \frac{\tilde{S}_\pi(\omega_1,\vec{q})\,\mathrm{Im}\, t^{M\pi}(\omega_2,\vec{q}+\vec{p})}{\omega_2-i\omega_n-\omega_1}\left[b^-(\omega_1)-b^-(\omega_2)\right]. \tag{4.77}$$

In deriving this result, the properties of the Bose-Einstein distribution given in Eqs. (4.64) and (4.65) have been used.

To make the structure of Eq. (4.77) more transparent, we separate the ω_1 and ω_2 integrals into their positive and negative branches. In doing so, we employ the definition of the compact spectral function $\tilde{S}$ introduced in Eq. (2.35) (taking into account that the pion and antipion spectral functions are the same), together with the property

$$\mathrm{Im}\, t^{M\pi}(-\omega_2,\vec{q}+\vec{p}) = -\,\mathrm{Im}\, t^{M\pi}(\omega_2,\vec{q}+\vec{p}), \tag{4.78}$$

which follows directly from the spectral decomposition of Eq. (4.74). We then perform a Wick rotation from imaginary frequencies to the real energy axis, $i\omega_n \to p^0 + i\varepsilon$, introducing the standard $i\varepsilon$ prescription. With these ingredients, the self-energy can be expressed as (taking $p^0 > 0$)

$$\Pi(p^0,\vec{p}) = \frac{1}{\pi}\int \frac{d^3q}{(2\pi)^3}\int_0^{\infty} d\omega_1 \int_0^{\infty} d\omega_2$$

$$
\begin{aligned}
&\times \Bigg\{ [1 + b^-(\omega_1) + b^-(\omega_2)] \\
&\times \left[\frac{1}{-p^0 + \omega_2 + \omega_1 - i\varepsilon} + \frac{1}{p^0 + \omega_2 + \omega_1 + i\varepsilon} \right] \\
&- [b^-(\omega_2) - b^-(\omega_1)] \\
&\times \left[\frac{1}{-p^0 + \omega_2 - \omega_1 - i\varepsilon} + \frac{1}{p^0 + \omega_2 - \omega_1 + i\varepsilon} \right] \Bigg\} \\
&\times \; S_\pi(\omega_1, \vec{q}) \; \mathrm{Im}\; t^{M\pi}(\omega_2, \vec{q} + \vec{p}).
\end{aligned} \tag{4.79}
$$

Now, as explained in Refs. [211, 316], an approximation is taken in order to simplify the self-energy. Since the interactions of a light meson with a dominantly pionic medium are weak, the pion propagator can be approximated by the free-space one, so that its spectral function becomes a Dirac delta function[18]

$$
S_\pi(\omega, \vec{q}) = \frac{1}{2\omega_\pi(q)} \delta\left[\omega - \omega_\pi(q)\right], \qquad \text{where } \omega_\pi(q) = \sqrt{m_\pi^2 + q^2}. \tag{4.80}
$$

With this, the meson self-energy becomes

$$
\begin{aligned}
\Pi(p^0, \vec{p}) = \frac{1}{\pi} \int \frac{d^3q}{(2\pi)^3} \frac{1}{2\omega_\pi(q)} \int_0^\infty d\omega_2 \\
&\times \Bigg\{ [1 + b^-(\omega_\pi(q)) + b^-(\omega_2)] \\
&\times \left[\frac{1}{-p^0 + \omega_2 + \omega_\pi(q) - i\varepsilon} + \frac{1}{p^0 + \omega_2 + \omega_\pi(q) + i\varepsilon} \right] \\
&- [b^-(\omega_2) - b^-(\omega_\pi(q))] \\
&\times \left[\frac{1}{-p^0 + \omega_2 - \omega_\pi(q) - i\varepsilon} + \frac{1}{p^0 + \omega_2 - \omega_\pi(q) + i\varepsilon} \right] \Bigg\} \\
&\times \mathrm{Im}\, t^{M\pi}(\omega_2, \vec{q} + \vec{p}).
\end{aligned} \tag{4.81}
$$

Although not made explicit in our notation, the temperature dependence of the previous expression arises in two ways: directly through the Bose–Einstein

[18] A similar approximation was taken when discussing the finite-nuclear density self energies in Sect. 2.3. One can see that in Eq. (2.17) no nucleon spectral function appears.

distributions b^- and indirectly through the unitarized amplitude $t^{M\pi}$. Consequently, the self-energy contains both a thermal correction and a vacuum contribution. To isolate the thermal effects in the real part of the self-energy, Ref. [323] proposed subtracting the vacuum contribution, i.e. the real part of the self-energy computed at $T = 0$, from the corresponding finite-temperature calculation. In the present work, we adopt an alternative procedure: we retain only the thermal contribution by dropping the constant "1" in the factor $[1 + b^-(\omega_\pi, T) + b^-(\omega_2, T)]$ appearing in Eq. (4.81). This term is precisely the piece that survives in the zero-temperature limit, where the Bose–Einstein distributions vanish, and therefore must be excluded. For the imaginary part of the self-energy, however, the vacuum term of Eq. (4.81) is also retained, since it is finite and physically meaningful.

The final expression for the thermal correction to the M-meson self-energy then reads

$$\begin{aligned}\tilde{\Pi}(p^0, \vec{p}) = \frac{1}{\pi} \int \frac{d^3q}{(2\pi)^3} \frac{1}{2\omega_\pi} \int_0^\infty d\omega \\ \times \Bigg\{ [b^-(\omega_\pi) + b^-(\omega)] \left[\frac{1}{-p^0 + \omega + \omega_\pi - i\varepsilon} + \frac{1}{p^0 + \omega + \omega_\pi + i\varepsilon} \right] \\ - [b^-(\omega) - b^-(\omega_\pi)] \left[\frac{1}{-p^0 + \omega - \omega_\pi - i\varepsilon} + \frac{1}{p^0 + \omega - \omega_\pi + i\varepsilon} \right] \Bigg\} \\ \times \operatorname{Im} t^{M\pi}(\omega, \vec{q} + \vec{p}). \end{aligned} \tag{4.82}$$

Equation (4.82) thus provides the working expression for the M-meson self-energy in a thermal pion bath, where medium effects are encoded in the Bose–Einstein factors and the finite-temperature $M\pi$ amplitude. This amplitude, however, depends itself on the M self-energy, leading to a self-consistent calculation—as was also the case in the dense nuclear medium (cf. Sect. 2.3.1). This calculation is briefly examined in the following subsection.

Although Eq. (4.82) may at first sight look quite different from the self-energy obtained in Eq. (2.17) for the case of finite nuclear density (see Sect. 2.3), the two expressions are in fact closely related. If one neglects the contribution of the $b^-(\omega)$ term—since the ω integral is relevant for ω around $\pm(p^0 \pm \omega_\pi)$, with p^0 near the heavy-meson mass—the spectral decomposition of the amplitude can be reverted, and the self-energy rewritten as

$$\tilde{\Pi}(p^0, \vec{p}) = \frac{1}{\pi} \int \frac{d^3q}{(2\pi)^3} \frac{b^-(\omega_\pi)}{2\omega_\pi} \left[t^{M\pi}(p^0 + \omega_\pi, \vec{q} + \vec{p}) - t^{M\pi}(p^0 - \omega_\pi, \vec{q} + \vec{p}) \right]. \tag{4.83}$$

This expression mirrors Eq. (2.17), with the following differences: 1) the replacement of the step function—encoding the Fermi–Dirac distribution of nucleons at zero temperature—by the Bose–Einstein distribution $b^-(\omega_\pi)$, describing pions in the thermal bath; 2) the additional contribution from the $t^{M\pi}(p^0-\omega_\pi,\vec{p}+\vec{q})$ amplitude, which explicitly makes the self-energy charge-conjugation symmetric; and 3) an overall normalization factor $1/(2\omega_\pi)$, which appears because the pions of the thermal bath are bosons.

The expression in Eq. (4.82) was employed in Refs. [211, 316] to evaluate the self-energies of the $D^{(*)}$ mesons in a hot medium populated by pions. In the present work, we follow the same strategy, using the results obtained in these references. Before discussing the unitarization procedure for the $M\pi$ T–matrix, it is convenient to first examine the spin–isospin structure of the finite-temperature self-energy.

We now concentrate on the case of interest: D and D^* mesons propagating in a thermal pion bath. Since pions carry no spin, the spin dependence of the charmed-meson self-energy is trivial, and the problem reduces to isospin. Making use of the general spin/isospin decomposition of the scattering amplitude derived in Sect. 2.3.3 (see Eq. (2.45)), one finds

$$\Pi^{D^{(*)}\pi} = \Pi^{D^{(*)}\pi}\left(I=\tfrac{1}{2}\right) + 2\,\Pi^{D^{(*)}\pi}\left(I=\tfrac{3}{2}\right), \tag{4.84}$$

where the isospin channel I is indicated in parentheses. This decomposition applies equally to both the D and D^* mesons.

Unitarization of the $D^{(*)}\pi$ amplitude

We now deal with the interaction between a heavy meson and a light meson, in particular between $D^{(*)}$ mesons and pions. Similarly to the finite-density study presented in Chap. 2, the T–matrix for $D\pi$ (or $D^*\pi$) scattering is unitarized using the BSE within the on-shell factorization scheme.

$$t^{D^{(*)}\pi} = \frac{v^{D^{(*)}\pi}}{1 - v^{D^{(*)}\pi} g^{D^{(*)}\pi}}. \tag{4.85}$$

In the following, we discuss the two main ingredients of this equation: the interaction kernel $v^{D^{(*)}\pi}$ and the finite-temperature loop function $g^{D^{(*)}\pi}$. In complete analogy to what was presented in Sect. 2.3 and 2.4, the medium effects are incorporated through the $D^{(*)}\pi$ loop, leaving the interaction kernel unmodified.

As discussed in the Introduction, the effective Lagrangian governing the interaction of light mesons and heavy mesons can be constructed by exploiting two symmetries of the QCD Lagrangian: chiral symmetry and HQSS. This

effective field theory is known as HMChPT, and we already made use of it when describing the DK interaction in Sect. 2.6.

Here, we present the S–wave $D\pi$ and $D^*\pi$ amplitude arising from the effective Lagrangian at next-to-leading order in chiral power counting and at strictly the lowest order in the heavy-quark mass expansion. At this order, there are no tree-level diagrams connecting the different HQSS partners—that is, the D and D^*—and the two sectors are decoupled. The S-wave tree-level amplitude—or *potential* in classical terms—is given by the following expression.

$$\begin{aligned} v^{M\pi}(s) = \frac{1}{f_\pi^2}\Bigg[& \frac{C_{\mathrm{LO}}}{4}\left(\frac{3}{2}\,s - \Delta_+ - \frac{\Delta_-^2}{2s}\right) \\ & - 4\,C_0 h_0 + 2\,C_1 h_1 \\ & + (-4\,C_{24}h_2 + 2\,C_{35}h_3)\,\frac{(s-\Delta_-)^2}{4s} \\ & + (-2\,C_{24}h_4 + 2\,C_{35}h_5)\,\frac{(s-\Delta_+)^2}{4} \\ & + (-2\,C_{24}h_4 + 2\,C_{35}h_5)\left(\frac{s}{4} - \frac{\Delta_-^2}{4s}\right)^2\Bigg]. \end{aligned} \tag{4.86}$$

In Eq. (4.86), the variable s denotes the total invariant mass squared of the system, $f_\pi = 92.4$ MeV is the pion decay constant, and $\Delta_\pm = m_{D^{(*)}}^2 \pm m_\pi^2$ with $m_{D^{(*)}}$ the mass of the considered charmed meson—either the pseudoscalar D or the vector D^*—and m_π the pion mass. In addition, the constants C_i (with $i = \{\mathrm{LO}, 0, 1, 24, 35\}$) are isospin coefficients, listed in Tab. 4.1. The lowercase h_i ($i = \{0, 1, 2, 3, 4, 5\}$) represent low-energy constants, and are provided in Tab. 4.2. Further discussion of this amplitude can be found in Sect. 2.3.2 of Ref. [322]—see Eq. (2.174) there—and in the references therein. As stated before, this interaction kernel is taken to be the same in vacuum and at finite temperature, and temperature effects are incorporated into the unitarized T–matrix through the $D^{(*)}\pi$ loop function, whose calculation is detailed in the next subsection.

I	C_{LO}	C_0	C_1	C_{24}	C_{35}
$\frac{1}{2}$	-2	m_π^2	$-m_\pi^2$	1	1
$\frac{3}{2}$	1	m_π^2	$-m_\pi^2$	1	1

Table 4.1: Isospin coefficients C_k appearing in the $D^{(*)}\pi \to D^{(*)}\pi$ interaction given in Eq. (4.86), considering the two possible isospin channels. These coefficients are taken from Table 14.5 in Ref. [322].

	h_0	h_1	h_2	h_3	h_4 [MeV^{-2}]	h_5 [MeV^{-2}]
$D\Phi$	0.033	0.45	−0.12	1.67	$-0.0054 \cdot 10^{-6}$	$-0.22 \cdot 10^{-6}$
$D^*\Phi$	0.033	0.45	−0.12	1.67	$-0.0047 \cdot 10^{-6}$	$-0.19 \cdot 10^{-6}$

Table 4.2: Values of the LECs for the interaction of D and D^* mesons with the light mesons (in particular pions) represented by Φ, taken from Fit-2B in [324].

With the expression for the loop function of Eq. (4.69), we are ready to discuss the unitarization procedure of the self-energy of the $D^{(*)}$ mesons. We shall now particularize it to the case of a charmed D meson and a pion—the extension to the $D^*\pi$ case being straightforward. Similarly to what was done when discussing the self-energy expression of Eq. (4.79), a delta-like spectral function is taken for the pion—cf. Eq. (4.80). Taking this approximation, the loop function yields

$$g^{D\pi}(p^0,\vec{p}) = \int \frac{d^3q}{(2\pi)^3}\,\frac{1}{2\omega_\pi}\int_0^\infty d\omega_1\; S_D(\omega_1,\vec{q}) \times \left\{ [1+b^-(\omega_1)+b^-(\omega_\pi)]\left(\frac{1}{p^0-\omega_1-\omega_\pi+i\varepsilon}-\frac{1}{E+\omega_1+\omega_\pi+i\varepsilon}\right) + [b^-(\omega_1)-b^-(\omega_\pi)]\left(\frac{1}{p^0+\omega_1-\omega_\pi+i\varepsilon}-\frac{1}{E-\omega_1+\omega_\pi+i\varepsilon}\right)\right\}. \quad (4.87)$$

where the energy of the pion is

$$\omega_\pi = \sqrt{m_\pi+(\vec{p}-\vec{q})^2}. \quad (4.88)$$

Taking the $g^{D\pi}$ loop of Eq. (4.87) and the interaction kernel $v^{D\pi}$ presented in Eq. (4.86), one can determine the unitarized amplitude $t^{D\pi}$ needed to obtain the self-energy of the D, presented in Eq. (4.81). However, since the loop function depends on the D spectral function—and therefore on its self-energy—this defines a self-consistent system of coupled equations for the T–matrix and the self-energy. This is in complete analogy to what was discussed in Sect. 2.3 for the case of a dense nuclear medium, and is also solved iteratively, as described in the paragraph following Eq. (2.28). Further details on the determination of the finite-temperature spectral functions of the D and D^* mesons can be found in Ref. [322]. In the present work, we rely on the results reported therein, although we reproduce some of them. In the following, we will provide a brief overview of these spectral functions. However, before showing the self-energies, we shall discuss the $D\pi$ loop function of Eq. (4.87).

$D\pi$ loop at finite temperature

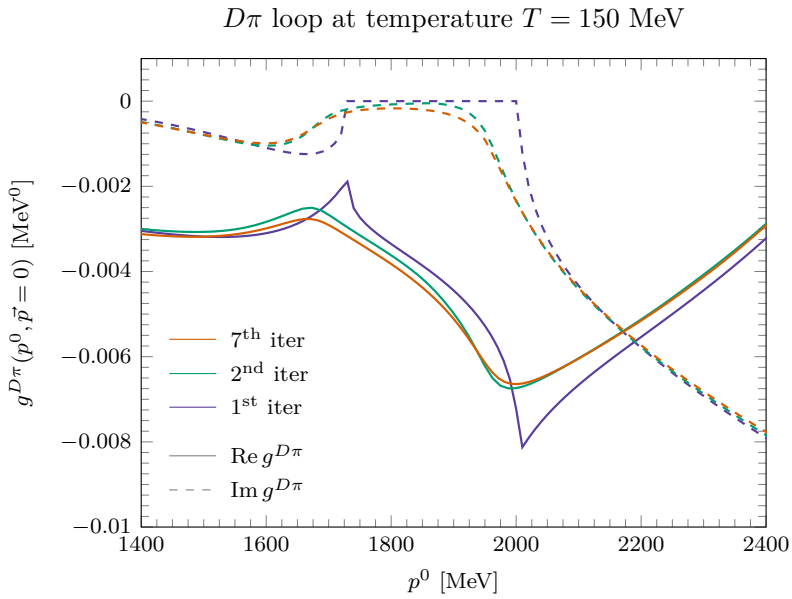

Figure 4.8: Three different iterations in the evaluation of the $D\pi$ loop. The solid lines correspond to the real part of the loop, while dashed lines represent its imaginary part. First and second iterations were computed by the authors, while the seventh iteration shown here is courtesy of Dr. Gloria Montaña.

Figure 4.8 shows the $D\pi$ loop for zero center-of-mass three momentum, evaluated at $T = 150$ MeV—a temperature close to the QCD crossover and the highest value considered in this analysis. The solid and dashed curves correspond to the real and imaginary parts of the loop, respectively. The three sets of curves, distinguished by color, correspond to successive iterations, beginning with the initial one in which the D-meson spectral function is taken as a Dirac delta. The evolution of the curves illustrates the rapid convergence of the iterative algorithm.

The most distinctive feature of the loop function presented in Fig. 4.8, in comparison to the loops at finite density shown in Chap. 2, is the appearance of the Landau cut, which can be observed in the imaginary part (dashed lines) below the threshold. In the first iteration, one observes a sharp onset of the $D\pi$-Landau cut—due to the delta-like D spectral function—that appears exactly at $p^0 = m_D - m_\pi \sim 1730$ MeV. This can be easily inferred from Eq. (4.87) when

$S_D(\omega_1, \vec{q})$ is approximated by a Dirac delta, reading

$$g^{D\pi}(p^0, \vec{p}=0) = \frac{1}{2\pi^2}\int q^2\, dq\, \frac{1}{4\omega_D\omega_\pi} \times \Bigg\{ [1 + b^-(\omega_D, T) + b^-(\omega_\pi, T)] \times \left(\frac{1}{p^0 - \omega_D - \omega_\pi + i\varepsilon} - \frac{1}{p^0 + \omega_D + \omega_\pi + i\varepsilon}\right) + [b^-(\omega_\pi, T) - b^-(\omega_D, T)] \times \left(\frac{1}{p^0 - \omega_D + \omega_\pi + i\varepsilon} - \frac{1}{p^0 + \omega_D - \omega_\pi + i\varepsilon}\right) \Bigg\}. \quad (4.89)$$

In this expression, $\omega_D = \sqrt{m_D^2 + q^2}$ and $\omega_\pi = \sqrt{m_\pi^2 + q^2}$, and the sign of the infinitesimal ε is the same as that of the external energy p^0. The imaginary part of this loop yields

$$\mathrm{Im}\, g^{D\pi}(p^0, \vec{p}=0) = -\frac{1}{2\pi}\int q^2\, dq\, \frac{1}{4\omega_D\omega_\pi} \times \Bigg\{ [1 + b^-(\omega_D, T) + b^-(\omega_\pi, T)]\, [\delta(p^0 - \omega_D - \omega_\pi) + \delta(p^0 + \omega_D + \omega_\pi)] + [b^-(\omega_\pi, T) - b^-(\omega_D, T)]\, [\delta(p^0 - \omega_D + \omega_\pi) + \delta(p^0 + \omega_D - \omega_\pi)] \Bigg\}, \quad (4.90)$$

which can be rewritten as

$$\mathrm{Im}\; g^{D\pi}(p^0, \vec{p}=0) = -\frac{1}{2\pi}\int q^2 dq \frac{1}{4\omega_D\omega_\pi} \times \Bigg\{ \big[1 + b^-(\omega_D, T) + b^-(\omega_\pi), T)\big] \times \frac{\omega_D\omega_\pi}{(\omega_D + \omega_\pi)q}\big[\theta(p^0 - m_D - m_\pi)\delta(q - k_1) + \theta(-p^0 - m_D - m_\pi)\delta(q - k_2)\big] + \big[b^-(\omega_\pi, T) - b^-(\omega_D, T)\big] \times \frac{\omega_D\omega_\pi}{(\omega_D - \omega_\pi)q}\big[\theta(p^0 + m_D - m_\pi)\theta(-p^0)\delta(q - k_4) + \theta(-p^0 + m_D - m_\pi)\theta(p^0)\delta(q - k_3)\big] \Bigg\}, \quad (4.91)$$

where θ represents the step function, and the different k_i denote the values of q that make the arguments of the different deltas zero. As it turns out,

$$k_1 = k_2 = k_3 = k_4 = \frac{\sqrt{\lambda[(p^0)^2, m_D^2, m_\pi^2]}}{2p^0} \equiv k(p^0) \tag{4.92}$$

which is the usual relativistic formula for the relative momentum of two particles in the center-of-mass frame. As indicated by the step functions, the arguments of the original deltas of Eq. (4.90) can only be zero for a determined sign of the external energy p^0. If we set $p^0 > 0$, then only two of the four deltas contribute, and so we can write

$$\begin{aligned} \text{Im } g^{D\pi}(p^0 > 0, \vec{p} = 0) = &-\frac{1}{8\pi}\frac{k(p^0)}{p^0} \\ &\times \Big\{ \theta(p^0 - m_D - m_\pi)[1 + b^-(\omega_D, T) + b^-(\omega_\pi), T)] \\ &+ \theta(-p^0 + m_D - m_\pi)[b^-(\omega_\pi, T) - b^-(\omega_D, T)] \Big\}, \end{aligned} \tag{4.93}$$

The first term gives rise to the unitarity cut for $p^0 \geq m_D + m_\pi$, while the second yields the Landau cut for $0 \leq p^0 \leq m_D - m_\pi$. The unitarity cut is very similar to that of the two-meson loop in vacuum, cf. Eq. (2.145), the only difference being the presence of the Bose-Einstein distributions. The Landau cut present in the finite-temperature loop is not found in the vacuum loop, its presence reflects different processes involving the absorption and creation of meson pairs from the thermal bath.[19] The fact that both the unitarity and the Landau cuts start sharply at a given value of the external energy arises from the Dirac-delta approximation for the meson spectral functions. When improving the determination of the spectral function of the D meson in successive iterations of the computation of its self-energy, these sharp thresholds smooth out, and as one can see in Fig. 4.8, where there is a non-zero imaginary part for all values of p^0.

Thermal D and D^* spectral functions

The main input from Refs. [211, 316] employed in our analysis are the D- and D^*-meson self-energies and spectral functions in a thermal pion bath. Their derivation has been summarized here, emphasizing the essential conceptual

[19] A detailed discussion on the physical interpretation of the cuts of the finite-temperature two-meson loop can be found in Ref. [322] after Fig. 3.5.

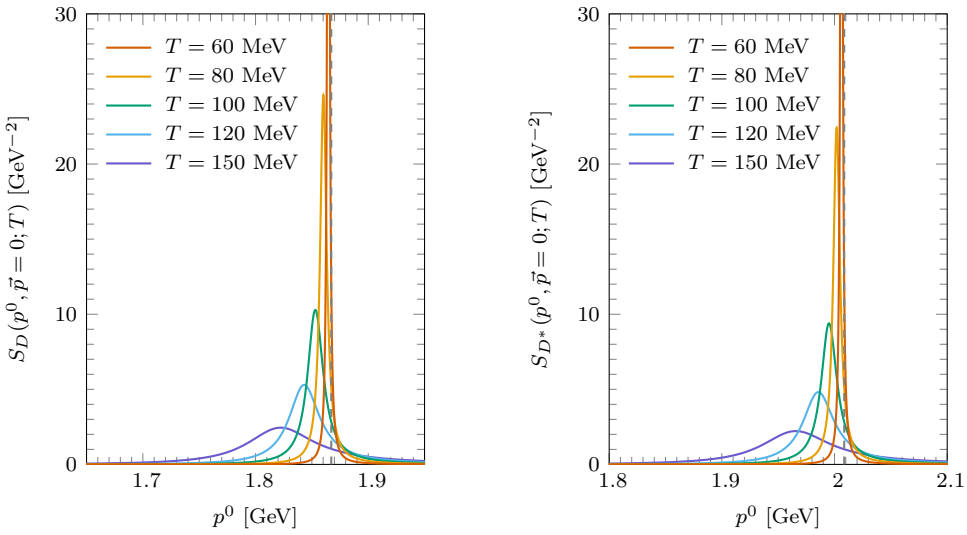

Figure 4.9: Spectral functions of the D (left) and D^* (right) mesons at zero three-momentum ($\vec{q} = 0$) as functions of the charm-meson energy p^0. Results are shown for five temperatures, distinguished by color. The vertical dashed lines indicate the vacuum masses of the corresponding mesons. Results have been taken from Refs. [211, 316].

steps. We now present the resulting spectral functions, which constitute a key ingredient in the finite-temperature analysis of the T_{cc}.

Figure 4.9 displays the D and D^* spectral functions at zero three-momentum as functions of the energy for several temperatures. Both cases show a qualitatively similar pattern: the widths broaden markedly with increasing temperature, while the quasi-particle peak shifts to energies below the corresponding vacuum mass. This similarity reflects the nearly identical $D\pi$ and $D^*\pi$ interaction kernels, governed by the comparable low-energy constants listed in Tab. 4.2.

It is also worth emphasizing that the temperature-dependent spectral functions of Fig. 4.9 exhibit far less structure than their nuclear-density-dependent counterparts (cf. Fig. 2.4). At finite density, resonance–hole excitations generate pronounced features in the spectral distributions, whereas, in a thermal medium, the spectral functions remain essentially Lorentzian in shape.

Having established the thermal D and D^* spectral functions, we can now incorporate them into the finite-temperature DD^* loop function, as presented at the beginning of Sect. 4.3. This provides the foundation for the study of DD^* scattering in a hot medium and, consequently, for investigating the temperature dependence of the exotic $T_{cc}(3875)$ state. This analysis represents one of the

central results of the present thesis. In the following section, we shall discuss the obtained thermal modifications to the T_{cc} and its HQSS partner.

4.4 Thermal modifications to the T_{cc} and T_{cc}^*

In this section, we present our results for the temperature-dependent behavior of the exotic doubly-charmed resonance $T_{cc}(3875)$. We will start by discussing the DD^* thermal loop function, switching afterwards to the scattering amplitude and the T_{cc} spectral function. We shall also devote a section to the discussion of the results for its HQSS partner, the T_{cc}^*.

4.4.1 The DD^* loop at finite temperature

We begin with the thermal DD^* loop function at finite temperature, shown in Fig. 4.10. As previously discussed, the real part is obtained from Eq. (4.70) using a cutoff regularization with $\Lambda = 0.7\,\text{GeV}$, while the imaginary part follows directly from Eq. (4.72). Both quantities are evaluated employing the D- and D^*-meson spectral functions determined in Refs. [211, 316] and previously described in Sect. 4.3.2.

The thermal modifications of the charmed mesons are clearly reflected in the dressed loop function. As the temperature increases, the onset of the unitarity cut in the imaginary part (dashed lines) softens and shifts toward lower energies, while the real part (solid lines) evolves accordingly: the cusp at the DD^* threshold decreases at higher temperatures, and the value of the real part around the vacuum threshold—and in particular just below it, where the T_{cc} state lies in the vacuum—increases, becoming less negative. If the in-medium T-matrix is rewritten as

$$T^{-1}(s;\rho) = V_{\text{eff}}^{-1}(s;\rho) - \Sigma_0(s)\,, \tag{4.94a}$$

$$V_{\text{eff}}^{-1}(s;\rho) = V^{-1}(s) + \left[\Sigma_0(s) - \Sigma(s;\rho)\right], \tag{4.94b}$$

as first shown in Eqs. (2.140), this increase in the real part of the loop can be interpreted as a corresponding increase in the effective interaction V_{eff} (see also the discussion following Eq. (2.140)). In this sense, the hot medium can be thought to induce an effective repulsive contribution. This interpretation, however, must be taken with caution, as a sizable imaginary part of the loop below the threshold may strongly affect this conclusion.

In Ref. [161], the authors studied the impact of a thermal pionic medium on the exotic $\chi_{c1}(3872)$ state as a $D\bar{D}^*$ molecule. In that work, they show the $D\bar{D}^*$ thermal loop function in Fig. 2. Since the thermal pionic medium does not distinguish between particles and antiparticles, the results for the $D\bar{D}^*$ loop reported in Ref. [161] should be similar to those found here for the

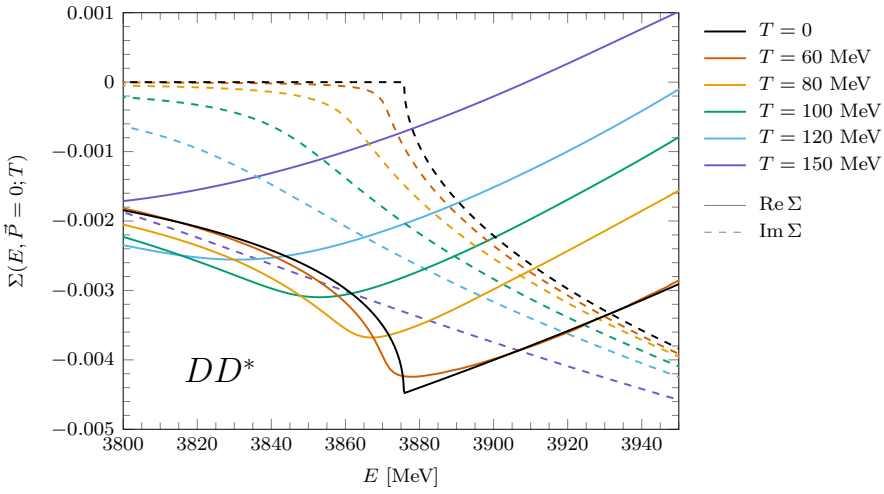

Figure 4.10: Real (solid) and imaginary (dashed) parts of the DD^* loop function at several temperatures, ranging from $T = 0$ to T =150 MeV.

DD^* loop. This is precisely the case, as can be observed when comparing the temperature dependence of the imaginary part of both loops. The real part also demonstrates the same qualitative behavior, although its precise values depend on the regularization scale, which differs here from that adopted in Ref. [161].

When contrasting the finite-temperature DD^* loop with its counterpart at finite nuclear density (see Fig. 2.9), one observes a markedly different qualitative behavior. The most striking difference is that, at the highest temperature considered in Fig. 4.10, the imaginary part becomes significantly larger below threshold than in the case of normal nuclear density. As a consequence, we expect that in this high-temperature scenario the T_{cc} peak will develop a much stronger broadening as compared to the dense nuclear medium scenario at normal nuclear density.

4.4.2 The DD^* amplitude and the T_{cc} spectral function

We now turn to the results for the DD^* scattering amplitude in the thermal medium, computed using the BSE as discussed in Eq. (4.53). The obtained results are displayed on Fig. 4.11 as a function of the center of mass energy of the meson pair, which is at rest in the frame of the hot medium. In the left column, we show results that come from the V_A interaction kernel, while the right column contains the results obtained when the V_B kernel is used. Two different molecular probabilities are considered, $P_0 = 0.2$ in the top row and $P_0 = 0.8$ in the bottom row.

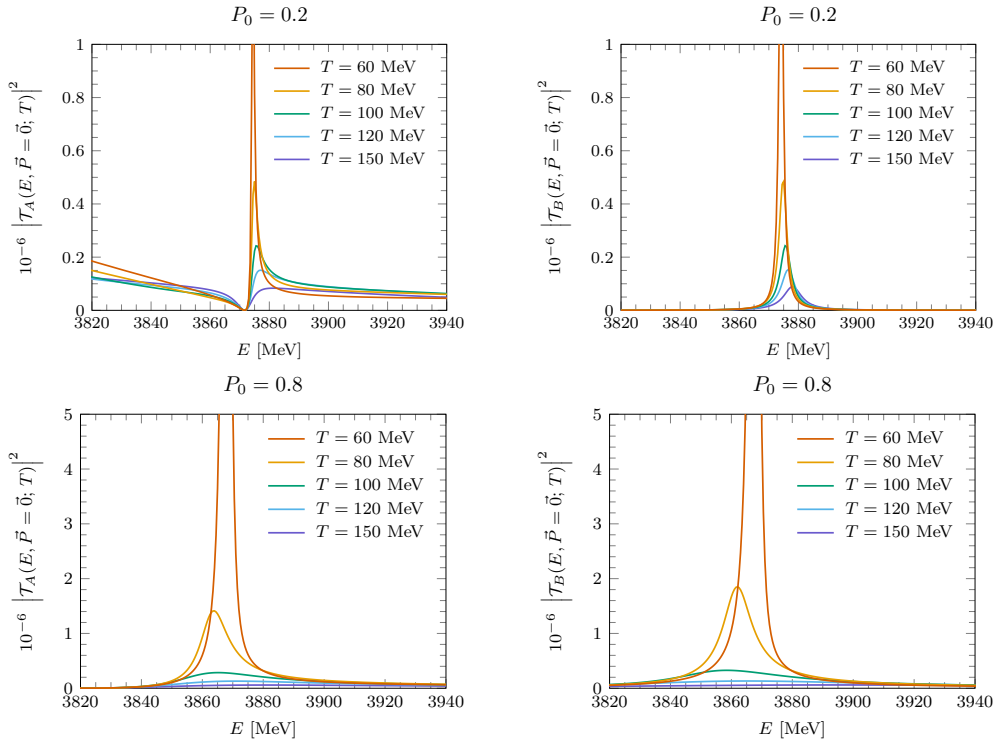

Figure 4.11: Squared modulus of the D^*D amplitudes obtained by solving the BSE using the $V_A(s)$ potential (left column) and the $V_B(s)$ potential (right column), as a function of the center-of-mass energy E, for several values of the temperature (different line colors) and for two values of the molecular probability P_0 ($P_0 = 0.2$ in the top row and 0.8 in the bottom row).

A comparison of the $\mathcal{T}$–matrices obtained from the V_A and V_B potentials[20] reveals that, for large molecular probabilities (right column), the results are practically indistinguishable at all temperatures. As already noted in Sect. 2.5 for the nuclear medium case, this agreement stems from the fact that the zero of V_A and the bare pole of V_B lie far from the physically relevant energy region and therefore introduce no substantial modifications. In contrast, for a small molecular component ($P_0 = 0.2$, left column), the two interactions lead to visible differences, producing distinct $\mathcal{T}$–matrices at finite temperature, despite reproducing the same $T_{cc}(3875)^+$ mass and DD^* coupling at zero temperature.

The temperature evolution of the $\mathcal{T}$–matrices also depends strongly on the value of P_0. For large compositeness, the width increases rapidly with temperature, and the $T_{cc}(3875)^+$ dissolves above $T \simeq 120$ MeV. By contrast, at

[20] See Fig. 2.8 for a plot of these potentials.

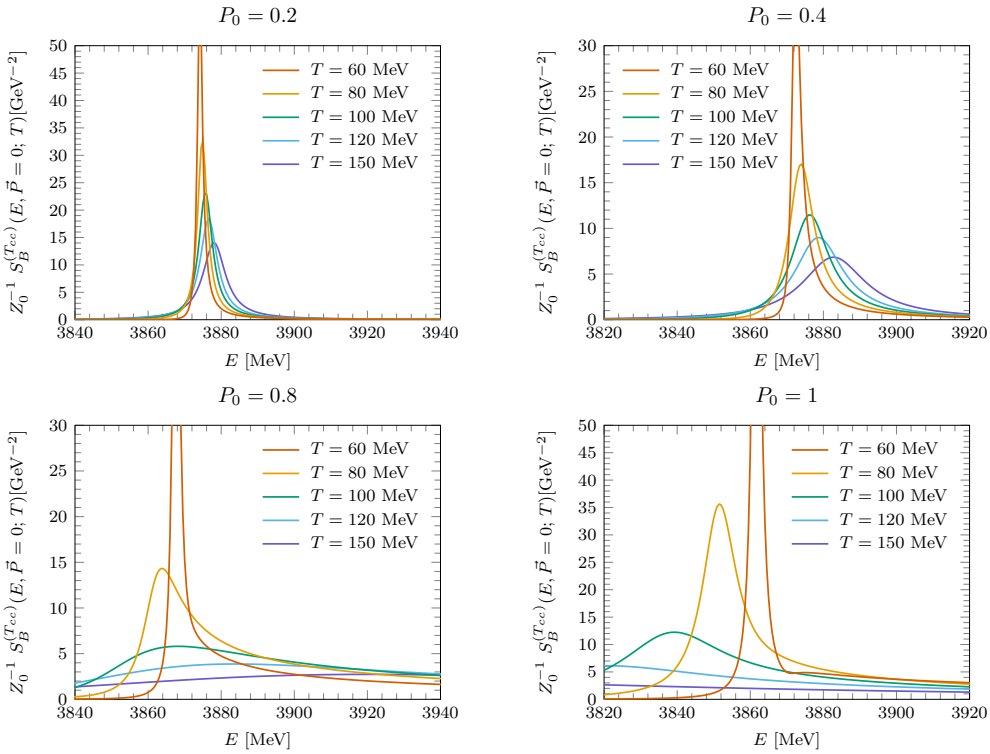

Figure 4.12: Spectral functions of the T_{cc}^+ state obtained from the $\mathcal{T}_B$ amplitude, which is equivalent to those derived directly from the propagator. The results are shown as functions of the center-of-mass energy E, for several temperature values T (indicated by different line colors), and for four choices of the molecular probability P_0 (corresponding to the four panels). All spectral functions are normalized by the field normalization factor Z_0.

small P_0, the modifications are less pronounced and sensitive to the choice of potential. In the case of V_A, the position of the zero characteristic of this interaction is unaffected by the temperature, as also observed in the finite-density scenario of Sect. 2.5. For V_B, on the other hand, the peak tied to the bare pole shifts toward higher energies and gradually diminishes as the temperature increases, in clear contrast to the behavior found for large P_0.

Similar remarks can be made about the results for the T_{cc} spectral functions stemming from the V_A and V_B interactions, as defined in Eq. (4.55). For conciseness, we restrict our discussion to the type–B case, with the corresponding results displayed in Fig. 4.12. The four subplots illustrate the dependence of the spectral function on the compositeness parameter, with values $P_0 = 0.2$, 0.4, 0.8, and 1. In analogy with Sect. 2.5, the spectral functions have been divided

by the field normalization factor Z_0 to compensate for their behavior when the compositeness tends to one. For the low-P_0 cases (top row), the quasi-particle peak, taken as the maximum of the spectral function, shifts toward higher energies. In contrast, for large molecular probabilities (bottom row), the peak moves toward lower energies. The latter behavior, however, is less sharply defined due to the substantial broadening of the peak, particularly at high temperatures. This observation is consistent with the thermal evolution of the squared modulus of the DD^* scattering amplitude shown in Fig. 4.11. It is again clear that, for high molecular probabilities, the T_{cc} state melts down at a temperature $T \sim 120$ MeV, its width becoming very large. Overall, the complete dissolution of the T_{cc} at high temperatures contrasts with its behavior in nuclear matter (see Fig. 2.12), where the width of the state increases only moderately. This difference arises because, at the temperatures considered here, the D and D^* spectral functions undergo substantial medium modifications, which in turn generate a much larger width. In contrast, the modifications induced at normal nuclear density, as shown in Fig. 2.12, are considerably milder.

As discussed previously, the $S_B^{(T_{cc})}$ spectral function may also be interpreted as originating from the genuine propagator of the T_{cc}, which is renormalized through its molecular component in the presence of the thermal pion bath. Figure 4.13 displays the inverse of this propagator for several values of the compositeness parameter P_0, with different temperatures represented by distinct line colors in each panel. Similarly to the spectral function, the propagator is also divided by the field renormalization constant Z_0.

For $P_0 = 0$, the propagator reduces to the vacuum propagator of the T_{cc}^+, which contains no imaginary part and whose inverse real part is linear in s, vanishing at $s = m_0^2$. As P_0 increases, the propagator acquires an additional contribution from $\tilde{\Pi}^{(T_{cc}^+)}$, cf. (4.59), which generates a nonzero imaginary part and simultaneously shifts the position of the zero in the real part. The location of this zero defines the quasi-particle mass, as given in Eq. (2.141). Overall, a qualitative correspondence can be identified between the evolution of the quasi-particle mass illustrated in Fig. 4.13 and the peak structure of the spectral functions shown in Fig. 4.12 for the small-molecular-probability scenarios. Nevertheless, this correspondence weakens at large molecular probabilities, where the imaginary part of the self-energy increases, and the real part exhibits a marked nonlinear behavior. For instance, in the $P_0 = 0.8$ case, the quasi-particle mass shifts upward, while the peak of the spectral function moves to lower energies.

The position of the quasi-particle mass is found to be largely insensitive to temperature variations at low molecular probabilities, as illustrated in the cases $P_0 = 0.2$ and 0.4. In contrast, and as already mentioned, for $P_0 = 0.8$ the

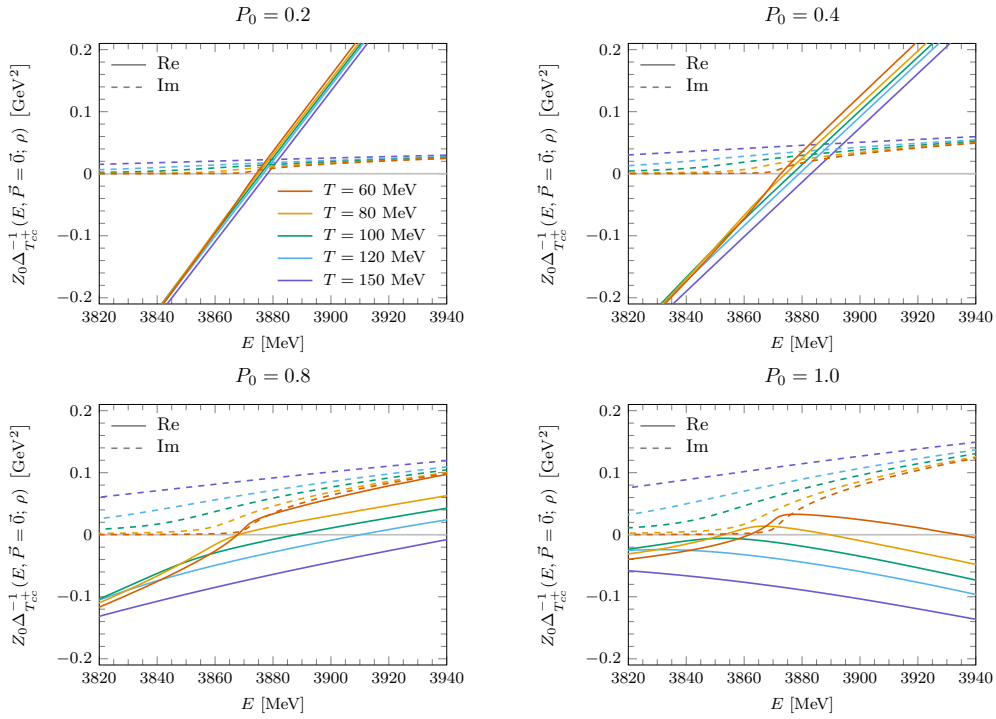

Figure 4.13: Plots of the inverse of the propagator of the $T_{cc}(3875)^+$ at zero three-momentum $\vec{P} = \vec{0}$ as a function of the center-of-mass energy E, for different values of the temperature T (different colors on the graphs) and for different values of the molecular probability P_0 on each graph. The solid (dashed) lines correspond to the real (imaginary) parts of the propagator. Also note that the propagator has been conveniently normalized with a Z_0 factor.

quasi-particle mass exhibits a clear shift toward higher values with increasing temperature. This trend originates from the fact that thermal modifications to the bare T_{cc} state are included only through its coupling to the DD^* mesons, which vanishes in the limit $P_0 \to 0$. For high molecular probabilities, particularly in the fully composite case $P_0 = 1$, additional nontrivial features emerge. At high temperatures, no quasi-particle mass solution is obtained from the condition that the real part of the self-energy is zero. At lower temperatures, however, specifically for $T = 60$ and 80 MeV, the real part becomes zero at two distinct energy values. In general, only the leftmost of these solutions gives rise to a significant peak in the spectral function, as the rightmost one is associated with a large imaginary part. This behavior can be explicitly confirmed by comparison with the spectral functions shown in Fig. 4.12.

Since the $D^{(*)}\pi$ and $\overline{D}^{(*)}\pi$ interactions are identical owing to isospin symme-

try, the results obtained for the charge-conjugated partner of the T^+_{cc}, namely the $T^-_{\bar{c}\bar{c}}$, are exactly the same. This behavior contrasts with that observed in a dense nuclear medium, where a clear charge-conjugation asymmetry arises, depending on the molecular probability.

In the following section, we discuss the results obtained in the HQSS symmetric D^*D^* sector, paying attention to the thermal behavior of the HQSS sibling of the $T_{cc}(3875)$, as we did when studying the modifications due to the nuclear density of these states.

4.4.3 Results for the HQSS partner: the $T^*_{cc}(4016)$

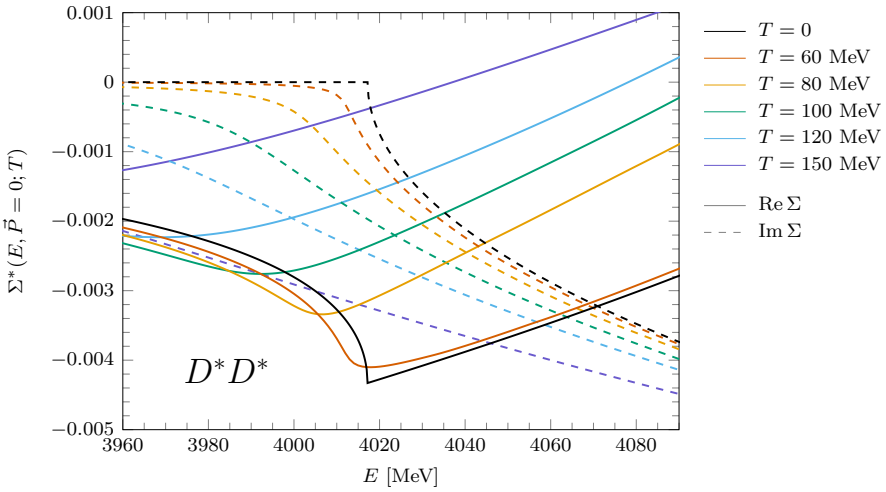

Figure 4.14: Real (solid) and imaginary (dashed) parts of the D^*D^* loop function at several temperatures, ranging from $T = 0$ to $T =$150 MeV.

The T^+_{cc}, interpreted as a D^*D bound state, with quantum numbers $I(J^P) = 0(1^+)$, is expected to have a HQSS partner in the $I(J^P) = 0(1^+)$ D^*D^* channel, referred to as $T_{cc}(4016)^*$. Although not yet experimentally confirmed, theory predicts its mass to lie roughly one pion mass above the T_{cc}, leading to a similar or slightly larger binding energy. Estimates suggest a binding of about 1.5 MeV for T^*_{cc}, compared to 0.8 MeV for T_{cc} [52]. In this section, and similarly to the study of Sect. 2.5.4, the parameters of the potential are fixed to produce a T^*_{cc} pole in the D^*D^* amplitude, and the analysis explores variations within the expected binding energy range of 0.8–1.6 MeV.

The temperature effects are incorporated through the loop function of Eq. (4.70), which in this case involves only the lowest-lying charmed vector mesons. Results are shown in Fig. 4.14 for several temperatures. The behavior

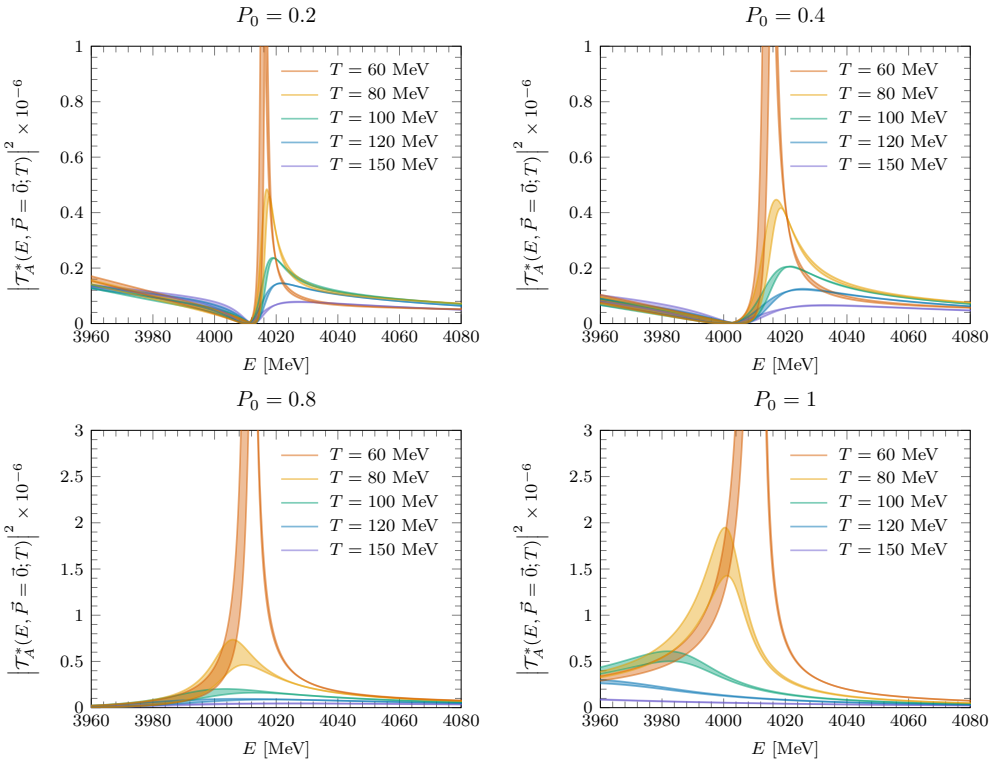

Figure 4.15: Squared modulus of the D^*D^* amplitudes obtained by solving the BSE using the V_A potential, as a function of the center-of-mass energy E, for several values of the hot pion bath temperature (different line colors) and for different values of the molecular probability P_0. The bands cover the solutions corresponding to taking the T_{cc}^{*+} binding energy to be in the interval [0.8, 1.6].

of this loop function closely resembles that of the DD^* loop discussed earlier in Fig. 4.10, with the main distinction being a shift in the position of the threshold. The thermal effects manifest as a pronounced increase in the imaginary part of the loop and a shift of the unitarity threshold towards lower energies.

In Fig. 4.15 we present the results for the $\mathcal{T}$-matrix obtained with the type–A interaction kernel. The corresponding amplitudes stemming from the type–B kernel, although differing from $\mathcal{T}_A$ at small compositeness, exhibit an overall behavior comparable to that discussed in Fig. 4.11 for the DD^* channel, aside from the expected mass shift in this new system. The LECs of the D^*D^* effective interaction are fixed to reproduce both the molecular probability P_0 indicated in each plot and the vacuum mass of the T_{cc}^*, assumed to lie 0.8–1.6 MeV below the D^*D^* threshold. This range of binding energies, introduced to account for systematic uncertainties of the model, generates a band of

$\mathcal{T}$–matrix solutions, shown in Fig. 4.15. As in the study of nuclear-density effects on the T–matrices in Sect. 2.5, the amplitudes in Fig. 4.15 display a behavior qualitatively similar to that of the D^*D case. Thermal effects become increasingly significant at large values of the molecular probability, while the uncertainty associated with the T_{cc}^* binding energy produces only a minor band compared to the much larger temperature-driven modifications.

4.5 Conclusions

In this chapter, we have investigated the behavior of hadrons at finite temperature, and shown results for the exotic doubly charmed state $T_{cc}(3875)^+$ and its HQSS partner, the $T_{cc}^*(4016)$. We began in Sect. 4.2 by introducing the ITF, emphasizing the statistical origin of thermal modifications for both fermions and bosons. Sect. 4.3 was devoted to two-meson scattering in a hot medium. First, we revisited the general framework for two-meson scattering in a many-body system, originally presented in Sect. 2.4, and introduced the modifications induced by the thermal medium through the two-meson loop function. Then, we presented the computation of this finite-temperature two-meson loop within the ITF, followed by a discussion on the required D and D^* spectral functions, summarizing the formalism and results of Refs. [211, 316]. Finally, in Sect. 4.4, we presented our results for the spectral properties of the tetraquark-like states $T_{cc}(3875)^+$ and $T_{cc}^*(4016)^+$, described as isoscalar DD^* and D^*D^* S–wave bound states, respectively, in a hot pion environment.

At zero temperature—in close analogy with the nuclear matter study of Chapt. 2—we have employed two families of energy-dependent Bethe–Salpeter kernels, with their LECs tuned so as to perform a systematic exploration of the compositeness parameter. Finite-temperature effects up to $T = 150$ MeV were incorporated through the $D^{(*)}$ thermal spectral functions of Ref. [316], which were implemented in the propagators within the ITF.

Our results show significant modifications of the $D^{(*)}D^*$ scattering amplitudes already at $T = 80$ MeV. These arise from the dressing of the two open-charm meson loop functions with the D and D^* spectral functions, which soften and shift the onset of the unitarity cut of the imaginary part toward lower energies as the temperature increases. The real part evolves consistently, with the cusp at the DD^* threshold decreasing at higher temperatures. We then examined the sensitivity of the thermal line shapes of these tetraquark-like states to their Weinberg molecular content. The $D^{(*)}D^*$ scattering amplitudes and the $T_{cc}^{(*)}$ spectral functions have been found to vary more rapidly with temperature for large molecular probabilities than for low ones. Furthermore, the widths grow substantially, leading to the dissolution of these states above $T \sim 100 - 120$ MeV. In contrast, for small molecular components, the ther-

mal modifications are milder and depend strongly on the choice of the BSE interaction kernel.

Together, these findings highlight that experimental determinations of $D^{(*)}D^*$ scattering amplitudes at finite temperature—such as those achievable in RHIC or the LHC—can provide valuable insight into the molecular nature of the $T_{cc}(3875)^+$ and $T_{cc}(4016)^{*+}$. Moreover, by combining the thermal line-shape patterns of these states with future measurements at FAIR (CBM, PANDA) of their spectral properties in dense nuclear matter (as discussed in Chap. 2), as well as of their antiparticles, it should be possible to place strong constraints on the structure and composition of these exotic tetraquark-like states.

5

Three–body bound states: the DND^* system

5.1 Introduction

Three–body bound states have attracted increasing attention in recent years, with a comprehensive overview provided in the review of Ref. [325] (see Table 1 therein). Additional perspectives are offered in Ref. [326], which discusses different strategies for extracting information on the nature of such states from experimental data. A complementary argument is made in Ref. [327], where it is emphasized that, although meson number is not conserved—favoring the decay of multimeson systems into states with fewer mesons—flavor is conserved in strong interactions. As a result, multimeson states with different flavor content are expected to be relatively stable. Another mechanism that enhances stability is large spin, since high-spin states typically decay through channels requiring high orbital angular momentum, which are suppressed. Along these lines, multi-rho configurations [328] as well as K^* plus multi-rho states with high spin [329] have been explored and found to be compatible with existing experimental observations.

Among the many possibilities, systems containing one nucleon and two mesons have received particular attention. The $\pi\pi N$ system was investigated in Ref. [330], while the $K\bar{K}N$ state was studied in Refs. [83, 331, 332]. More recently, the systems NDK, $ND\bar{K}$, and $ND\bar{D}$ were addressed in Ref. [333]. In particular, the $ND\bar{D}$ configuration was shown to be bound [333]. This result is not unexpected: the $D\bar{D}$ interaction is known to be rather strong and capable of generating a bound state [188, 334–337], while the DN interaction is also attractive, as will be discussed later in Sect. 5.2.1.

In the broader context of hadron physics, the discovery of the T_{cc} resonance by the LHCb Collaboration [45, 142] represents a major milestone. As already

mentioned, the T_{cc} has been widely interpreted as a DD^* molecular state [46–58, 60–62, 149, 338–340], raising the natural question of whether the DND^* system could also form a bound state. This possibility has already been addressed in Ref. [341] using the Gaussian expansion method. Alternative interpretations in terms of compact tetraquarks have also been proposed [65, 66, 342–347]. However, a detailed analysis in Ref. [246] shows that, although the pole position alone cannot exclude a compact tetraquark description, the predicted scattering lengths and effective ranges in that scenario are in strong disagreement with current experimental data.

The work of Ref. [341] constructs the potentials for the DN, D^*N, and DD^* interactions within a one-boson-exchange model, and subsequently applies the Gaussian expansion method [348, 349] to investigate the binding of the DND^* system. Their analysis concludes that bound-state solutions are possible in the channels $I(J^P) = \frac{1}{2}\left(\frac{1}{2}^+\right)$ and $\frac{1}{2}\left(\frac{3}{2}^+\right)$, although the predicted binding energies exhibit a strong dependence on the cutoff used in the loop regularization and on other model parameters. As is common in variational approaches, the widths of the states are not evaluated.

In the present chapter, we revisit this problem from a different perspective by employing the fixed center approximation (FCA) to the Faddeev equations. While this method is, in principle, less accurate, it benefits from being constrained by empirical input and, importantly, provides access to the widths of the states [123, 325, 350].

This chapter is organized as follows. In Sect. 5.2 we introduce the three–body scattering formalism within the FCA. We begin with the two–body interactions in Sect. 5.2.1, which provide the basic building blocks of the three–body amplitude. Sect. 5.2.2 presents the FCA framework, followed by a discussion of the cluster form factor in Sect. 5.2.3. Applying these ingredients to the DND^* system, we conclude the formalism with an analysis of the spin and isospin structure of the amplitudes, as well as their normalization. The results for the DND^* scattering amplitude are given in Sect. 5.3, where both systematic and statistical uncertainties are assessed in a qualitative way. Finally, Sect. 5.4 summarizes our main findings.

5.2 Three–body DND^* scattering: formalism

The three–body problem has long been recognized as one of the most challenging questions in physics. Even in classical mechanics, it played a central role in the development of dynamical systems theory, from Lagrange's pioneering solutions [351] to Poincaré's groundbreaking insights into chaos [352, 353]. Its fame has even extended into popular culture, as in the science fiction of Cixin Liu [354]. From the quantum perspective, the problem is equally

demanding. Directly solving the Schrödinger equation for a three–body system is hindered by the coexistence of multiple scattering channels and the difficulty of disentangling different dynamical contributions [355].

A rigorous framework to address this challenge was provided by L. D. Faddeev in the 1960s, with the formulation of what are now known as the Faddeev equations [356, 357]. These equations, in principle exact, decompose the full three–body wave function into well-defined components corresponding to the different pairwise interactions. While they represent a major theoretical achievement, their exact solution remains highly non-trivial, and practical applications often require controlled approximations.

One such approximation is the FCA to the Faddeev equations [328, 333, 358, 359]. The central idea is simple and physically intuitive: if two of the particles form a tightly bound and relatively heavy cluster, it can be treated as an approximately rigid core with which the third particle scatters. In this way, the three–body problem is effectively reduced to a sequence of two–body scatterings. The FCA thus provides a powerful and computationally manageable tool, especially relevant in hadronic and nuclear physics, where cluster structures are common [360]. Although approximate, it has been successfully applied to identify bound states and resonances, demonstrating its utility as a bridge between the exact but difficult Faddeev framework and phenomenological descriptions.

The applicability of the FCA depends crucially on the stability of the chosen cluster. This requirement is naturally satisfied when the two–body subsystem is strongly bound and when the external particle is lighter than the constituents of the cluster. In principle, one might consider the DD^* system—identified with the T_{cc}—as the cluster, with the nucleon acting as the external particle. However, this possibility is discarded: the very small binding energy of the T_{cc} (0.36 MeV with respect to the $D^{*+}D^0$ threshold [45]) makes it unlikely to survive the interaction with a nucleon without being broken apart. By contrast, both the DN and D^*N systems are predicted to be more strongly bound in a variety of models, making them more suitable candidates for the role of the cluster within the FCA framework.

In what follows, we primarily focus on the configuration with a D^*N cluster and an external D meson, while also examining the complementary case of a DN cluster with an external D^*. We will first discuss the model used for these interactions. Once this issue has been settled, we will examine the FCA formalism.

5.2.1 D^*N, DN and DD^* two body interactions

In this section, we briefly discuss the interaction model used for the D^*N, DN, and DD^* systems, which is central for analyzing the three–body interaction in

the FCA. These interactions were already brought up when studying the T_{cc} in a dense nuclear medium in Chapter 2. However, in this chapter, we take a simplified model; thus, a brief discussion of them is in order here.

We begin by discussing the DD^* interaction, which has recently become a popular topic in hadron physics. The discovery of the T_{cc} state by the LHCb Collaboration [45] has stimulated extensive studies of the DD^* system, where the T_{cc} naturally emerges as a dynamically generated state [46–64]. As discussed in Chapter 2, although compact tetraquark interpretations of the T_{cc} have also been proposed [65, 66], the near-threshold location of the state with respect to $D^{*+}D^0$ and $D^{*0}D^+$ strongly suggests that hadronic degrees of freedom must be explicitly included in order to achieve a quantitative description of the experimental data [146].

Furthermore, the DN interaction has been the subject of intense study. Early work in Refs. [279, 280] approached it by analogy with the $\bar{K}N$ interaction. More refined calculations were later carried out in Refs. [210, 222, 223, 281, 361], where all coupled channels to DN were considered, and their dynamics described through vector-meson exchange—a mechanism that, under some approximations, fulfills the chiral symmetry of the chiral SU(3) Lagrangian [362] (see Appendix A of Ref. [363] for practical applications). In these studies, the free parameters, in particular the cutoffs regulating the loops, were fitted by requiring that the interaction generates the $\Lambda_c(2595)$ resonance. An alternative view was presented in Ref. [220], where a meson-exchange model constrained by the $SU(6)_{\rm lsf} \times HQSS$ spin–flavor symmetry[1] was employed, mixing pseudoscalar-baryon and vector-baryon channels. In that framework, it was found that the $\Lambda_c(2595)$ also couples strongly to D^*N, and that the latter channel predominantly generates the $\Lambda_c(2625)$. Similar results were obtained in Ref. [256]. The possible interpretation of $\Lambda_c(2625)$ $(3/2^-)$ as the spin partner of $\Lambda_c(2595)$ $(1/2^-)$ has been revisited in Ref. [364] within a heavy-quark spin-flavor symmetry approach supplemented by lattice QCD input, showing that significant deviations from the simple HQSS-partner picture are possible.

There are nonetheless strong arguments suggesting that the $\Lambda_c(2595)$ is not predominantly a molecular state of DN, $\pi\Sigma_c$, or related channels, in analogy to the $\Lambda(1405)$. Whereas the higher $\Lambda(1405)$ pole ($\Lambda(1420)$) lies only about 10 MeV below the $\bar{K}N$ threshold, the $\Lambda_c(2595)$ is located approximately 200 MeV below the DN threshold. In this region, constituent quark model calculations predict nearby states [365], which could account, at least in part, for the $\Lambda_c(2595)$. This interpretation is discussed in Ref. [366] and elaborated further in Ref. [367]. Additional evidence comes from coupled-channel studies of

[1]This corresponds to an $SU(6)_{\rm lsf} \times HQSS$ extension of the Weinberg–Tomozawa πN interaction, where "lsf" denotes light quark spin–flavor symmetry and HQSS stands for heavy-quark spin symmetry.

pseudoscalar-baryon and vector-baryon systems. In Ref. [368], the two sectors were coupled through pion exchange, while each sector was described via vector exchange. Tensor exchange was found to be negligible both in SU(2) [369] and SU(3) [370], and likewise in extensions to the charm sector [371]. With suitable choices of cutoff parameters, this approach successfully reproduces the $\Lambda_c(2595)$ $(1/2^-)$ and $\Lambda_c(2625)$ $(3/2^-)$. However, when the same parameters are applied to hidden-charm systems [372], the predicted masses lie significantly below the experimentally observed P_c states [137]. This indicates that the large cutoff values needed to accommodate $\Lambda_c(2595)$ and $\Lambda_c(2625)$ as molecular states are incompatible with the spectroscopy of the P_c states. Conversely, adopting cutoffs consistent with the P_c sector suggests that $\Lambda_c(2595)$ and $\Lambda_c(2625)$ cannot be understood as pure molecular states.

More realistic intermediate scenarios have been put forward. For instance, Ref. [341] proposes that the $\Lambda_c(2940)$ could be interpreted as a D^*N molecular state, in line with earlier suggestions [373–378]. A recent work [379] highlights the newly reported $\Lambda_c(2910)$ from the Belle Collaboration and suggests that the $\Lambda_c(2940)$ and $\Lambda_c(2910)$ may correspond to the $3/2^-$ and $1/2^-$ D^*N states (or vice versa). In this chapter we adopt the same perspective. Based on the analysis of Ref. [368] for Λ_c^* states and Ref. [380] for the $P_c(4440)$ $(3/2^-)$ and $P_c(4457)$ $(1/2^-)$, we favor the assignment $\Lambda_c(2940)$ $(1/2^-)$ and $\Lambda_c(2910)$ $(3/2^-)$. An alternative interpretation is proposed in the pionless theory of Ref. [381], where the spin-parities of $P_c(4440)$ and $P_c(4457)$ are reversed. While we prefer the first assignment, results for both scenarios will be discussed. Finally, heavy-quark symmetry arguments imply the existence of a DN bound state at a mass around

$$\frac{2940 + 2910}{2} - M_{D^*} + M_D \simeq 2783 \text{ MeV}.$$

Interestingly, there is indeed a Λ_c^* resonance near this energy, the $\Lambda_c(2765)$, with currently unknown spin and parity. We interpret this state as the heavy-quark spin partner of $\Lambda_c(2940)$ and $\Lambda_c(2910)$, corresponding to a DN bound state with $J^P = 1/2^-$.

Form of the two–body scattering amplitudes

To describe the various two–body interactions required in this work, we adopt a simplified model in which each scattering amplitude is dominated by the most relevant resonance in the corresponding channel. Accordingly, the amplitudes are parametrized by a single Breit–Wigner distribution, which provides an adequate description in the energy region around the resonance. In addition, we neglect isovector contributions and restrict our analysis to the dominant isoscalar amplitudes.

In more detail, for the DD^* interaction we take the following amplitude:

$$t^{I=0}_{DD^*}(s) = \frac{(g^{I=0}_{DD^*})^2}{s - M^2_{T_{cc}} + iM_{T_{cc}}\Gamma_{T_{cc}}}, \tag{5.1}$$

for which we take the experimental values of $M_{T_{cc}}$ and $\Gamma_{T_{cc}}$ of Ref. [45]:[2]

$$M_{T_{cc}} = M_{D^0D^{*+}} - 360 \text{ keV}, \qquad \Gamma_{T_{cc}} = 48 \text{ keV}. \tag{5.2}$$

We obtain the coupling to the isoscalar DD^* channel from the analysis of Ref. [47]. However, in this reference, only the couplings to the physical channels $D^{*0}D^+$ and $D^{*+}D^0$ are given. Therefore, we need to perform a change of basis to the isospin states. This is done as described in the following.

The isoscalar combination is taken as[3]

$$|DD^*, I = 0\rangle = -\frac{1}{\sqrt{2}}\left(|D^+D^{*0}\rangle - |D^0D^{*+}\rangle\right). \tag{5.3}$$

From here, we obtain

$$\langle DD^*, I = 0|t|DD^*, I = 0\rangle = \frac{1}{2}\left(t_{11} - t_{12} - t_{21} + t_{22}\right), \tag{5.4}$$

where the subscripts 1 and 2 in the t amplitudes stand for the particle-basis states D^+D^{*0} and D^0D^{*+}, respectively, so that

$$t_{12} \equiv \langle D^+D^{*0}|t|D^0D^{*+}\rangle, \tag{5.5}$$

and similarly for the remaining matrix elements. By writing the amplitudes in the particle basis as

$$t_{ij} = \frac{g_i g_j}{s - M^2_{T_{cc}} + iM_{T_{cc}}\Gamma_{T_{cc}}}, \tag{5.6}$$

the coupling to the isoscalar channel of Eq. (5.1) results in the following expression:

$$(g^{I=0}_{DD^*})^2 = \frac{1}{2}\left(g^2_{D^+D^{*0}} + g^2_{D^0D^{*+}} - 2g_{D^+D^{*0}}g_{D^0D^{*+}}\right) = \left(\frac{g_{D^+D^{*0}} - g_{D^0D^{*+}}}{\sqrt{2}}\right)^2. \tag{5.7}$$

[2]Since we treat the resonance width as constant, the amplitude does not strictly satisfy elastic unitarity. Our FCA approach of Eq. (5.21) nevertheless relies on the assumption that the underlying two–body amplitudes are unitary. We expect the resulting deviation to be small compared to other sources of uncertainty in our approach, especially when studying the sub-threshold region.

[3]Note that this definition is consistent with the $(D^+, -D^0)$, $(D^{*+}, -D^{*0})$ isospin doublet convention, which is the same used in the analysis of Sect. 2.5.1, cf. Eq. (2.133).

Using now the values from Ref. [47]:

$$g_{D^+D^{*0}} = -3921 \text{ MeV}, \qquad g_{D^0D^{*+}} = 3658 \text{ MeV}, \tag{5.8}$$

one finds

$$g_{DD^*}^{I=0} = 5359 \text{ MeV} . \tag{5.9}$$

With this, the amplitude of Eq. (5.1) is completely defined.

We deal next with the DN interaction, which we parametrize as

$$t_{DN}^{I=0}(s) = \frac{g_{DN}^2}{\sqrt{s} - M_{\Lambda_c(2765)} + i\Gamma_{\Lambda_c(2765)}/2}, \tag{5.10}$$

with $M_{\Lambda_c(2765)}$ and $\Gamma_{\Lambda_c(2765)}$ corresponding to $\Lambda_c(2765)$ as listed in the PDG [18],

$$M_{\Lambda_c(2765)} = 2766.6 \text{ MeV}, \qquad \Gamma_{\Lambda_c(2765)} = 50 \text{ MeV}. \tag{5.11}$$

Contrary to the case of the T_{cc}, we do not rely on any previous model calculations for the coupling of the $\Lambda_c(2765)$ to the isoscalar DN channel. Instead, we determine g_{DN} through Weinberg's compositeness condition [209], assuming a fully molecular $\Lambda_c(2765)$.[4] Specifically, we use the expression of Eq. (59) in Ref. [226], adapted in Appendix D to the normalization of Eq. (5.10). This leads to

$$g_{DN}^2 = \frac{M_{\Lambda_c^*}}{4M_N\mu}\, 16\pi\gamma, \qquad \gamma = \sqrt{2\mu B_{\Lambda_c^*}}. \tag{5.12}$$

Applied to the case at hand, μ denotes the DN reduced mass, $M_{\Lambda_c^*}$ is the mass of the $\Lambda_c(2765)$ resonance and B its binding energy with respect to the DN threshold. Numerically, we obtain

$$g_{DN} = 3.70, \tag{5.13}$$

a value consistent with the couplings reported for the Λ_c^* states in Ref. [368].

It is worth noting that the corresponding scattering length predicted within this model is

$$a = (1.25 - i\,0.73) \text{ fm}.$$

The real part agrees, within uncertainties, with the result of Ref. [382], obtained from the analysis of the pD^0 mass distribution near threshold in the $\Lambda_b \to \pi^- pD^0$ decay, after accounting for the opposite sign convention of a (the imaginary part is not quoted in Ref. [382]).

[4] This resonance may also contain a molecular $\Sigma_c\pi$ component, as discussed in Ref. [367]. In the present exploratory study, however, we do not consider this possibility, nor do we include the potential contribution from the quark-model radial $2S$ excitation.

For the D^*N interaction, two spin channels are possible: $S^P = 1/2^-$ and $3/2^-$. We assume these to be dominated by the $\Lambda_c(2940)$ and $\Lambda_c(2910)$ resonances, respectively, as discussed at the beginning of this section. Accordingly, we model the scattering amplitudes as

$$t^{I=0,\,S=1/2}_{D^*N}(s) = \frac{(g^{S=1/2}_{D^*N})^2}{\sqrt{s} - M_{\Lambda_c(2940)} + i\Gamma_{\Lambda_c(2940)}/2}, \tag{5.14}$$

$$t^{I=0,\,S=3/2}_{D^*N}(s) = \frac{(g^{S=3/2}_{D^*N})^2}{\sqrt{s} - M_{\Lambda_c(2910)} + i\Gamma_{\Lambda_c(2910)}/2}. \tag{5.15}$$

The mass and width parameters of the resonances in these previous expressions are taken from the PDG [18].

$$M_{\Lambda_c(2940)} = 2939.6 \ \text{MeV}\,, \qquad \Gamma_{\Lambda_c(2940)} = 20 \ \text{MeV}\,, \tag{5.16}$$

$$M_{\Lambda_c(2910)} = 2914 \ \text{MeV}\,, \qquad \Gamma_{\Lambda_c(2910)} = 52 \ \text{MeV}\,. \tag{5.17}$$

The couplings of the D^*N pair to the corresponding Λ_c^* states are again obtained using Eq. (5.12), taking now into account the mass and binding of the corresponding Λ_c^* resonance and the reduced mass of the D^*N system. This yields the following coupling constants.

$$g^{S=1/2}_{D^*N} = 2.63, \qquad g^{S=3/2}_{D^*N} = 3.71. \tag{5.18}$$

These values are consistent with those reported in Ref. [368]. A summary table with the resonance parameters used in our model is presented in Tab. 5.1.

System	$I(J^P)$	Resonance	B [MeV]	Γ [MeV]	g
DD^*	$0(1^+)$	$T_{cc}(3875)^+$	1	0.048	5359 MeV
DN	$0\left(\frac{1}{2}^-\right)$	$\Lambda_c(2765)^+$	40	50	3.70
D^*N	$0\left(\frac{1}{2}^-\right)$	$\Lambda_c(2940)^+$	8	20	2.63
	$0\left(\frac{3}{2}^-\right)$	$\Lambda_c\,(2910)^+$	33	52	3.71

Table 5.1: Summary of the resonances taken into account in the different two–body amplitudes. B represents their binding energy with respect to the threshold of the considered channel, in the isospin limit. Γ and g represent their width and coupling, respectively.

Before proceeding any further, however, a discussion on the applicability of Eq. (5.12) for the determination of the couplings of the different Λ_c^* resonances is appropriate. The coupling of Eq. (5.12) was derived in Ref. [226] under the

assumption of a bound state generated by an energy-independent potential in the limit of small binding energy. The precise meaning of "small binding" is, however, somewhat ambiguous. In the present case the binding energies of the different Λ_c^* resonances considered range from 8 to 40 MeV, corresponding to $\gamma = 100 \sim 220$ MeV. It is usually assumed that the approximation holds when $\gamma \ll m_\pi$, which is clearly not satisfied for all the cases under consideration here. Nevertheless, the formula appears to remain accurate even at binding energies larger than naively expected.

A useful comparison can be made with the $D_{s0}^*(2317)$, which is predominantly a KD bound state in $I = 0$, with a binding energy of about 45 MeV relative to the KD threshold. Applying Eq. (5.12) directly to this system yields $g_{DK} = 12.57$ GeV. This value is essentially identical to the result $g_{DK} = 12.6$ GeV obtained in Ref. [383] using lattice QCD input, and is also consistent with the determination of Ref. [207] from K^+D^0, K^0D^+ correlation functions computed within the local hidden gauge approach [27, 28, 32, 384], which was tuned to reproduce the correct binding energy of the state and yields $g_{KD} = 10.5 \pm 3.3$ GeV. Another illustrative case is the $f_2(1270)$, commonly interpreted as a $\rho\rho$ bound state in $I = 0$, $J = 2$, with an even larger binding energy of about 270 MeV relative to the nominal $\rho\rho$ threshold (ignoring the ρ width). For this system, the coupling obtained using the formalism of Ref. [226] (for meson–meson interactions) agrees very well with the more sophisticated treatment of Ref. [385], as discussed in Ref. [371].

Once all the two–body interactions and dominant states have been presented, we examine in the next section the three–body formalism, based on the FCA.

5.2.2 The fixed center approximation

In this section, we summarize the main features of the FCA. Consider three particles, A, B, and C. The FCA assumes that two of them (say, A and B) interact strongly and form a (quasi-)bound cluster, denoted by Λ^*, whose internal dynamics are encoded in its wave function (or form factor).[5] The third particle, C, can undergo successive scatterings with the constituents of the cluster. Representative contributions to the total amplitude are shown in Fig. 5.1. We denote by $t_1 \equiv t_{CA}$ and $t_2 \equiv t_{CB}$ the two–body scattering amplitudes of C with A and B, respectively. Panels a) and b) display single–scattering processes off A and B, while c) illustrates a typical multiple–scattering sequence of C between the two constituents. By contrast, diagrams with two consecutive scatterings from the *same* constituent [panel d)] are not included explicitly: their effect is

[5]Throughout this chapter, the term "bound" is used in a loose sense, referring to narrow near-threshold states. In practice, the cluster is a resonance with a finite width.

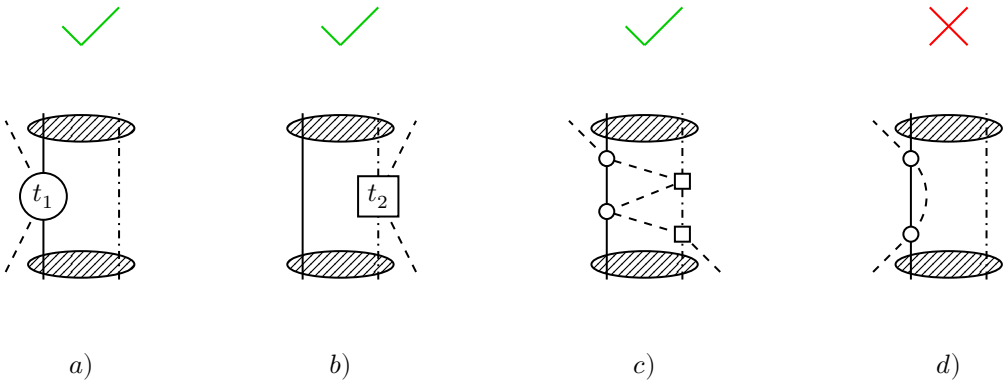

Figure 5.1: Representative FCA diagrams, with increasing time in the upward direction. a) Single scattering of C from A (t_1). b) Single scattering of C from B (t_2). c) Multiple C scatterings alternating between A and B. d) Two consecutive scatterings from the same constituent (double counting of the two–body t_1 and thus omitted in the FCA series).

assumed to be already summed in the corresponding two–body amplitude t_1 or t_2, and adding them would double count the CA or CB dynamics.[6] The interaction between A and B inside the cluster does not appear as an explicit vertex in these graphs; instead, it enters through the cluster wave function/form factor that weights each C-cluster collision in momentum space.

Next, we present how to perform the resummation of all diagrams within the FCA. Two partition amplitudes, T_1 and T_2, are defined, each accounting for every sequence of interactions that begins with the external particle C scattering off particle A or B, respectively, of the compound system. Therefore, the sum of these two partition amplitudes results in the full amplitude for the process, T. Diagrammatically, one can write

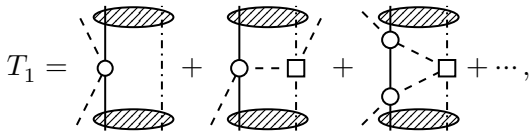

(5.19a)

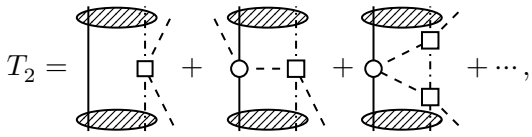

(5.19b)

[6] In the present approach, we assume that the t_1 and t_2 amplitudes are approximately unitary. If unitarity is not fulfilled, additional contributions from diagrams of the type shown in panel d) must be included. However, as discussed in Refs. [386, 387], this effect is most relevant above threshold.

$$T = T_1 + T_2. \tag{5.19c}$$

Translating now the previous diagrams into mathematical expressions (employing the usual on-shell factorization), we can write

$$T_1 = t_1 + t_1 G t_2 + t_1 G t_2 G t_1 + \cdots = t_1 + t_1 G T_2, \tag{5.20a}$$

$$T_2 = t_2 + t_2 G t_1 + t_2 G t_1 G t_2 + \cdots = t_2 + t_2 G T_1, \tag{5.20b}$$

$$T = T_1 + T_2, \tag{5.20c}$$

where G is the C particle propagator weighted by the cluster form factor (we shall show this in Sect. 5.2.3). With this, we have obtained a coupled system of algebraic equations, whose solution,

$$T = \frac{t_1 + t_2 + 2t_1 G t_2}{1 - t_1 G t_2 G}, \tag{5.21}$$

presents an approximation to the three–body transition matrix T.

It should be noted that the normalization of the two–body amplitudes t_1 and t_2 does not, in general, coincide with that of the three–body amplitude T. To ensure the consistency of Eq. (5.21), we introduce properly normalized quantities $\tilde{t}_1$, $\tilde{t}_2$, and $\tilde{G}$, a point that will be discussed in detail in Sect. 5.2.5.

Another important point concerns the kinematic dependence of the amplitudes. While the full three–body amplitude T depends on the invariant mass of the entire system, s, the two–body amplitudes t_1 and t_2 involve instead the invariant masses of the subsystems CA and CB, respectively. In our approach, these are evaluated approximately in the rest frame of the Λ^* cluster by neglecting the internal momentum of A and B, leading to

$$s_1 = (p_C + p_A)^2 \simeq M_C^2 + (\xi M_A)^2 + 2p_C^0(\xi M_A), \tag{5.22a}$$

$$s_2 = (p_C + p_B)^2 \simeq M_C^2 + (\xi M_B)^2 + 2p_C^0(\xi M_B), \tag{5.22b}$$

where

$$p_C^0 = \frac{s - M_C^2 - M_{\Lambda^*}^2}{2M_{\Lambda^*}} \tag{5.23}$$

denotes the energy of particle C in this frame. We include a correction factor $\xi = M_{\Lambda^*}/(M_A + M_B)$ for the masses of the A and B particles inside the Λ^* cluster, in order to account for their *off-shellness*.[7] With this factor, the effective (off-shell) masses satisfy the natural condition that their sum equals the cluster mass:

$$\xi M_A + \xi M_B = M_{\Lambda^*}. \tag{5.24}$$

[7]The expressions for s_1 and s_2 differ slightly from those used in Refs. [329, 333], but become exactly equivalent in the limit $\xi \to 1$.

Up to this point, we have introduced the main equation governing the three–body amplitude within the FCA formalism [Eq. (5.21)], together with the relations connecting the two–body invariant masses s_1 and s_2—which enter the factorized two–body amplitudes—to the total three–body invariant mass s. We now turn to the discussion of the loop function G appearing in Eq. (5.21). For this purpose, we will define the cluster form factor.

5.2.3 The loop function and form factor of the cluster

In order to illustrate how the form factor of the cluster weights the C propagator, in this section we compute the S–matrix elements corresponding to the diagrams of a single and double scattering, following the reasoning of Ref. [328]. In doing this, we will obtain an expression for the G factor appearing in Eqs. (5.20).

Single scattering contribution

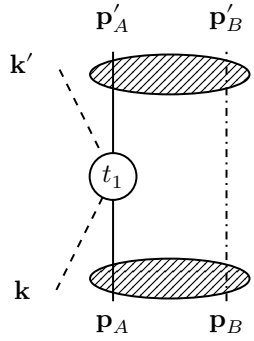

Figure 5.2: Single-scattering diagram where particle C (four momentum $\mathbf{k}$) interacts with particle A (four momentum $\mathbf{p}_A$), described by the amplitude t_1.

Let us examine the single-scattering diagram entering the T_1 contribution of Eq. (5.19a), shown in Fig. 5.2. The wave functions of the incoming (outgoing) C particle are taken as plane waves with four-momentum $\mathbf{k}$ ($\mathbf{k}'$),[8] normalized in a box of volume $\mathcal{V}$. The internal wave functions of the A and B particles are denoted φ_A and φ_B, respectively. For normalization, A and C are treated as mesons, while B is treated as a baryon, in analogy with the DND^* system. At the same time, some generality is preserved, as we will also allow for clusters formed by either DN or D^*N pairs. Under these definitions, the S–matrix element for single scattering takes the form

[8] In this chapter, as in the rest of the thesis, we adopt the following notation: four-vectors are written in bold ($\mathbf{k}$), three-vectors with the usual vector notation ($\vec{k}$), and the magnitude of a three-vector without additional markings (k).

$$S^{(1)} = \int d^4\mathbf{x}\ \frac{1}{\sqrt{2\omega_k \mathcal{V}}} e^{-i\mathbf{k}\mathbf{x}} \frac{1}{\sqrt{2\omega_{k'} \mathcal{V}}} e^{i\mathbf{k}'\mathbf{x}} \times \frac{1}{\sqrt{2\omega_{p_A}}} e^{-ip_A^0 x^0}\ \varphi_A(\vec{x})\ \frac{1}{\sqrt{2\omega_{p'_A}}} e^{ip'^0_A x^0}\ \varphi^*_A(\vec{x})\,(-it_1). \quad (5.25)$$

The momentum labels used here are shown schematically in Fig. 5.2, and the asterisk denotes the complex conjugation of the wave function. We also assume that the B particle in the cluster acts as a spectator, so that $p_B^0 = p'^0_B$ (impulse approximation). Integrating now over the time component x^0 imposes energy conservation at the interaction point $\mathbf{x}$:

$$\int dx^0 e^{-ik^0 x^0} e^{ik'^0 x^0} e^{-ip_A^0 x^0} e^{ip'^0_A x^0} = 2\pi\ \delta(k^0 + p_A^0 - k'^0 - p'^0_A) = 2\pi\ \delta(k^0 + E_{\Lambda^*} - k'^0 - E'_{\Lambda^*}). \quad (5.26)$$

Given the normalization condition of the B particle wave function, we can multiply the expression of Eq. (5.25) by

$$\int d^3x' \varphi_B(\vec{x}')\varphi^*_B(\vec{x}') = 1, \quad (5.27)$$

and then perform a change of variables to the center-of-mass and relative coordinates,

$$\vec{R} = \frac{M_A\vec{x} + M_B\vec{x}'}{M_A + M_B}, \qquad \vec{r} = \vec{x} - \vec{x}'. \quad (5.28)$$

With this, it is customary to the write the product of A and B wave functions as the product of the center-of-mass wave function—described by a plane wave due to its free motion—and the relative wave function Ψ_{Λ^*}:

$$\varphi_A(\vec{x})\varphi_B(\vec{x}') = \frac{1}{\sqrt{\mathcal{V}}} e^{i\vec{K}_{\Lambda^*}\cdot\vec{R}} \Psi_{\Lambda^*}(\vec{r}), \quad (5.29a)$$

$$\varphi^*_A(\vec{x})\varphi^*_B(\vec{x}') = \frac{1}{\sqrt{\mathcal{V}}} e^{-i\vec{K}'_{\Lambda^*}\cdot\vec{R}} \Psi^*_{\Lambda^*}(\vec{r}). \quad (5.29b)$$

Here, $\vec{K}_{\Lambda^*}$ ($\vec{K}'_{\Lambda^*}$) denotes the incoming (outgoing) three-momentum of the cluster. Carrying out the integral over the center-of-mass coordinate gives total three-momentum conservation:

$$\int d^3R\ e^{i\vec{k}\cdot\vec{R}} e^{-i\vec{k}'\cdot\vec{R}} e^{i\vec{K}_{\Lambda^*}\cdot\vec{R}} e^{-i\vec{K}'_{\Lambda^*}\cdot\vec{R}} = (2\pi)^3\ \delta^3\left(\vec{k} + \vec{K}_{\Lambda^*} - \vec{k}' - \vec{K}'_{\Lambda^*}\right). \quad (5.30)$$

Likewise, integrating over the relative coordinate yields

$$\int d^3r\ e^{i\frac{M_B}{M}\vec{k}\cdot\vec{r}} e^{-i\frac{M_B}{M}\vec{k}'\cdot\vec{r}} \Psi_{\Lambda^*}(\vec{r})\Psi^*_{\Lambda^*}(\vec{r}) = F_{\Lambda^*}\left[\frac{M_B}{M}(\vec{k}' - \vec{k})\right], \quad (5.31)$$

where $M = M_A + M_B$. This expression—the Fourier transform of the spatial probability density of the cluster—defines the cluster form factor F_{Λ^*}. It is customary to approximate the momentum of the external particle C as nearly unchanged, so that

$$\vec{k} \simeq \vec{k}' \qquad \rightarrow \qquad F_{\Lambda^*}\left[\frac{M_B}{M}(\vec{k}' - \vec{k})\right] \simeq F_{\Lambda^*}[\vec{0}] = 1, \tag{5.32}$$

with the form factor normalized to unity at the origin due to the normalization of the $\Psi_{\Lambda^*}(\vec{r})$ wave function. Finally, the S–matrix element for the diagram of Fig. 5.2 takes the form

$$S^{(1)} = -it_1 \frac{1}{\mathcal{V}^2} \frac{1}{\sqrt{2\omega_k}} \frac{1}{\sqrt{2\omega_{k'}}} \frac{1}{\sqrt{2\omega_{p_A}}} \frac{1}{\sqrt{2\omega_{p'_A}}} \times (2\pi)^4 \delta^4 \left(\mathbf{k} + \mathbf{K}_{\Lambda^*} - \mathbf{k}' - \mathbf{K}'_{\Lambda^*}\right). \tag{5.33}$$

One can proceed similarly for the single scattering diagram involving t_2 and find an analogous result.

Double scattering contribution

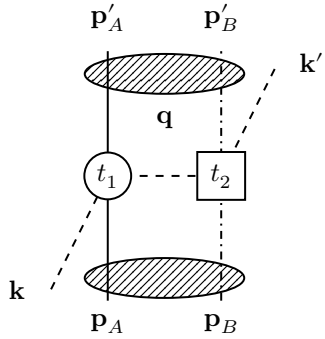

Figure 5.3: Double-scattering of the external particle C (momentum $\mathbf{k}$) with particles A ($\mathbf{p}_A$) and B ($\mathbf{p}_B$) inside the cluster.

Next, we evaluate the amplitude of the double–scattering contribution, shown in the second diagram of Eq. (5.19a) and depicted in Fig. 5.3. The corresponding S–matrix element is

$$S^{(2)} = \int d^4\mathbf{x} \int d^4\mathbf{x}' \frac{1}{\sqrt{2\omega_{p_A}}} e^{-ip_A^0 x^0} \varphi_A(\vec{x}) \frac{1}{\sqrt{2\omega_{p'_A}}} e^{ip'^0_A x^0} \varphi^*_A(\vec{x})$$

$$\times \sqrt{\frac{M_B}{E_{p_B}}} e^{-ip_B^0 x'^0} \varphi_B(\vec{x}') \sqrt{\frac{M_B}{E_{p'_B}}} e^{ip'^0_B x'^0} \varphi_B^*(\vec{x}')$$

$$\times \frac{1}{\sqrt{2\omega_k \mathcal{V}}} e^{-i\mathbf{k}\mathbf{x}} \frac{1}{\sqrt{2\omega_{k'} \mathcal{V}}} e^{i\mathbf{k}'\mathbf{x}'}$$

$$\times i \int \frac{d^4\mathbf{q}}{(2\pi)^4} \frac{e^{i\mathbf{q}(\mathbf{x}-\mathbf{x}')}}{\mathbf{q}^2 - M_C^2 + i\varepsilon} (-it_1)(-it_2). \tag{5.34}$$

As in the single-scattering case, integration over the time components of $\mathbf{x}$ and $\mathbf{x}'$ enforces energy conservation at each interaction point:

$$\int dx^0 \, e^{-ip_A^0 x^0} e^{ip'^0_A x^0} e^{-ik^0 x^0} e^{iq^0 x^0} = 2\pi \, \delta(p_A^0 + k^0 - p'^0_A - q^0) \,, \tag{5.35}$$

$$\int dx'^0 \, e^{-ip_B^0 x'^0} e^{ip'^0_B x'^0} e^{ik^0 x'^0} e^{-iq^0 x'^0} = 2\pi \, \delta(p_B^0 + q^0 - p'^0_B - k'^0) \,. \tag{5.36}$$

Implementing the change of variables of Eq. (5.28), the integral over the center-of-mass coordinate yields overall three-momentum conservation, identical to Eq. (5.30). The remaining integral over the relative coordinate gives

$$\int d^3r \, \Psi_{\Lambda^*}(\vec{r}) \Psi^*_{\Lambda^*}(\vec{r}) e^{i\frac{M_B}{M}\vec{k}\cdot\vec{r}} e^{i\frac{M_A}{M}\vec{k}'\cdot\vec{r}} e^{-i\vec{q}\cdot\vec{r}} = F_{\Lambda^*}\left(\vec{q} - \frac{M_B\vec{k} + M_A\vec{k}'}{M}\right) . \tag{5.37}$$

Altogether, the double-scattering S–matrix element becomes

$$S^{(2)} = -i(2\pi)^4 \, \delta^4(\mathbf{k} + \mathbf{K}_{\Lambda^*} - \mathbf{k}' - \mathbf{K}'_{\Lambda^*})$$

$$\times \frac{1}{\mathcal{V}^2} \frac{1}{\sqrt{2\omega_k}} \frac{1}{\sqrt{2\omega_{k'}}} \frac{1}{\sqrt{2\omega_{p_A}}} \frac{1}{\sqrt{2\omega_{p'_A}}} \sqrt{\frac{M_B}{E_{p_B}}} \sqrt{\frac{M_B}{E_{p'_B}}}$$

$$\times \int \frac{d^3q}{(2\pi)^3} F_{\Lambda^*}(q) \frac{1}{(q^0)^2 - \vec{q}^2 - M_C^2 + i\varepsilon} \, t_1 t_2. \tag{5.38}$$

Factoring out the two–body amplitudes t_1 and t_2 (on-shell approximation) and comparing with Eq. (5.20a), the loop function G can be identified, up to a normalization, as

$$G = \int \frac{d^3q}{(2\pi)^3} \frac{F_{\Lambda^*}(q)}{(q^0)^2 - \vec{q}^2 - M_C^2 + i\varepsilon}, \tag{5.39}$$

that is, the propagator of the exchanged particle C weighted by the form factor of the Λ^* cluster.

Two remarks are in order in these previous two expressions. First, we shall evaluate q^0 in the Λ^* rest frame, so that

$$q^0(s) = \frac{s - M_C^2 - M_{\Lambda^*}^2}{2M_{\Lambda^*}^2}, \tag{5.40}$$

where s represents the total invariant mass $s = (\mathbf{k} + \mathbf{K}_{\Lambda^*})^2$, and we have considered $p_A^0 = p_A'^0$ and $p_B^0 = p_B'^0$, which is true on average. Second, we have neglected

$$\frac{M_B\vec{k} + M_A\vec{k}'}{M} \simeq \vec{0} \tag{5.41}$$

in the argument of the form factor, which is also true on average.

Evaluation of the form factor

We now turn to the evaluation of the form factor that first appeared in Eq. (5.37). For this purpose, we follow the approach of Ref. [226], also adopted in Ref. [328]. The formalism of Ref. [226] was already introduced in Sect. 2.4.2 in connection with the concept of compositeness (or molecular probability). Here, we make use of it to obtain the explicit expression of the bound-state wave function in momentum space, which provides the basis for the form factor.

In Ref. [226], a separable potential of the form

$$V(\vec{q}, \vec{q}') = v\ \theta(q_{\max} - q)\,\theta(q_{\max} - q') \tag{5.42}$$

was employed, where θ denotes the Heaviside step function and $q_{\max}$ is a three-momentum cutoff. This choice reduces the standard integral equation for the scattering matrix to a simple algebraic relation. In this thesis, we consistently adopt the on-shell prescription, which achieves the same simplification.

Starting from the time-independent Schrödinger equation governing the relative motion of the AB system, with the cluster state $|\Psi_{\Lambda^*}\rangle$ as an eigenstate of energy E_{Λ^*},

$$\hat{H}|\Psi_{\Lambda^*}\rangle = E_{\Lambda^*}|\Psi_{\Lambda^*}\rangle, \tag{5.43}$$

we separate the Hamiltonian into a free part, $\hat{H}_0$, and an interaction part, $\hat{V}$, so that

$$(\hat{H}_0 + \hat{V})|\Psi_{\Lambda^*}\rangle = E_{\Lambda^*}|\Psi_{\Lambda^*}\rangle, \tag{5.44}$$

$$|\Psi_{\Lambda^*}\rangle = \frac{\hat{V}}{E_{\Lambda^*} - \hat{H}_0}|\Psi_{\Lambda^*}\rangle. \tag{5.45}$$

Inserting two complete sets of momentum states, the wave function in momentum space can be written as

$$\langle \vec{p}|\Psi_{\Lambda^*}\rangle = \int \frac{d^3q}{(2\pi)^3}\int \frac{d^3q'}{(2\pi)^3}\langle \vec{p}|\frac{1}{E_{\Lambda^*}-\hat{H}_0}|\vec{q}\rangle\,\langle \vec{q}|\hat{V}|\vec{q}'\rangle\,\langle \vec{q}'|\Psi_{\Lambda^*}\rangle$$
$$= \frac{v\,\theta(q_{\max}-p)}{E_{\Lambda^*}-\omega_A(p)-\omega_B(p)}\int \frac{d^3q'}{(2\pi)^3}\langle \vec{q}'|\Psi_{\Lambda^*}\rangle. \quad (5.46)$$

Given that the quantity

$$v\int \frac{d^3q'}{(2\pi)^3}\langle \vec{q}'|\Psi_{\Lambda^*}\rangle = g \quad (5.47)$$

is a constant, the momentum-space wave function of the bound state takes the form

$$\langle \vec{p}|\Psi_{\Lambda^*}\rangle = \theta(q_{\max}-p)\,\frac{g}{M_{\Lambda^*}-\omega_A(p)-\omega_B(p)}. \quad (5.48)$$

Since $|\Psi_{\Lambda^*}\rangle$ is an eigenstate of the relative-motion Hamiltonian of the AB system, the above expression is written in the rest frame of the Λ^* cluster. There, $\vec{p}$ denotes the relative momentum, M_{Λ^*} the cluster mass, and g the coupling constant, while $\omega_{A(B)}$ are the relativistic energies of particles A and B. The coordinate-space wave function then follows as the Fourier transform:

$$\langle \vec{r}|\Psi_{\Lambda^*}\rangle = \int \frac{d^3p}{(2\pi)^3}e^{i\vec{p}\cdot\vec{r}}\,\langle \vec{p}|\Psi_{\Lambda^*}\rangle. \quad (5.49)$$

We now compute the Λ^* cluster form factor from its definition in Eq. (5.31), using the coordinate-space cluster wave function. This gives

$$\tilde{F}_{\Lambda^*}(q) = \int d^3r\, e^{-i\vec{q}\cdot\vec{r}}$$
$$\times \int \frac{d^3p}{(2\pi)^3}e^{i\vec{p}\cdot\vec{r}}\,\theta(q_{\max}-p)\,\frac{1}{M_{\Lambda^*}-\omega_A(p)-\omega_B(p)}$$
$$\times \int \frac{d^3p'}{(2\pi)^3}e^{i\vec{p}'\cdot\vec{r}}\,\theta(q_{\max}-p')\,\frac{1}{M_{\Lambda^*}-\omega_A(p')-\omega_B(p')}$$
$$= \int \frac{d^3p}{(2\pi)^3}\,\theta(q_{\max}-p)\,\theta(q_{\max}-|\vec{q}-\vec{p}|)$$
$$\times \frac{1}{M_{\Lambda^*}-\omega_A(p)-\omega_B(p)}\,\frac{1}{M_{\Lambda^*}-\omega_A(|\vec{q}-\vec{p}|)-\omega_B(|\vec{q}-\vec{p}|)}. \quad (5.50)$$

Finally, we normalize the form factor so that it equals unity at the origin:

$$F_{\Lambda^*}(q) = \frac{\tilde{F}_{\Lambda^*}(q)}{\tilde{F}_{\Lambda^*}(0)}. \quad (5.51)$$

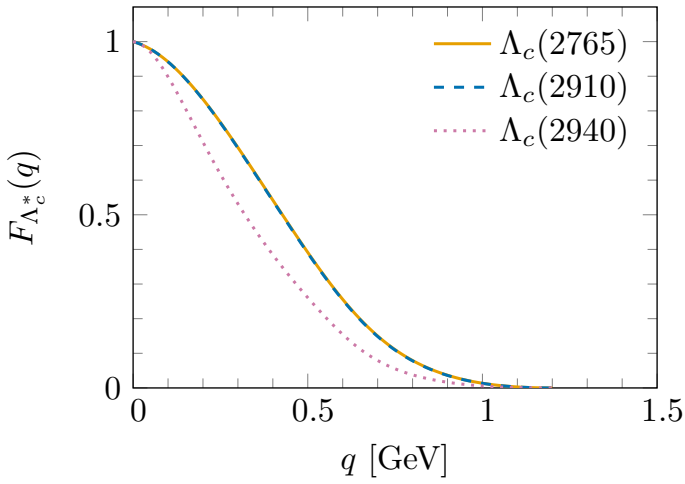

Figure 5.4: Form factors of the considered Λ_c^* states as a function of the three-momentum.

For the evaluation of Eq. (5.50), we adopt a cutoff of $q_{\max} = 600$ MeV. This value is of natural size and was also found suitable for reproducing the P_{cs} states in Ref. [388]. In what follows, we consider three possible clusters. The DN system is associated with the $\Lambda_c(2765)$ resonance, while the D^*N system may correspond either to the $\Lambda_c(2940)$ or to the $\Lambda_c(2910)$, depending on its spin assignment. Figure 5.4 displays the form factors obtained for each of these three resonances, which serve as input for the subsequent calculations. It is apparent that the $\Lambda_c(2940)$ form factor is significantly narrower than those of the other states. This behavior reflects its relatively shallow binding: a less bound state exhibits a broader wave function in coordinate space, which translates into a narrower distribution in momentum space.

Once the form factors are determined, the G function of Eq. (5.39) can be directly evaluated. It should be emphasized that, unlike the standard loop functions discussed in previous chapters, G does not require any explicit regularization. This is because the loop integral remains finite: the cluster form factor suppresses contributions from large momenta and vanishes in the high-momentum limit.

In the following sections, two additional aspects must be addressed in order to complete the formalism. On the one hand, it is necessary to carefully account for the spin and isospin structure of the amplitudes. On the other hand, the normalization of these amplitudes also requires attention.

5.2.4 Isospin and spin considerations

In this section we analyze the isospin and spin structure of the two–body amplitudes t_1 and t_2, which enter the three–body amplitude through Eq. (5.21) within the FCA. Two cluster configurations are considered: one where the ND^* pair forms the cluster, denoted $D(ND^*)$, and another where the ND pair forms the cluster, denoted $D^*(ND)$.

$D(ND^*)$ configuration

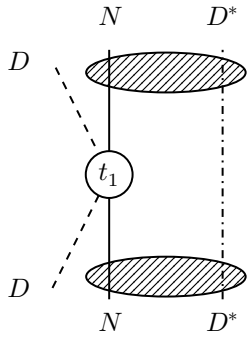

Figure 5.5: FCA single-scattering diagram with an external D meson scattering off a nucleon within the ND^* cluster, corresponding to the configuration we shall refer to as $D(ND^*)$.

We begin by examining the isospin structure of the two–body amplitudes, focusing first on the case where the ND^* pair forms either the $\Lambda_c(2940)$ or the $\Lambda_c(2910)$, both of which are isoscalar resonances. In the FCA framework, the external D meson interacts with one of the cluster constituents. As a starting point, we consider the case where the D meson interacts with the nucleon (see Fig. 5.5). The relevant isospin doublets are

$$N = \begin{pmatrix} p \\ n \end{pmatrix}, \qquad D^{(*)} = \begin{pmatrix} D^{(*)+} \\ -D^{(*)0} \end{pmatrix}, \tag{5.52}$$

where p and n denote the proton and neutron, and the standard isospin convention is adopted for the $D^{(*)}$ mesons.

Take for example the case of an external D^+ meson (the particular choice of the third component of isospin is irrelevant owing to the Wigner–Eckart theorem). Since the ND^* system is coupled in an isoscalar state, the full three–body state will have isospin 1/2. We may write it as

$$|\tfrac{1}{2},+\tfrac{1}{2}\rangle \otimes |0,0\rangle = |\tfrac{1}{2},+\tfrac{1}{2}\rangle \otimes \frac{1}{\sqrt{2}}\left[|\tfrac{1}{2},+\tfrac{1}{2}\rangle \otimes |\tfrac{1}{2},-\tfrac{1}{2}\rangle - |\tfrac{1}{2},-\tfrac{1}{2}\rangle \otimes |\tfrac{1}{2},+\tfrac{1}{2}\rangle\right]$$
$$= \frac{1}{\sqrt{2}}\left\{|1,1\rangle \otimes |\tfrac{1}{2},-\tfrac{1}{2}\rangle - \frac{1}{\sqrt{2}}\left(|1,0\rangle + |0,0\rangle\right) \otimes |\tfrac{1}{2},+\tfrac{1}{2}\rangle\right\}. \quad (5.53)$$

The corresponding T–matrix element is

$$t_1^{I=1/2} = \langle \tfrac{1}{2},+\tfrac{1}{2}| \otimes \langle 0,0|t_{DN}|\tfrac{1}{2},+\tfrac{1}{2}\rangle \otimes |0,0\rangle$$
$$= \frac{1}{2}\left\{t_{DN}^{I=1} + \frac{1}{2}\left(t_{DN}^{I=1} + t_{DN}^{I=0}\right)\right\} = \tfrac{1}{4}\, t_{DN}^{I=0} + \tfrac{3}{4}\, t_{DN}^{I=1}. \quad (5.54)$$

A similar analysis applies when the external D meson interacts with the D^* inside the cluster, leading to

$$t_2^{I=1/2} = \tfrac{1}{4}\, t_{DD^*}^{I=0} + \tfrac{3}{4}\, t_{DD^*}^{I=1}. \quad (5.55)$$

Following Refs. [328, 333, 389], and as already noted in Sect. 5.2.1, we assume that the dominant contribution arises from the isoscalar channel,

$$t_1^{I=1/2} \simeq \tfrac{1}{4}\, t_{DN}^{I=0}, \quad (5.56a)$$
$$t_2^{I=1/2} \simeq \tfrac{1}{4}\, t_{DD^*}^{I=0}. \quad (5.56b)$$

The validity of this assumption will be reassessed when discussing our results.

Next, we deal with the spin structure of the amplitudes. Now, the structure depends on whether the ND^* system is clustered together in either the $\Lambda_c(2940)$ or the $\Lambda_c(2910)$, which we take to be spin 1/2 and 3/2, respectively. Let us focus firstly on the spin 1/2 case, where an external D meson interacts with the nucleon within the cluster. We take the system in the following state

$$|0,0\rangle \otimes |\tfrac{1}{2},+\tfrac{1}{2}\rangle = |0,0\rangle \otimes \left[\frac{1}{\sqrt{3}}|\tfrac{1}{2},+\tfrac{1}{2}\rangle \otimes |1,0\rangle - \sqrt{\frac{2}{3}}|\tfrac{1}{2},-\tfrac{1}{2}\rangle \otimes |1,+1\rangle\right]$$
$$= \frac{1}{\sqrt{3}}|\tfrac{1}{2},+\tfrac{1}{2}\rangle \otimes |1,0\rangle - \sqrt{\frac{2}{3}}|\tfrac{1}{2},-\tfrac{1}{2}\rangle \otimes |1,+1\rangle. \quad (5.57)$$

With this, the DN T–matrix element is found to have the following decomposition:

$$t_1^{J=1/2} = \langle 0,0| \otimes \langle \tfrac{1}{2},+\tfrac{1}{2}|t_{DN}|0,0\rangle \otimes |\tfrac{1}{2},+\tfrac{1}{2}\rangle$$
$$= \frac{1}{3}t_{DN}^{S=1/2} + \frac{2}{3}t_{DN}^{S=1/2} = t_{DN}^{S=1/2}. \quad (5.58)$$

Since the D meson is a scalar particle and the nucleon has spin 1/2, the DN amplitude can only be spin 1/2. We can perform a similar reasoning for the DD^* amplitude and readily find

$$t_2^{J=1/2} = t_{DD^*}^{S=1}. \tag{5.59}$$

If we now consider the ND^* cluster to have spin 3/2, the state of the system being

$$|\overset{D}{0},0\rangle \otimes |\overset{ND^*}{\tfrac{3}{2}},+\tfrac{3}{2}\rangle = |\overset{D}{0},0\rangle \otimes |\overset{N}{\tfrac{1}{2}},+\tfrac{1}{2}\rangle \otimes |\overset{D^*}{1},+1\rangle, \tag{5.60}$$

we similarly find

$$t_1^{J=3/2} = t_{DN}^{S=1/2}, \tag{5.61}$$

$$t_2^{J=3/2} = t_{DD^*}^{S=1}. \tag{5.62}$$

In summary, bringing together all the previous results on spin and isospin, we have two possible channels:

$$I(J^P) = \tfrac{1}{2}(\tfrac{1}{2}^+),\ ND^* \text{ bound into } \Lambda_c(2940),\ \begin{cases} t_1^{I=1/2,J=1/2} = \dfrac{1}{4} t_{DN}^{I=0,\,S=1/2} \\ t_2^{I=1/2,J=1/2} = \dfrac{1}{4} t_{DD^*}^{I=0,\,S=1} \end{cases}, \tag{5.63a}$$

$$I(J^P) = \tfrac{1}{2}(\tfrac{3}{2}^+),\ ND^* \text{ bound into } \Lambda_c(2910),\ \begin{cases} t_1^{I=1/2,J=3/2} = \dfrac{1}{4} t_{DN}^{I=0,\,S=1/2} \\ t_2^{I=1/2,J=3/2} = \dfrac{1}{4} t_{DD^*}^{I=0,\,S=1} \end{cases}. \tag{5.63b}$$

As we can see, the amplitudes t_1 and t_2 are the same in both total spin scenarios. This is due to the fact that the D meson carries no spin, so the total spin is solely determined by the spin of the ND^* pair, whether they are bound into the $\Lambda_c(2940)$ or the $\Lambda_c(2910)$. Therefore, total spin dependence will enter through the form factor within the loop function G, not through the amplitudes t_1 and t_2. In the alternate configuration studied in the following subsection, this will not be the case.

$D^*(ND)$ configuration

Alternatively, one may assume the cluster to be composed of the D and the nucleon, with the D^* as the external particle, see Fig. 5.6. We denote this configuration as $D^*(ND)$. From the isospin point of view, this case is fully

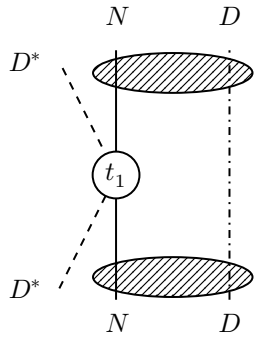

Figure 5.6: FCA single-scattering diagram with an external D^* meson interacting with the nucleon inside the ND cluster, corresponding to the configuration $D^*(ND)$.

equivalent to the $D(ND^*)$, since all particles are isodoublets and combine in the same way, leading to

$$t_1^{I=1/2} \simeq \tfrac{1}{4}\, t_{D^*N}^{I=0}, \tag{5.64a}$$

$$t_2^{I=1/2} \simeq \tfrac{1}{4}\, t_{DD^*}^{I=0}. \tag{5.64b}$$

With respect to the spin structure, the ND cluster only has one spin possibility: $S = \frac{1}{2}$, corresponding to the $\Lambda_c(2765)$. Depending on how the external D^* spin adds up to the spin of the cluster, we can have total spin $J = \frac{1}{2}$ and $\frac{3}{2}$. Starting with the first possibility, we may write the state of the system as

$$|\tfrac{1}{2},\tfrac{1}{2}\rangle^{D^*ND} = \sqrt{\frac{2}{3}}|1,+1\rangle^{D^*} \otimes |\tfrac{1}{2},-\tfrac{1}{2}\rangle^{ND} - \frac{1}{\sqrt{3}}|1,0\rangle^{D^*} \otimes |\tfrac{1}{2},+\tfrac{1}{2}\rangle^{ND} = |\tfrac{1}{2},\tfrac{1}{2}\rangle^{D^*N} \otimes |0,0\rangle^{D}. \tag{5.65}$$

Thus, for the D^*N interaction we have

$$t_1^{J=1/2} = t_{D^*N}^{S=1/2}, \tag{5.66}$$

since the total spin is determined by the D^*N pair, the D being a scalar meson. With respect to the D^*D interaction, we can easily find

$$t_2^{J=1/2} = t_{D^*D}^{S=1}, \tag{5.67}$$

since there is no other possibility for the combination of the scalar D with the vector D^*.

Turning now to the total spin $J = 3/2$ case, an analogous argument leads to the amplitudes

$$t_1^{J=3/2} = t_{D^*N}^{S=3/2}, \tag{5.68}$$

$$t_2^{J=3/2} = t_{D^*N}^{S=1}. \tag{5.69}$$

In summary, taking together the isospin and spin decompositions previously shown, in this scenario we have the following:

$$I(J^P) = \tfrac{1}{2}(\tfrac{1}{2}^+),\ ND \text{ bound into } \Lambda_c(2765),\ \begin{cases} t_1^{I=1/2,J=1/2} = \dfrac{1}{4} t_{D^*N}^{I=0,\,S=1/2} \\ t_2^{I=1/2,J=1/2} = \dfrac{1}{4} t_{DD^*}^{I=0,\,S=1} \end{cases}, \tag{5.70a}$$

$$I(J^P) = \tfrac{1}{2}(\tfrac{3}{2}^+),\ ND \text{ bound into } \Lambda_c(2765),\ \begin{cases} t_1^{I=1/2,J=3/2} = \dfrac{1}{4} t_{D^*N}^{I=0,\,S=3/2} \\ t_2^{I=1/2,J=3/2} = \dfrac{1}{4} t_{DD^*}^{I=0,\,S=1} \end{cases}. \tag{5.70b}$$

With respect to the $D(ND^*)$ configuration diagrammatically reviewed in Eq. (5.63), the spin dependence is contained in the t_1 amplitudes, while the form factor is the same in both spin scenarios. The t_2 amplitude, corresponding to DD^*, is the same in both approaches. Note that, in all scenarios, a universal factor of $1/4$ multiplies the isoscalar amplitudes. While this reduces the overall strength of the total T–matrix, it does not significantly affect the position of the generated peaks. This completes our discussion of the isospin structure.

5.2.5 Some considerations on the normalizations

Next, we deal with the important issue of the normalization of the different T–matrix elements and loops. As one can see from the FCA equations for the three–body amplitude, Eq. (5.20), the amplitude T must share the same normalization as the different terms t_1, t_2, $t_1 G t_2$, and so on. Actually, analyzing these three first terms is sufficient to impose the correct normalization on all the terms of the perturbative resummation. We will refer to the correctly normalized amplitudes as $\tilde{t}_1$ and $\tilde{t}_2$, and similarly for the loop function $\tilde{G}$.

We impose that the total T–matrix is normalized as a two–body $C\Lambda^*$ scattering, with C the external particle and Λ^* the cluster. Let us apply this for the $D(ND^*)$ scenario, where the ND^* system is bound into either the $\Lambda_c(2940)$ or the $\Lambda_c(2910)$ depending on the spin. The S–matrix element corresponding to the full amplitude will be written as

$$S = -i(2\pi)^4 \delta^4(\cdots) \times \frac{1}{\mathcal{V}^2} \frac{1}{\sqrt{2\omega_D}} \frac{1}{\sqrt{2\omega'_D}} \sqrt{\frac{M_{\Lambda^*}}{E_{\Lambda^*}}} \sqrt{\frac{M_{\Lambda^*}}{E'_{\Lambda^*}}}\ T. \tag{5.71}$$

where the $\delta^4(\cdots)$ denotes the total energy-momentum conservation delta, and the subscript Λ^* denotes the $\Lambda_c^*(2940)/\Lambda_c^*(2910)$ state. Turning now to the DN S–matrix, we may write it as

$$S^{(1)} = -i(2\pi)^4\delta^4(\cdots)\times\frac{1}{\mathcal{V}^2}\frac{1}{\sqrt{2\omega_D}}\frac{1}{\sqrt{2\omega'_D}}\sqrt{\frac{M_N}{E_N}}\sqrt{\frac{M_N}{E'_N}}\,t_1, \tag{5.72}$$

while for DD^* we have

$$S^{(2)} = -i(2\pi)^4\delta^4(\cdots)\times\frac{1}{\mathcal{V}^2}\frac{1}{\sqrt{2\omega_D}}\frac{1}{\sqrt{2\omega'_D}}\frac{1}{\sqrt{2\omega_{D^*}}}\frac{1}{\sqrt{2\omega'_{D^*}}}\,t_2. \tag{5.73}$$

Imposing now that both $\tilde{t}_1$ and $\tilde{t}_2$ have the same normalization as T, we have

$$\sqrt{\frac{M_{\Lambda^*}}{E_{\Lambda^*}}}\sqrt{\frac{M_{\Lambda^*}}{E'_{\Lambda^*}}}\,\tilde{t}_1 = \sqrt{\frac{M_N}{E_N}}\sqrt{\frac{M_N}{E'_N}}\,t_1 \qquad \Rightarrow \qquad \tilde{t}_1 = t_1, \tag{5.74}$$

$$\sqrt{\frac{M_{\Lambda^*}}{E_{\Lambda^*}}}\sqrt{\frac{M_{\Lambda^*}}{E'_{\Lambda^*}}}\,\tilde{t}_2 = \frac{1}{\sqrt{2\omega_{D^*}}}\frac{1}{\sqrt{2\omega'_{D^*}}}\,t_2 \qquad \Rightarrow \qquad \tilde{t}_2 = \frac{1}{2M_{D^*}}t_2. \tag{5.75}$$

In these relations, we have approximated the different energies by their values at zero three-momentum. Note that these relations do not depend on whether we consider the ND^* system to be bound into the $\Lambda_c(2940)$ or the $\Lambda_c(2910)$.

We also need to pay attention to the normalization of the loop function first presented in Eq. (5.39). For that, we analyze the normalization of the double-scattering contribution to the S–matrix. In the normalization of the full amplitude of Eq. (5.71), we would have

$$S^{(2)} = -i(2\pi)^4\delta^4(\cdots)\times\frac{1}{\mathcal{V}^2}\frac{1}{\sqrt{2\omega_D}}\frac{1}{\sqrt{2\omega'_D}}\sqrt{\frac{M_{\Lambda^*}}{E_{\Lambda^*}}}\sqrt{\frac{M_{\Lambda^*}}{E'_{\Lambda^*}}}\,\tilde{t}_1\tilde{G}\tilde{t}_2. \tag{5.76}$$

However, as seen in Eq. (5.38), we actually obtained

$$S^{(2)} = -i(2\pi)^4\,\delta^4(\cdots)\frac{1}{\mathcal{V}^2}\frac{1}{\sqrt{2\omega_D}}\frac{1}{\sqrt{2\omega'_D}}\frac{1}{\sqrt{2\omega_{D^*}}}\frac{1}{\sqrt{2\omega'_{D_*}}}\sqrt{\frac{M_N}{E_N}}\sqrt{\frac{M_N}{E'_N}}t_1Gt_2. \tag{5.77}$$

Therefore, we need to impose the following normalization for the $\tilde{G}$ function:

$$\sqrt{\frac{M_{\Lambda^*}}{E_{\Lambda^*}}}\sqrt{\frac{M_{\Lambda^*}}{E'_{\Lambda^*}}}\tilde{t}_1\tilde{G}\tilde{t}_2 = \frac{1}{\sqrt{2\omega_{D^*}}}\frac{1}{\sqrt{2\omega'_{D_*}}}\sqrt{\frac{M_N}{E_N}}\sqrt{\frac{M_N}{E'_N}}t_1Gt_2$$

$$\Rightarrow \tilde{t}_1\tilde{G}\tilde{t}_2 = \frac{1}{2M_{D^*}}t_1Gt_2. \tag{5.78}$$

Configuration	$I(J^P)$	$\tilde{t}_1$	$\tilde{t}_2$	$\tilde{G}$
$D(ND^*)$	$\frac{1}{2}(\frac{1}{2}^+)$	$\frac{1}{4}t_{DN}^{I=0,S=1/2}$	$\frac{1}{8M_{D^*}}t_{DD^*}^{I=0,S=1}$	$\int \frac{d^3q}{(2\pi)^3}\frac{F_{\Lambda_c(2940)}(q)}{(q^0)^2-\vec{q}^2-M_D^2}$
	$\frac{1}{2}(\frac{3}{2}^+)$	*idem*	*idem*	$\int \frac{d^3q}{(2\pi)^3}\frac{F_{\Lambda_c(2910)}(q)}{(q^0)^2-\vec{q}^2-M_D^2}$
$D^*(ND)$	$\frac{1}{2}(\frac{1}{2}^+)$	$\frac{1}{4}t_{D^*N}^{I=0,S=1/2}$	$\frac{1}{8M_D}t_{DD^*}^{I=0,S=1}$	$\int \frac{d^3q}{(2\pi)^3}\frac{F_{\Lambda_c(2765)}(q)}{(q^0)^2-\vec{q}^2-M_{D^*}^2}$
	$\frac{1}{2}(\frac{3}{2}^+)$	$\frac{1}{4}t_{D^*N}^{I=0,S=3/2}$	*idem*	*idem*

Table 5.2: Values of $\tilde{t}_1$, $\tilde{t}_2$ and $\tilde{G}$ entering the FCA equation for the three–body amplitude in each possible spin channel, for the two cluster configurations considered. The notation *idem* indicates that the corresponding entry is identical to the one in the row immediately above.

Given the normalization of $\tilde{t}_1$ and $\tilde{t}_2$, this previous relation is trivially fulfilled for

$$\tilde{G} = G. \tag{5.79}$$

In the $D^*(ND)$ configuration, the results are completely equivalent, provided we exchange the D and D^* mesons. Therefore, the correct normalization of the amplitudes and loop function reads in this case

$$\tilde{t}_1 = t_1, \tag{5.80a}$$

$$\tilde{t}_2 = \frac{1}{2M_D}t_2, \tag{5.80b}$$

$$\tilde{G} = G. \tag{5.80c}$$

In Table 5.2 we present a summary detailing the different normalizations discussed here, as well as the spin-isospin structure of the amplitudes that was presented in Sect, 5.2.4.

Having presented the FCA formalism and its application to the DND^* three–body system, we show in the next section our results for the DND^* amplitude.

5.3 Results for the three–body DND^* T–matrix

In Fig. 5.7 we present the squared amplitude $|T|^2$ for the configuration $D(ND^*)$, where the ND^* subsystem is bound into either the $\Lambda_c(2940)$ or the $\Lambda_c(2910)$. We assume $J^P = 1/2^-$ for the $\Lambda_c(2940)$ and $J^P = 3/2^-$ for the $\Lambda_c(2910)$. Two prominent states are generated: one with total $J^P = 1/2^+$ and another

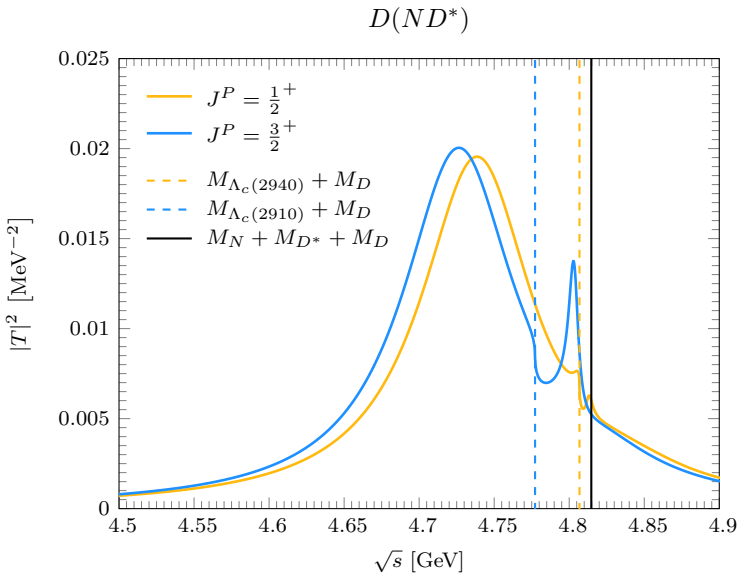

Figure 5.7: $|T|^2$ as a function of the total three–body energy $\sqrt{s}$ for $q_{\rm max} = 600$ MeV, assuming the ND^* cluster to be bound into the $\Lambda_c(2940)$ and $\Lambda_c(2910)$ with spins 1/2 and 3/2, respectively. The vertical dashed lines indicate the thresholds of the $\Lambda_c(2940)D$ and $\Lambda_c(2910)D$ channels, while the vertical solid line marks the position of the genuine three–body threshold (which, however, has no impact on the calculation within the FCA).

with $J^P = 3/2^+$. With respect to the corresponding thresholds, $M_{\Lambda_c(2940)} + M_D = 4807$ MeV and $M_{\Lambda_c(2910)} + M_D = 4781$ MeV, the binding energies are approximately 70 and 50 MeV, respectively. The resulting $|T|^2$ distributions exhibit clear peaks, whose widths—of the order of 90 MeV—reflect those of the three–body system. Reversing the spin assignments of the $\Lambda_c(2940)$ and $\Lambda_c(2910)$ states leads to equivalent results, with the J^P assignments exchanged (red solid line $\leftrightarrow$ blue dashed line in Fig. 5.7). The position and width of the states listed here are extracted from the inspection of $|T|^2$. This extraction is done in this way since it is not evident how to analytically continue the amplitudes to unphysical Riemann sheets within the FCA framework, nor how to relate possible pole structures to the physical properties observed on the real energy axis.

It is interesting to discuss the origin of the structures observed in Fig. 5.7. The peaks are largely driven by $\tilde{t}_1$ (the DN amplitude of Eq. (5.10)) and $\tilde{t}_2$ (corresponding to the DD^* amplitude, Eq. (5.1)) in Eq. (5.21), the latter however playing a minor role. This follows from the relative strengths of the underlying interactions: the DN system binds the $\Lambda_c(2765)$ by about 40 MeV,

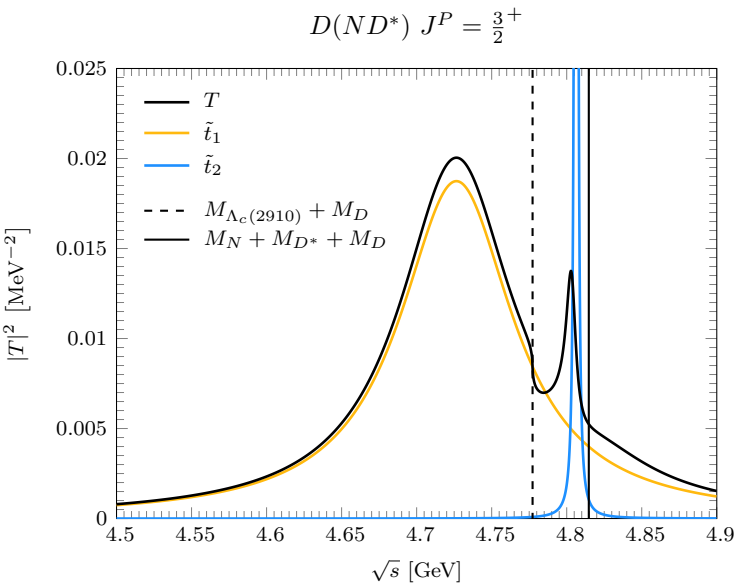

Figure 5.8: Squared modulus of the amplitude $T(s)$ in the $D(ND^*)$ configuration for the $J^P = \frac{3}{2}^+$ scenario, compared with the single-scattering amplitudes $\tilde{t}_1(s_1)$ and $\tilde{t}_2(s_2)$. As one can see, the features of the full amplitude basically arise from the single-scattering amplitudes.

whereas the DD^* system forms the T_{cc} with only 360 keV of binding. Thus, the DN force is far stronger than the DD^* one, yielding a physical picture in which the nucleon acts as the *glue* binding both D and D^*, with the direct DD^* interaction playing a negligible role.

This situation is illustrated in Fig. 5.8, where we present the squared modulus of the three–body amplitude together with that of $\tilde{t}_1$ and $\tilde{t}_2$. Recall that the single-scattering two–body amplitudes are taken as a function of the invariant mass of the considered pair, which in turn depends on the total invariant mass s, as defined in Eqs. (5.22). As shown in the figure, the narrow peak observed in the $J^P = 3/2^+$ channel between thresholds originates from the T_{cc} amplitude. Additional structures appear near the thresholds, particularly in the $J^P = 1/2^+$ channel, which may be interpreted as threshold effects or, potentially, as less bound excited states of the system. Similar features have been reported in the $D^*D^*D^*$ system [389], where they were identified as excited states above the ground three–body configuration within ladder-resummed amplitudes [390–392] and connected to the Efimov effect [393].

As an alternative, we also studied the configuration $D^*(ND)$, where the ND pair forms the $\Lambda_c(2765)$ ($J^P = 1/2^-$) and the external particle is a D^*.

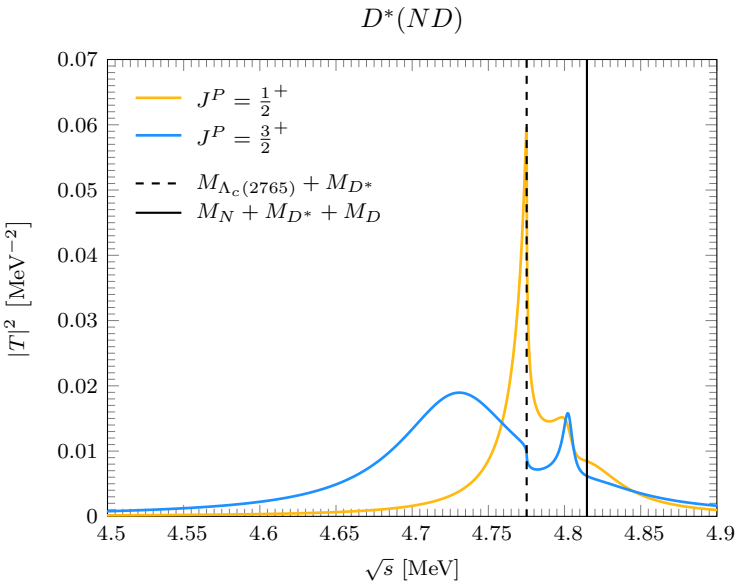

Figure 5.9: $|T|^2$ as a function of the total three–body energy $\sqrt{s}$ for $q_{\max} = 600$ MeV, assuming the ND subsystem is bound into the $\Lambda_c(2765)$. The vertical lines indicate the thresholds of the relevant two- and three–body channels in this scenario. This figure is modified with respect to Fig. 3 of Ref. [4]: the results reported there had the *offshellness* factor ξ appearing in Eqs. (5.22) set to one.

The corresponding results are shown in Fig. 5.9. In this case, we find the $3/2^+$ state to be bound by about 70 MeV with respect to the 2765 MeV + M_{D^*} threshold, while the $1/2^+$ state has likely become a virtual state, producing a cusp at the $\Lambda_c(2765)D$ threshold. Compared to Fig. 5.7, the most notable change occurs for the $J^P = 1/2^+$ amplitude, where this cusp structure has arisen. This reflects the smaller binding energy of the $1/2^+$ state relative to the $\Lambda_c(2765)D^*$ threshold. In this scenario, we also observe a secondary peak between the $\Lambda_c(2765)D$ threshold and the true three–body threshold, produced again by the T_{cc} amplitude.

Note that the plot in Fig. 5.9 differs from Fig. 3 of Ref. [4]. The discrepancy arises because, in that reference, the *offshellness* factor ξ in the evaluation of the two–body invariant masses (5.22) was set to unity, thereby neglecting offshell effects on the cluster constituents. A comparison between the present results and those of Ref. [4] thus illustrates how different approximations for the invariant masses impact the resulting lineshapes, offering an estimate of the associated uncertainties.

For completeness, the absolute masses extracted from the peak positions in

$D(ND^*)$

$q_{\max}$ [MeV]	J^P	mass [MeV]	width [MeV]
600	$1/2^+$	4738.6	91.4
	$3/2^+$	4726.5	93.3
650	$1/2^+$	4738.6	91.9
	$3/2^+$	4726.6	92.3

$D^*(ND)$

$q_{\max}$ [MeV]	J^P	mass [MeV]	width [MeV]
600	$1/2^+$	cusp	—
	$3/2^+$	4706.8	98.3
650	$1/2^+$	cusp	—
	$3/2^+$	4706.9	97.6

Table 5.3: Masses and widths of the DND^* bound states (in MeV). The table on the top shows the results obtained when assuming the ND^* pair to be bound, while the table on the bottom corresponds to the case where the ND pair is taken as the bound cluster.

both configurations, as well as the full widths at half maximum, are compiled in Table 5.3. As seen in this table, the masses obtained for the $J^P = 3/2^+$ state in both cluster configurations differ by about 20 MeV, which we interpret as an estimate of the theoretical uncertainty inherent to the FCA approach. On the other hand, while the width of the $3/2^+$ state remains nearly unchanged across the two scenarios, the shape and possibly the nature of the $1/2^+$ state is quite distinct when comparing both scenarios, a consequence of its proximity to the $\Lambda_c(2765)D^*$ threshold. Variations of the cutoff parameter $q_{\max}$ induce only negligible shifts in the peak positions and overall lineshapes. However, some of the threshold-related structures are sensitive to the cutoff. In particular, the narrow peak seen in the $3/2^+$ amplitude in Fig. 5.7—or in both amplitudes in Fig. 5.9—between thresholds is strongly reduced for larger values of the cutoff and for $q_{\max} = 700$ MeV we see that it nearly disappears. This behavior parallels the findings of Ref. [393], where analogous excited states in the $D^*D^*D^*$ system were suppressed when larger cutoffs were employed.

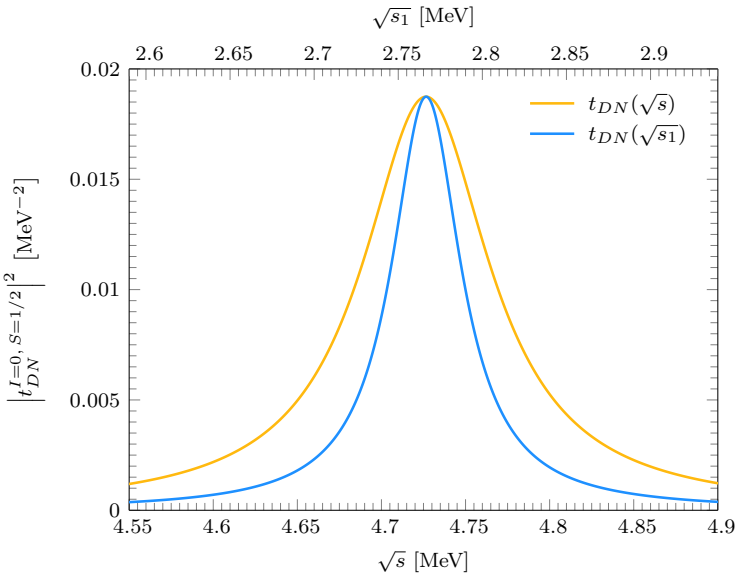

Figure 5.10: $|t_{DN}|^2$ from Eq. (5.10) as a function of $\sqrt{s_1}$ or as a function of $\sqrt{s}$, substituting s_1 by Eq. (5.22) with q_0 from Eq. (5.23). Figure taken from Ref. [4].

At this point, an important observation is in order. Consider, for instance, the case of $D(ND^*)$ presented in Fig. 5.7, where we argued that the DN amplitude $\tilde{t}_1$ largely drives the results. In the FCA approach, the system involves explicitly both DN and DD^* interactions. The DN channel is dominated in our model by the $\Lambda_c(2765)$, which has a width of about 50 MeV, while in the DD^* channel the T_{cc} contributes only about 48 keV. Nevertheless, the resulting width of the three–body system is around 90 MeV. Although this may appear surprising, the explanation lies in the fact that the three–body amplitude is expressed in terms of the total invariant mass $\sqrt{s}$ of the system rather than the two–body invariant mass $\sqrt{s_1}$. To illustrate this point, in Fig. 5.10 we plot $|t_{DN}|^2$ from Eq. (5.10) as a function of $\sqrt{s_1}$, treating s_1 as an independent variable. We also show it as a function of $\sqrt{s}$, where s_1 and s are related through Eq. (5.22), with q_0 given by Eq. (5.23). Since the relation between s_1 and s is linear, the use of $\sqrt{s}$ as the variable effectively broadens the $|t_{DN}|^2$ distribution. Further discussion of this effect is given in Appendix E, where we also provide a general derivation of the apparent width enhancement in many-body systems and illustrate it with both the present case and the analogous situation of nucleon–nucleus scattering in the limit of negligible nuclear binding energy.

5.3.1 Consideration of DN isospin $I = 1$

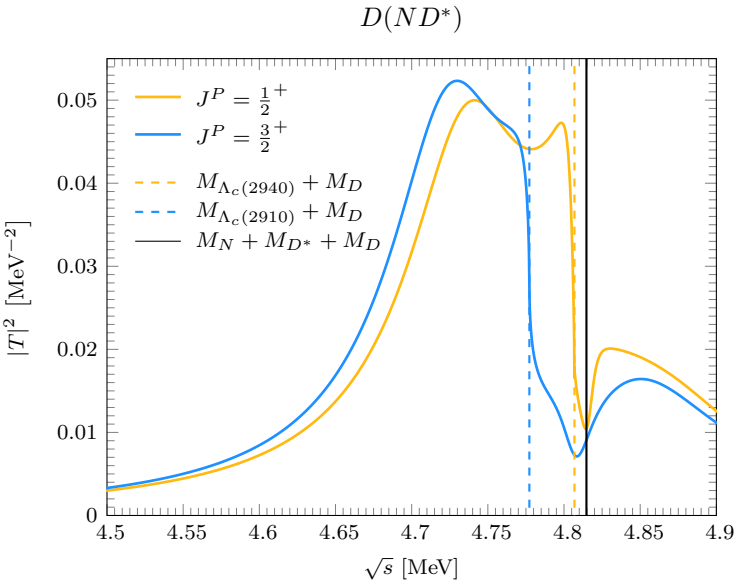

Figure 5.11: Same as Fig. 5.7, now including the DN $I = 1$ amplitude of Eq. (5.54). Figure taken from Ref. [4].

We now return to our preferred configuration of a D meson scattering off the ND^* cluster. In Eq. (5.54), the amplitude t_1 contained both $I = 0$ and $I = 1$ contributions, but only the isoscalar part was retained under the assumption of its dominance. This assumption is well motivated: in most molecular approaches, the DN interaction is considerably stronger in $I = 0$ than in $I = 1$. Nevertheless, many studies also predict the existence of an $I = 1$ state, which is much less bound than its $I = 0$ counterpart (see, e.g., Refs. [281, 368]). This has led to the interpretation of the $\Sigma_c(2800)$, located near the DN threshold, as a dynamically generated DN state in the $I = 1$ channel [341, 382]. Following this perspective, we describe the DN $I = 1$ amplitude as

$$t_{DN}^{I=1} = \frac{(g_{DN}^{I=1})^2}{\sqrt{s_1} - M_{\Sigma_c(2800)} + i\Gamma_{\Sigma_c(2800)}/2}, \tag{5.81}$$

with the mass and width taken as

$$M_{\Sigma_c(2800)} = 2800 \text{ MeV}, \tag{5.82a}$$
$$\Gamma_{\Sigma_c(2800)} = 75 \text{ MeV}, \tag{5.82b}$$

in agreement with [18]. The coupling $g_{DN}^{I=1}$, determined from Eq. (5.12), is found to be $g_{DN}^{I=1} = 2.51$. From this, we obtain the DN scattering length,

$$a = (0.20 - i\,0.84)\ \text{fm}. \tag{5.83}$$

The imaginary part is consistent with Ref. [382], while the real part, although smaller in magnitude, has the same sign and is closer to the results of Refs. [220, 361].

In this analysis, we employ the full t_1 amplitude of Eq. (5.54), rather than the $I = 0$ truncated form of Eq. (5.56). The resulting $|T|^2$ distribution is displayed in Fig. 5.11. The main peaks already present in Fig. 5.7 remain essentially unchanged, but a new enhancement emerges between the two $\Lambda^* D$ thresholds, most pronounced in the $J^P = 1/2^+$ channel. At the same time, the smaller contribution from the DD^* amplitude and the threshold effects seen in Fig. 5.7 vanish, replaced by the new isovector structure. Despite this additional contribution, the overall $|T|^2$ lineshape continues to be dominated by the isoscalar DN amplitude of Eq. (5.10).

5.3.2 Uncertainties in our results and three–body decay channels

There remains the question of the uncertainties in our predictions, which we now address using the Monte Carlo resampling method [194, 394, 395]. We focus again on the case of D scattering with the ND^* cluster, neglecting the contribution of the isovector ND amplitude considered in the previous subsection. The experimental uncertainties in the input masses and widths of the two–body amplitudes are taken into account. For the $\Lambda_c(2765)$, the PDG [18] and the original measurement [396] quote a width of 50 MeV but provide no error estimate. We therefore assign a conservative 20% uncertainty, treating it as 50 ± 10 MeV. For the masses of the $\Lambda_c(2765)$, $\Lambda_c(2940)$, and $\Lambda_c(2910)$, we adopt the PDG values and errors,

$$M_{\Lambda_c(2765)} = 2766.6 \pm 2.4\ \text{MeV}, \tag{5.84}$$

$$M_{\Lambda_c(2940)} = 2939.6 \pm 1.5\ \text{MeV}, \tag{5.85}$$

$$M_{\Lambda_c(2910)} = 2914 \pm 7\ \text{MeV}, \tag{5.86}$$

and for the $\Lambda_c(2765) \to DN$ coupling, we assume a 10% uncertainty, i.e., $g_{DN} = 3.70 \pm 0.37$.

We then perform multiple runs, generating Gaussian-distributed random values for these parameters within their quoted uncertainties,[9] and extract the

[9] We neglect possible correlations of these values, since we do not have any experimental indication of them.

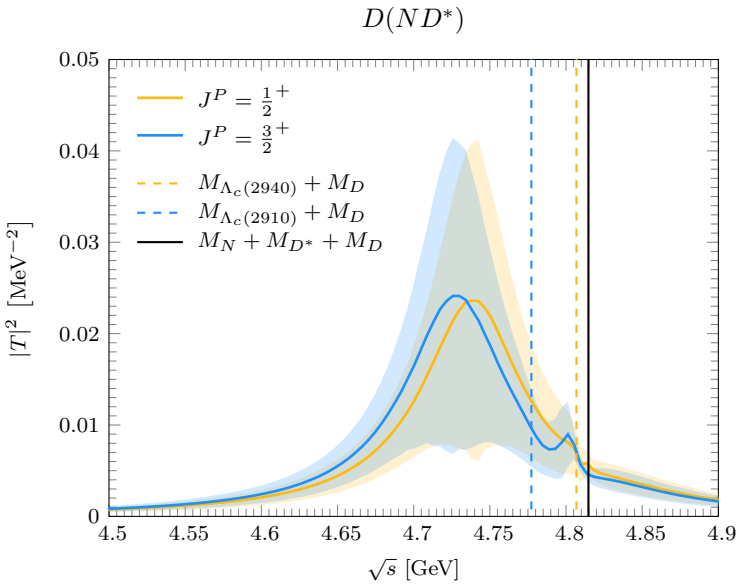

Figure 5.12: Same as Fig. 5.7, but now showing the mean values of the $J^P = 1/2^+$ and $3/2^+$ amplitudes, computed using Monte Carlo resampling (solid lines). The transparent bands indicate the corresponding one–standard–deviation uncertainties.

average peak position and width together with their standard deviations. For the $J^P = 3/2^+$ channel (with similar results found for $J^P = 1/2^+$), we obtain

$$M = 4733 \pm 7 \text{ MeV}, \qquad \Gamma = 87 \pm 13 \text{ MeV}. \tag{5.87}$$

In addition, and mirroring the results of Fig. 5.7, we show in Fig. 5.12 the mean values obtained for the squared modulus of the amplitude in both spin channels, together with the associated error bands, defined as the mean value plus or minus one standard deviation.

Systematic uncertainties, stemming from the limitations of the FCA in describing such systems, are harder to quantify. A reasonable estimate can be inferred from the spread of results obtained with different cluster configurations (see Table 5.3), which exceed the statistical errors of Eq. (5.87). Nevertheless, even when these systematic differences are included, the predicted binding and moderate widths strongly support the existence of these states and their potential experimental observation.

Finally, let us address the origin of the widths of the predicted states, as this is directly linked to their possible experimental observation. These widths arise from the imaginary parts of the two–body amplitudes entering our calculation, which themselves reflect the finite widths of the T_{cc} [Eq. (5.1)], the $\Lambda_c(2765)$

[Eq. (5.10)], and the $\Lambda_c(2940)$ and $\Lambda_c(2910)$ [Eqs. (5.14)–(5.15)]. Since the T_{cc} width is extremely small, the dominant contributions come from the decay channels of the Λ_c^* states. According to the PDG, their main decay modes are $\Lambda_c\pi\pi$ and $\Sigma_c\pi$. Thus, depending on the choice of cluster, the relevant decay channels would be $\Sigma_c\pi D^*$ or $\Sigma_c\pi D$, with DND also kinematically allowed in the $D^*(ND)$ configuration. The experimental identification of possible DND^* three–body bound states therefore involves analyzing the invariant mass distributions of these three-particle channels.

5.4 Conclusions

We have investigated the possible bound states of the DND^* system within the FCA, which allows us to evaluate the three–body scattering amplitude by selecting a bound two–body cluster and letting the third particle scatter from its constituents. As the cluster, we first considered the ND^* system, with the external particle being a D meson. The discovery of the $\Lambda_c(2940)$ and $\Lambda_c(2910)$, located near the D^*N threshold, has motivated their interpretation as D^*N molecular states with $J^P = 1/2^-$ and $3/2^-$, respectively. The proximity of such states to meson–baryon thresholds strongly supports their molecular nature [143, 147], though alternative explanations exist [245, 246, 397], which typically require unnaturally small scattering lengths and large effective ranges. Through heavy-quark symmetry, we further associate the $\Lambda_c(2765)$ with the analogous DN bound state. As an alternative configuration, we also studied the case where the ND system forms the cluster and the D^* interacts with it.

In both pictures, bound states with $J^P = 1/2^+$ and $3/2^+$ are obtained, relative to the $\Lambda_c(2765)D$ or $\Lambda_c(2765)D^*$ thresholds, with qualitatively similar features. Moreover, the inclusion of the DN isovector amplitude in addition to the isoscalar one generates an additional structure between the two Λ^*D thresholds, while leaving the $I = 0$ peaks essentially unchanged.

Although our preferred configuration is $D(ND^*)$, the modest differences between the results of the two scenarios can be regarded as an estimate of the theoretical uncertainties of the FCA approach. Within these assumptions, our analysis points to the existence of such bound states, driven mainly by the attractive DN and D^*N forces. Their experimental observation would provide valuable insight into the nature of the DN and D^*N interactions and help clarify the role of molecular dynamics in the Λ_c^* spectrum.

6

Conclusions

Over the past two decades, hadron spectroscopy has been transformed by the discovery of a rich spectrum of *exotic* states that cannot be easily accommodated within the conventional constituent quark model. This progress has been driven by the notable increase in heavy-hadron production in B-factories such as Belle II, BES III, and LHCb, as well as at heavy-ion colliders. In particular, the charmonium-like sector—the so-called XYZ family—has undergone decisive advances since the pioneering observation of the $\chi_{c1}(3872)$. These findings have triggered intense debate over the nature of such states, with competing interpretations ranging from compact multiquark configurations (tetraquarks and pentaquarks) and hadro-quarkonium to loosely bound hadronic molecules, kinematical cusps, or hybrids of these pictures. While no consensus has been reached regarding their internal structure, it is universally recognized that their study provides valuable insight into the non-perturbative dynamics of QCD at low energies.

A complementary venue to probe QCD is the study of strongly interacting matter under extreme density or temperature conditions. Mapping out the QCD phase diagram remains one of the central challenges in contemporary hadron physics, involving significant efforts not only within the hadronic community but also across neighboring fields such as astrophysics, general relativity, and mathematical physics. In this thesis, we have brought together these two lines of research—exotic hadrons and matter under extreme conditions—with the purpose of shedding light on the internal structure of the T_{cc} and the D_{s0}^*, two prominent tetraquark-like candidates.

At its core, this thesis presents a systematic study of hadronic molecular states of two (or three) hadrons containing charmed mesons. Starting from Chap. 2, we have studied the nuclear-medium behavior of the T_{cc}, the D_{s0}^* and their HQSS siblings, paying also attention to their charge-conjugated partners, treating them as dynamically generated states in unitarized S-wave meson–

meson amplitudes. We have shown that different HQSS-consistent interactions, with distinct analytic structures, allow one to tune the molecular probability of the generated states, and to follow the density- and compositeness-governed pole trajectories in the complex energy plane. Medium effects have been incorporated through the two-meson loop functions, where the dressing of the constituent mesons by the surrounding nucleons has been taken into account. We have found that the response of these states to the nuclear-medium density depends strongly on both their molecular content and the different strengths of the meson–nucleon versus anti-meson–nucleon interactions. In particular, the T_{cc}^{+} broadens and shifts upward, while its antiparticle is moderately affected and moves downward. As for the strange–charm $D_{s0}^{*\pm}$ states, they exhibit an even more pronounced particle–antiparticle asymmetry driven by the kaon–antikaon dynamics. These results highlight how the study of density-dependent mass and width modifications can provide valuable insight into the internal structure of these exotic candidates.

Having established the density-dependent modifications to the T_{cc} and the D_{s0}^{*} states, Chapter 3 then tackled the key question of how to experimentally access these nuclear medium modifications. Through the transparency ratio technique, we have shown that this method is well suited to determine the in-medium widths of the charmed constituents of T_{cc} and the D_{s0}^{*} states, providing essential input for future experiments. In particular, we have explored the feasibility of probing the in-medium width of D mesons through nuclear transparency measurements in the reaction $\gamma A \to D^{+}D^{-}A'$, where A and A' represent the initial and final nuclei. Using an estimate for the imaginary part of the D–meson self–energy motivated by previous studies, and restricting to a photon–nucleus c.m. energy of about 10 GeV—where the fraction of emitted low–momentum D mesons in the LAB frame is maximal—we find that the transparency ratio decreases markedly with nuclear mass number, reaching values around 0.6 for heavy nuclei relative to ^{12}C. This level of suppression should be experimentally accessible at forthcoming facilities such as the EIC, EicC, or an upgraded GlueX. Although our calculation relied on simplifying assumptions and was carried out under optimal kinematic conditions to maximize the reliability of the available in-medium D-meson self-energies, it clearly demonstrates the feasibility of such measurements.

In Chap. 4, we have shifted our focus from the density to the temperature axis of the QCD phase diagram, studying the thermal behavior of the exotic T_{cc} and its HQSS partner using thermal field theory in the ITF. We have used the same EFT S–wave approach for their description as in the finite-density case of Chap. 2, parameterized in terms of the compositeness of these states. The thermal medium effects have been incorporated similarly through the two-meson loop functions, taking into account both the dressing of the constituent

mesons by the hot bath of pions and the contribution from the Bose-Einstein factors arising naturally within the ITF. The thermal D and D^* spectral functions employed, which were already available in the literature, were found to induce significant modifications in the $D^{(*)}D^*$ scattering amplitudes already at $T \simeq 80$ MeV. With increasing temperature, the unitarity cut is softened and shifted to lower energies, the cusp at the threshold is smoothed out, and the widths of the T_{cc} and the T_{cc}^* states grow rapidly, leading to their dissolution above $T \simeq 100 \sim 120$ MeV. The sensitivity of these effects to the molecular probability of the states has been demonstrated. Similarly to the finite-density case, large molecular components result in stronger thermal modifications, whereas compact-like configurations remain more stable. These results suggest that experimental determinations of $D^{(*)}D^*$ scattering amplitudes in heavy-ion collisions at RHIC or LHC could provide decisive information on the internal structure of the T_{cc} family. Combined with future measurements in dense matter at FAIR, such studies would offer a powerful tool to constrain the degree of molecular compositeness of these exotic states.

Finally, Chap. 5 has shifted the focus from many-body systems to few-body dynamics, exploring the possibility of forming genuine three-body bound states. In particular, we have investigated the DND^* system using the fixed-center approximation (FCA). Two cluster configurations have been considered: $D(ND^*)$, motivated by the interpretation of the $\Lambda_c(2940)$ and $\Lambda_c(2910)$ as D^*N molecules, and $D^*(ND)$, where the $\Lambda_c(2765)$ was linked by HQSS to be a DN bound state. In both scenarios, states with $J^P = 1/2^+$ and $3/2^+$ have been found near the corresponding $\Lambda_c^* D^{(*)}$ thresholds. The overall similarity between the two cluster choices indicates moderate theoretical uncertainties within the FCA framework, but consistently points to the existence of such bound states, driven by the attractive DN and D^*N dynamics. Their eventual experimental confirmation would shed light on the underlying meson–baryon interactions and the molecular nature of the Λ_c^* spectrum.

Taken together, the results presented in this thesis highlight the importance of molecular components in the description of exotic charmed hadrons, and the crucial role that dense or hot medium effects may play in determining their structure. The methods employed here, ranging from unitarized effective field theories to finite-temperature or dense medium theory and three-body scattering techniques, provide a coherent framework for addressing these questions.

Looking ahead, several directions remain open. On the theoretical side, it would be desirable to go beyond the FCA in the three-body problem, incorporate coupled-channel effects more systematically in all the calculations, and explore the impact of chiral symmetry restoration near the critical temperature, among other possible refinements. On the experimental side, the next generation of facilities offers unique opportunities to test the predictions

presented here. Such progress will be essential to deepen our understanding of the interplay between QCD symmetries, hadronic interactions, and the formation of exotic states in the charm sector, ultimately contributing to clarify the role of hadronic molecules in the QCD spectrum.

Appendix A

Computation of the density loop

In this appendix, we give some additional details on how the numerical computation of the finite-density two-meson loop function of Eq. (2.88) was performed. However, we first give some details on the derivation of the formula of Eq. (2.89).

Starting from the definition first given in Eq. (2.86),

$$\Sigma(s;\rho) = i \int \frac{d^4q}{(2\pi)^4} g^M(E-q^0, \vec{P}-\vec{q};\rho) g^{M'}(q^0,\vec{q};\rho), \tag{A.1}$$

we use the Källen-Lehmann spectral representation of the meson propagators to write

$$\begin{aligned}\Sigma(s;\rho) = i \int \frac{d^4q}{(2\pi)^4} & \\ \times \int_0^\infty d\omega \left(\frac{S_M(\omega,|\vec{P}-\vec{q}|;\rho)}{E-q^0-\omega+i\varepsilon} - \frac{S_{\overline{M}}(\omega,|\vec{P}-\vec{q}|;\rho)}{E-q^0+\omega-i\varepsilon} \right) & \\ \times \int_0^\infty d\omega' \left(\frac{S_{M'}(\omega',|\vec{q}|;\rho)}{q^0-\omega'+i\varepsilon} - \frac{S_{\overline{M}'}(\omega',|\vec{q}|;\rho)}{q^0+\omega'-i\varepsilon} \right). &\end{aligned} \tag{A.2}$$

Now, we can perform the q^0 integration. There are four poles lying on the real axis, namely

$$\begin{aligned} q_1^0 &= E-\omega+i\varepsilon, & q_2^0 &= E+\omega-i\varepsilon, \\ q_3^0 &= \omega'-i\varepsilon, & q_4^0 &= -\omega'+i\varepsilon. \end{aligned} \tag{A.3}$$

Closing the integration contour in the upper half plane, as shown in Fig. A.1, the integral over the infinite-radius semi-circumference vanishes, and we sum the residues coming from the poles q_1^0 and q_4^0 to obtain

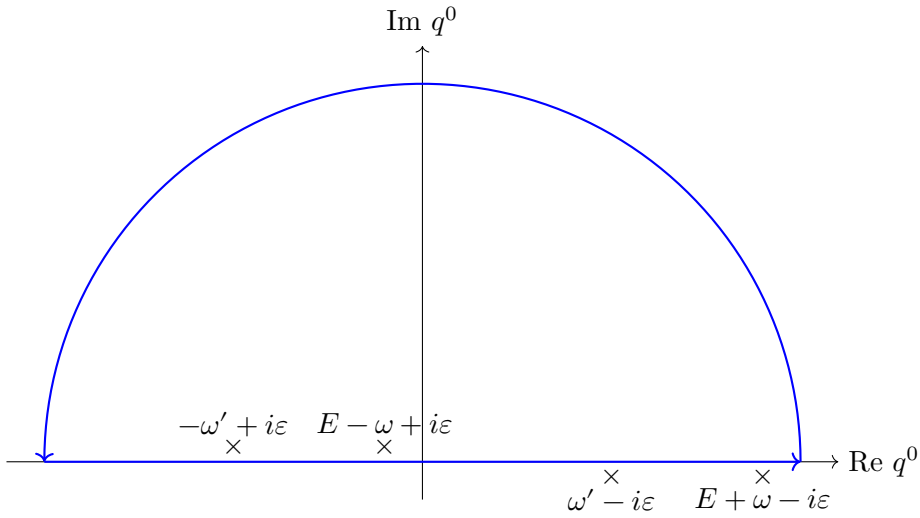

Figure A.1: Representation of the integration contour used for the q^0 integral of Eq. (A.2). The position of the four poles of the integrand are represented with the $\times$ symbols.

$$\Sigma(s;\rho) = i \int \frac{d^3q}{(2\pi)^4} 2\pi i \int_0^\infty d\omega \int_0^\infty d\omega' \Bigg\{ \Big[-S_M(\omega, |\vec{P}-\vec{q}|;\rho)\Big] \left(\frac{S_{M'}(\omega', |\vec{q}|;\rho)}{E-\omega-\omega'+2i\varepsilon} - \frac{S_{\overline{M}'}(\omega', |\vec{q}|;\rho)}{E-\omega+\omega'} \right) + \left(\frac{S_M(\omega, |\vec{P}-\vec{q}|;\rho)}{E+\omega'-\omega} - \frac{S_{\overline{M}}(\omega, |\vec{P}-\vec{q}|;\rho)}{E+\omega'+\omega-2i\varepsilon} \right) \Big[-S_{\overline{M}'}(\omega', |\vec{q}|;\rho)\Big] \Bigg\}. \quad \text{(A.4)}$$

The second and third terms cancel out, and one obtains the expression given in Eq. (2.88),

$$\Sigma(s;\rho) = \int \frac{d^3q}{(2\pi)^3} \int_0^\infty d\omega \int_0^\infty d\omega' \left(\frac{S_M(\omega, |\vec{P}-\vec{q}|;\rho) S_{M'}(\omega', |\vec{q}|;\rho)}{E-\omega-\omega'+i\varepsilon} - \frac{S_{\overline{M}}(\omega, |\vec{P}-\vec{q}|;\rho) S_{\overline{M}'}(\omega', |\vec{q}|;\rho)}{E+\omega+\omega'-i\varepsilon} \right). \quad \text{(A.5)}$$

In order to perform the integration over the ω and ω' variables, it is useful to define the following change of variables:

$$\Omega = \omega + \omega' \qquad\qquad \Omega' = \omega'. \quad \text{(A.6)}$$

The Jacobian matrix and determinant of this change of variables read

$$J = \begin{pmatrix} \frac{\partial\Omega}{\partial\omega} & \frac{\partial\Omega}{\partial\omega'} \\ \frac{\partial\Omega'}{\partial\omega} & \frac{\partial\Omega'}{\partial\omega'} \end{pmatrix} = \begin{pmatrix} 1 & 1 \\ 0 & 1 \end{pmatrix} \qquad \rightarrow \qquad \det(J) = 1 \tag{A.7}$$

and the integration volume transforms as shown in Fig. A.2.

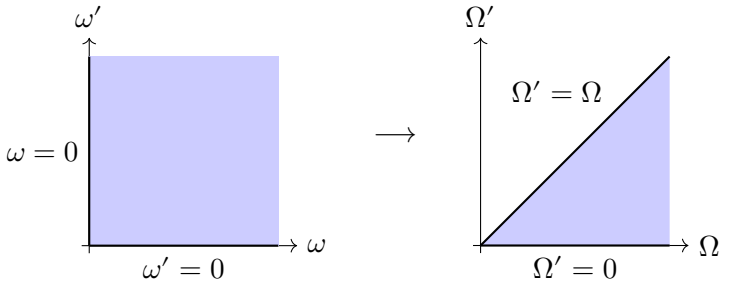

Figure A.2: Transformation of the integration volume with the change of variables of Eq. (A.6). The region shaded in blue represents the integration volume in the original (left panel) and the transformed (right panel) coordinates, respectively.

With this change, Eq. (A.5) is rewritten as

$$\begin{aligned} \Sigma(s;\rho) = \int \frac{d^3q}{(2\pi)^3} \int_0^\infty d\Omega \int_0^\Omega d\Omega' \\ \times \left(\frac{S_M(\Omega-\Omega', |\vec{P}-\vec{q}|;\rho) S_{M'}(\Omega', |\vec{q}|;\rho)}{E-\Omega+i\varepsilon} \right. \\ \left. - \frac{S_{\overline{M}}(\Omega-\Omega', |\vec{P}-\vec{q}|;\rho) S_{\overline{M}'}(\Omega', |\vec{q}|;\rho)}{E+\Omega-i\varepsilon} \right). \end{aligned} \tag{A.8}$$

Since the denominator depends only on the Ω integration variable, we can write

$$\Sigma(s;\rho) = \frac{1}{2\pi^2} \int_0^\infty d\Omega \left(\frac{f_{MM'}(\Omega, |\vec{P}|;\rho)}{E-\Omega+i\varepsilon} - \frac{f_{\overline{M}\overline{M}'}(\Omega, |\vec{P}|;\rho)}{E+\Omega-i\varepsilon} \right), \tag{A.9}$$

where the auxiliary function $f_{MM'}$ is defined as

$$\begin{aligned} f_{MM'}(\Omega, |\vec{P}|;\rho) \\ = \int_0^\Lambda dq\, q^2 \int_0^\Omega d\Omega'\ S_M\left(\Omega-\Omega',\ |\vec{P}-\vec{q}|;\ \rho\right) S_{M'}\left(\Omega',\ |\vec{q}|;\ \rho\right). \end{aligned} \tag{A.10}$$

These last two formulas are given in the main text in Eqs. (2.89) and (2.90). We have shown the derivation of this equation for the general case where the two-meson system is moving with a center-of-mass momentum $\vec{P}$. However, we only evaluate this function for the case where the two-meson system is at rest in the reference frame of the nuclear medium, so that $\vec{P} = \vec{0}$.

In the free space—where both spectral functions are Dirac deltas—the $f_{MM'}$ functions are

$$f_{MM'}(\Omega;0) \equiv f_{MM'}(\Omega, |\vec{0}|;\rho=0) = \int_0^\Lambda dq\; q^2 \int_0^\Omega d\Omega' \frac{\delta\left(\Omega' - \omega_q^M\right)}{2\omega_q^M} \frac{\delta\left(\Omega - \Omega' - \omega_q^{M'}\right)}{2\omega_q^{M'}}, \quad \text{(A.11)}$$

with $\omega_q^{M^{(\prime)}}$ the energy of the meson $M^{(\prime)}$, dependent on the three momentum $\vec{q}$. Performing the integration over the two Dirac deltas one obtains

$$f_{MM'}(\Omega;0) = \theta(\Omega - m_M - m_{M'})\theta(\Lambda - k)\frac{k}{4\Omega}. \quad \text{(A.12)}$$

In this expression, the θ functions represent Heaviside (or step) functions, m_M and $m_{M'}$ are the meson masses, and k is the on-shell center of mass momentum, given by

$$k(\Omega) = \frac{\sqrt{\lambda(\Omega^2, m_M^2, m_{M'}^2)}}{2\Omega} \quad \text{(A.13)}$$

with λ the Källen or triangular function.

Actually, the imaginary part of the loop function is proportional to the value of $f_{MM'}$, since from Eq. (A.9) we have

$$\Sigma(E\,;\,\rho) = \frac{1}{2\pi^2}\left\{ \text{PV} \int_0^\infty d\Omega \left(\frac{f_{MM'}(\Omega\,;\,\rho)}{E - \Omega + i\varepsilon} - \frac{f_{\overline{M}\overline{M}'}(\Omega\,;\,\rho)}{E + \Omega - i\varepsilon} \right) - i\pi f_{MM'}(E\,;\,\rho) \right\} \quad \text{(A.14)}$$

where PV stands for the principal value of the integral and the imaginary part arises from the residue of the integrand at the pole $\Omega = E$. We check that in vacuum

$$\text{Im}\ \Sigma_0(E) = -\frac{f_{MM'}(E;0)}{2\pi} = -\theta(E - m_M - m_{M'})\theta(\Lambda - k)\frac{k}{8\pi E}, \quad \text{(A.15)}$$

which is the same imaginary part as that arising from the analytic formula for the vacuum loop function of Eq. (2.58). This result was also shown

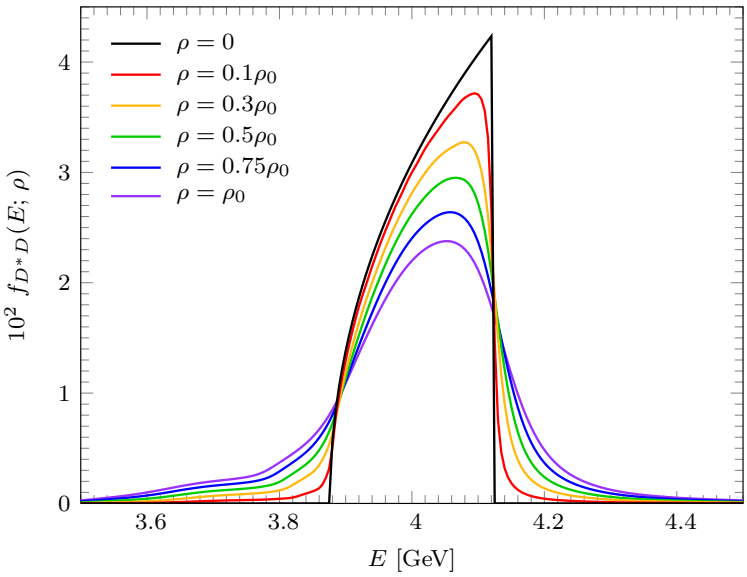

Figure A.3: Auxiliary function f_{D^*D} for the D^*D pair as a function of the center of mass energy E for several values of the density (different line colors). The cutoff is chosen to be $\Lambda = 700$ MeV.

in Eq. (2.145) (modulo the step functions). For finite density, the sharp discontinuities of the step functions appearing in Eq. (A.15) typically get smoothed out, as well as the general shape of the function. In Fig. A.3 we show the behavior of the function f_{D^*D} with density for the specific case of the D^* and D mesons. For the evaluation of the real part of $\Sigma(E;\rho)$, the cutoff-dependent f_{DD^*} shown in the figure is used. However, when determining the imaginary part of the loop, no such cutoff is necessary. However, in the energy region of interest for the problem at hand (cf. Fig. 2.9), the difference between including or not the cutoff for the evaluation of the imaginary part is not found to be relevant.

From a numerical point of view, the determination of $f_{MM'}$ is the more demanding task. It is necessary to define an integration grid that is sufficiently dense around the regions where the spectral functions peak. These regions vary with both integration variables, namely the modulus of the three-momentum q, and the internal energy variable Ω', as well as with the external energy Ω, cf. Eq. (A.10). We perform this and save the computed values for $f_{MM'}(E;\rho)$ in a data file. Afterwards, when computing the two-meson loop function from Eq. (A.14), we read the corresponding values of $f_{MM'}$ from the data file and interpolate them in the energy variable using cubic splines (we do not interpolate in density).

Appendix B

Three-body phase space integration

In this appendix, we aim to show the step-by-step derivation of the phase-space integration formula of Eq. (3.24), corresponding to the process $\gamma N \to D^+ D^- N'$, starting from the following general expression.

$$\sigma_N = \frac{1}{4 m_N k_{\text{lab}}} \int \frac{d^3p}{(2\pi)^3} \frac{1}{2\omega(p)} \int \frac{d^3p'}{(2\pi)^3} \frac{1}{2\omega(p')} \int \frac{d^3q}{(2\pi)^3} \frac{1}{2E(q)} \times 4m_N^2 \left|t\right|^2 (2\pi)^4 \delta^4(\mathbf{k} + \mathbf{q_i} - \mathbf{p} - \mathbf{p}' - \mathbf{q}), \quad \text{(B.1)}$$

This expression was first shown in Eq. (3.22). We recall that $\mathbf{k}$ and $\mathbf{q_i}$ represent the four-momenta of the incident photon and the initial nucleon, respectively; while $\mathbf{q}$, $\mathbf{p}$ and $\mathbf{p}'$ are the four-momenta associated to the N', D^+ and D^- particles (respectively) in the final state. Furthermore, m_N is the nucleon mass. Using the relativistic formula for the momentum of the photon in the LAB frame (k_{lab}) in terms of the total invariant mass s, cf. (3.23), we can write

$$\sigma_N = \frac{4m_N^2}{2(s - m_N^2)} \int \frac{d^3p}{(2\pi)^3} \frac{1}{2\omega(p)} \int \frac{d^3p'}{(2\pi)^3} \frac{1}{2\omega(p')} \int \frac{d^3q}{(2\pi)^3} \frac{1}{2E(q)} \times \left|t\right|^2 (2\pi)^4 \delta^4(\mathbf{k} + \mathbf{q_i} - \mathbf{p} - \mathbf{p}' - \mathbf{q}). \quad \text{(B.2)}$$

Next, since the integrals

$$\int \frac{d^3p}{(2\pi)^3} \frac{1}{2\omega(p)}, \qquad \int \frac{d^3p'}{(2\pi)^3} \frac{1}{2\omega(p')}, \qquad \int \frac{d^3q}{(2\pi)^3} \frac{1}{2E(q)} \quad \text{(B.3)}$$

are Lorentz invariant, we can choose to evaluate them in the $D^- N'$ rest frame, where

$$\vec{q} + \vec{p}' = \vec{0}, \quad \text{(B.4a)}$$

$$\vec{k} + \vec{q}_i - \vec{p} = \vec{0}, \tag{B.4b}$$

$$k + E(q_i) - \omega(p) = \omega(p') + E(q) = m_{\text{inv}}. \tag{B.4c}$$

with m_{inv} the invariant mass of the $D^- N'$ pair. Now, we perform the integration over $\vec{q}$. Leaving for the moment the first factor and the integral over $\vec{p}$ out, we can write

$$\begin{aligned}
&\int \frac{d^3p'}{(2\pi)^3}\frac{1}{2\omega(p')}\int \frac{d^3q}{(2\pi)^3}\frac{1}{2E(q)}\,|t|^2\,(2\pi)^4\delta^4(\mathbf{k}+\mathbf{q_i}-\mathbf{p}-\mathbf{p}'-\mathbf{q}) \\
&= \int \frac{d^3p'}{(2\pi)^3}\frac{1}{2\omega(p')}\frac{1}{2E(p')}\,|t|^2\,(2\pi)\delta\left[k+E(q_i)-\omega(p)-\omega(p')-E(p')\right].
\end{aligned} \tag{B.5}$$

We shall now perform the integration over $\vec{p}'$

$$\begin{aligned}
&\int \frac{d^3p'}{(2\pi)^3}\frac{1}{2\omega(p')}\frac{1}{2E(p')}\,|t|^2\,(2\pi)\delta\left[m_{\text{inv}}-\omega(p')-E(p')\right] \\
&\quad= \frac{4\pi}{(2\pi)^3}\int dp'(p')^2\frac{1}{2\omega(p')}\frac{1}{2E(p')}\,|t|^2\,(2\pi)\frac{\delta\left[p'-\frac{\lambda^{1/2}(m_{\text{inv}}^2,m_D^2,m_N^2)}{2m_{\text{inv}}}\right]}{\frac{p'}{\omega(p')}+\frac{p'}{E(p')}} \\
&\quad= \frac{1}{\pi}\frac{(p')^2}{4\omega(p')E(p')}|t|^2\frac{\omega(p')E(p')}{p'\left[\omega(p')+E(p')\right]} = \frac{1}{4\pi}\frac{p'}{m_{\text{inv}}}|t|^2.
\end{aligned} \tag{B.6}$$

In this last expression, we have fixed p' to the value given by the delta, as a function of m_{inv}.

Going back to the full nucleon cross section, we now have[1]

$$\begin{aligned}
\sigma_N &= \frac{4m_N^2}{2(s-m_N^2)}\int \frac{d^3p}{(2\pi)^3}\frac{1}{2\omega(p)}\frac{1}{4\pi}\frac{p'}{m_{\text{inv}}}|t|^2 \\
&= \frac{m_N^2}{s-m_N^2}\frac{1}{32\pi^4}\int_{p^{\min}}^{p^{\max}} dp\,p^2\int_0^{2\pi}d\phi\int_{-1}^{+1}d\cos\theta\,\frac{1}{2\omega(p)}\frac{p'}{m_{\text{inv}}}|t|^2.
\end{aligned} \tag{B.7}$$

The remaining step to get to the formula shown in Eq. (3.24) is to relate the integration over the momentum of the D^+ meson (p) to an integration over the invariant mass m_{inv} of the $D^- N'$ system. We can relate m_{inv} with p taking into account total energy-momentum conservation:

$$\mathbf{k}+\mathbf{q_i}-\mathbf{p} = \mathbf{p}'+\mathbf{q} \quad\rightarrow\quad m_{\text{inv}}^2 = (\mathbf{p}'+\mathbf{q})^2 = (\mathbf{k}+\mathbf{q_i}-\mathbf{p})^2. \tag{B.8}$$

In this previous equation, we have used the definition of m_{inv}. Now, since m_{inv} is a Lorentz-invariant quantity, we can choose to evaluate it in any frame. In the γN rest frame, its expression results

$$m_{\text{inv}}^2 = (\mathbf{k}+\mathbf{q_i})^2 + \mathbf{p}^2 - 2\,(\mathbf{k}+\mathbf{q_i})_\mu\,\mathbf{p}^\mu = s + m_D^2 - 2\sqrt{s}\,\omega(p). \tag{B.9}$$

[1] The integration limits $p^{\min}$ and $p^{\max}$ depend on the frame of reference where the integration is evaluated.

Therefore, we obtain the following expressions for the energy and momentum of the D^+ meson in terms of the D^-N' invariant mass:

$$\omega(p) = \frac{s + m_D^2 - m_{\text{inv}}^2}{2\sqrt{s}}, \tag{B.10a}$$

$$p = \sqrt{\omega(p)^2 - m_D^2} = \frac{\sqrt{\lambda(s, m_D^2, m_{\text{inv}}^2)}}{2\sqrt{s}}. \tag{B.10b}$$

The change of variable $p \to m_{\text{inv}}$ in the integration will be given by

$$2m_{\text{inv}} dm_{\text{inv}} = -2\sqrt{s}\frac{d\omega(p)}{dp}dp = -2\sqrt{s}\frac{p}{\omega(p)}dp$$

$$\to \quad pdp = -\frac{m_{\text{inv}}\omega(p)}{\sqrt{s}}dm_{\text{inv}} \tag{B.11}$$

where the integration limits are

$$(m_{\text{inv}}^{\min})^2 = s + m_D^2 - 2\sqrt{s}\,\omega(p^{\max}) = (m_{D^-} + m_N)^2, \tag{B.12a}$$

$$(m_{\text{inv}}^{\max})^2 = s + m_D^2 - 2\sqrt{s}\,\omega(p^{\min} = 0) = (\sqrt{s} - m_D)^2. \tag{B.12b}$$

By inserting this change into the integral of Eq. (B.7), we can finally arrive at the expression of Eq. (3.24):

$$\sigma_N = \frac{m_N^2}{(s - m_N^2)\sqrt{s}}\frac{1}{32\pi^4}\int_{m_{\text{inv}}^{\min}}^{m_{\text{inv}}^{\max}} pp' dm_{\text{inv}} \int_{-1}^{1} d\cos\theta \int_0^{2\pi} d\phi\ |t|^2. \tag{B.13}$$

Appendix C

Numerical computation of the thermal loop

In this appendix, we discuss the numerical evaluation of the thermal DD^* loop function presented in Eq. (4.54):

$$\Sigma(E,\vec{P}=0;T) = \int \frac{d^3q}{(2\pi)^3} \int_0^\infty d\omega \int_0^\infty d\omega'\, S_D(\omega,|\vec{q}|;T)\, S_{D^*}(\omega',|\vec{q}|;T)$$
$$\times \Bigg\{ [1+b^-(\omega;T)+b^-(\omega';T)] \left(\frac{1}{E-\omega-\omega'+i\varepsilon} - \frac{1}{E+\omega+\omega'+i\varepsilon} \right)$$
$$+ [b^-(\omega;T)-b^-(\omega';T)] \left(\frac{1}{E+\omega-\omega'+i\varepsilon} - \frac{1}{E-\omega+\omega'+i\varepsilon} \right) \Bigg\}. \quad \text{(C.1)}$$

This expression may be separated into two terms, namely

$$\Sigma^{\mathrm{U}}(E,\vec{P}=0;T) = \int \frac{d^3q}{(2\pi)^3} \int_0^\infty d\omega \int_0^\infty d\omega'\, S_D(\omega,|\vec{q}|;T)\, S_{D^*}(\omega',|\vec{q}|;T)$$
$$\times [1+b^-(\omega;T)+b^-(\omega';T)] \left(\frac{1}{E-\omega-\omega'+i\varepsilon} - \frac{1}{E+\omega+\omega'+i\varepsilon} \right) \quad \text{(C.2)}$$

and

$$\Sigma^{\mathrm{L}}(E,\vec{P}=0;T) = \int \frac{d^3q}{(2\pi)^3} \int_0^\infty d\omega \int_0^\infty d\omega'\, S_D(\omega,|\vec{q}|;T)\, S_{D^*}(\omega',|\vec{q}|;T)$$
$$\times [b^-(\omega;T)-b^-(\omega';T)] \left(\frac{1}{E+\omega-\omega'+i\varepsilon} - \frac{1}{E-\omega+\omega'+i\varepsilon} \right), \quad \text{(C.3)}$$

so that

$$\Sigma = \Sigma^{\mathrm{U}} + \Sigma^{\mathrm{L}}. \quad \text{(C.4)}$$

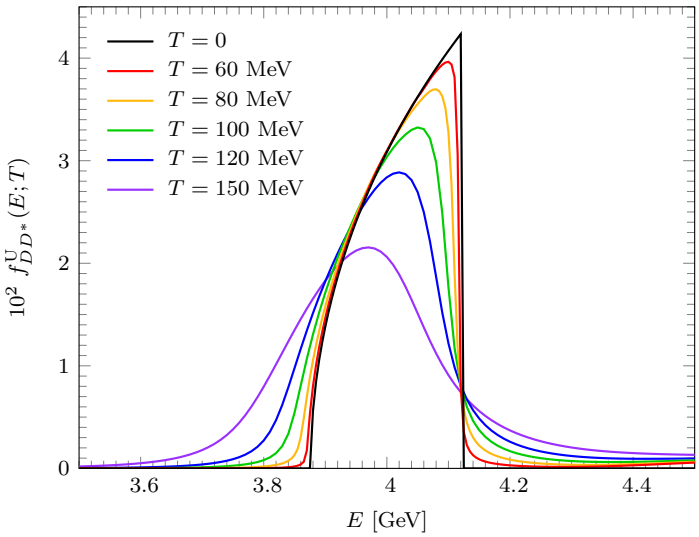

Figure C.1: Auxiliary function $f^{\mathrm{U}}_{DD^*}$ for the DD^* pair as a function of the center of mass energy E for several temperatures (different line colors). The cutoff is chosen to be $\Lambda = 700$ MeV.

The first term [Eq. (C.2)] may be evaluated in the same way as the finite-density loop of Eq. (A.5), since that expression is identical to Eq. (C.2) apart from the presence of the Bose–Einstein factors. With the change of variables

$$\Omega = \omega + \omega', \qquad \Omega' = \omega', \tag{C.5}$$

and following the steps of App. A, one arrives at the expression:

$$\Sigma^{\mathrm{U}}(E;T) = \frac{1}{2\pi^2}\int_0^\infty d\Omega\ f^{U}_{DD^*}(\Omega;T)\left(\frac{1}{E-\Omega+i\varepsilon} - \frac{1}{E+\Omega+i\varepsilon}\right), \tag{C.6}$$

where we are omitting the $\vec{P} = \vec{0}$ external momentum label, and where the auxiliary function $f_{MM'}$ is defined as

$$f^{\mathrm{U}}_{DD^*}(\Omega;T) = \int_0^\Lambda dq\, q^2 \int_0^\Omega d\Omega'\ \left[1 + b^-(\Omega-\Omega';T) + b^-(\Omega';T)\right] \times S_D\left(\Omega-\Omega',\,|\vec{q}|;\,T\right) S_{D^*}\left(\Omega',\,|\vec{q}|;\,T\right). \tag{C.7}$$

These expressions are equivalent to Eqs. (A.9) and (A.10) modulo the Bose-Einstein factors.

Using the D and D^* spectral functions from Refs. [211, 316], and introducing a three-momentum cutoff $\Lambda = 0.7$ GeV in the three-momentum integration, we

compute the auxiliary function $f^{\mathrm{U}}(\Omega;T)$. We use a Gauss-Legendre integration algorithm, ensuring that the sampling of the integrand around the points where the spectral functions peak is sufficiently dense. The results are presented in Fig. C.1. Note that, contrary to the finite density case, we no longer define a $f^{\mathrm{U}}_{D\overline{D}^*}$ function. This is because the particle and antiparticle spectral functions are the same at finite temperature, as was discussed in the main body of Chap. 4.

Regarding the cutoff dependence of $f^{\mathrm{U}}_{DD^*}$, in Fig. C.1 we display the results obtained with $\Lambda = 0.7$ GeV, in analogy to our finite nuclear density study (compare with Fig. A.3). An ultraviolet cutoff is required to properly describe the real part of the loop. In contrast, the imaginary part of the Σ^{U} contribution, which gives rise to the unitarity cut, does not require any regularization, as it is directly proportional to $f^{\mathrm{U}}_{DD^*}$:

$$\mathrm{Im}\,\Sigma^{\mathrm{U}}(E;T) = -\frac{f^{\mathrm{U}}_{DD^*}(E;T)}{2\pi}. \tag{C.8}$$

When analyzing the auxiliary function $f_{D^*D}(E;T)$ in the finite-density case (see App. A), we observed that in the region of interest near the DD^* threshold the choice of cutoff had little impact on the overall shape of the function. In contrast, in the present finite-temperature study the situation changes: increasing the cutoff produces significant distortions of $f^{\mathrm{U}}_{DD^*}(E;T)$ around threshold, especially at higher temperatures. This behavior is illustrated in Fig. C.2.

Physically, the $\Lambda = 0.7$ GeV cutoff is not adequate for computing the imaginary part because of the specific behavior of the charmed meson spectral functions at finite temperature. Unlike the nuclear case, the quasi-particle masses of the D and D^* mesons in a hot pion bath decrease significantly with increasing temperature. As a consequence, cutoff effects on $f^{\mathrm{U}}_{DD^*}$ become relevant already at lower energies. This is evident in the $T = 150$ MeV case, shown by the dashed purple line in Fig. C.2, where the function $f^{\mathrm{U}}_{DD^*}$, which should monotonically increase, instead starts to decrease around $E \simeq 3.95$ GeV. This occurs well below the expected onset of cutoff effects, estimated at $E_\Lambda \simeq m_D + m_{D^*} + \Lambda^2/m_{D^*} \sim 4.1$ GeV.

Ideally, one should remove the cutoff in the evaluation of the momentum integration within $f^{\mathrm{U}}_{DD^*}$, and integrate over all momenta. However, this is also not possible, as one would need complete knowledge of the $D\pi$ and $D^*\pi$ interactions for all energy values. More specifically, one should know the behavior of the S_D and S_{D^*} spectral functions up to arbitrarily large momenta, which is not possible. Therefore, one must adopt a compromise between using a large enough cutoff value so that cutoff effects on $f^{\mathrm{U}}_{DD^*}$—and therefore on Im Σ^{U}—are not relevant in the region around the DD^* threshold, but small enough so that one does not need to evaluate the involved spectral functions at very large momentum, where the effective theory predictions clearly fall apart.

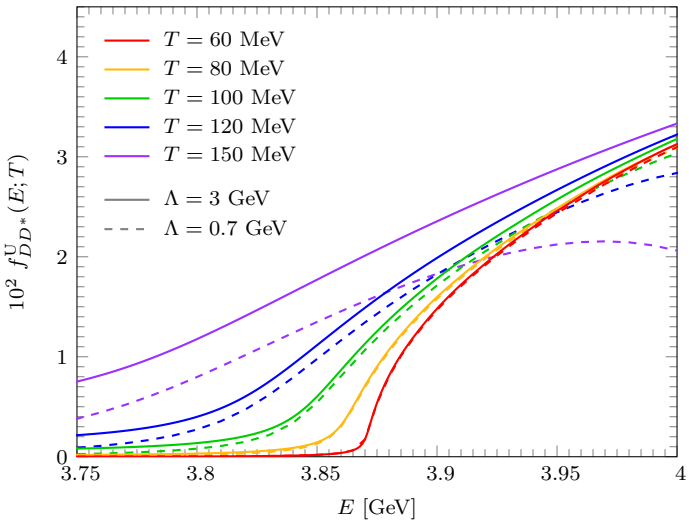

Figure C.2: Auxiliary function $f^{\mathrm{U}}_{DD^*}$ for the DD^* pair as a function of the center of mass energy E for several temperatures (different line colors). Solid lines display the results obtained using $\Lambda = 3$ GeV, while in dashed lines we represent the original results of Fig. C.1.

Following the prescription of Ref. [161], we adopt a cutoff value of $\Lambda = 3$ GeV for the evaluation of the imaginary part of the loop function. The resulting $f^{U}_{DD^*}$ with this cutoff is shown by the solid lines in Fig. C.2. Even for this relatively moderate cutoff, some extrapolation of the spectral functions to higher energies and momenta is required. As in Ref. [161], we employ a linear extrapolation of the D and D^* self-energies. Depending on the chosen extrapolation scheme, the results vary slightly, which we take as indicative of the uncertainties inherent in this approach. In practice, the strongest variations of $f^{U}_{DD^*}$ with the cutoff value or extrapolation method appear at $T = 150$ and $T = 120$ MeV, i.e., close to the crossover region. Since our model does not explicitly incorporate critical-temperature effects such as chiral symmetry restoration, we do not expect it to remain quantitatively predictive at such high temperatures.

The second contribution in Eq. (C.3) can be treated in a similar manner. Unlike the previous case, however, this term has no analogue in the finite-density loop, so a more detailed discussion is required. Since the denominators now involve the frequency difference $\omega' - \omega$, it is convenient to introduce the following change of variables:

$$\tilde{\Omega} = \omega' - \omega, \qquad \tilde{\Omega}' = \omega. \tag{C.9}$$

The Jacobian of this transformation is equal to 1. The corresponding transformation of the integration region is shown schematically in Fig. C.3.

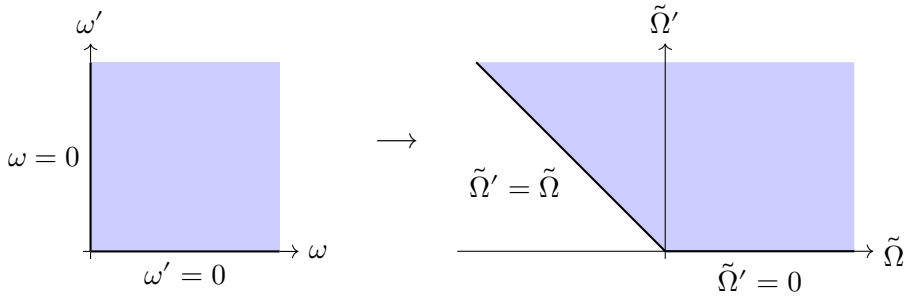

Figure C.3: Transformation of the integration volume with the change of variables of Eq. (C.9). The regions shaded in blue represent the integration volume in the original (left panel) and the transformed (right panel) coordinates.

With this change, the Σ^{L} term can be expressed as

$$\Sigma^{\mathrm{L}}(E;T) = \frac{1}{2\pi^2}\int_{-\infty}^{+\infty} d\tilde{\Omega}\; f^{L}_{DD^*}(\tilde{\Omega};T)\left(\frac{1}{E-\tilde{\Omega}+i\varepsilon} - \frac{1}{E+\tilde{\Omega}+i\varepsilon}\right), \quad \text{(C.10)}$$

where the auxiliary function $f^{\mathrm{L}}_{DD^*}$ is defined as

$$f^{\mathrm{L}}_{DD^*}(\tilde{\Omega};T) = \int_0^{\Lambda} dq\, q^2 \int_{\substack{\tilde{\Omega}'>0 \\ \tilde{\Omega}'>-\tilde{\Omega}}} d\tilde{\Omega}' \;\left[b^-(\tilde{\Omega}';T) - b^-(\tilde{\Omega}'+\tilde{\Omega};T)\right] \times S_D\left(\tilde{\Omega}',\,|\vec{q}|;\,T\right)\, S_{D^*}\left(\tilde{\Omega}'+\tilde{\Omega},\,|\vec{q}|;\,T\right). \quad \text{(C.11)}$$

The contribution of the Σ^{L} term to the imaginary part of the loop function defines the Landau cut:

$$\mathrm{Im}\,\Sigma^{\mathrm{L}}(E;T) = -\frac{f^{\mathrm{L}}_{DD^*}(E;T) - f^{\mathrm{L}}_{DD^*}(-E;T)}{2\pi}. \quad \text{(C.12)}$$

This result can be directly compared with Eq. (4.72). By construction, $f^{\mathrm{L}}_{DD^*}(\tilde{\Omega};T)$ is positive for $\tilde{\Omega} > 0$ and negative for $\tilde{\Omega} < 0$, ensuring the correct sign of the imaginary part. One can further show that

$$f^{\mathrm{L}}_{DD^*}(-\tilde{\Omega};T) = -f^{\mathrm{L}}_{D^*D}(\tilde{\Omega};T), \quad \text{(C.13)}$$

where $f^{\mathrm{L}}_{D^*D}$ is defined as in Eq. (C.11) but with the D and D^* spectral functions interchanged.

As discussed in the main body of Chap. 4, the Landau cut appearing in the finite-temperature loop is absent in both the vacuum and finite-density cases. Its presence reflects additional processes in which meson pairs are absorbed from or created within the thermal bath. From the definition of $f^{\mathrm{L}}_{DD^*}$ one

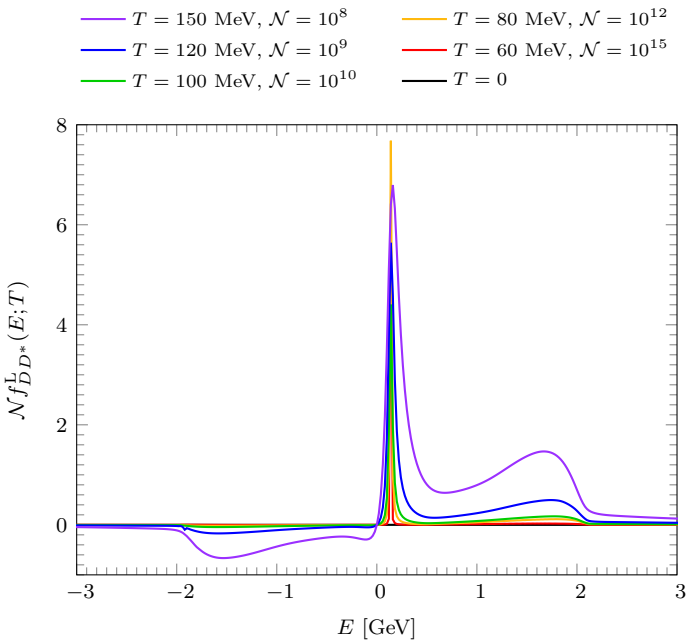

Figure C.4: Auxiliary function $f^{\mathrm{L}}_{DD^*}$ as a function of the center-of-mass energy E of the DD^* pair for several temperatures (distinguished by line colors). Each curve has been rescaled by a factor $\mathcal{N}$, with the corresponding value indicated in the legend next to its temperature.

can see that, in DD^* scattering, this contribution is strongly suppressed: the Bose–Einstein factors are very small at the energies where the D and D^* spectral functions peak. A plot of $f^{\mathrm{L}}_{DD^*}$ obtained with a cutoff $\Lambda = 0.7$ GeV is shown in Fig. C.4. In this figure, a different rescaling constant $\mathcal{N}$ is applied for each of the considered temperatures, since the results span several orders of magnitude between the highest ($T = 150$ MeV) and the lowest ($T = 60$ MeV) temperatures. For the numerical computation, we again use a Gauss-Legendre algorithm with a custom grid, defined in a way that it is sufficiently dense around the regions where the spectral functions peak.

As a check, let us consider the spectral functions to be those in the free space. In this situation, the auxiliary function $f^{\mathrm{L}}_{DD^*}$ can be written as

$$\tilde{f}^{\mathrm{L}}_{DD^*}(\tilde{\Omega};T) = \int_0^\Lambda dq\, q^2 \int_{\substack{\tilde{\Omega}'>0\\ \tilde{\Omega}'>\tilde{\Omega}}} d\tilde{\Omega}' \;\Big[b^-(\tilde{\Omega}';T) - b^-(\tilde{\Omega}'+\tilde{\Omega};T)\Big] \times \frac{\delta\big[\tilde{\Omega}' - \omega_D(q)\big]}{2\omega_D(q)} \frac{\delta\big[\tilde{\Omega}' + \tilde{\Omega} - \omega_{D^*}(q)\big]}{2\omega_{D^*}(q)}$$

$$
\begin{aligned}
&= \int_0^\Lambda dq\, q^2 \left[b^-(\omega_D(q);T) - b^-(\omega_D(q)+\tilde{\Omega};T) \right] \\
&\qquad \times \frac{1}{4\omega_D(q)\,\omega_{D^*}(q)}\, \delta\left[\omega_D(q) + \tilde{\Omega} - \omega_{D^*}(q)\right] \\
&= \int_0^\Lambda dq\, q^2 \left[b^-(\omega_D(q);T) - b^-(\omega_D(q)+\tilde{\Omega};T) \right] \\
&\qquad \times \frac{1}{4\omega_D(q)\,\omega_{D^*}(q)}\, \frac{\omega_{D^*}(k)\,\omega_D(k)}{[\omega_{D^*}(k)-\omega_D(k)]\,k}\, \delta\left[q - k(\tilde{\Omega})\right] \\
&= \left[b^-(\omega_D(k);T) - b^-(\omega_{D^*}(k);T) \right] \frac{k}{4\tilde{\Omega}}\, \theta(\Lambda - k), \qquad \text{(C.14)}
\end{aligned}
$$

where θ is the Heaviside step function. In this derivation, the on-shell momentum is defined as

$$
k = \frac{\sqrt{\lambda\left[\tilde{\Omega}^2, m_D^2, m_\pi^2\right]}}{2\tilde{\Omega}}, \qquad \text{(C.15)}
$$

and we have used the property of the Dirac delta function

$$
\delta[f(x)] = \frac{\delta(x-x_0)}{|f'(x_0)|}, \qquad \text{with } f(x_0) = 0. \qquad \text{(C.16)}
$$

Thus, we arrive at an expression for the Landau cut equivalent to Eq. (4.93). This result is shown in Fig. C.5.

A comparison between Figs. C.4 and C.5 is quite instructive. First, note the different energy scales used on the lower axis of the two plots. In Fig. C.5, the DD^* Landau cut sets in sharply at $E = m_{D^*} - m_D \sim 141$ MeV, followed by the effect of the momentum cutoff at

$$
E_\Lambda \simeq m_{D^*} - m_D + \tfrac{1}{2}\left(\tfrac{1}{m_{D^*}} - \tfrac{1}{m_D}\right)\Lambda^2 \sim m_{D^*} - m_D - 9 \text{ MeV}. \qquad \text{(C.17)}
$$

On the broader energy scale of Fig. C.4, this appears as a sharp, peak-like structure. Once the finite widths of the D and D^* spectral functions are included in Eq. (C.3), this sharp peak becomes smoothed out but still remains relatively narrow. It shows up in Fig. C.4 as the most prominent maximum, visible across all the considered temperatures.

The function of Fig. C.4, however, exhibits more than just this narrow enhancement. A second maximum consistently appears around $E \simeq 1.7$ GeV for all temperatures, accompanied by a minimum at the roughly symmetric point $E \simeq -1.7$ GeV.[1] These structures occur far above the onset of the

[1] This behavior stems from the near equality of the D and D^* masses. In the limit of exact mass degeneracy one finds $f^{\mathrm{L}}_{MM}(-E;T) = -f^{\mathrm{L}}_{MM}(E;T)$.

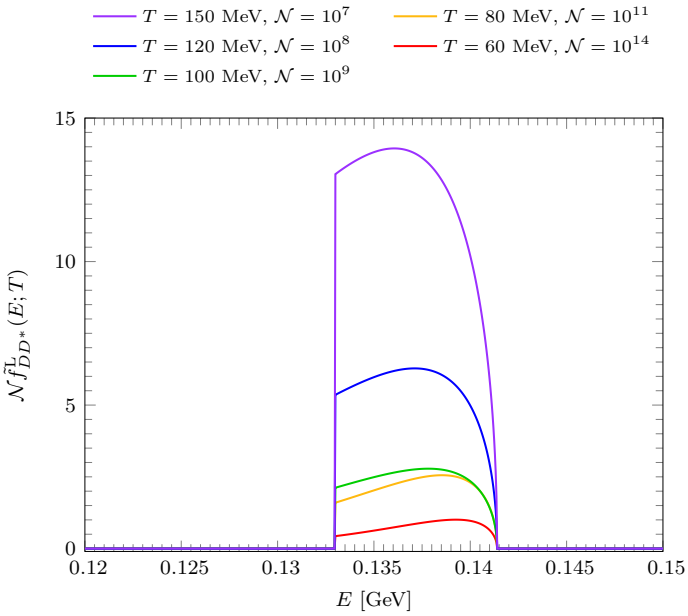

Figure C.5: Same as in Fig. C.4, but considering now the function $\tilde{f}^{\mathrm{L}}_{DD^*}$ in which the D and D^* spectral functions are approximated by Dirac deltas.

Landau cut for zero-width D and D^* mesons, located at $E \simeq 0.14$ GeV, and become increasingly pronounced at higher temperatures. They originate from the overlap of the tail of one of the spectral functions with the maximum of the other. Consequently, they are highly sensitive to both the extrapolation of the spectral functions and the chosen cutoff. Following the prescription of Ref. [161], we adopt $\Lambda = 3$ GeV and use a linear extrapolation of the D and D^* self-energies. Under this scheme, the broad structures in Fig. C.4 become more prominent, with their influence extending close to the DD^* threshold. However, within the energy scale considered in Fig. 4.10, where the thermal DD^* loop function was first presented, their effect is hardly noticeable.

For the D^*D^* thermal loop function, employed in the study of the thermal properties of the HQSS partner of the $T_{cc}(3875)$, analogous considerations were applied in its evaluation.

Appendix D

The normalization of the coupling constant

In this appendix we derive the correct normalization of the formula of Eq. (5.12) used for computing the different couplings of the Λ_c^* states to DN or D^*N two-body channels. We start from Eq. (59) of Ref. [226], tailored for meson–meson scattering, which reads

$$g_{MM} \simeq m\sqrt{16\pi\gamma/\mu} \qquad \text{with } \gamma = \sqrt{2\mu B}. \tag{D.1}$$

In this previous expression, m denotes the mass of the bound state, while B is its binding energy. However, we are interested in the coupling to a meson–baryon state, g_{MB}. In order to relate these two quantities, we start from their definitions in terms of their respective T–matrices.

$$g_{MM}^2 = \lim_{s\to m^2}(s-m^2)T_{MM} \tag{D.2}$$

$$g_{MB}^2 = \lim_{\sqrt{s}\to m}(\sqrt{s}-m)T_{MB} \tag{D.3}$$

Furthermore, the meson–meson T–matrix T_{MM} and the meson–baryon one T_{MB} have a different normalization. This normalization can be related through the BSE,

$$T = \frac{V}{1-VG}, \tag{D.4}$$

where one can explicitly see that the product VG must be independent of normalization, and that T and V share the same normalization. Therefore, by comparing the different normalization of the meson–meson loop versus the meson–baryon loop, one can easily infer the different normalization of T_{MM} versus T_{MB}.

$$G_{MB} = 2m_B G_{MM} \quad \Rightarrow \quad V_{MB} = \frac{1}{2m_B}V_{MM} \quad \Rightarrow \quad T_{MB} = \frac{1}{2m_B}T_{MM}, \tag{D.5}$$

where m_B represents the mass of the baryon. Taking all these previous considerations into account, we may write

$$m^2 16\pi\gamma/\mu = g_{MM}^2 = \lim_{s\to m^2}(s-m^2)T_{MM} \\ = \lim_{\sqrt{s}\to m}(\sqrt{s}+m)(\sqrt{s}-m)\left[2m_B T_{MB}\right] = 2m2m_B g_{MB}^2. \quad \text{(D.6)}$$

Therefore, we have found

$$g_{MB}^2 = \frac{m}{4m_B\mu}16\pi\gamma, \quad \text{(D.7)}$$

which is equivalent to Eq. (5.12).

Appendix E

Apparent width in the many-body invariant mass

In Sec. 5.3 we observed that the width of the three-body state is nearly twice that of the $\Lambda_c(2765)$, even though it arises primarily from the decays of this resonance. Although this result may appear surprising at first, it reflects a general feature of particle–cluster collisions when observables are expressed in terms of the invariant mass $\sqrt{s_1}$ of the particle–particle system versus the total invariant mass $\sqrt{s}$ of the particle–cluster system. In this appendix, we present a general derivation of the relation between the width of the state as seen in the $\sqrt{s_1}$ variable or in the $\sqrt{s}$ variable, before presenting an application to nucleon-nucleus scattering.

We start by considering two particles A and B, whose T–matrix is described by a resonance shape in some given spin-isospin channel and in a given energy region:

$$t_{AB}(s_1) = \frac{g^2}{s_1 - s_1^0 + i\sqrt{s_1^0}\Gamma}, \tag{E.1}$$

where s_1^0 represents the invariant mass of the resonant state and Γ its width at half maximum. The invariant mass at which the resonance has one half the strength of its maximum, s_1^Γ, is defined from its width as

$$s_1^\Gamma - s_1^0 = \sqrt{s_1^0}\Gamma, \qquad\qquad \sqrt{s_1^\Gamma} - \sqrt{s_1^0} = \frac{\Gamma}{2}. \tag{E.2}$$

We consider now the B particle to be bound in a cluster $\mathcal{C}$ of several particles, as depicted in Fig. E.1. If the B particle is bound in the cluster with negligible binding and internal momentum, we can approximate the invariant mass of the AB system as

$$s_1 = m_A^2 + (\xi m_B)^2 + 2E_A(\xi m_B), \tag{E.3}$$

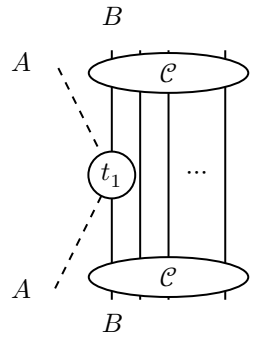

Figure E.1: FCA single-scattering diagram with an external A particle scattering off a B particle within the $\mathcal{C}$ cluster.

where again ξ is a correction factor

$$\xi = \frac{m_{\mathcal{C}}}{\sum_{\text{particles in } \mathcal{C}}^{\text{masses of}}}. \tag{E.4}$$

On the other hand, the invariant mass of the full system $A\mathcal{C}$ can be written as

$$s = m_A^2 + m_{\mathcal{C}}^2 + 2E_A m_{\mathcal{C}}^2. \tag{E.5}$$

By equating now the energy of the external particle E_A in both equations (E.3) and (E.5), we obtain a linear relation between s_1 and s.

$$\frac{s_1 - m_A^2 - (\xi m_B)^2}{2(\xi m_B)} = \frac{s - m_A^2 - m_{\mathcal{C}}^2}{2m_{\mathcal{C}}}. \tag{E.6}$$

Equipped with this transformation, we can deduce now the apparent width of the state in the s variable starting from the width of the state in s_1:

$$\Gamma = \frac{s_1^\Gamma - s_1^0}{\sqrt{s_1^0}} = \frac{1}{\sqrt{s_1^0}} \frac{\xi m_B}{m_{\mathcal{C}}} \left(s^\Gamma - s^0\right), \tag{E.7}$$

where s^Γ and s^0 are obtained from s_1^Γ and s_1^0 through Eq. (E.6). Defining now the apparent width of the state as that obeying

$$s^\Gamma - s^0 = \sqrt{s^0}\Gamma^{(\text{app.})} \qquad \sqrt{s^\Gamma} - \sqrt{s^0} = \frac{\Gamma^{(\text{app.})}}{2}, \tag{E.8}$$

we can finally write

$$\Gamma^{(\text{app.})} = \sqrt{\frac{s_1^0}{s^0}} \frac{m_{\mathcal{C}}}{\xi m_B} \Gamma. \tag{E.9}$$

Applying (E.9) to the case where the external particle is a D meson, the interaction with the nucleon in the ND^* cluster described by the $\Lambda_c(2765)$ resonance, a direct evaluation of the apparent width through Eq. (E.9) yields

$$\Gamma^{(\text{app.})}_{\Lambda_c(2765)} = 1.906 \times \Gamma_{\Lambda_c(2765)} \simeq 95 \text{ MeV}, \tag{E.10}$$

result which was observed in Fig. 5.10.

We can also apply this result to the case of an external nucleon interacting with one of the nucleons inside of a nucleus of mass number A. In this case, neglecting the offshellness effect by setting $\xi = 1$, we have

$$\Gamma^{(\text{app.})} = \frac{m_A^2}{m_N\sqrt{s^0}}\Gamma, \tag{E.11}$$

where s^0 is obtained in the zero binding energy limit from Eq. (E.6) by setting $s_1^0 = (2m_N)^2$ as

$$s^0 = \frac{m_A}{m_N}\left((2m_N)^2 - 2m_N^2\right) + m_N^2 + m_A^2 = A2m_N^2 + m_N^2 + A^2m_N^2 = (A+1)^2m_N^2. \tag{E.12}$$

Using now Eq. (E.9), we obtain

$$\frac{\Gamma^{(\text{app.})}}{\Gamma} = \frac{2m_N}{(A+1)m_N}\frac{Am_N}{m_N} = \frac{2A}{(A+1)}. \tag{E.13}$$

We can see that for $A = 1$ the two magnitudes are obviously equal, but as A increases then $\Gamma^{(\text{app.})}$ becomes larger than Γ, doubling it in the limit $A \to \infty$. Although this specific behavior with the mass number is particular to the nuclear scenario, the apparent width increase of a two-body resonance when studying a three or more particle system is a general result, as we have shown here.

Bibliography

[1] V. Montesinos, M. Albaladejo, J. Nieves, and L. Tolos, *Properties of the Tcc(3875)+ and Tc¯c¯(3875)− and their heavy-quark spin partners in nuclear matter*, Phys. Rev. C **108**, 035205 (2023), arXiv:2306.17673 [hep-ph].

[2] V. Montesinos, M. Albaladejo, J. Nieves, and L. Tolos, *Charge-conjugation asymmetry and molecular content: The Ds0*(2317)± in matter*, Phys. Lett. B **853**, 138656 (2024), arXiv:2403.00451 [hep-ph].

[3] V. Montesinos, N. Ikeno, E. Oset, M. Albaladejo, J. Nieves, and L. Tolos, *On the determination of the D meson width in the nuclear medium with the transparency ratio*, Phys. Lett. B **860**, 139172 (2025), arXiv:2407.19295 [nucl-th].

[4] V. Montesinos, J. Song, W.-H. Liang, E. Oset, J. Nieves, and M. Albaladejo, *Study of possible DND* bound states*, Phys. Rev. D **110**, 054043 (2024), arXiv:2405.09467 [hep-ph].

[5] V. Montesinos, G. Montana, M. Albaladejo, J. Nieves, and L. Tolos, *Melting down a tetraquark: $D^*D^{(*)}$ interactions and $T_{cc}(3875)^+$ in a hot environment*, (2025), arXiv:2507.13319 [hep-ph].

[6] V. Montesinos, M. Albaladejo, J. Nieves, and L. Tolos, *Properties of the Tcc(3875)+ and the Tcc (3875)− states in nuclear matter*, EPJ Web Conf. **291**, 03003 (2024), arXiv:2310.02057 [hep-ph].

[7] J. Nieves, M. Albadalejo, V. Montesinos, and L. Tolos, *Charge-conjugation asymmetry and molecular content: the $T_{cc}(3875)$ and $D^*_{s0}(2317)$ in nuclear matter*, PoS **QNP2024**, 077 (2025).

[8] V. Montesinos, J. Song, W.-H. Liang, E. Oset, J. Nieves, and M. Albaladejo, *$NDD^\star$ three-body molecular states*, PoS **QNP2024**, 045 (2025).

[9] T. A. Lähde and U.-G. Meißner, *Nuclear Lattice Effective Field Theory: An introduction*, Vol. 957 (Springer, 2019).

[10] D. Lee, *Lattice Effective Field Theory Simulations of Nuclei*, (2025), arXiv:2501.03303 [nucl-th].

[11] S. Weinberg, *Phenomenological Lagrangians*, Physica A **96**, edited by S. Deser, 327–340 (1979).

[12] J. Gasser and H. Leutwyler, *Chiral Perturbation Theory to One Loop*, Annals Phys. **158**, 142 (1984).

[13] J. Gasser and H. Leutwyler, *Chiral Perturbation Theory: Expansions in the Mass of the Strange Quark*, Nucl. Phys. B **250**, 465–516 (1985).

[14] A. Pich, *Chiral perturbation theory*, Rept. Prog. Phys. **58**, 563–610 (1995), arXiv:hep-ph/9502366.

[15] J. A. Oller and U. G. Meissner, *Chiral dynamics in the presence of bound states: Kaon nucleon interactions revisited*, Phys. Lett. B **500**, 263–272 (2001), arXiv:hep-ph/0011146.

[16] D. Jido, J. A. Oller, E. Oset, A. Ramos, and U. G. Meissner, *Chiral dynamics of the two Lambda(1405) states*, Nucl. Phys. A **725**, 181–200 (2003), arXiv:nucl-th/0303062.

[17] C. Garcia-Recio, J. Nieves, E. Ruiz Arriola, and M. J. Vicente Vacas, *S = -1 meson baryon unitarized coupled channel chiral perturbation theory and the S(01) Lambda(1405) and Lambda(1670) resonances*, Phys. Rev. D **67**, 076009 (2003), arXiv:hep-ph/0210311.

[18] S. Navas et al. (Particle Data Group), *Review of particle physics*, Phys. Rev. D **110**, 030001 (2024).

[19] A. V. Manohar and M. B. Wise, *Heavy quark physics*, Vol. 10 (Cambridge University Press, 2000).

[20] M. Neubert, *Heavy quark symmetry*, Phys. Rept. **245**, 259–396 (1994), arXiv:hep-ph/9306320.

[21] N. Isgur and M. B. Wise, *Weak Decays of Heavy Mesons in the Static Quark Approximation*, Phys. Lett. B **232**, 113–117 (1989).

[22] N. Isgur and M. B. Wise, *Weak transition form factors between heavy mesons*, Phys. Lett. B **237**, 527–530 (1990).

[23] M. B. Wise, *Chiral perturbation theory for hadrons containing a heavy quark*, Phys. Rev. D **45**, R2188 (1992).

[24] T.-M. Yan, H.-Y. Cheng, C.-Y. Cheung, G.-L. Lin, Y. C. Lin, and H.-L. Yu, *Heavy quark symmetry and chiral dynamics*, Phys. Rev. D **46**, [Erratum: Phys.Rev.D 55, 5851 (1997)], 1148–1164 (1992).

[25] G. Burdman and J. F. Donoghue, *Union of chiral and heavy quark symmetries*, Phys. Lett. B **280**, 287–291 (1992).

[26] R. Casalbuoni, A. Deandrea, N. Di Bartolomeo, R. Gatto, F. Feruglio, and G. Nardulli, *Phenomenology of heavy meson chiral Lagrangians*, Phys. Rept. **281**, 145–238 (1997), arXiv:hep-ph/9605342.

[27] M. Bando, T. Kugo, S. Uehara, K. Yamawaki, and T. Yanagida, *Is rho Meson a Dynamical Gauge Boson of Hidden Local Symmetry?*, Phys. Rev. Lett. **54**, 1215 (1985).

[28] U. G. Meissner, *Low-Energy Hadron Physics from Effective Chiral Lagrangians with Vector Mesons*, Phys. Rept. **161**, 213 (1988).

[29] C. W. Xiao, J. Nieves, and E. Oset, *Combining heavy quark spin and local hidden gauge symmetries in the dynamical generation of hidden charm baryons*, Phys. Rev. D **88**, 056012 (2013), arXiv:1304.5368 [hep-ph].

[30] L. S. Geng and E. Oset, *Vector meson-vector meson interaction in a hidden gauge unitary approach*, Phys. Rev. D **79**, 074009 (2009), arXiv:0812.1199 [hep-ph].

[31] R. Molina, D. Nicmorus, and E. Oset, *The rho rho interaction in the hidden gauge formalism and the f(0)(1370) and f(2)(1270) resonances*, Phys. Rev. D **78**, 114018 (2008), arXiv:0809.2233 [hep-ph].

[32] H. Nagahiro, L. Roca, A. Hosaka, and E. Oset, *Hidden gauge formalism for the radiative decays of axial-vector mesons*, Phys. Rev. D **79**, 014015 (2009).

[33] M. Gell-Mann, *The Eightfold Way: A Theory of strong interaction symmetry*, Report No. CTSL-20, TID-12608, doi: 10.2172/4008239 (1961).

[34] Y. Neeman, *GAUGES, GROUPS AND AN INVARIANT THEORY OF THE STRONG INTERACTIONS*, Report No. IA-698 (1961).

[35] V. E. Barnes et al., *Observation of a Hyperon with Strangeness Minus Three*, Phys. Rev. Lett. **12**, 204–206 (1964).

[36] M. Gell-Mann, *A Schematic Model of Baryons and Mesons*, Phys. Lett. **8**, 214–215 (1964).

[37] G. Zweig, *An SU(3) model for strong interaction symmetry and its breaking. Version 1*, doi: 10.17181/CERN-TH-401 (1964).

[38] R. E. Taylor, *Deep inelastic scattering: The Early years*, Rev. Mod. Phys. **63**, 573–595 (1991).

[39] H. W. Kendall, *Deep inelastic scattering: Experiments on the proton and the observation of scaling*, Rev. Mod. Phys. **63**, 597–614 (1991).

[40] J. I. Friedman, *Deep inelastic scattering: Comparisons with the quark model*, Rev. Mod. Phys. **63**, 615–629 (1991).

[41] S. K. Choi et al. (Belle), *Observation of a narrow charmonium-like state in exclusive $B^{\pm} \to K^{\pm}\pi^{+}\pi^{-}J/\psi$ decays*, Phys. Rev. Lett. **91**, 262001 (2003), arXiv:hep-ex/0309032.

[42] N. A. Tornqvist, *Possible large deuteron - like meson meson states bound by pions*, Phys. Rev. Lett. **67**, 556–559 (1991).

[43] Z. Yang, X. Cao, F.-K. Guo, J. Nieves, and M. P. Valderrama, *Strange molecular partners of the $Z_c(3900)$ and $Z_c(4020)$*, Phys. Rev. D **103**, 074029 (2021), arXiv:2011.08725 [hep-ph].

[44] M.-L. Du, M. Albaladejo, F.-K. Guo, and J. Nieves, *Combined analysis of the Zc(3900) and the Zcs(3985) exotic states*, Phys. Rev. D **105**, 074018 (2022), arXiv:2201.08253 [hep-ph].

[45] R. Aaij et al. (LHCb), *Study of the doubly charmed tetraquark T_{cc}^{+}*, Nature Commun. **13**, 3351 (2022), arXiv:2109.01056 [hep-ex].

[46] X.-K. Dong, F.-K. Guo, and B.-S. Zou, *A survey of heavy−heavy hadronic molecules*, Commun. Theor. Phys. **73**, 125201 (2021), arXiv:2108.02673 [hep-ph].

[47] A. Feijoo, W. H. Liang, and E. Oset, *D0D0π+ mass distribution in the production of the Tcc exotic state*, Phys. Rev. D **104**, 114015 (2021), arXiv:2108.02730 [hep-ph].

[48] X.-Z. Ling, M.-Z. Liu, L.-S. Geng, E. Wang, and J.-J. Xie, *Can we understand the decay width of the Tcc+ state?*, Phys. Lett. B **826**, 136897 (2022), arXiv:2108.00947 [hep-ph].

[49] S. Fleming, R. Hodges, and T. Mehen, *Tcc+ decays: Differential spectra and two-body final states*, Phys. Rev. D **104**, 116010 (2021), arXiv:2109.02188 [hep-ph].

[50] H. Ren, F. Wu, and R. Zhu, *Hadronic Molecule Interpretation of Tcc+ and Its Beauty Partners*, Adv. High Energy Phys. **2022**, 9103031 (2022), arXiv:2109.02531 [hep-ph].

[51] K. Chen, R. Chen, L. Meng, B. Wang, and S.-L. Zhu, *Systematics of the heavy flavor hadronic molecules*, Eur. Phys. J. C **82**, 581 (2022), arXiv:2109.13057 [hep-ph].

[52] M. Albaladejo, *T_{cc}^{+} coupled channel analysis and predictions*, Phys. Lett. B **829**, 137052 (2022), arXiv:2110.02944 [hep-ph].

[53] M.-L. Du, V. Baru, X.-K. Dong, et al., *Coupled-channel approach to Tcc+ including three-body effects*, Phys. Rev. D **105**, 014024 (2022), arXiv:2110.13765 [hep-ph].

[54] V. Baru, X.-K. Dong, M.-L. Du, et al., *Effective range expansion for narrow near-threshold resonances*, Phys. Lett. B **833**, 137290 (2022), arXiv:2110.07484 [hep-ph].

[55] N. Santowsky and C. S. Fischer, *Four-quark states with charm quarks in a two-body Bethe – Salpeter approach*, Eur. Phys. J. C **82**, 313 (2022), arXiv:2111.15310 [hep-ph].

[56] C. Deng and S.-L. Zhu, *Tcc+ and its partners*, Phys. Rev. D **105**, 054015 (2022), arXiv:2112.12472 [hep-ph].

[57] H.-W. Ke, X.-H. Liu, and X.-Q. Li, *Possible molecular states of $D^{(*)}D^{(*)}$ and $B^{(*)}B^{(*)}$ within the Bethe – Salpeter framework*, Eur. Phys. J. C **82**, 144 (2022), arXiv:2112.14142 [hep-ph].

[58] S. S. Agaev, K. Azizi, and H. Sundu, *Hadronic molecule model for the doubly charmed state T_{cc}^{+}*, JHEP **06**, 057 (2022), arXiv:2201.02788 [hep-ph].

[59] L. Meng, B. Wang, G.-J. Wang, and S.-L. Zhu, *Chiral perturbation theory for heavy hadrons and chiral effective field theory for heavy hadronic molecules*, Phys. Rept. **1019**, 1–149 (2023), arXiv:2204.08716 [hep-ph].

[60] L. M. Abreu, *A note on the possible bound D(*)D(*),B¯(*)B¯(*) and D(*)B¯(*) states*, Nucl. Phys. B **985**, 115994 (2022), arXiv:2206.01166 [hep-ph].

[61] S. Chen, C. Shi, Y. Chen, M. Gong, Z. Liu, W. Sun, and R. Zhang, *Tcc+(3875) relevant DD* scattering from Nf = 2 lattice QCD*, Phys. Lett. B **833**, 137391 (2022), arXiv:2206.06185 [hep-lat].

[62] M. Albaladejo and J. Nieves, *Compositeness of S-wave weakly-bound states from next-to-leading order Weinberg' s relations*, Eur. Phys. J. C **82**, 724 (2022), arXiv:2203.04864 [hep-ph].

[63] L. R. Dai, L. M. Abreu, A. Feijoo, and E. Oset, *The isospin and compositeness of the $T_{cc}(3875)$ state*, Eur. Phys. J. C **83**, 983 (2023), arXiv:2304.01870 [hep-ph].

[64] G.-J. Wang, Z. Yang, J.-J. Wu, M. Oka, and S.-L. Zhu, *New insight into the exotic states strongly coupled with the $D\overline{D}*$ from the T_{cc}^{+}*, Sci. Bull. **69**, 3036–3041 (2024), arXiv:2306.12406 [hep-ph].

[65] J. l. Ballot and J. M. Richard, *FOUR QUARK STATES IN ADDITIVE POTENTIALS*, Phys. Lett. B **123**, 449–451 (1983).

[66] S. Zouzou, B. Silvestre-Brac, C. Gignoux, and J. M. Richard, *FOUR QUARK BOUND STATES*, Z. Phys. C **30**, 457 (1986).

[67] B. Aubert et al. (BaBar), *Observation of a narrow meson decaying to $D_s^+\pi^0$ at a mass of 2.32-GeV/c^2*, Phys. Rev. Lett. **90**, 242001 (2003), arXiv:hep-ex/0304021.

[68] D. Besson et al. (CLEO), *Observation of a narrow resonance of mass 2.46-GeV/c**2 decaying to D*+(s) pi0 and confirmation of the D*(sJ)(2317) state*, Phys. Rev. D **68**, [Erratum: Phys.Rev.D 75, 119908 (2007)], 032002 (2003), arXiv:hep-ex/0305100.

[69] M.-L. Du, M. Albaladejo, P. Fernández-Soler, F.-K. Guo, C. Hanhart, U.-G. Meißner, J. Nieves, and D.-L. Yao, *Towards a new paradigm for heavy-light meson spectroscopy*, Phys. Rev. D **98**, 094018 (2018), arXiv:1712.07957 [hep-ph].

[70] S. Godfrey and N. Isgur, *Mesons in a Relativized Quark Model with Chromodynamics*, Phys. Rev. D **32**, 189–231 (1985).

[71] F.-K. Guo, C. Hanhart, S. Krewald, and U.-G. Meissner, *Subleading contributions to the width of the D*(s0)(2317)*, Phys. Lett. B **666**, 251–255 (2008), arXiv:0806.3374 [hep-ph].

[72] M. Albaladejo, P. Fernandez-Soler, F.-K. Guo, and J. Nieves, *Two-pole structure of the $D_0^*(2400)$*, Phys. Lett. B **767**, 465–469 (2017), arXiv:1610.06727 [hep-ph].

[73] D. Mohler, C. B. Lang, L. Leskovec, S. Prelovsek, and R. M. Woloshyn, *$D_{s0}^*(2317)$ Meson and D-Meson-Kaon Scattering from Lattice QCD*, Phys. Rev. Lett. **111**, 222001 (2013), arXiv:1308.3175 [hep-lat].

[74] C. B. Lang, L. Leskovec, D. Mohler, S. Prelovsek, and R. M. Woloshyn, *Ds mesons with DK and D*K scattering near threshold*, Phys. Rev. D **90**, 034510 (2014), arXiv:1403.8103 [hep-lat].

[75] G. S. Bali, S. Collins, A. Cox, and A. Schäfer, *Masses and decay constants of the $D_{s0}^*(2317)$ and $D_{s1}(2460)$ from $N_f = 2$ lattice QCD close to the physical point*, Phys. Rev. D **96**, 074501 (2017), arXiv:1706.01247 [hep-lat].

[76] G. K. C. Cheung, C. E. Thomas, D. J. Wilson, G. Moir, M. Peardon, and S. M. Ryan (Hadron Spectrum), *DK I = 0,$D\overline{K}$ I = 0, 1 scattering and the D_{s0}^*(2317) from lattice QCD*, JHEP **02**, 100 (2021), arXiv:2008.06432 [hep-lat].

[77] P. Colangelo and F. De Fazio, *Understanding D(sJ)(2317)*, Phys. Lett. B **570**, 180–184 (2003), arXiv:hep-ph/0305140.

[78] L. Maiani, F. Piccinini, A. D. Polosa, and V. Riquer, *Diquark-antidiquarks with hidden or open charm and the nature of X(3872)*, Phys. Rev. D **71**, 014028 (2005), arXiv:hep-ph/0412098.

[79] P. G. Ortega, J. Segovia, D. R. Entem, and F. Fernandez, *Molecular components in P-wave charmed-strange mesons*, Phys. Rev. D **94**, 074037 (2016), arXiv:1603.07000 [hep-ph].

[80] L. D. Faddeev, *Scattering Theory for a Three-Particle System*, Sov. Phys. JETP **12**, 1014–1019 (1961).

[81] R. Chand and R. H. Dalitz, *Charge-independence in K- -deuterium capture reactions*, Annals Phys. **20**, 1–19 (1962).

[82] Y. Akaishi and T. Yamazaki, *Nuclear anti-K bound states in light nuclei*, Phys. Rev. C **65**, 044005 (2002).

[83] D. Jido and Y. Kanada-En'yo, *K anti-K N molecule state with I = 1/2 and J**P = 1/2+ studied with three-body calculation*, Phys. Rev. C **78**, 035203 (2008).

[84] A. Martinez Torres, K. P. Khemchandani, L. S. Geng, M. Napsuciale, and E. Oset, *The X(2175) as a resonant state of the phi K anti-K system*, Phys. Rev. D **78**, 074031 (2008), arXiv:0801.3635 [nucl-th].

[85] X.-L. Ren, B. B. Malabarba, L.-S. Geng, K. P. Khemchandani, and A. Martínez Torres, *K^* mesons with hidden charm arising from $KX(3872)$ and $KZ_c(3900)$ dynamics*, Phys. Lett. B **785**, 112–117 (2018), arXiv:1805.08330 [hep-ph].

[86] M. Agnello et al. (FINUDA), *Evidence for a kaon-bound state K- p p produced in K- absorption reactions at rest*, Phys. Rev. Lett. **94**, 212303 (2005).

[87] T. Yamaga et al. (J-PARC E15), *Observation of a $\bar{K}NN$ bound state in the ^{3}He$(K^-, \Lambda p)n$ reaction*, Phys. Rev. C **102**, 044002 (2020), arXiv:2006.13433 [nucl-ex].

[88] T. Yamaga et al. (J-PARC E15), *Measurement of the mesonic decay branch of the K^-NN quasibound state*, Phys. Rev. C **110**, 014002 (2024), arXiv:2404.01773 [nucl-ex].

[89] J. C. Collins and M. J. Perry, *Superdense Matter: Neutrons Or Asymptotically Free Quarks?*, Phys. Rev. Lett. **34**, 1353 (1975).

[90] N. Cabibbo and G. Parisi, *Exponential Hadronic Spectrum and Quark Liberation*, Phys. Lett. B **59**, 67–69 (1975).

[91] Y. Aoki, G. Endrodi, Z. Fodor, S. D. Katz, and K. K. Szabo, *The Order of the quantum chromodynamics transition predicted by the standard model of particle physics*, Nature **443**, 675–678 (2006), arXiv:hep-lat/0611014.

[92] S. Borsanyi, Z. Fodor, C. Hoelbling, S. D. Katz, S. Krieg, C. Ratti, and K. K. Szabo (Wuppertal-Budapest), *Is there still any T_c mystery in lattice QCD? Results with physical masses in the continuum limit III*, JHEP **09**, 073 (2010), arXiv:1005.3508 [hep-lat].

[93] A. Bazavov et al., *The chiral and deconfinement aspects of the QCD transition*, Phys. Rev. D **85**, 054503 (2012), arXiv:1111.1710 [hep-lat].

[94] K. Fukushima and T. Hatsuda, *The phase diagram of dense QCD*, Rept. Prog. Phys. **74**, 014001 (2011), arXiv:1005.4814 [hep-ph].

[95] J. N. Guenther, *Overview of the QCD phase diagram: Recent progress from the lattice*, Eur. Phys. J. A **57**, 136 (2021), arXiv:2010.15503 [hep-lat].

[96] F. Weber, *Strange quark matter and compact stars*, Prog. Part. Nucl. Phys. **54**, 193–288 (2005), arXiv:astro-ph/0407155.

[97] M. G. Alford, A. Schmitt, K. Rajagopal, and T. Schäfer, *Color superconductivity in dense quark matter*, Rev. Mod. Phys. **80**, 1455–1515 (2008), arXiv:0709.4635 [hep-ph].

[98] L. Tolos and L. Fabbietti, *Strangeness in Nuclei and Neutron Stars*, Prog. Part. Nucl. Phys. **112**, 103770 (2020), arXiv:2002.09223 [nucl-ex].

[99] G. F. Burgio, H. .-. Schulze, I. Vidana, and J. .-. Wei, *Neutron stars and the nuclear equation of state*, Prog. Part. Nucl. Phys. **120**, 103879 (2021), arXiv:2105.03747 [nucl-th].

[100] J. Schaffner-Bielich, *Compact Star Physics* (Cambridge University Press, Aug. 2020).

[101] U. W. Heinz and M. Jacob, *Evidence for a new state of matter: An Assessment of the results from the CERN lead beam program*, (2000), arXiv:nucl-th/0002042.

[102] I. Arsene et al. (BRAHMS), *Quark gluon plasma and color glass condensate at RHIC? The Perspective from the BRAHMS experiment*, Nucl. Phys. A **757**, 1–27 (2005), arXiv:nucl-ex/0410020.

[103] B. B. Back et al. (PHOBOS), *The PHOBOS perspective on discoveries at RHIC*, Nucl. Phys. A **757**, 28–101 (2005), arXiv:nucl-ex/0410022.

[104] J. Adams et al. (STAR), *Experimental and theoretical challenges in the search for the quark gluon plasma: The STAR Collaboration's critical assessment of the evidence from RHIC collisions*, Nucl. Phys. A **757**, 102–183 (2005), arXiv:nucl-ex/0501009.

[105] K. Adcox et al. (PHENIX), *Formation of dense partonic matter in relativistic nucleus-nucleus collisions at RHIC: Experimental evaluation by the PHENIX collaboration*, Nucl. Phys. A **757**, 184–283 (2005), arXiv:nucl-ex/0410003.

[106] J. Chen et al., *Properties of the QCD matter: review of selected results from the relativistic heavy ion collider beam energy scan (RHIC BES) program*, Nucl. Sci. Tech. **35**, 214 (2024), arXiv:2407.02935 [nucl-ex].

[107] Q.-Y. Shou et al., *Properties of QCD matter: a review of selected results from ALICE experiment*, Nucl. Sci. Tech. **35**, 219 (2024), arXiv:2409.17964 [nucl-ex].

[108] H. H. Gutbrod, *International Facility for Antiproton and Ion Research (FAIR) at GSI, Darmstadt*, Nucl. Phys. A **752**, edited by B. Jonson, M. Meister, G. Nyman, and M. Zhukov, 457–469 (2005).

[109] G. Baym, T. Hatsuda, T. Kojo, P. D. Powell, Y. Song, and T. Takatsuka, *From hadrons to quarks in neutron stars: a review*, Rept. Prog. Phys. **81**, 056902 (2018), arXiv:1707.04966 [astro-ph.HE].

[110] R. Kumar et al. (MUSES), *Theoretical and experimental constraints for the equation of state of dense and hot matter*, Living Rev. Rel. **27**, 3 (2024), arXiv:2303.17021 [nucl-th].

[111] J. Nieves, E. Oset, and C. Garcia-Recio, *Many body approach to low-energy pion nucleus scattering*, Nucl. Phys. A **554**, 554–579 (1993).

[112] L. Tolos, A. Ramos, and E. Oset, *Chiral approach to antikaon s and p-wave interactions in dense nuclear matter*, Phys. Rev. C **74**, 015203 (2006), arXiv:nucl-th/0603033.

[113] C.-H. Lee, G. E. Brown, D.-P. Min, and M. Rho, *An Effective chiral Lagrangian approach to kaon - nuclear interactions: Kaonic atom and kaon condensation*, Nucl. Phys. A **585**, 401–449 (1995), arXiv:hep-ph/9406311.

[114] Y. Iizawa, D. Jido, N. Ikeno, J. Yamagata-Sekihara, and S. Hirenzaki, *Origin of energy shift in kaonic atom and kaon-nucleus interaction*, (2019), arXiv:1907.05626 [nucl-th].

[115] J. Yamagata-Sekihara, Y. Iizawa, D. Jido, N. Ikeno, T. Hashimoto, S. Okada, and S. Hirenzaki, *Investigation of Kaonic Atom Optical Potential by the High-Precision Data of Kaonic* ^{3}*He and* ^{4}*He Atoms*, PTEP **2025**, 013D02 (2025), arXiv:2407.20012 [nucl-th].

[116] A. Cieply and J. Smejkal, *Chirally motivated $\bar{K}N$ amplitudes for in-medium applications*, Nucl. Phys. A **881**, edited by A. Gal, O. Hashimoto, and J. Pochodzalla, 115–126 (2012), arXiv:1112.0917 [nucl-th].

[117] Y. Ikeda, T. Hyodo, and W. Weise, *Chiral SU(3) theory of antikaon-nucleon interactions with improved threshold constraints*, Nucl. Phys. A **881**, 98–114 (2012), arXiv:1201.6549 [nucl-th].

[118] A. Feijoo, V. Magas, and A. Ramos, *S=−1 meson-baryon interaction and the role of isospin filtering processes*, Phys. Rev. C **99**, 035211 (2019), arXiv:1810.07600 [hep-ph].

[119] M. Bazzi et al. (SIDDHARTA), *A New Measurement of Kaonic Hydrogen X-rays*, Phys. Lett. B **704**, 113–117 (2011), arXiv:1105.3090 [nucl-ex].

[120] A. Hosaka, T. Hyodo, K. Sudoh, Y. Yamaguchi, and S. Yasui, *Heavy Hadrons in Nuclear Matter*, Prog. Part. Nucl. Phys. **96**, 88–153 (2017), arXiv:1606.08685 [hep-ph].

[121] C. F. V. Weizsacker, *Zur Theorie der Kernmassen*, Z. Phys. **96**, 431–458 (1935).

[122] M. Goeppert-Mayer and J. H. D. Jensen, *Elementary theory of nuclear shell structure* (New York: John Wiley & Sons, 1955).

[123] K. A. Brueckner, *Multiple Scattering Corrections to the Impulse Approximation in the Two-Body System*, Phys. Rev. **89**, 834–838 (1953).

[124] K. A. Brueckner and J. L. Gammel, *Properties of Nuclear Matter*, Phys. Rev. **109**, 1023–1039 (1958).

[125] J. P. Jeukenne, A. Lejeune, and C. Mahaux, *Many Body Theory of Nuclear Matter*, Phys. Rept. **25**, 83–174 (1976).

[126] F. Coester, S. Cohen, B. Day, and C. M. Vincent, *Variation in Nuclear-Matter Binding Energies with Phase-Shift-Equivalent Two-Body Potentials*, Phys. Rev. C **1**, 769–776 (1970).

[127] S. Weinberg, *Nuclear forces from chiral Lagrangians*, Phys. Lett. B **251**, 288–292 (1990).

[128] E. Epelbaum, H.-W. Hammer, and U.-G. Meissner, *Modern Theory of Nuclear Forces*, Rev. Mod. Phys. **81**, 1773–1825 (2009), arXiv:0811.1338 [nucl-th].

[129] N. Ishii, S. Aoki, and T. Hatsuda, *The Nuclear Force from Lattice QCD*, Phys. Rev. Lett. **99**, 022001 (2007), arXiv:nucl-th/0611096.

[130] S. R. Beane, W. Detmold, K. Orginos, and M. J. Savage, *Nuclear Physics from Lattice QCD*, Prog. Part. Nucl. Phys. **66**, 1–40 (2011), arXiv:1004.2935 [hep-lat].

[131] J. Carlson, S. Gandolfi, F. Pederiva, S. C. Pieper, R. Schiavilla, K. E. Schmidt, and R. B. Wiringa, *Quantum Monte Carlo methods for nuclear physics*, Rev. Mod. Phys. **87**, 1067 (2015), arXiv:1412.3081 [nucl-th].

[132] R. Hagedorn, *Statistical thermodynamics of strong interactions at high-energies*, Nuovo Cim. Suppl. **3**, 147–186 (1965).

[133] T. Matsubara, *A New approach to quantum statistical mechanics*, Prog. Theor. Phys. **14**, 351–378 (1955).

[134] R. L. Kobes and G. W. Semenoff, *Discontinuities of Green Functions in Field Theory at Finite Temperature and Density*, Nucl. Phys. B **260**, 714–746 (1985).

[135] R. Aaij et al. (LHCb), *Observation of $J/\psi p$ Resonances Consistent with Pentaquark States in $\Lambda_b^0 \to J/\psi K^- p$ Decays*, Phys. Rev. Lett. **115**, 072001 (2015), arXiv:1507.03414 [hep-ex].

[136] R. Aaij et al. (LHCb), *Study of the production of Λ_b^0 and $\overline{B}^0$ hadrons in pp collisions and first measurement of the $\Lambda_b^0 \to J/\psi p K^-$ branching fraction*, Chin. Phys. C **40**, 011001 (2016), arXiv:1509.00292 [hep-ex].

[137] R. Aaij et al. (LHCb), *Observation of a narrow pentaquark state, $P_c(4312)^+$, and of two-peak structure of the $P_c(4450)^+$*, Phys. Rev. Lett. **122**, 222001 (2019), arXiv:1904.03947 [hep-ex].

[138] R. Aaij et al. (LHCb), *Evidence of a $J/\psi\Lambda$ structure and observation of excited Ξ^- states in the $\Xi_b^- \to J/\psi\Lambda K^-$ decay*, Sci. Bull. **66**, 1278–1287 (2021), arXiv:2012.10380 [hep-ex].

[139] R. Aaij et al. (LHCb), *Observation of a $J/\psi\Lambda$ Resonance Consistent with a Strange Pentaquark Candidate in $B^- \to J/\psi\Lambda p^-$ Decays*, Phys. Rev. Lett. **131**, 031901 (2023), arXiv:2210.10346 [hep-ex].

[140] R. Aaij et al. (LHCb), *A model-independent study of resonant structure in $B^+ \to D^+D^-K^+$ decays*, Phys. Rev. Lett. **125**, 242001 (2020), arXiv:2009.00025 [hep-ex].

[141] R. Aaij et al. (LHCb), *Amplitude analysis of the $B^+ \to D^+D^-K^+$ decay*, Phys. Rev. D **102**, 112003 (2020), arXiv:2009.00026 [hep-ex].

[142] R. Aaij et al. (LHCb), *Observation of an exotic narrow doubly charmed tetraquark*, Nature Phys. **18**, 751–754 (2022), arXiv:2109.01038 [hep-ex].

[143] F.-K. Guo, C. Hanhart, U.-G. Meißner, Q. Wang, Q. Zhao, and B.-S. Zou, *Hadronic molecules*, Rev. Mod. Phys. **90**, [Erratum: Rev.Mod.Phys. 94, 029901 (2022)], 015004 (2018), arXiv:1705.00141 [hep-ph].

[144] N. Brambilla, S. Eidelman, C. Hanhart, A. Nefediev, C.-P. Shen, C. E. Thomas, A. Vairo, and C.-Z. Yuan, *The XYZ states: experimental and theoretical status and perspectives*, Phys. Rept. **873**, 1–154 (2020), arXiv:1907.07583 [hep-ex].

[145] Y.-R. Liu, H.-X. Chen, W. Chen, X. Liu, and S.-L. Zhu, *Pentaquark and Tetraquark states*, Prog. Part. Nucl. Phys. **107**, 237–320 (2019), arXiv:1903.11976 [hep-ph].

[146] X.-K. Dong, F.-K. Guo, and B. S. Zou, *Near Threshold Structures and Hadronic Molecules*, Few Body Syst. **62**, 61 (2021).

[147] X.-K. Dong, F.-K. Guo, and B.-S. Zou, *A survey of heavy-antiheavy hadronic molecules*, Progr. Phys. **41**, 65–93 (2021), arXiv:2101.01021 [hep-ph].

[148] M. Albaladejo et al. (JPAC), *Novel approaches in hadron spectroscopy*, Prog. Part. Nucl. Phys. **127**, 103981 (2022), arXiv:2112.13436 [hep-ph].

[149] Y. Kamiya, T. Hyodo, and A. Ohnishi, *Femtoscopic study on DD^* and $D\bar{D}^*$ interactions for T_{cc} and X(3872)*, Eur. Phys. J. A **58**, 131 (2022), arXiv:2203.13814 [hep-ph].

[150] I. Vidana, A. Feijoo, M. Albaladejo, J. Nieves, and E. Oset, *Femtoscopic correlation function for the Tcc(3875)+ state*, Phys. Lett. B **846**, 138201 (2023), arXiv:2303.06079 [hep-ph].

[151] S. Cho et al. (ExHIC), *Multi-quark hadrons from Heavy Ion Collisions*, Phys. Rev. Lett. **106**, 212001 (2011), arXiv:1011.0852 [nucl-th].

[152] S. Cho et al. (ExHIC), *Studying Exotic Hadrons in Heavy Ion Collisions*, Phys. Rev. C **84**, 064910 (2011), arXiv:1107.1302 [nucl-th].

[153] S. Cho et al. (ExHIC), *Exotic hadrons from heavy ion collisions*, Prog. Part. Nucl. Phys. **95**, 279–322 (2017), arXiv:1702.00486 [nucl-th].

[154] S. Cho and S. H. Lee, *Hadronic effects on the X(3872) meson abundance in heavy ion collisions*, Phys. Rev. C **88**, 054901 (2013), arXiv:1302.6381 [nucl-th].

[155] L. M. Abreu, K. P. Khemchandani, A. Martinez Torres, F. S. Navarra, and M. Nielsen, $X(3872)$ *production and absorption in a hot hadron gas*, Phys. Lett. B **761**, 303–309 (2016), arXiv:1604.07716 [hep-ph].

[156] C. E. Fontoura, G. Krein, A. Valcarce, and J. Vijande, *Production of exotic tetraquarks $QQ\bar{q}\bar{q}$ in heavy-ion collisions at the LHC*, Phys. Rev. D **99**, 094037 (2019), arXiv:1905.03877 [hep-ph].

[157] H. Zhang, J. Liao, E. Wang, Q. Wang, and H. Xing, *Deciphering the Nature of X(3872) in Heavy Ion Collisions*, Phys. Rev. Lett. **126**, 012301 (2021), arXiv:2004.00024 [hep-ph].

[158] A. Andronic, P. Braun-Munzinger, M. K. Köhler, K. Redlich, and J. Stachel, *Transverse momentum distributions of charmonium states with the statistical hadronization model*, Phys. Lett. B **797**, 134836 (2019), arXiv:1901.09200 [nucl-th].

[159] B. Wu, X. Du, M. Sibila, and R. Rapp, $X(3872)$*transport in heavy-ion collisions*, Eur. Phys. J. A **57**, [Erratum: Eur.Phys.J.A 57, 314 (2021)], 122 (2021), arXiv:2006.09945 [nucl-th].

[160] M. Cleven, V. K. Magas, and A. Ramos, *X(3872) in a hot pion bath*, Phys. Lett. B **799**, 135050 (2019), arXiv:1906.06116 [hep-ph].

[161] G. Montaña, A. Ramos, L. Tolos, and J. M. Torres-Rincon, *X(3872), X(4014), and their bottom partners at finite temperature*, Phys. Rev. D **107**, 054014 (2023), arXiv:2211.01896 [hep-ph].

[162] M. Albaladejo, J. M. Nieves, and L. Tolos, DD^{-*} *scattering and* $\chi c1(3872)$ *in nuclear matter*, Phys. Rev. C **104**, 035203 (2021), arXiv:2102.08589 [hep-ph].

[163] K. Azizi and N. Er, $X(3872)$*: propagating in a dense medium*, Nucl. Phys. B **936**, 151–168 (2018), arXiv:1710.02806 [hep-ph].

[164] K. Azizi and N. Er, *Properties of* $Z_c(3900)$ *tetraquark in a cold nuclear matter*, Phys. Rev. D **101**, 074037 (2020), arXiv:2001.09356 [hep-ph].

[165] S. Godfrey and R. Kokoski, *The Properties of p Wave Mesons with One Heavy Quark*, Phys. Rev. D **43**, 1679–1687 (1991).

[166] J. Zeng, J. W. Van Orden, and W. Roberts, *Heavy mesons in a relativistic model*, Phys. Rev. D **52**, 5229–5241 (1995), arXiv:hep-ph/9412269.

[167] S. N. Gupta and J. M. Johnson, *Quantum chromodynamic potential model for light heavy quarkonia and the heavy quark effective theory*, Phys. Rev. D **51**, 168–175 (1995), arXiv:hep-ph/9409432.

[168] D. Ebert, V. O. Galkin, and R. N. Faustov, *Mass spectrum of orbitally and radially excited heavy - light mesons in the relativistic quark model*, Phys. Rev. D **57**, [Erratum: Phys.Rev.D 59, 019902 (1999)], 5663–5669 (1998), arXiv:hep-ph/9712318.

[169] T. A. Lahde, C. J. Nyfalt, and D. O. Riska, *Spectra and M1 decay widths of heavy light mesons*, Nucl. Phys. A **674**, 141–167 (2000), arXiv:hep-ph/9908485.

[170] M. Di Pierro and E. Eichten, *Excited Heavy - Light Systems and Hadronic Transitions*, Phys. Rev. D **64**, 114004 (2001), arXiv:hep-ph/0104208.

[171] R. L. Workman et al. (Particle Data Group), *Review of Particle Physics*, PTEP **2022**, 083C01 (2022).

[172] Y.-B. Dai, C.-S. Huang, C. Liu, and S.-L. Zhu, *Understanding the D+(sJ)(2317) and D+(sJ)(2460) with sum rules in HQET*, Phys. Rev. D **68**, 114011 (2003), arXiv:hep-ph/0306274.

[173] S. Narison, *Open charm and beauty chiral multiplets in QCD*, Phys. Lett. B **605**, 319–325 (2005), arXiv:hep-ph/0307248.

[174] W. A. Bardeen, E. J. Eichten, and C. T. Hill, *Chiral multiplets of heavy - light mesons*, Phys. Rev. D **68**, 054024 (2003), arXiv:hep-ph/0305049.

[175] I. W. Lee, T. Lee, D. P. Min, and B.-Y. Park, *Chiral radiative corrections and D(s)(2317)/D(2308) mass puzzle*, Eur. Phys. J. C **49**, 737–741 (2007), arXiv:hep-ph/0412210.

[176] Z. G. Wang and S. L. Wan, *Structure of the D(s0)(2317) and the strong coupling constant g(D(s0)) DK with the light-cone QCD sum rules*, Phys. Rev. D **73**, 094020 (2006), arXiv:hep-ph/0603007.

[177] O. Lakhina and E. S. Swanson, *A Canonical Ds(2317)?*, Phys. Lett. B **650**, 159–165 (2007), arXiv:hep-ph/0608011.

[178] H.-Y. Cheng and W.-S. Hou, *B decays as spectroscope for charmed four quark states*, Phys. Lett. B **566**, 193–200 (2003), arXiv:hep-ph/0305038.

[179] K. Terasaki, *BABAR resonance as a new window of hadron physics*, Phys. Rev. D **68**, 011501 (2003), arXiv:hep-ph/0305213.

[180] Y.-Q. Chen and X.-Q. Li, *A Comprehensive four-quark interpretation of D(s)(2317), D(s)(2457) and D(s)(2632)*, Phys. Rev. Lett. **93**, 232001 (2004), arXiv:hep-ph/0407062.

[181] M. E. Bracco, A. Lozea, R. D. Matheus, F. S. Navarra, and M. Nielsen, *Disentangling two- and four-quark state pictures of the charmed scalar mesons*, Phys. Lett. B **624**, 217–222 (2005), arXiv:hep-ph/0503137.

[182] Z.-G. Wang and S.-L. Wan, *D(s)(2317) as a tetraquark state with QCD sum rules in heavy quark limit*, Nucl. Phys. A **778**, 22–29 (2006), arXiv:hep-ph/0602080.

[183] T. Barnes, F. E. Close, and H. J. Lipkin, *Implications of a DK molecule at 2.32-GeV*, Phys. Rev. D **68**, 054006 (2003), arXiv:hep-ph/0305025.

[184] A. P. Szczepaniak, *Description of the D*(s)(2320) resonance as the D pi atom*, Phys. Lett. B **567**, 23–26 (2003), arXiv:hep-ph/0305060.

[185] E. E. Kolomeitsev and M. F. M. Lutz, *On Heavy light meson resonances and chiral symmetry*, Phys. Lett. B **582**, 39–48 (2004), arXiv:hep-ph/0307133.

[186] J. Hofmann and M. F. M. Lutz, *Open charm meson resonances with negative strangeness*, Nucl. Phys. A **733**, 142–152 (2004), arXiv:hep-ph/0308263.

[187] F.-K. Guo, P.-N. Shen, H.-C. Chiang, R.-G. Ping, and B.-S. Zou, *Dynamically generated 0+ heavy mesons in a heavy chiral unitary approach*, Phys. Lett. B **641**, 278–285 (2006), arXiv:hep-ph/0603072.

[188] D. Gamermann, E. Oset, D. Strottman, and M. J. Vicente Vacas, *Dynamically generated open and hidden charm meson systems*, Phys. Rev. D **76**, 074016 (2007), arXiv:hep-ph/0612179.

[189] A. Faessler, T. Gutsche, V. E. Lyubovitskij, and Y.-L. Ma, *Strong and radiative decays of the D(s0)*(2317) meson in the DK-molecule picture*, Phys. Rev. D **76**, 014005 (2007), arXiv:0705.0254 [hep-ph].

[190] J. M. Flynn and J. Nieves, *Elastic s-wave B pi, D pi, D K and K pi scattering from lattice calculations of scalar form-factors in semileptonic decays*, Phys. Rev. D **75**, 074024 (2007), arXiv:hep-ph/0703047.

[191] F.-K. Guo, C. Hanhart, and U.-G. Meissner, *Interactions between heavy mesons and Goldstone bosons from chiral dynamics*, Eur. Phys. J. A **40**, 171–179 (2009), arXiv:0901.1597 [hep-ph].

[192] L. Liu, K. Orginos, F.-K. Guo, C. Hanhart, and U.-G. Meissner, *Interactions of charmed mesons with light pseudoscalar mesons from lattice QCD and implications on the nature of the* $D_{s0}^*(2317)$, Phys. Rev. D **87**, 014508 (2013), arXiv:1208.4535 [hep-lat].

[193] Z.-H. Guo, U.-G. Meißner, and D.-L. Yao, *New insights into the* $D_{s0}^*(2317)$ *and other charm scalar mesons*, Phys. Rev. D **92**, 094008 (2015), arXiv:1507.03123 [hep-ph].

[194] M. Albaladejo, D. Jido, J. Nieves, and E. Oset, $D_{s0}^*(2317)$ *and DK scattering in B decays from BaBar and LHCb data*, Eur. Phys. J. C **76**, 300 (2016), arXiv:1604.01193 [hep-ph].

[195] T. E. Browder, S. Pakvasa, and A. A. Petrov, *Comment on the new D(s)(*)+ pi0 resonances*, Phys. Lett. B **578**, 365–368 (2004), arXiv:hep-ph/0307054.

[196] E. van Beveren and G. Rupp, *Observed* $D_s(2317)$ *and tentative* $D(2100–2300)$ *as the charmed cousins of the light scalar nonet*, Phys. Rev. Lett. **91**, 012003 (2003), arXiv:hep-ph/0305035.

[197] M. Albaladejo, P. Fernandez-Soler, J. Nieves, and P. G. Ortega, *Contribution of constituent quark model* $c\bar{s}$ *states to the dynamics of the* $D_{s0}^*(2317)$ *and* $D_{s1}(2460)$ *resonances*, Eur. Phys. J. C **78**, 722 (2018), arXiv:1805.07104 [hep-ph].

[198] G. S. Bali, *The D+(sJ)(2317): What can the lattice say?*, Phys. Rev. D **68**, 071501 (2003), arXiv:hep-ph/0305209.

[199] A. Dougall, R. D. Kenway, C. M. Maynard, and C. McNeile (UKQCD), *The Spectrum of D(s) mesons from lattice QCD*, Phys. Lett. B **569**, 41–44 (2003), arXiv:hep-lat/0307001.

[200] D. Mohler, S. Prelovsek, and R. M. Woloshyn, *$D\pi$ scattering and D meson resonances from lattice QCD*, Phys. Rev. D **87**, 034501 (2013), arXiv:1208.4059 [hep-lat].

[201] G. Moir, M. Peardon, S. M. Ryan, C. E. Thomas, and D. J. Wilson, *Coupled-Channel $D\pi$, $D\eta$ and $D_s\bar{K}$ Scattering from Lattice QCD*, JHEP **10**, 011 (2016), arXiv:1607.07093 [hep-lat].

[202] L. Gayer, N. Lang, S. M. Ryan, D. Tims, C. E. Thomas, and D. J. Wilson (Hadron Spectrum), *Isospin-1/2 $D\pi$ scattering and the lightest D_0^* resonance from lattice QCD*, JHEP **07**, 123 (2021), arXiv:2102.04973 [hep-lat].

[203] R. Aaij et al. (LHCb), *Amplitude analysis of $B^- \to D^+\pi^-\pi^-$ decays*, Phys. Rev. D **94**, 072001 (2016), arXiv:1608.01289 [hep-ex].

[204] R. Aaij et al. (LHCb), *Dalitz plot analysis of $B_s^0 \to \bar{D}^0 K^-\pi^+$ decays*, Phys. Rev. D **90**, 072003 (2014), arXiv:1407.7712 [hep-ex].

[205] Z.-W. Liu, J.-X. Lu, and L.-S. Geng, *Study of the DK interaction with femtoscopic correlation functions*, Phys. Rev. D **107**, 074019 (2023), arXiv:2302.01046 [hep-ph].

[206] M. Albaladejo, J. Nieves, and E. Ruiz-Arriola, *Femtoscopic signatures of the lightest S-wave scalar open-charm mesons*, Phys. Rev. D **108**, 014020 (2023), arXiv:2304.03107 [hep-ph].

[207] N. Ikeno, G. Toledo, and E. Oset, *Model independent analysis of femtoscopic correlation functions: An application to the Ds0*(2317)*, Phys. Lett. B **847**, 138281 (2023), arXiv:2305.16431 [hep-ph].

[208] J. M. Torres-Rincon, À. Ramos, and L. Tolos, *Femtoscopy of D mesons and light mesons upon unitarized effective field theories*, Phys. Rev. D **108**, 096008 (2023), arXiv:2307.02102 [hep-ph].

[209] S. Weinberg, *Evidence That the Deuteron Is Not an Elementary Particle*, Phys. Rev. **137**, B672–B678 (1965).

[210] R. Molina, D. Gamermann, E. Oset, and L. Tolos, *Charm and hidden charm scalar mesons in the nuclear medium*, Eur. Phys. J. A **42**, 31–42 (2009), arXiv:0806.3711 [nucl-th].

[211] G. Montaña, À. Ramos, L. Tolos, and J. M. Torres-Rincon, *Impact of a thermal medium on D mesons and their chiral partners*, Phys. Lett. B **806**, 135464 (2020), arXiv:2001.11877 [hep-ph].

[212] A. L. Fetter and J. D. Walecka, *Quantum theory of many-particle systems* (McGraw-Hill, New York, 1971).

[213] R. D. Mattuck, *A Guide to Feynman Diagrams in the Many Body Problem (Second Edition)* (Dover Publications, 1976).

[214] L. Tolos, D. Cabrera, and A. Ramos, *Strange mesons in nuclear matter at finite temperature*, Phys. Rev. C **78**, 045205 (2008), arXiv:0807.2947 [nucl-th].

[215] L. Tolos, C. Garcia-Recio, and J. Nieves, *The Properties of D and D* mesons in the nuclear medium*, Phys. Rev. C **80**, 065202 (2009), arXiv:0905.4859 [nucl-th].

[216] C. Garcia-Recio, J. Nieves, L. L. Salcedo, and L. Tolos, *D^- mesic atoms*, Phys. Rev. C **85**, 025203 (2012), arXiv:1111.6535 [nucl-th].

[217] E. Oset and A. Ramos, *Nonperturbative chiral approach to s wave anti-K N interactions*, Nucl. Phys. A **635**, 99–120 (1998), arXiv:nucl-th/9711022.

[218] J. Nieves and E. Ruiz Arriola, *Bethe-Salpeter approach for unitarized chiral perturbation theory*, Nucl. Phys. A **679**, 57–117 (2000), arXiv:hep-ph/9907469.

[219] C. Garcia-Recio, J. Nieves, and L. Tolos, *D mesic nuclei*, Phys. Lett. B **690**, 369–375 (2010), arXiv:1004.2634 [nucl-th].

[220] C. Garcia-Recio, V. K. Magas, T. Mizutani, J. Nieves, A. Ramos, L. L. Salcedo, and L. Tolos, *The s-wave charmed baryon resonances from a coupled-channel approach with heavy quark symmetry*, Phys. Rev. D **79**, 054004 (2009), arXiv:0807.2969 [hep-ph].

[221] D. Gamermann, C. Garcia-Recio, J. Nieves, L. L. Salcedo, and L. Tolos, *Exotic dynamically generated baryons with negative charm quantum number*, Phys. Rev. D **81**, 094016 (2010), arXiv:1002.2763 [hep-ph].

[222] L. Tolos, A. Ramos, and T. Mizutani, *Open charm in nuclear matter at finite temperature*, Phys. Rev. C **77**, 015207 (2008), arXiv:0710.2684 [nucl-th].

[223] M. F. M. Lutz and C. L. Korpa, *Open-charm systems in cold nuclear matter*, Phys. Lett. B **633**, 43–48 (2006).

[224] D. Cabrera, L. Tolós, J. Aichelin, and E. Bratkovskaya, *Antistrange meson-baryon interaction in hot and dense nuclear matter*, Phys. Rev. C **90**, 055207 (2014), arXiv:1406.2570 [hep-ph].

[225] J. A. Oller, E. Oset, and J. R. Pelaez, *Meson meson interaction in a nonperturbative chiral approach*, Phys. Rev. D **59**, [Erratum: Phys.Rev.D 60, 099906 (1999), Erratum: Phys.Rev.D 75, 099903 (2007)], 074001 (1999), arXiv:hep-ph/9804209.

[226] D. Gamermann, J. Nieves, E. Oset, and E. Ruiz Arriola, *Couplings in coupled channels versus wave functions: application to the X(3872) resonance*, Phys. Rev. D **81**, 014029 (2010), arXiv:0911.4407 [hep-ph].

[227] I. Matuschek, V. Baru, F.-K. Guo, and C. Hanhart, *On the nature of near-threshold bound and virtual states*, Eur. Phys. J. A **57**, 101 (2021), arXiv:2007.05329 [hep-ph].

[228] A. Esposito, L. Maiani, A. Pilloni, A. D. Polosa, and V. Riquer, *From the line shape of the X(3872) to its structure*, Phys. Rev. D **105**, L031503 (2022), arXiv:2108.11413 [hep-ph].

[229] Y. Li, F.-K. Guo, J.-Y. Pang, and J.-J. Wu, *Generalization of Weinberg's compositeness relations*, Phys. Rev. D **105**, L071502 (2022), arXiv:2110.02766 [hep-ph].

[230] J. Song, L. R. Dai, and E. Oset, *How much is the compositeness of a bound state constrained by a and r_0? The role of the interaction range*, Eur. Phys. J. A **58**, 133 (2022), arXiv:2201.04414 [hep-ph].

[231] V. Baru, J. Haidenbauer, C. Hanhart, Y. Kalashnikova, and A. E. Kudryavtsev, *Evidence that the a(0)(980) and f(0)(980) are not elementary particles*, Phys. Lett. B **586**, 53–61 (2004), arXiv:hep-ph/0308129.

[232] V. Baru, C. Hanhart, Y. S. Kalashnikova, A. E. Kudryavtsev, and A. V. Nefediev, *Interplay of quark and meson degrees of freedom in a near-threshold resonance*, Eur. Phys. J. A **44**, 93–103 (2010), arXiv:1001.0369 [hep-ph].

[233] C. Hanhart, Y. S. Kalashnikova, and A. V. Nefediev, *Interplay of quark and meson degrees of freedom in a near-threshold resonance: multi-channel case*, Eur. Phys. J. A **47**, 101–110 (2011), arXiv:1106.1185 [hep-ph].

[234] F. Aceti and E. Oset, *Wave functions of composite hadron states and relationship to couplings of scattering amplitudes for general partial waves*, Phys. Rev. D **86**, 014012 (2012), arXiv:1202.4607 [hep-ph].

[235] T. Hyodo, D. Jido, and A. Hosaka, *Compositeness of dynamically generated states in a chiral unitary approach*, Phys. Rev. C **85**, 015201 (2012), arXiv:1108.5524 [nucl-th].

[236] T. Sekihara, T. Hyodo, and D. Jido, *Comprehensive analysis of the wave function of a hadronic resonance and its compositeness*, PTEP **2015**, 063D04 (2015), arXiv:1411.2308 [hep-ph].

[237] Y. Kamiya and T. Hyodo, *Structure of near-threshold quasibound states*, Phys. Rev. C **93**, 035203 (2016), arXiv:1509.00146 [hep-ph].

[238] C. Garcia-Recio, C. Hidalgo-Duque, J. Nieves, L. L. Salcedo, and L. Tolos, *Compositeness of the strange, charm, and beauty odd parity* Λ *states*, Phys. Rev. D **92**, 034011 (2015), arXiv:1506.04235 [hep-ph].

[239] Z.-H. Guo and J. A. Oller, *Probabilistic interpretation of compositeness relation for resonances*, Phys. Rev. D **93**, 096001 (2016), arXiv:1508.06400 [hep-ph].

[240] Y. Kamiya and T. Hyodo, *Generalized weak-binding relations of compositeness in effective field theory*, PTEP **2017**, 023D02 (2017), arXiv:1607.01899 [hep-ph].

[241] T. Sekihara, *Two-body wave functions and compositeness from scattering amplitudes. I. General properties with schematic models*, Phys. Rev. C **95**, 025206 (2017), arXiv:1609.09496 [quant-ph].

[242] J. A. Oller, *New results from a number operator interpretation of the compositeness of bound and resonant states*, Annals Phys. **396**, 429–458 (2018), arXiv:1710.00991 [hep-ph].

[243] T. Kinugawa and T. Hyodo, *Role of the effective range in the weak-binding relation*, EPJ Web Conf. **262**, 01019 (2022), arXiv:2112.00249 [hep-ph].

[244] H. Sazdjian, *The Interplay between Compact and Molecular Structures in Tetraquarks*, Symmetry **14**, 515 (2022), arXiv:2202.01081 [hep-ph].

[245] J. Song, L. R. Dai, and E. Oset, *Evolution of compact states to molecular ones with coupled channels: The case of the X(3872)*, Phys. Rev. D **108**, 114017 (2023), arXiv:2307.02382 [hep-ph].

[246] L. R. Dai, J. Song, and E. Oset, *Evolution of genuine states to molecular ones: The Tcc(3875) case*, Phys. Lett. B **846**, 138200 (2023), arXiv:2306.01607 [hep-ph].

[247] L. R. Dai, R. Molina, and E. Oset, *Prediction of new Tcc states of D*D* and Ds*D* molecular nature*, Phys. Rev. D **105**, [Erratum: Phys.Rev.D 106, 099902 (2022)], 016029 (2022), arXiv:2110.15270 [hep-ph].

[248] F. Aceti, L. R. Dai, L. S. Geng, E. Oset, and Y. Zhang, *Meson-baryon components in the states of the baryon decuplet*, Eur. Phys. J. A **50**, 57 (2014), arXiv:1301.2554 [hep-ph].

[249] T. Hyodo, *Structure and compositeness of hadron resonances*, Int. J. Mod. Phys. A **28**, 1330045 (2013), arXiv:1310.1176 [hep-ph].

[250] M. Albaladejo, M. Nielsen, and E. Oset, $D_{s0}^{*\pm}(2317)$ *and* KD *scattering from* B_s^0 *decay*, Phys. Lett. B **746**, 305–310 (2015), arXiv:1501.03455 [hep-ph].

[251] J. P. Lees et al. (BaBar), *Dalitz plot analyses of* $B^0 \to D^0 D^- K^+$ *and* $B^+ \to \overline{D}^0 D^0 K^+$ *decays*, Phys. Rev. D **91**, 052002 (2015), arXiv:1412.6751 [hep-ex].

[252] A. Ramos and E. Oset, *The Properties of anti-K in the nuclear medium*, Nucl. Phys. A **671**, 481–502 (2000), arXiv:nucl-th/9906016.

[253] A. Baca, C. Garcia-Recio, and J. Nieves, *Deeply bound levels in kaonic atoms*, Nucl. Phys. A **673**, 335–353 (2000), arXiv:nucl-th/0001060.

[254] S. Hirenzaki, Y. Okumura, H. Toki, E. Oset, and A. Ramos, *Chiral unitary model for the kaonic atom*, Phys. Rev. C **61**, 055205 (2000).

[255] C. Garcia-Recio, L. S. Geng, J. Nieves, and L. L. Salcedo, *Low-lying even parity meson resonances and spin-flavor symmetry*, Phys. Rev. D **83**, 016007 (2011), arXiv:1005.0956 [hep-ph].

[256] O. Romanets, L. Tolos, C. Garcia-Recio, J. Nieves, L. L. Salcedo, and R. G. E. Timmermans, *Charmed and strange baryon resonances with heavy-quark spin symmetry*, Phys. Rev. D **85**, 114032 (2012), arXiv:1202.2239 [hep-ph].

[257] J. A. Oller, E. Oset, and A. Ramos, *Chiral unitary approach to meson meson and meson - baryon interactions and nuclear applications*, Prog. Part. Nucl. Phys. **45**, 157–242 (2000), arXiv:hep-ph/0002193.

[258] E. Friedman and A. Gal, *In-medium nuclear interactions of low-energy hadrons*, Phys. Rept. **452**, 89–153 (2007), arXiv:0705.3965 [nucl-th].

[259] M. Nanova et al. (CBELSA/TAPS), *Determination of the* η*'-nucleus optical potential*, Phys. Lett. B **727**, 417–423 (2013), arXiv:1311.0122 [nucl-ex].

[260] M. Nanova et al. (CBELSA/TAPS), *The* η' *-carbon potential at low meson momenta*, Eur. Phys. J. A **54**, 182 (2018), arXiv:1810.01288 [nucl-ex].

[261] Y. K. Tanaka et al. (n-PRiME/Super-FRS), *Measurement of excitation spectra in the* $^{12}C(p,d)$ *reaction near the* η' *emission threshold*, Phys. Rev. Lett. **117**, 202501 (2016), arXiv:1611.02948 [nucl-ex].

[262] N. Tomida et al. (LEPS2/BGOegg), *Search for* η' *bound nuclei in the* $^{12}\mathrm{C}(\gamma,p)$ *reaction with simultaneous detection of decay products*, Phys. Rev. Lett. **124**, 202501 (2020), arXiv:2005.03449 [nucl-ex].

[263] S. D. Bass, V. Metag, and P. Moskal, "The η- and η'-Nucleus Interactions and the Search for η, η'- Mesic States", in *Handbook of Nuclear Physics*, edited by I. Tanihata, H. Toki, and T. Kajino (2022), pp. 1–28, arXiv:2111.01388 [hep-ph].

[264] J.-J. Xie, W.-H. Liang, E. Oset, P. Moskal, M. Skurzok, and C. Wilkin, *Determination of the η^3**He** threshold structure from the low energy $pd \to \eta^3$**He** reaction*, Phys. Rev. C **95**, 015202 (2017), arXiv:1609.03399 [nucl-th].

[265] J.-J. Xie, W.-H. Liang, and E. Oset, *η-^{4}He interaction from the $dd \to \eta^4$He reaction near threshold*, Eur. Phys. J. A **55**, 6 (2019), arXiv:1805.12532 [nucl-th].

[266] N. Ikeno, H. Nagahiro, D. Jido, and S. Hirenzaki, *η-nucleus interaction from the $d+d$ reaction around the η production threshold*, Eur. Phys. J. A **53**, 194 (2017), arXiv:1708.07692 [nucl-th].

[267] M. Skurzok, P. Moskal, N. G. Kelkar, S. Hirenzaki, H. Nagahiro, and N. Ikeno, *Constraining the optical potential in the search for η-mesic ^{4}He*, Phys. Lett. B **782**, 6–12 (2018), arXiv:1802.08597 [nucl-ex].

[268] N. Ikeno, Y. Higashi, H. Fujioka, et al., *Feasibility of the observation of η' mesic nuclei in the semi-exclusive $^{12}C(p,dp)$ reaction*, (2024), arXiv:2406.06058 [nucl-th].

[269] E. Hernandez and E. Oset, *Many body modes of anti-proton annihilation tested with anti-proton production*, Z. Phys. A **341**, 201–204 (1992).

[270] V. K. Magas, L. Roca, and E. Oset, *The phi meson width in the medium from proton induced phi production in nuclei*, Phys. Rev. C **71**, 065202 (2005), arXiv:nucl-th/0403067.

[271] M. Kaskulov, E. Hernandez, and E. Oset, *Inclusive omega photoproduction from nuclei and omega in the nuclear medium*, Eur. Phys. J. A **31**, 245–254 (2007), arXiv:nucl-th/0610067.

[272] K. Garrow et al., *Nuclear transparency from quasielastic A(e,e-prime p) reactions up to Q**2 = 8.1-(GeV/c)**2*, Phys. Rev. C **66**, 044613 (2002), arXiv:hep-ex/0109027.

[273] P. Lava, M. C. Martinez, J. Ryckebusch, J. A. Caballero, and J. M. Udias, *Nuclear transparencies in relativistic A(e, e-prime p) models*, Phys. Lett. B **595**, 177–186 (2004), arXiv:nucl-th/0401041.

[274] M. Nanova et al. (CBELSA/TAPS), *Transparency ratio in $\gamma A \to \eta' A'$ and the in-medium η' width*, Phys. Lett. B **710**, 600–606 (2012), arXiv:1204.2914 [nucl-ex].

[275] O. Hen et al. (CLAS), *Measurement of transparency ratios for protons from short-range correlated pairs*, Phys. Lett. B **722**, 63–68 (2013), arXiv:1212.5343 [nucl-ex].

[276] L. Tolos, R. Molina, E. Oset, and A. Ramos, $\bar{K}^*$ *meson in dense matter*, Phys. Rev. C **82**, 045210 (2010), arXiv:1006.3454 [nucl-th].

[277] T. Ishikawa et al., *phi photo-production from Li, C, Al, and Cu nuclei at E(gamma) = 1.5-GeV to 2.4-GeV*, Phys. Lett. B **608**, 215–222 (2005), arXiv:nucl-ex/0411016.

[278] D. Cabrera, L. Roca, E. Oset, H. Toki, and M. J. Vicente Vacas, *Mass dependence of inclusive nuclear phi photoproduction*, Nucl. Phys. A **733**, 130–141 (2004), arXiv:nucl-th/0310054.

[279] L. Tolos, J. Schaffner-Bielich, and A. Mishra, *Properties of D-mesons in nuclear matter within a self-consistent coupled-channel approach*, Phys. Rev. C **70**, 025203 (2004), arXiv:nucl-th/0404064.

[280] L. Tolos, J. Schaffner-Bielich, and H. Stoecker, *D-mesons: In-medium effects at FAIR*, Phys. Lett. B **635**, 85–92 (2006), arXiv:nucl-th/0509054.

[281] T. Mizutani and A. Ramos, *D mesons in nuclear matter: A DN coupled-channel equations approach*, Phys. Rev. C **74**, 065201 (2006), arXiv:hep-ph/0607257.

[282] L. Tolos and J. M. Torres-Rincon, *D-meson propagation in hot dense matter*, Phys. Rev. D **88**, 074019 (2013), arXiv:1306.5426 [hep-ph].

[283] L. Tolos, *Charming mesons with baryons and nuclei*, Int. J. Mod. Phys. E **22**, 1330027 (2013), arXiv:1309.7305 [nucl-th].

[284] C. Sasaki, *Fate of charmed mesons near chiral symmetry restoration in hot matter*, Phys. Rev. D **90**, 114007 (2014), arXiv:1409.3420 [hep-ph].

[285] S. Reddy P., A. Jahan C. S., N. Dhale, A. Mishra, and J. Schaffner-Bielich, *D mesons in strongly magnetized asymmetric nuclear matter*, Phys. Rev. C **97**, 065208 (2018), arXiv:1712.07997 [nucl-th].

[286] T. Buchheim, T. Hilger, B. Kämpfer, and S. Leupold, *Chiral-partner D mesons in a heat bath within QCD sum rules*, J. Phys. G **45**, 085104 (2018), arXiv:1801.01472 [nucl-th].

[287] P. Fernandez de Cordoba, Y. Ratis, E. Oset, J. Nieves, M. J. Vicente-Vacas, B. Lopez-Alvaredo, and F. Gareev, *Projectile delta excitation in alpha - proton scattering*, Nucl. Phys. A **586**, 586–606 (1995).

[288] H. De Vries, C. De Jager, and C. De Vries, *Nuclear charge-density-distribution parameters from elastic electron scattering*, Atomic Data and Nuclear Data Tables **36**, 495–536 (1987), https://www.sciencedirect.com/science/article/pii/0092640X87900131.

[289] J. Nieves, E. Oset, and C. Garcia-Recio, *A Theoretical approach to pionic atoms and the problem of anomalies*, Nucl. Phys. A **554**, 509–553 (1993).

[290] M. Siddikov and I. Schmidt, *Exclusive photoproduction of D-meson pairs with large invariant mass*, Phys. Rev. D **108**, 096031 (2023), arXiv:2309.09748 [hep-ph].

[291] A. Ali et al. (GlueX), *First Measurement of Near-Threshold J/ψ Exclusive Photoproduction off the Proton*, Phys. Rev. Lett. **123**, 072001 (2019), arXiv:1905.10811 [nucl-ex].

[292] A. Accardi et al., *Strong interaction physics at the luminosity frontier with 22 GeV electrons at Jefferson Lab*, Eur. Phys. J. A **60**, 173 (2024), arXiv:2306.09360 [nucl-ex].

[293] R. Abdul Khalek et al., *Science Requirements and Detector Concepts for the Electron-Ion Collider: EIC Yellow Report*, Nucl. Phys. A **1026**, 122447 (2022), arXiv:2103.05419 [physics.ins-det].

[294] D. P. Anderle et al., *Electron-ion collider in China*, Front. Phys. (Beijing) **16**, 64701 (2021), arXiv:2102.09222 [nucl-ex].

[295] D. Janc and M. Rosina, *The $T_{cc} = DD^*$ molecular state*, Few Body Syst. **35**, 175–196 (2004), arXiv:hep-ph/0405208.

[296] T. F. Carames, A. Valcarce, and J. Vijande, *Doubly charmed exotic mesons: A gift of nature?*, Phys. Lett. B **699**, 291–295 (2011).

[297] S. Ohkoda, Y. Yamaguchi, S. Yasui, K. Sudoh, and A. Hosaka, *Exotic mesons with double charm and bottom flavor*, Phys. Rev. D **86**, 034019 (2012), arXiv:1202.0760 [hep-ph].

[298] N. Li, Z.-F. Sun, X. Liu, and S.-L. Zhu, *Coupled-channel analysis of the possible $D^{(*)}D^{(*)}, \overline{B}^{(*)}\overline{B}^{(*)}$ and $D^{(*)}\overline{B}^{(*)}$ molecular states*, Phys. Rev. D **88**, 114008 (2013), arXiv:1211.5007 [hep-ph].

[299] M.-Z. Liu, T.-W. Wu, M. Pavon Valderrama, J.-J. Xie, and L.-S. Geng, *Heavy-quark spin and flavor symmetry partners of the X(3872) revisited: What can we learn from the one boson exchange model?*, Phys. Rev. D **99**, 094018 (2019), arXiv:1902.03044 [hep-ph].

[300] F. S. Navarra, M. Nielsen, and S. H. Lee, *QCD sum rules study of QQ - anti-u anti-d mesons*, Phys. Lett. B **649**, 166–172 (2007), arXiv:hep-ph/0703071.

[301] D. Ebert, R. N. Faustov, V. O. Galkin, and W. Lucha, *Masses of tetraquarks with two heavy quarks in the relativistic quark model*, Phys. Rev. D **76**, 114015 (2007), arXiv:0706.3853 [hep-ph].

[302] M. Karliner and J. L. Rosner, *Discovery of doubly-charmed Ξ_{cc} baryon implies a stable ($bb\bar{u}\bar{d}$) tetraquark*, Phys. Rev. Lett. **119**, 202001 (2017), arXiv:1707.07666 [hep-ph].

[303] G. Yang, J. Ping, and J. Segovia, *Doubly-heavy tetraquarks*, Phys. Rev. D **101**, 014001 (2020), arXiv:1911.00215 [hep-ph].

[304] X.-K. Dong, F.-K. Guo, and B.-S. Zou, *Explaining the Many Threshold Structures in the Heavy-Quark Hadron Spectrum*, Phys. Rev. Lett. **126**, 152001 (2021), arXiv:2011.14517 [hep-ph].

[305] M. Padmanath and S. Prelovsek, *Signature of a Doubly Charm Tetraquark Pole in DD* Scattering on the Lattice*, Phys. Rev. Lett. **129**, 032002 (2022), arXiv:2202.10110 [hep-lat].

[306] Y. Lyu, S. Aoki, T. Doi, T. Hatsuda, Y. Ikeda, and J. Meng, *Doubly Charmed Tetraquark Tcc+ from Lattice QCD near Physical Point*, Phys. Rev. Lett. **131**, 161901 (2023), arXiv:2302.04505 [hep-lat].

[307] S. Collins, A. Nefediev, M. Padmanath, and S. Prelovsek, *Toward the quark mass dependence of Tcc+ from lattice QCD*, Phys. Rev. D **109**, 094509 (2024), arXiv:2402.14715 [hep-lat].

[308] T. Whyte, D. J. Wilson, and C. E. Thomas (Hadron Spectrum), *Near-threshold states in coupled DD*-D*D* scattering from lattice QCD*, Phys. Rev. D **111**, 034511 (2025), arXiv:2405.15741 [hep-lat].

[309] M.-L. Du, A. Filin, V. Baru, et al., *Role of Left-Hand Cut Contributions on Pole Extractions from Lattice Data: Case Study for Tcc(3875)+*, Phys. Rev. Lett. **131**, 131903 (2023), arXiv:2303.09441 [hep-ph].

[310] F. Gil-Domínguez, A. Giachino, and R. Molina, *Quark mass dependence of the Tcc(3875)+ pole*, Phys. Rev. D **111**, 016029 (2025), arXiv:2409.15141 [hep-ph].

[311] M. Albaladejo, A. Feijoo, I. Vidaña, J. Nieves, and E. Oset, *Inverse problem in femtoscopic correlation functions: the $T_{cc}(3875)^+$ state*, Eur. Phys. J. A **61**, 187 (2025), arXiv:2307.09873 [hep-ph].

[312] Y. Hu, J. Liao, E. Wang, Q. Wang, H. Xing, and H. Zhang, *Production of doubly charmed exotic hadrons in heavy ion collisions*, Phys. Rev. D **104**, L111502 (2021), arXiv:2109.07733 [hep-ph].

[313] H. Yun, D. Park, S. Noh, et al., *X(3872) and Tcc: Structures and productions in heavy ion collisions*, Phys. Rev. C **107**, 014906 (2023), arXiv:2208.06960 [hep-ph].

[314] P. Braun-Müzinger, B. Döngius, and N. Löher, *ALICE investigates "snowballs in hell"*, CERN Courier **55** (2015), https://cerncourier.com/a/alice-investigates-snowballs-in-hell/.

[315] E. Braaten, K. Ingles, and J. Pickett, *Explaining Snowball-in-Hell Phenomena in Heavy-Ion Collisions Using a Novel Thermodynamic Variable*, Phys. Rev. Lett. **134**, 252301 (2025), arXiv:2408.03935 [hep-ph].

[316] G. Montaña, À. Ramos, L. Tolos, and J. M. Torres-Rincon, *Pseudoscalar and vector open-charm mesons at finite temperature*, Phys. Rev. D **102**, 096020 (2020), arXiv:2007.12601 [hep-ph].

[317] F. Bacon, *Novum organum; or, true suggestions for the interpretation of nature*, Ebook #45988. Originally published 1620 (Project Gutenberg, 2014), https://www.gutenberg.org/cache/epub/45988.

[318] J. Maxwell, *Illustrations of the dynamical theory of gases. Part I. On the motions and collisions of perfectly elastic spheres*, Philosophical Magazine, 4th series **20**, 21–37 (1860).

[319] R. Kubo, *Statistical mechanical theory of irreversible processes. 1. General theory and simple applications in magnetic and conduction problems*, J. Phys. Soc. Jap. **12**, 570–586 (1957).

[320] P. C. Martin and J. S. Schwinger, *Theory of many particle systems. 1.* Phys. Rev. **115**, edited by K. A. Milton, 1342–1373 (1959).

[321] L. V. Keldysh, *Diagram Technique for Nonequilibrium Processes*, Sov. Phys. JETP **20**, 1018–1026 (1965).

[322] G. Montaña Faiget, "Effective-theory description of heavy-flavored hadrons and their properties in a hot medium", PhD thesis (Barcelona U., 2022), arXiv:2207.10752 [hep-ph].

[323] M. Cleven, V. K. Magas, and A. Ramos, *Properties of open and hidden charm mesons in light quark matter*, Phys. Rev. C **96**, 045201 (2017), arXiv:1707.05728 [hep-ph].

[324] Z.-H. Guo, L. Liu, U.-G. Meißner, J. A. Oller, and A. Rusetsky, *Towards a precise determination of the scattering amplitudes of the charmed and light-flavor pseudoscalar mesons*, Eur. Phys. J. C **79**, 13 (2019), arXiv:1811.05585 [hep-ph].

[325] A. Martinez Torres, K. P. Khemchandani, L. Roca, and E. Oset, *Few-body systems consisting of mesons*, Few Body Syst. **61**, 35 (2020).

[326] M.-Z. Liu, Y.-W. Pan, Z.-W. Liu, T.-W. Wu, J.-X. Lu, and L.-S. Geng, *Three ways to decipher the nature of exotic hadrons: Multiplets, three-body hadronic molecules, and correlation functions*, Phys. Rept. **1108**, 1–108 (2025), arXiv:2404.06399 [hep-ph].

[327] T.-W. Wu, Y.-W. Pan, M.-Z. Liu, and L.-S. Geng, *Multi-hadron molecules: status and prospect*, Sci. Bull. **67**, 1735–1738 (2022).

[328] L. Roca and E. Oset, *A description of the f2(1270), rho3(1690), f4(2050), rho5(2350) and f6(2510) resonances as multi-rho(770) states*, Phys. Rev. D **82**, 054013 (2010).

[329] J. Yamagata-Sekihara, L. Roca, and E. Oset, *On the nature of the* $K_2^*(1430)$*,* $K_3^*(1780)$*,* $K_4^*(2045)$*,* $K_5^*(2380)$ *and* K^*6 *as* K^* *- multi-*ρ *states*, Phys. Rev. D **82**, [Erratum: Phys.Rev.D 85, 119905 (2012)], 094017 (2010).

[330] B. Desplanques and Y. B. Dong, *Form-factors in RQM approaches: Constraints from space-time translations*, Eur. Phys. J. A **37**, 33–54 (2008).

[331] A. Martinez Torres and D. Jido, $K\Lambda(1405)$ *configuration of the* $K\bar{K}N$ *system*, Phys. Rev. C **82**, 038202 (2010).

[332] J.-J. Xie, A. Martinez Torres, and E. Oset, *Faddeev fixed center approximation to the* $N\bar{K}K$ *system and the signature of a* $N^*(1920)(1/2^+)$ *state*, Phys. Rev. C **83**, 065207 (2011).

[333] C. W. Xiao, M. Bayar, and E. Oset, NDK*,* $\bar{K}DN$ *and* $ND\bar{D}$ *molecules*, Phys. Rev. D **84**, 034037 (2011).

[334] J. Nieves and M. P. Valderrama, *The Heavy Quark Spin Symmetry Partners of the X(3872)*, Phys. Rev. D **86**, 056004 (2012), arXiv:1204.2790 [hep-ph].

[335] C. Hidalgo-Duque, J. Nieves, and M. P. Valderrama, *Light flavor and heavy quark spin symmetry in heavy meson molecules*, Phys. Rev. D **87**, 076006 (2013), arXiv:1210.5431 [hep-ph].

[336] S. Prelovsek, S. Collins, D. Mohler, M. Padmanath, and S. Piemonte, *Charmonium-like resonances with* $J^{PC} = 0^{++}$*,* 2^{++} *in coupled* $\mathrm{D\overline{D}}$*,* $\mathrm{D_s\overline{D}_s}$ *scattering on the lattice*, JHEP **06**, 035 (2021).

[337] O. Deineka, I. Danilkin, and M. Vanderhaeghen, *Dispersive analysis of the* $\gamma\gamma \to DD^-$ *data and the confirmation of the* DD^- *bound state*, Phys. Lett. B **827**, 136982 (2022).

[338] P. G. Isar, *Radio signals from highly energetic extensive air showers: Status and newprospective*, Rom. Rep. Phys. **75**, 301 (2023).

[339] F.-Z. Peng, M. Sánchez Sánchez, M.-J. Yan, and M. Pavon Valderrama, *Heavy-hadron molecular spectrum from light-meson exchange saturation*, Phys. Rev. D **105**, 034028 (2022).

[340] P. G. Ortega, J. Segovia, D. R. Entem, and F. Fernandez, *Nature of the doubly-charmed tetraquark Tcc+ in a constituent quark model*, Phys. Lett. B **841**, [Erratum: Phys.Lett.B 847, 138308 (2023)], 137918 (2023).

[341] S.-Q. Luo, L.-S. Geng, and X. Liu, *Double-charm heptaquark states composed of two charmed mesons and one nucleon*, Phys. Rev. D **106**, 014017 (2022).

[342] J. Carlson, L. Heller, and J. A. Tjon, *Stability of Dimesons*, Phys. Rev. D **37**, 744 (1988).

[343] B. Silvestre-Brac and C. Semay, *Systematics of L = 0 q-2 anti-q-2 systems*, Z. Phys. C **57**, 273–282 (1993).

[344] C. Semay and B. Silvestre-Brac, *Diquonia and potential models*, Z. Phys. C **61**, 271–275 (1994).

[345] S. Pepin, F. Stancu, M. Genovese, and J. M. Richard, *Tetraquarks with color blind forces in chiral quark models*, Phys. Lett. B **393**, 119–123 (1997).

[346] T. Guo, J. Li, J. Zhao, and L. He, *Mass spectra of doubly heavy tetraquarks in an improved chromomagnetic interaction model*, Phys. Rev. D **105**, 014021 (2022).

[347] Q. Xin and Z.-G. Wang, *Analysis of the doubly-charmed tetraquark molecular states with the QCD sum rules*, Eur. Phys. J. A **58**, 110 (2022).

[348] E. Hiyama, *Gaussian expansion method for few-body systems and its applications to atomic and nuclear physics*, PTEP **2012**, 01A204 (2012).

[349] E. Hiyama, Y. Kino, and M. Kamimura, *Gaussian expansion method for few-body systems*, Prog. Part. Nucl. Phys. **51**, 223–307 (2003).

[350] L. L. Foldy, *The Multiple Scattering of Waves. 1. General Theory of Isotropic Scattering by Randomly Distributed Scatterers*, Phys. Rev. **67**, 107–119 (1945).

[351] J.-L. Lagrange, *Essai sur le problème des trois corps* (Prix de l' Académie Royale des Sciences de Paris, 1764).

[352] H. Poincaré, *Les méthodes nouvelles de la mécanique céleste* (Gauthier-Villars, 1892).

[353] V. I. Arnold, *Mathematical Methods of Classical Mechanics*, Graduate Texts in Mathematics (Springer, 1989).

[354] C. Liu, *The three-body problem*, Translated by Ken Liu (Tor Books, New York, 2014).

[355] E. Nielsen, D. V. Fedorov, A. S. Jensen, and E. Garrido, *The three-body problem with short-range interactions*, Phys. Rept. **347**, 373–459 (2001).

[356] L. D. Faddeev, *Mathematical aspects of the three-body problem in quantum scattering theory* (Steklov Institute, 1965).

[357] S. P. Merkuriev and L. D. Faddeev, *Quantum scattering theory for several particle systems*, 1st ed. (Springer, Dordrecht, 1993).

[358] A. Martinez Torres, K. P. Khemchandani, U.-G. Meissner, and E. Oset, *Searching for signatures around 1920-MeV of a N* state of three hadron nature*, Eur. Phys. J. A **41**, 361–368 (2009), arXiv:0902.3633 [nucl-th].

[359] A. Martinez Torres, E. J. Garzon, E. Oset, and L. R. Dai, *Limits to the Fixed Center Approximation to Faddeev equations: the case of the* $\phi(2170)$, Phys. Rev. D **83**, 116002 (2011), arXiv:1012.2708 [hep-ph].

[360] E. Oset, A. Martinez Torres, K. P. Khemchandani, L. Roca, and J. Yamagata, *Two, three, many body systems involving mesons*, Prog. Part. Nucl. Phys. **67**, edited by A. Faessler and V. Rodin, 455–460 (2012), arXiv:1110.6827 [nucl-th].

[361] J. Hofmann and M. F. M. Lutz, *Coupled-channel study of crypto-exotic baryons with charm*, Nucl. Phys. A **763**, 90–139 (2005).

[362] G. Ecker, J. Gasser, H. Leutwyler, A. Pich, and E. de Rafael, *Chiral Lagrangians for Massive Spin 1 Fields*, Phys. Lett. B **223**, 425–432 (1989).

[363] J. M. Dias, G. Toledo, L. Roca, and E. Oset, *Unveiling the K1(1270) double-pole structure in the* $B^- \to J/\psi \rho K^-$ *and* $B^- \to J/\psi K^{-*}\pi$ *decays*, Phys. Rev. D **103**, 116019 (2021).

[364] M.-L. Du, E. Hernández, and J. Nieves, *Is the* $\Lambda c(2625)+$ *the heavy quark spin symmetry partner of the* $\Lambda c(2595)+$*?*, Phys. Rev. D **106**, 114020 (2022).

[365] T. Yoshida, E. Hiyama, A. Hosaka, M. Oka, and K. Sadato, *Spectrum of heavy baryons in the quark model*, Phys. Rev. D **92**, 114029 (2015).

[366] J. Nieves and R. Pavao, *Nature of the lowest-lying odd parity charmed baryon* $\Lambda_c(2595)$ *and* $\Lambda_c(2625)$ *resonances*, Phys. Rev. D **101**, 014018 (2020).

[367] J. Nieves, A. Feijoo, M. Albaladejo, and M.-L. Du, *Lowest-lying* $\frac{1}{2}^-$ *and* $\frac{3}{2}^-$ Λ_Q *resonances: From the strange to the bottom sectors*, Prog. Part. Nucl. Phys. **137**, 104118 (2024), arXiv:2402.12726 [hep-ph].

[368] W. H. Liang, T. Uchino, C. W. Xiao, and E. Oset, *Baryon states with open charm in the extended local hidden gauge approach*, Eur. Phys. J. A **51**, 16 (2015).

[369] A. Dobado and J. R. Pelaez, *Chiral perturbation theory and the f(2)(1270) resonance*, Phys. Rev. D **65**, 077502 (2002), arXiv:hep-ph/0111140.

[370] G. Ecker and C. Zauner, *Tensor meson exchange at low energies*, Eur. Phys. J. C **52**, 315–323 (2007), arXiv:0705.0624 [hep-ph].

[371] L. M. Abreu, J. Song, P. C. S. Brandão, and E. Oset, *A note on the tensor and vector exchange contributions to* $K\bar{K} \to K\bar{K}, D\bar{D} \to D\bar{D}$ *and* $\pi^+\pi^- \to \pi^+\pi^-$ *reactions*, Eur. Phys. J. A **60**, 76 (2024), arXiv:2310.14015 [hep-ph].

[372] T. Uchino, W.-H. Liang, and E. Oset, *Baryon states with hidden charm in the extended local hidden gauge approach*, Eur. Phys. J. A **52**, 43 (2016).

[373] X.-G. He, X.-Q. Li, X. Liu, and X.-Q. Zeng, *Lambda+(c)(2940): A Possible molecular state?*, Eur. Phys. J. C **51**, 883–889 (2007).

[374] Y. Dong, A. Faessler, T. Gutsche, S. Kumano, and V. E. Lyubovitskij, *Radiative decay of* $\Lambda_c(2940)^+$ *in a hadronic molecule picture*, Phys. Rev. D **82**, 034035 (2010).

[375] J. He, Y.-T. Ye, Z.-F. Sun, and X. Liu, *The observed charmed hadron* $\Lambda_c(2940)^+$ *and the* D^*N *interaction*, Phys. Rev. D **82**, 114029 (2010).

[376] P. G. Ortega, D. R. Entem, and F. Fernandez, *The* $\Lambda_c(2940)^+$ *as a* D^*N *Molecule in a Constituent Quark Model and a Possible* $\Lambda_b(6248)$, Few Body Syst. **54**, edited by K. Sagara, E. Hiyama, S. Ishikawa, and A. Tamii, 1101–1104 (2013).

[377] B. Wang, L. Meng, and S.-L. Zhu, $D^{(*)}N$ *interaction and the structure of* $\Sigma_c(2800)$ *and* $\Lambda_c(2940)$ *in chiral effective field theory*, Phys. Rev. D **101**, 094035 (2020).

[378] S.-Y. Kong, J.-T. Zhu, S. Chen, and J. He, *Production of open-charm pentaquark molecules in decay B0→D¯0pp¯*, Phys. Rev. D **110**, 094042 (2024), arXiv:2402.02703 [hep-ph].

[379] Z.-L. Yue, Q.-Y. Guo, and D.-Y. Chen, *Strong decays of the Λc(2910) and Λc(2940) in the ND* molecular frame*, Phys. Rev. D **109**, 094049 (2024), arXiv:2402.10594 [hep-ph].

[380] M.-L. Du, V. Baru, F.-K. Guo, C. Hanhart, U.-G. Meißner, J. A. Oller, and Q. Wang, *Revisiting the nature of the* P_c *pentaquarks*, JHEP **08**, 157 (2021).

[381] Z. Zhang, J. Liu, J. Hu, Q. Wang, and U.-G. Meißner, *Revealing the nature of hidden charm pentaquarks with machine learning*, Sci. Bull. **68**, 981–989 (2023).

[382] S. Sakai, F.-K. Guo, and B. Kubis, *Extraction of ND scattering lengths from the $\Lambda_b \to \pi^- p D^0$ decay and properties of the $\Sigma_c(2800)^+$*, Phys. Lett. B **808**, 135623 (2020).

[383] A. Martínez Torres, E. Oset, S. Prelovsek, and A. Ramos, *Reanalysis of lattice QCD spectra leading to the $D^*_{s0}(2317)$ and $D^*_{s1}(2460)$*, JHEP **05**, 153 (2015), arXiv:1412.1706 [hep-lat].

[384] M. Bando, T. Kugo, and K. Yamawaki, *Nonlinear Realization and Hidden Local Symmetries*, Phys. Rept. **164**, 217–314 (1988).

[385] L.-S. Geng, R. Molina, and E. Oset, *On the chiral covariant approach to $\rho\rho$ scattering*, Chin. Phys. C **41**, 124101 (2017), arXiv:1612.07871 [nucl-th].

[386] P. Encarnación, A. Feijoo, and E. Oset, *Correlation function for the pf1(1285) interaction*, Phys. Rev. D **111**, 114023 (2025), arXiv:2502.19329 [hep-ph].

[387] N. Ikeno and E. Oset, *Correlation function for the $n\bar{D}^*_{s0}(2317)$ interaction and the issue of elastic unitarity*, (2025), arXiv:2507.16367 [hep-ph].

[388] A. Feijoo, W.-F. Wang, C.-W. Xiao, J.-J. Wu, E. Oset, J. Nieves, and B.-S. Zou, *A new look at the Pcs states from a molecular perspective*, Phys. Lett. B **839**, 137760 (2023).

[389] M. Bayar, A. Martinez Torres, K. P. Khemchandani, R. Molina, and E. Oset, *Exotic states with triple charm*, Eur. Phys. J. C **83**, 46 (2023).

[390] M. T. Hansen and S. R. Sharpe, *Expressing the three-particle finite-volume spectrum in terms of the three-to-three scattering amplitude*, Phys. Rev. D **92**, 114509 (2015), arXiv:1504.04248 [hep-lat].

[391] A. W. Jackura, R. A. Briceño, S. M. Dawid, M. H. E. Islam, and C. McCarty, *Solving relativistic three-body integral equations in the presence of bound states*, Phys. Rev. D **104**, 014507 (2021), arXiv:2010.09820 [hep-lat].

[392] S. M. Dawid, M. H. E. Islam, and R. A. Briceño, *Analytic continuation of the relativistic three-particle scattering amplitudes*, Phys. Rev. D **108**, 034016 (2023), arXiv:2303.04394 [nucl-th].

[393] P. G. Ortega, *Exploring the Efimov effect in the D*D*D* system*, Phys. Rev. D **110**, 034015 (2024), arXiv:2403.10244 [hep-ph].

[394] W. H. Press, S. A. Teukolsky, W. T. Vetterling, and B. P. Flannery, *Numerical Recipes in FORTRAN: The Art of Scientific Computing* (Cambridge University Press, Sept. 1992).

[395] B. Efron and R. Tibshirani, *An introduction to the bootstrap*, Statist. Sci. **57**, 54–75 (1986).

[396] M. Artuso et al. (CLEO), *Observation of new states decaying into Lambda+(c) pi- pi+*, Phys. Rev. Lett. **86**, 4479–4482 (2001), arXiv:hep-ex/0010080.

[397] H.-P. Li, J. Song, W.-H. Liang, R. Molina, and E. Oset, *Contrasting observables related to the $N^*(1535)$ from the molecular or a genuine structure*, Eur. Phys. J. C **84**, 656 (2024), arXiv:2311.14365 [hep-ph].

Resumen extenso en castellano

Motivación

QCD y estados exóticos

La Cromodinámica Cuántica (QCD por sus siglas en inglés: *Quantum ChromoDynamics*), teoría que describe la interacción fuerte entre quarks y gluones, constituye uno de los pilares fundamentales del Modelo Estándar de la física de partículas. Existen seis *sabores* (especies) de quarks: arriba (*up*), abajo (*down*), extraño (*strange*), encanto (*charm*), fondo o belleza (*bottom* o *beauty*) y cima (*top*). Además, tienen carga de color, que puede tomar tres valores distintos (rojo, verde y azul), junto con sus correspondientes anti-colores. La interacción fuerte es transmitida por los gluones, partículas vectoriales que también llevan carga de color y, a diferencia de los fotones en la interacción electromagnética, interactúan entre sí. Esta propiedad distintiva de QCD es la responsable de fenómenos tan característicos como el *confinamiento*, que impide la existencia de quarks libres en la naturaleza; y, complementariamente, la *libertad asintótica*, que predice que a altas energías las interacciones entre quarks se debilitan, permitiendo un tratamiento perturbativo de la teoría.

A bajas energías, sin embargo, la constante de acoplamiento de QCD crece y el cálculo perturbativo deja de ser aplicable. Es precisamente en este régimen no perturbativo donde se forman los hadrones (los estados ligados de quarks y gluones que observamos experimentalmente) y donde surge la gran riqueza del espectro hadrónico. Comprender la dinámica de QCD en este régimen constituye uno de los retos más profundos de la física teórica contemporánea. Un hito decisivo en el camino hacia esta comprensión fue el desarrollo del Modelo de Quarks de Godfrey e Isgur, cuyas predicciones reprodujeron con un éxito notable gran parte del espectro hadrónico observado. Este marco teórico permitió organizar de forma sistemática los mesones y bariones conocidos, estableciendo un marco de referencia que, a día de hoy, aún resulta influyente.

No obstante, como todo modelo, presenta limitaciones inherentes y no puede dar cuenta de todos los estados observados.

En el Modelo de Quarks clásico, los mesones se describen como estados quark–antiquark ($q\bar{q}$), mientras que los bariones se componen de tres quarks (qqq). Este esquema, introducido en la década de 1960, explicó de manera elegante la existencia de los multipletes de sabor y proporcionó una imagen intuitiva de la estructura de la materia hadrónica. Sin embargo, con el paso de los años se hizo evidente que esta imagen no estaba completa. Existen estados que no encajan en este marco simple o cuya descripción en términos de $q\bar{q}$ o qqq resulta poco natural. Más aún, algunos estados presentan números cuánticos imposibles de obtener en configuraciones convencionales de quarks, lo que les otorga un carácter genuinamente *exótico*.

Desde el punto de vista de QCD, el único requisito fundamental para un hadrón es que sea un singlete de color. Esto abre la puerta a una gran variedad de configuraciones más complejas: tetraquarks ($qq\bar{q}\bar{q}$), pentaquarks ($qqqq\bar{q}$), bolas de gluones (estados compuestos únicamente de gluones), híbridos que incluyen gluones de valencia junto con quarks, o incluso moléculas hadrónicas formadas por interacciones residuales entre estados singletes (sin carga) de color. En la práctica, estas etiquetas no son absolutas, ya que configuraciones distintas pero con los mismos números cuánticos globales pueden mezclarse, dando lugar a estados cuya naturaleza interna es difícil de precisar.

Durante décadas, estos estados permanecieron en gran medida como hipótesis teóricas sin confirmación experimental. Sin embargo, en los últimos veinte años, la espectroscopía hadrónica ha vivido un auge extraordinario, en lo que algunos autores han denominado la "segunda revolución de la física hadrónica". Algunos experimentos como Belle, BaBar, BESIII y LHCb han descubierto un amplio abanico de estados que no se pueden describir de manera natural en el esquema del modelo de quarks convencional. Entre ellos se incluyen mesones cargados que no pueden ser interpretados como $c\bar{c}$ o $b\bar{b}$ puros, resonancias extremadamente cercanas a umbrales de producción de dos hadrones, y pentaquarks con contenido de quarks pesados.

Un ejemplo histórico de especial relevancia es el descubrimiento del $\chi_{c1}(3872)$ (antiguo $X(3872)$) por la colaboración Belle en 2003. Este estado, extremadamente estrecho y situado justo en el umbral $D^0\overline{D}^{*0}$, se convirtió rápidamente en uno de los principales candidatos a estado molecular hadrónico. Desde entonces, se han observado numerosos estados adicionales en el sector del *charmonium* que no pueden describirse como $c\bar{c}$ convencionales. Más recientemente, la observación del $T_{cc}(3875)^+$ por LHCb ha supuesto un hito aún mayor: al tratarse de un estado con dos unidades de *charm*, su composición mínima exige cuatro quarks de valencia ($cc\bar{u}\bar{d}$). Su masa extremadamente cercana al umbral DD^* y su anchura inusualmente pequeña lo convierten en uno

de los candidatos más claros a hadrón tipo tetraquark de naturaleza molecular, hecho que ha despertado un intenso debate teórico y ha constituído una de las principales motivaciones de este trabajo.

En paralelo, en el sector *charm–strange* se descubrieron en 2003 los estados $D_{s0}^{*}(2317)^{\pm}$ y $D_{s1}(2460)^{\pm}$, cuyas masas resultaron sorprendentemente bajas respecto a las predicciones del modelo de Godfrey e Isgur. Estas anomalías pueden explicarse de manera natural si se interpretan como estados ligados DK y $D^{*}K$, hipótesis reforzada por estudios de QCD en el retículo (*Lattice QCD*, LQCD). De este modo, tanto el $T_{cc}(3875)^{+}$ como el $D_{s0}^{*}(2317)$ se han consolidado como casos de referencia en el estudio de hadrones exóticos y motivan de manera directa la investigación presentada en esta tesis.

Materia fuertemente interactuante en condiciones extremas

Una segunda gran frontera en la física hadrónica se encuentra en el comportamiento de la materia fuertemente interactuante bajo condiciones extremas de densidad bariónica y/o temperatura. El estudio de estas condiciones no es un mero ejercicio teórico, ya que conecta de manera directa con problemas fundamentales en astrofísica y cosmología, así como con la búsqueda experimental de nuevas fases de la materia en colisiones de iones pesados.

A temperaturas y densidades suficientemente altas, se espera que los hadrones pierdan su identidad y se disocien en sus constituyentes fundamentales: quarks y gluones. Bajo estas circunstancias, QCD predice la formación de un nuevo estado de la materia conocido como *plasma de quarks y gluones* (QGP, por sus siglas en inglés: *Quark-Gluon Plasma*). La existencia de esta fase desconfinada fue propuesta ya a mediados de los años 70, pocos años después de la formulación de QCD, por trabajos pioneros de Collins y Perry, y de Cabibbo y Parisi. Estos autores plantearon que, debido a la libertad asintótica, las interacciones entre quarks se debilitan a altas energías, lo que sugiere de manera natural una transición desde la fase hadrónica confinada hacia un QGP desconfinado cuando la temperatura y/o la densidad bariónica superan ciertos valores críticos.

En la actualidad, cálculos de LQCD a densidad bariónica nula confirman este escenario: la transición desde la materia hadrónica hacia el QGP es un cruce suave (*crossover*) en torno a una temperatura crítica $T_c \simeq 155$ MeV. Esta transición está acompañada de la restauración aproximada de la simetría quiral en el sector de quarks ligeros, otro de los pilares conceptuales de QCD. Dicho resultado constituye uno de los mayores éxitos de LQCD, ya que proporciona una predicción cuantitativa robusta que ha podido ser contrastada con los experimentos de colisiones de iones pesados en el RHIC (Brookhaven) y el LHC (CERN), donde se han recreado condiciones similares a las del Universo primitivo.

Sin embargo, a densidades bariónicas más altas la situación es mucho más incierta. El problema fundamental es que los cálculos de LQCD se ven seriamente limitados por el denominado *problema del signo*, que dificulta enormemente la simulación numérica cuando el potencial químico bariónico es finito. Por ello, gran parte del conocimiento actual proviene de aproximaciones efectivas, teorías funcionales como la de los potenciales de interacción de Nambu–Jona–Lasinio, o cálculos perturbativos en el límite de altas densidades. Estos estudios sugieren la existencia de una transición de fase de primer orden en el plano densidad–temperatura, que terminaría en un punto crítico al disminuir la densidad. La localización experimental de dicho punto crítico es uno de los objetivos prioritarios de programas actuales como el *Beam Energy Scan* en RHIC o las futuras investigaciones previstas en FAIR (Darmstadt).

El diagrama de fases de QCD podría contener además otras regiones aún más exóticas, como las fases superconductoras de color, que se predicen a densidades asintóticamente altas y que podrían ser relevantes para describir el interior de las estrellas de neutrones. En estas fases, los quarks cercanos a la superficie de Fermi formarían pares de Cooper de manera análoga a lo que sucede en la superconductividad electrónica, pero mediada aquí por interacciones de color. El estudio detallado de estas fases sigue siendo un campo abierto y de intensa investigación teórica.

Más allá de su interés intrínseco para la física de partículas, la materia de QCD en condiciones extremas está ligada a cuestiones fundamentales de la cosmología y la astrofísica. Se cree que el Universo primitivo, durante sus primeros microsegundos tras el Big Bang, estuvo completamente compuesto por plasma de quarks y gluones. Al expandirse y enfriarse, el QGP se transformó gradualmente en hadrones y, posteriormente, en núcleos, dando lugar a la materia ordinaria que observamos hoy. Por tanto, comprender la transición de fase en QCD no solo aclara aspectos de la teoría de la interacción fuerte, sino que también aporta piezas clave a nuestra narrativa cosmológica.

En el extremo opuesto, el régimen de altas densidades y temperaturas moderadas es fundamental para la astrofísica de objetos compactos. La composición de la materia a varias veces la densidad de saturación nuclear determina la ecuación de estado que gobierna la relación masa–radio de las estrellas de neutrones. Ésta, a su vez, juega un papel central en la interpretación de señales multimensajero, como las ondas gravitacionales y la emisión electromagnética observada en fusiones de estrellas de neutrones, registradas por LIGO/Virgo y observatorios asociados. En este contexto, saber si la materia en el núcleo de una estrella de neutrones está formada por nucleones, hiperones, quarks desconfinados o grados de libertad más exóticos es un problema abierto de primera magnitud.

En términos del contenido de esta tesis, el estudio de estados hadrónicos

exóticos en regímenes de alta densidad y temperatura, si bien no persigue directamente la exploración global del diagrama de fases de QCD, aprovecha dichos entornos como una fuente adicional de información sobre su naturaleza interna. Las modificaciones en sus masas, anchuras y funciones espectrales (sensibles tanto al grado de composición molecular como a la disparidad entre las interacciones de mesones y antimesones con nucleones) constituyen magnitudes observables clave para poner a prueba las teorías efectivas de baja energía, según los resultados aquí expuestos. De este modo, el análisis en un medio denso o caliente ofrece una perspectiva complementaria a los estudios en el vacío y se perfila como una herramienta esencial para discriminar entre las diferentes posibles estructuras internas de los hadrones exóticos. En conjunto, estos estudios contribuyen a una comprensión más profunda de la interacción fuerte y del papel que juegan los estados exóticos en el espectro de QCD.

Metodología general

La presente tesis combina distintas herramientas teóricas y numéricas para el estudio de estados hadrónicos exóticos en condiciones extremas de densidad y temperatura, así como en el vacío. A continuación, se describen brevemente las principales metodologías empleadas, antes de discutir el formalismo y los resultados principales obtenidos en cada capítulo.

Teorías efectivas

El punto de partida lo constituye la Cromodinámica Cuántica, cuya naturaleza fuertemente acoplada a bajas energías obliga al uso de teorías efectivas. Las *teorías de campos efectivas* (*Effective Field Theories*, EFTs) ofrecen un marco general para describir fenómenos en regímenes donde un tratamiento completo de la dinámica subyacente resulta desconocido o intratable. Su idea central consiste en identificar los grados de libertad relevantes a una cierta escala de energía y construir con ellos el lagrangiano más general compatible con las simetrías de la teoría fundamental. La dinámica a cortas distancias, que no se resuelve explícitamente, se incorpora de manera sistemática en un número finito de constantes de baja energía (*Low-Energy Constants*, LECs). Algunos ejemplos de teorías efectivas especialmente relevantes en el marco de QCD son la teoría quiral de perturbaciones (*Chiral Perturbation Theory*, ChPT), la teoría efectiva de quarks pesados (*Heavy-Quark Effective Theory*, HQET) y su "combinación": la *teoría quiral de perturbaciones de hadrones pesados* (*Heavy-Hadron ChPT*, HHChPT). Estas teorías están matemáticamente definidas por lagrangianos efectivos consistentes con las simetrías quiral y/o de espín de quark pesado (*Heavy-Quark Spin Symmetry*, HQSS) de QCD, que sirven como base para de-

scribir las interacciones hadrónicas relevantes dentro de un *contaje perturbativo* (*power counting*). En particular, a lo largo de esta tesis se han considerado estas teorías para describir interacciones como $D^{(*)}N$, KN, $D^{(*)}\pi$, $K\pi$, $D^{(*)}D^*$ y $D^{(*)}K$. Estas interacciones constituyen uno de los bloques fundamentales del formalismo de los distintos capítulos de este trabajo.

Estados en el medio y funciones espectrales

Para describir el comportamiento de hadrones inmersos en materia nuclear o en un medio térmico se emplean las técnicas de teoría cuántica de campos en el medio. En el caso de temperatura finita, el marco teórico está dado por la *teoría térmica de campos* (*thermal field theory* en inglés), en particular mediante el formalismo de tiempo imaginario (*Imaginary Time Formalism*, ITF) introducido por Matsubara. El concepto central en teoría cuántica de campos en el medio es la *autoenergía*, que codifica las modificaciones en las propiedades de una partícula debidas a sus interacciones con el entorno. A partir de ella se construyen las *funciones espectrales*, que proporcionan información sobre masas efectivas, anchuras de desintegración y modos colectivos en el medio. Herramientas como el formalismo de funciones de Green y la ecuación de Bethe–Salpeter unitarizada desempeñan un papel esencial en este marco.

Ecuaciones de tres cuerpos y aproximación de centro fijo

El estudio de sistemas de tres hadrones requiere resolver las ecuaciones de Faddeev, que incorporan de manera sistemática las múltiples interacciones posibles entre los constituyentes del sistema. En este trabajo se emplea la *aproximación de centro fijo* (*Fixed-Center Approximation*, FCA), adecuada cuando dos de las partículas forman un estado ligado compacto que actúa como centro de dispersión para la tercera. Este método simplifica notablemente la dinámica manteniendo las características esenciales del problema.

Observables experimentales: transparencia nuclear

Una parte de la tesis está dedicada a explorar la viabilidad de acceder experimentalmente a las propiedades en el medio nuclear de mesones pesados. Para ello, se estudia el observable conocido como cociente de transparencia (*transparency ratio*), ya utilizado con éxito en el caso del mesón η'. Este cociente compara la producción de mesones en distintos núcleos y permite extraer información sobre la absorción del mesón en el medio, directamente relacionada con la parte imaginaria de su autoenergía.

Herramientas numéricas

El desarrollo de los cálculos ha requerido un uso intensivo de programación científica. La evaluación de integrales y la resolución de las ecuaciones dinámicas se han implementado principalmente en `FORTRAN`, aprovechando su eficiencia en cómputo numérico. Además, se ha empleado `Wolfram Mathematica` como apoyo analítico, tanto para la manipulación simbólica de expresiones como para la verificación de resultados intermedios.

Formalismo y análisis de los resultados

A continuación se resumen tanto el formalismo como los principales resultados obtenidos en cada uno de los capítulos de esta tesis. La organización sigue la misma estructura que el cuerpo principal del manuscrito.

Capítulo 2: Estados exóticos en medio nuclear

El primer bloque de resultados de esta tesis se centra en el estudio del comportamiento de estados exóticos en un medio nuclear denso (materia nuclear). Este medio está descrito como un mar de Fermi de nucleones no interactuantes, caracterizado por el momento de Fermi k_F y por la densidad de nucleones ρ. Los candidatos analizados en detalle han sido el $T_{cc}(3875)$ y el $D_{s0}^*(2317)$, junto con sus compañeros de HQSS. Estos estados, entendidos como moléculas hadrónicas formadas por $D^{(*)}D^*$ y $D^{(*)}K$, respectivamente, se han modelado como estados generados dinámicamente en las correspondientes amplitudes de dispersión mesón–mesón en onda S unitarizadas.

El marco teórico se basa en el concepto de autoenergía, que describe la modificación del propagador de una partícula debido a sus interacciones con el medio. Para un mesón M propagándose en materia nuclear, la autoenergía se calcula como

$$\Pi^M(p^0,\vec{p};\rho) = \int_{q<k_F} \frac{d^3q}{(2\pi)^3}\, t^{MN}\left(p^0 + E_N(\vec{q}), \vec{p}+\vec{q};\rho\right),$$

donde t^{MN} es la amplitud mesón–nucleón. En la anterior expresión, $(p^0,\vec{p})$ es la energía y el trimomento del mesón M, y $E_N(\vec{q})$ es la energía de un nucleón del medio con trimomento $\vec{q}$. La amplitud unitarizada t^{MN} se determina mediante la ecuación de Bethe–Salpeter:

$$t^{MN}(P^0,\vec{P};\rho) = \frac{v^{MN}(\sqrt{s})}{1 - v^{MN}(\sqrt{s}) g^{MN}(P^0,\vec{P};\rho)},$$

donde v^{MN} proviene de un lagrangiano efectivo con simetría $\mathrm{SU}(6)_{\mathrm{lsf}} \times \mathrm{HQSS}$ para los mesones $D^{(*)}$ ($\mathrm{SU}(6)_{\mathrm{lsf}}$ constituyendo el grupo de simetría de espín-sabor ligero) y de la teoría quiral en el caso de los kaones. En esta expresión, $\mathbf{P} = (P^0, \vec{P})$ es el cuadrimomento total del sistema MN, y $s = \mathbf{P}^2$ es la masa invariante del sistema. La función de loop $g^{MN}(P^0, \vec{P}; \rho)$ incorpora los efectos de densidad a través de las autoenergías, por lo que el cálculo numérico de las autoenergías se resuelve de forma autoconsistente.

Una vez determinadas las autoenergías de $D^{(*)}$ y K (tomadas de la literatura), se introdujeron en la ecuación de Bethe–Salpeter para la matriz de transición de dos mesones. Se parte de la dinámica en el espacio libre

$$T(s) = \frac{V(s)}{1 - \Sigma_0(s)V(s)},$$

donde T, V y Σ_0 son, respectivamente, la matriz de transición, la interacción efectiva y la función de *loop* mesón–mesón en el vacío (usamos en este caso letras mayúsculas para evidenciar que hablamos de unas magnitudes distintas a las de las ecuaciones anteriores), siendo s la masa invariante del sistema mesón–mesón. Se han utilizado dos familias de interacciones efectivas, V_A (lineal en s) y V_B (inversamente lineal en s), parametrizadas para que la matriz T unitarizada en el vacío genere un polo en $s = m_0^2$ con probabilidad molecular P_0. Los efectos del medio se han tenido en cuenta sustituyendo Σ_0 por la función de loop en el medio nuclear,

$$\Sigma(s; \rho) = i \int \frac{d^4q}{(2\pi)^4} \Delta^M(E - q^0, \vec{P} - \vec{q}; \rho) \Delta^{M'}(q^0, \vec{q}; \rho),$$

con los propagadores de los mesones vestidos

$$\Delta^M(q^0, \vec{q}; \rho) = \frac{1}{(q^0)^2 - \vec{q}^{\,2} - m_M^2 - \Pi^M(q^0, \vec{q}; \rho)}.$$

Los resultados obtenidos han mostrado un comportamiento muy distinto entre partículas y antipartículas, debido a la presencia del medio nuclear, que rompe la simetría de conjugación de carga. En el caso del $T_{cc}(3875)^+$ y su antipartícula $T_{\bar{c}\bar{c}}(3875)^-$, cuando domina la componente molecular, el primer estado exótico se ensancha de manera notable y su polo se desplaza hacia energías más altas, mientras que el segundo sufre un ensanchamiento moderado y un desplazamiento hacia energías más bajas. Esta asimetría refleja la fuerte diferencia entre la interacción atractiva $D^{(*)}N$ y la mucho más débil $\overline{D}^{(*)}N$. Haciendo uso de HQSS se ha extendido el estudio a los compañeros $T_{cc}^*(4016)^+$ y $T_{\bar{c}\bar{c}}^*(4016)^-$ generados en la matriz de dispersión D^*D^* y $\overline{D}^*\overline{D}^*$, respectivamente. Se ha encontrado que la interacción D^*N, que en el modelo $\mathrm{SU}(6)_{\mathrm{lsf}} \times \mathrm{HQSS}$

es más atractiva que DN, amplifica las modificaciones obtenidas para estos estados, manteniendo no obstante una asimetría partícula–antipartícula similar.

Un patrón análogo, pero aún más marcado, se ha observado en los estados *charm–strange* $D_{s0}^{*}(2317)^{\pm}$ y $D_{s1}(2460)^{\pm}$. En este caso, las autoenergías de kaones y antikaones muestran un gran contraste entre la fuerte atracción en el canal $\overline{K}N$ y la débil repulsión en KN. Como consecuencia, incluso a la mitad de la densidad de saturación nuclear, el $D_{s0}^{*}(2317)^{+}$ se desplaza a energías superiores y se estrecha, mientras que su antipartícula migra hacia energías menores con un perfil Breit–Wigner mucho más ancho (hasta el punto de que ambas amplitudes apenas se solapan para altas probabilidades moleculares). En los compañeros $D_{s1}(2460)^{\pm}$ aparece la misma tendencia, aunque con anchuras globalmente mayores debido a la intensidad de las interacciones $D^{*}N$ y $\overline{D}^{*}N$. En cualquier caso, las diferencias entre las dinámicas del kaón y el antikaón en el medio nuclear constituyen el motor principal de la asimetría de conjugación de carga tan acusada que hemos encontrado en nuestro estudio.

En conjunto, estos resultados han mostrado que la magnitud (e incluso el signo) de los desplazamientos de masa y anchura inducidos por la densidad dependen críticamente de dos factores: la probabilidad molecular del estado y la diferencia entre las interacciones mesón–nucleón y antimesón–nucleón. Por ello, si se realizaran medidas de las funciones espectrales en un medio denso de las familias $T_{cc}(3875)$ y $D_{s0}^{*}(2317)$ (por ejemplo, en colisiones relativistas de iones pesados en CBM/FAIR o en experimentos de blanco fijo con antiprotones en PANDA), se obtendría una prueba experimental directa de su estructura interna. La confirmación de los desplazamientos y ensanchamientos predichos respaldaría la interpretación molecular, mientras que un comportamiento más tenue o distinto apoyaría el escenario de tetraquarks compactos. Además, tales observaciones aportarían restricciones valiosas sobre las autoenergías (aún poco conocidas) de kaones, antikaones y mesones con *charm* en materia nuclear densa.

Capítulo 3: Transparencia nuclear

Tras haber caracterizado las modificaciones en medio de los estados $T_{cc}(3875)$ y $D_{s0}^{*}(2317)$, se ha abordado la cuestión clave de cómo acceder experimentalmente a estas propiedades. En particular, se ha tratado el problema de la determinación experimental de la anchura en el medio del mesón D, que constituye uno de los componentes básicos de los estados estudiados anteriormente. Para ello, se ha analizado el observable conocido como *cociente de transparencia* (*transparency ratio*), que mide la probabilidad relativa de que un mesón pesado atraviese un núcleo sin ser absorbido en comparación con un núcleo ligero de referencia (normalmente ^{12}C). Este observable ya ha demostrado ser eficaz en el caso del mesón η', permitiendo extraer su anchura en el medio nuclear.

El análisis se ha basado en la reacción de fotoproducción $\gamma A \to D^+ D^- A'$, donde A y A' denotan el núcleo inicial y final (A también representa el número másico). El observable de interés se define como

$$T_A = \frac{\sigma(\gamma A \to D^+ D^- A')}{\sigma(\gamma\ {}^{12}\mathrm{C} \to D^+ D^-\ {}^{12}\mathrm{C}')} \frac{12}{A},$$

cociente que cuantifica la reducción de la sección eficaz debida a la absorción de los mesones D en el interior nuclear. En esta expresión, σ denota la sección eficaz de la reacción de fotoproducción en el núcleo de interés. Esta cantidad se calcula en el sistema laboratorio, en el que el núcleo inicial está en reposo, como

$$\sigma(\gamma A \to D^+ D^- A') = \\ = \frac{1}{4 m_N p_\gamma} \int_{\substack{\text{espacio} \\ \text{físico}}} \int_{\substack{\text{volumen} \\ \text{núcleo}}} d^3 r\, \rho(\vec{r})\, |t|^2 \exp\left[\int_{\vec{r}'} \frac{\mathrm{Im}\,\Pi\,(E_D, p_D; \rho(\vec{r}'))}{p_D} d\vec{r}' \right],$$

donde $\rho(\vec{r})$ representa la densidad numérica de nucleones en el punto $\vec{r}$, $|t|^2$ es la amplitud diferencial del proceso de fotoproducción en un nucleón dentro del núcleo, y la exponencial final constituye el factor de atenuación que describe la probabilidad de supervivencia del mesón D en su trayecto de salida del núcleo (parametrizado por $\vec{r}'$). Este factor depende de manera directa de la parte imaginaria de su autoenergía en el medio. Para evaluar la sección eficaz se ha empleado una estimación de dicha parte imaginaria, inspirada en estudios previos, y se ha restringido la energía total del sistema en el centro de masas fotón–núcleo a unos 10 GeV, región donde la emisión de mesones D de bajo momento en el sistema laboratorio resulta máxima.

Inicialmente, se han adoptado dos aproximaciones para simplificar los cálculos: se ha considerado una amplitud diferencial $|t|^2$ constante y se ha modelado la densidad nuclear ρ mediante una distribución esférica uniforme (modelo de esfera dura). Posteriormente, ambas partes del modelo han sido refinadas, incorporando la dependencia dominante de $|t|^2$ con la energía, motivada por estudios anteriores, y empleando distribuciones de densidad más realistas, basadas en funciones de oscilador armónico y de tipo Fermi. Estas mejoras han permitido comprobar la robustez de las predicciones iniciales y reducir las incertidumbres asociadas al cálculo.

Los resultados numéricos han mostrado que el cociente de transparencia decrece de forma marcada con el número másico nuclear: en núcleos pesados se alcanzan valores en torno a 0.6 relativos al caso de ^{12}C. Esta reducción refleja directamente el ensanchamiento en el medio de los mesones D, y constituye una vía experimental accesible para determinar su autoenergía.

En conjunto, este estudio ha propuesto el cociente de transparencia como una vía experimental para explorar las propiedades en el medio del mesón D, mostrando su alta sensibilidad a la absorción teóricamente estimada para este mesón. Aunque en el cálculo se han utilizado ciertas simplificaciones, se han establecido las condiciones cinemáticas óptimas para maximizar la sensibilidad a los efectos del medio, y se ha mostrado que el nivel de supresión predicho debería ser accesible en futuras instalaciones como el EIC, el EicC o una mejora de GlueX.

Capítulo 4: Estados exóticos a temperatura finita

En el Cap. 4 se ha analizado el comportamiento térmico del $T_{cc}(3875)^+$ y de su compañero de HQSS, el $T^*_{cc}(4016)^+$, a temperatura finita. El objetivo ha sido explorar cómo un baño térmico de piones modifica las propiedades de estos estados exóticos, descritos como moléculas $D^{(*)}D^*$ generadas dinámicamente en amplitudes de dispersión unitarizadas en onda S, de manera análoga al estudio del Cap. 2. Para ello, se ha propuesto de nuevo una matriz de transición unitarizada a través de la ecuación de Bethe–Salpeter, utilizando las familias de potenciales V_A y V_B, parametrizadas en términos de la probabilidad molecular de estos estados.

El marco teórico empleado para describir un medio térmico poblado por piones ha sido la teoría de campos térmica en el formalismo del tiempo imaginario (ITF). De nuevo, los efectos del entorno se han incorporado mediante las funciones de loop de dos mesones, modificadas ahora por la presencia de la distribución de Bose–Einstein y por la renormalización de los mesones constituyentes a través de sus autoenergías dependientes de la temperatura. Su expresión explícita en términos de las funciones espectrales de los mesones (S^M) es

$$\Sigma^{MM'}(P^0,\vec{P};T) = \int \frac{d^3q}{(2\pi)^3}\int d\omega_1 \int d\omega_2 \times [1+b^-(\omega_1;T)+b^-(\omega_2;T)]\,\frac{S_M(\omega_1,\vec{q};T)\,S_{M'}(\omega_2,\vec{P}-\vec{q});T}{P^0-\omega_1-\omega_2+\mathrm{sign}(p^0)\,i\varepsilon},$$

donde las funciones $b^-(\omega_i;T)$ representan distribuciones de Bose–Einstein, dependientes de la temperatura T. La función espectral S^M se relaciona con la autoenergía mediante

$$S^M(p^0,\vec{p};T) = -\frac{1}{\pi}\,\mathrm{Im}\,\Delta^M(p^0,\vec{p};T),$$

siendo Δ^M el propagador del mesón en el medio, que con la incorporación de

su autoenergía se escribe como

$$\Delta^M(p^0,\vec{p};T)=\frac{1}{(p^0)^2-\vec{p}^2-m_M^2-\Pi(i\omega_n,\vec{p};T)}.$$

Tras realizar la suma sobre las frecuencias de Matsubara y una rotación de Wick del eje temporal imaginario al real, la autoenergía dependiente de la temperatura se puede expresar de la siguiente manera:

$$\Pi(p^0,\vec{p};T)=-\frac{1}{\pi}\int\frac{d^3q}{(2\pi)^3}\int_{-\infty}^{+\infty}d\omega_1\int_{-\infty}^{+\infty}d\omega_2 \times[b^-(\omega_1)-b^-(\omega_2)]\,\frac{\tilde{S}_\pi(\omega_1,\vec{q})\,\mathrm{Im}\,t^{M\pi}(\omega_2,\vec{q}+\vec{p};T)}{p^0-\omega_2+\omega_1+\mathrm{sign}(p^0)i\varepsilon},$$

donde $t^{M\pi}$ es la matriz de transición mesón-pión a temperatura finita, calculada de forma autoconsistente a través de la ecuación de Bethe-Salpeter.

En este trabajo se han utilizado resultados previos para las funciones espectrales dependientes de la temperatura de los mesones D y D^* inmersos en un baño térmico de piones, con el fin de evaluar la función de loop del par DD^* y describir así las modificaciones en la matriz de transición DD^*. Esta última se definió en el vacío de forma idéntica a como se presentó en el Cap. 2.

Los resultados numéricos han mostrado que, ya a temperaturas moderadas ($T\simeq 80$ MeV), las amplitudes $D^{(*)}D^*$ se ven significativamente modificadas: el corte de unitariedad se suaviza y se desplaza hacia energías más bajas, mientras que el pico en el umbral se atenúa. Con el incremento de la temperatura, los estados T_{cc} y T_{cc}^* experimentan un rápido ensanchamiento de sus funciones espectrales, que desemboca en la disolución de ambas resonancias en torno a $T\simeq 100$–120 MeV.

Un aspecto clave de estas modificaciones es su sensibilidad a la probabilidad molecular de los estados. En configuraciones dominadas por componentes moleculares, los efectos térmicos han resultado mucho más pronunciados, mientras que las estructuras más compactas han mostrado una notable estabilidad frente al aumento de temperatura, además de una mayor dependencia respecto a la forma específica de la familia de potenciales escogida.

En conjunto, el análisis ha demostrado que la evolución térmica del $T_{cc}(3875)^+$ y de su compañero de HQSS ofrece una vía novedosa para explorar su estructura interna. Medidas experimentales de amplitudes $D^{(*)}D^*$ en colisiones de iones pesados en instalaciones como RHIC o LHC podrían proporcionar información decisiva sobre la naturaleza de estos estados. Combinadas con futuros estudios en materia densa en FAIR, estas medidas abrirían la posibilidad de imponer mayores restricciones sobre la probabilidad molecular de estos hadrones exóticos con doble *charm*.

Capítulo 5: Estados ligados de tres cuerpos

En el Cap. 5 se ha trasladado el análisis desde los sistemas de dos cuerpos hacia la dinámica de tres hadrones, con el objetivo de explorar la posible formación de estados ligados genuinos. El sistema estudiado ha sido DND^*, compuesto por dos mesones con *charm* y un nucleón. La motivación para este análisis se basa en la interpretación molecular de varios bariones en el sector *charm*, como el $\Lambda_c(2940)$ y el $\Lambda_c(2910)$, propuestos como estados ligados D^*N, y el $\Lambda_c(2765)$, que se puede relacionar mediante argumentos de HQSS con un estado DN. La existencia de estos candidatos sugiere que configuraciones de tres cuerpos podrían dar lugar a nuevos estados ligados.

El tratamiento de este problema se ha abordado mediante la *aproximación de centro fijo* (FCA, por sus siglas en inglés). En esta aproximación, dos de las partículas forman un par (*cluster*) ligado relativamente compacto, que actúa como centro de dispersión para la tercera. De esta manera, las ecuaciones de Faddeev se simplifican en un sistema de ecuaciones integrales acopladas para las amplitudes T_1 y T_2:

$$\begin{aligned} T_1 &= t_1 + t_1\, G_0\, T_2, \\ T_2 &= t_2 + t_2\, G_0\, T_1, \end{aligned}$$

donde $t_{1,2}$ son las amplitudes de dispersión dos a dos (por ejemplo, si el *cluster* está formado por D^*N, corresponden a las interacciones DD^* y DN con la partícula externa), y G_0 es la función de propagación de la partícula externa dentro del *cluster*. La amplitud total se obtiene como $T = T_1 + T_2$. Este esquema captura de manera controlada los efectos más relevantes de la dinámica de tres cuerpos cuando uno de los subsistemas forma un estado ligado robusto.

Se han considerado dos posibles configuraciones de *cluster*:

- $D(ND^*)$, motivada por la interpretación molecular de los estados $\Lambda_c(2940)$ y $\Lambda_c(2910)$ como sistemas D^*N.
- $D^*(ND)$, en la que el *cluster* DN se relaciona con la resonancia $\Lambda_c(2765)$.

En el primer caso, se ha supuesto que los estados $\Lambda_c(2940)$ y $\Lambda_c(2910)$ tienen espín $J = 1/2$ y $3/2$, respectivamente (aunque también se considera la asignación contraria). El espín de estas resonancias determina el momento angular total del sistema de tres cuerpos. En el segundo caso, el momento angular total del sistema lo fija la interacción del mesón D^* con los constituyentes del *cluster* DN.

Los resultados numéricos obtenidos han mostrado la aparición de dos estados ligados con números cuánticos $J^P = 1/2^+$ y $3/2^+$, localizados cerca de los correspondientes umbrales $\Lambda_c^* D^{(*)}$. La similitud de los espectros obtenidos

en las dos configuraciones indica que las incertidumbres teóricas introducidas por la elección del *cluster* son moderadas y que la predicción de estados ligados es robusta dentro de este marco. En todos los casos, se ha identificado la atracción en los canales DN y D^*N como el mecanismo principal responsable de la formación de estos estados de tres cuerpos.

En conjunto, el estudio ha demostrado que el sistema DND^* constituye un sistema natural para albergar estados ligados de tres partículas, impulsados por las interacciones atractivas $D^{(*)}N$. Su eventual confirmación experimental proporcionaría información valiosa sobre la naturaleza molecular de los bariones Λ_c^* y sobre el papel de las interacciones DN y D^*N en la espectroscopía en el sector *charm*. Además, extender este tipo de análisis a otros sistemas de tres cuerpos podría abrir nuevas direcciones en la exploración de hadrones exóticos más allá del esquema convencional.

Conclusiones generales

En conjunto, los resultados de esta tesis han mostrado cómo los estados hadrónicos exóticos con *charm*, en particular el $T_{cc}(3875)$ y el $D_{s0}^*(2317)$, constituyen sistemas privilegiados para investigar la dinámica no perturbativa de QCD a bajas energías. Se ha puesto de manifiesto que sus propiedades no son estáticas, sino que dependen de manera sensible del entorno nuclear y térmico en el que se encuentren. La fuerte correlación entre la probabilidad molecular de los estados y la magnitud de las modificaciones inducidas, estas últimas marcadas por la diferente respuesta de partículas y antipartículas frente a los efectos del medio nuclear, ha destacado el papel central de la probabilidad molecular en la espectroscopía de hadrones exóticos.

El estudio del cociente de transparencia ha mostrado que la medida de este observable es realista y podrá realizarse en instalaciones de próxima generación, permitiendo extraer la anchura en medio de los mesones D. Se trataría de la primera determinación experimental de esta magnitud, ampliamente analizada desde el punto de vista teórico y con implicaciones notables para las propiedades en medio nuclear de estados exóticos como el T_{cc} y el D_{s0}^*.

Asimismo, el análisis térmico ha revelado que un baño térmico de piones a temperaturas moderadas es suficiente para modificar de manera sustancial las amplitudes de dispersión $D^{(*)}D^*$, conduciendo a la disolución de los estados T_{cc} y T_{cc}^* en torno a $T \simeq 100$–120 MeV. Este resultado sugiere que los experimentos en colisiones de iones pesados podrían aportar información clave sobre la naturaleza molecular de estos estados, en sinergia con los estudios en materia densa previstos en FAIR.

Finalmente, la exploración del sistema de tres cuerpos DND^* ha evidenciado la posibilidad de formar estados ligados de tres cuerpos impulsados por las

interacciones atractivas DN y D^*N. La predicción de estos candidatos amplía el horizonte de la espectroscopía con *charm*, conectando de manera natural con los bariones Λ_c^* ya observados.

En perspectiva, los avances teóricos aquí presentados constituyen un marco coherente y sistemático para abordar la física de hadrones exóticos en condiciones extremas. No obstante, los cálculos aquí contenidos admiten futuros refinamientos. Por ejemplo, se podrían extender los cálculos de la dinámica de tres cuerpos más allá de la FCA, incorporar sistemáticamente canales acoplados en todas las amplitudes consideradas, o estudiar los efectos de la restauración de la simetría quiral en las amplitudes DD^* a temperatura finita. Del lado experimental, la próxima generación de instalaciones (EIC, EicC, PANDA y las mejoras en RHIC y LHC) ofrece oportunidades únicas para comprobar las predicciones de este trabajo.

El progreso conjunto, tanto en el frente teórico como en el experimental, será esencial para aclarar el papel de las moléculas hadrónicas en el espectro de QCD y, en última instancia, para avanzar en la comprensión de cómo emergen los estados ligados a partir de las simetrías y dinámicas fundamentales de la interacción fuerte.